KENS REPORT-VI

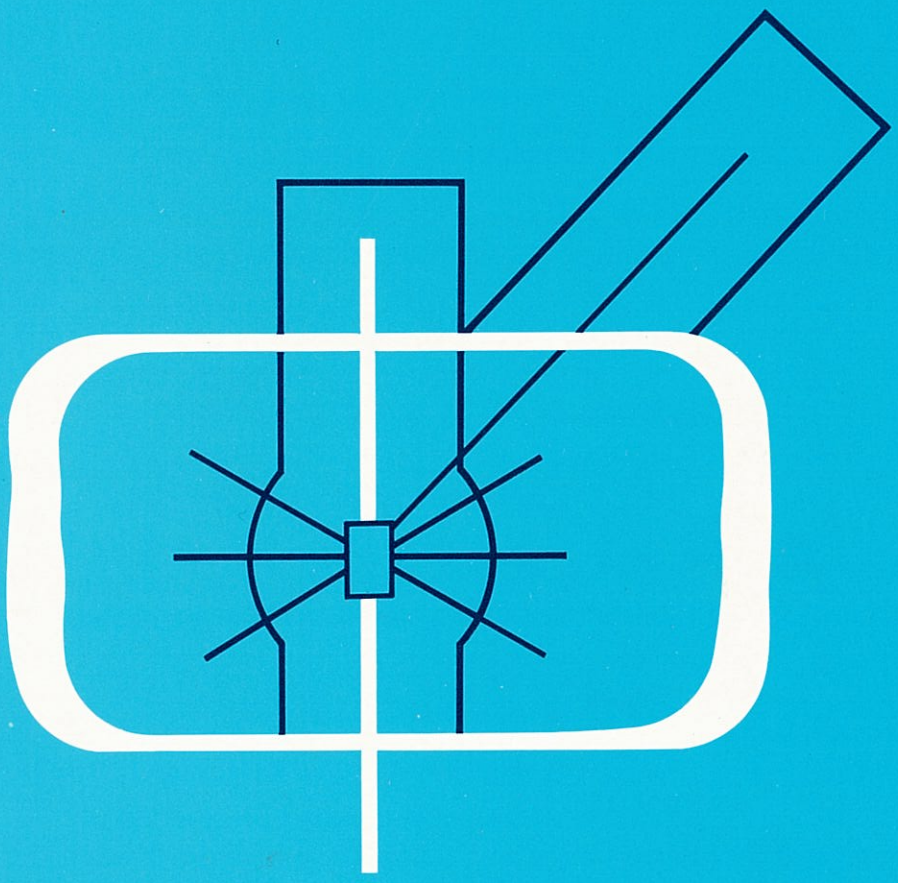

1985/86

NATIONAL LABORATORY FOR HIGH ENERGY PHYSICS, KEK

KENS REPORT-Ⅵ

1985/86

Edited by

N. WATANABE
M. ARAI
Y. ENDOH
M. KOHGI

KEK Reports are available from:

Technical Information Office
National Laboratory for High Energy Physics
Oho-machi, Tsukuba-gun
Ibaraki-ken, 305
JAPAN

Phone: 0298-64-1171
Telex: 3652-534 (Domestic)
(0)3652-534 (International)
Cable: KEKOHO

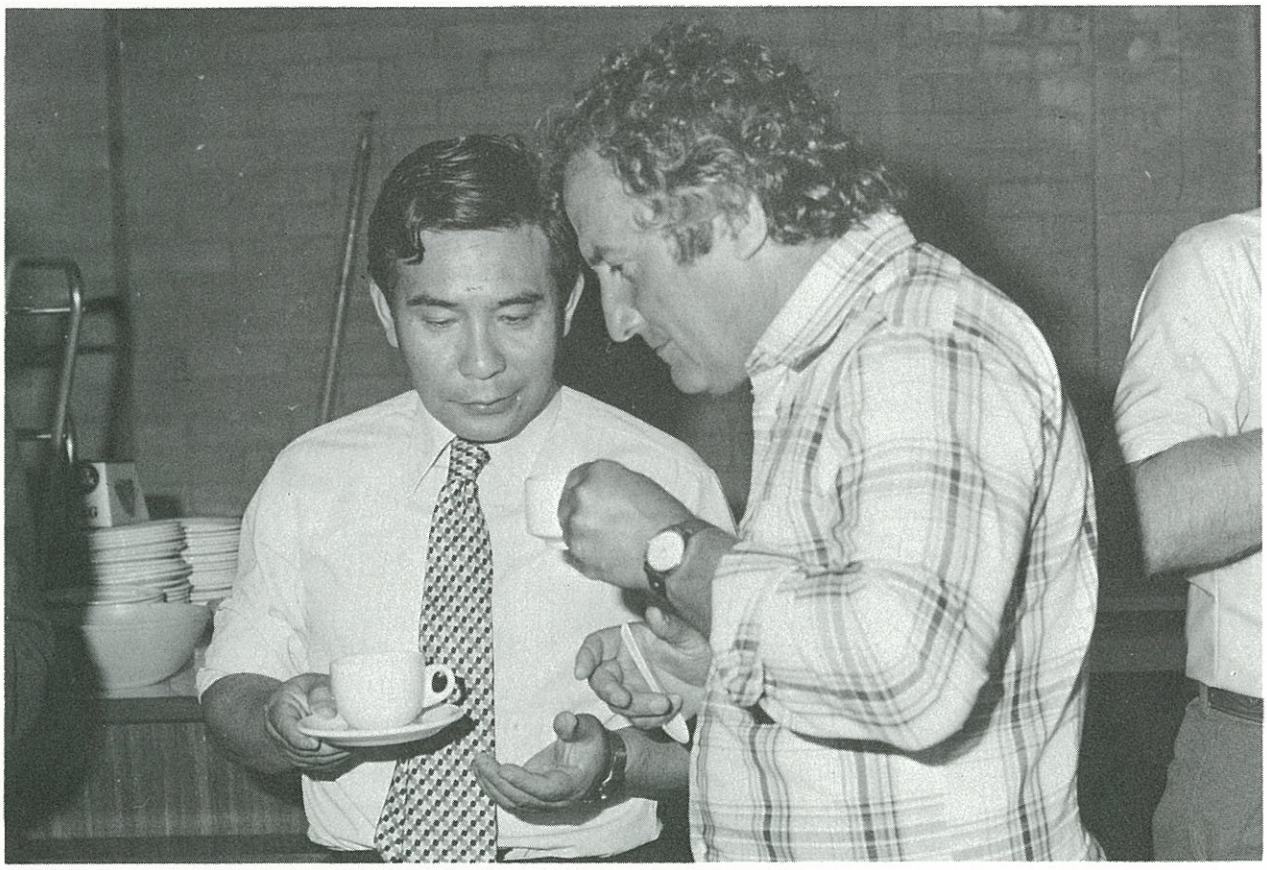

The late Prof. Yoshikazu Ishikawa, discussing with Dr. Kley in attendance at ICANS-II (the second meeting of the International Collaboration on Advanced Neutron Sources) held at Rutherford Laboratory (U.K.) on 1978.

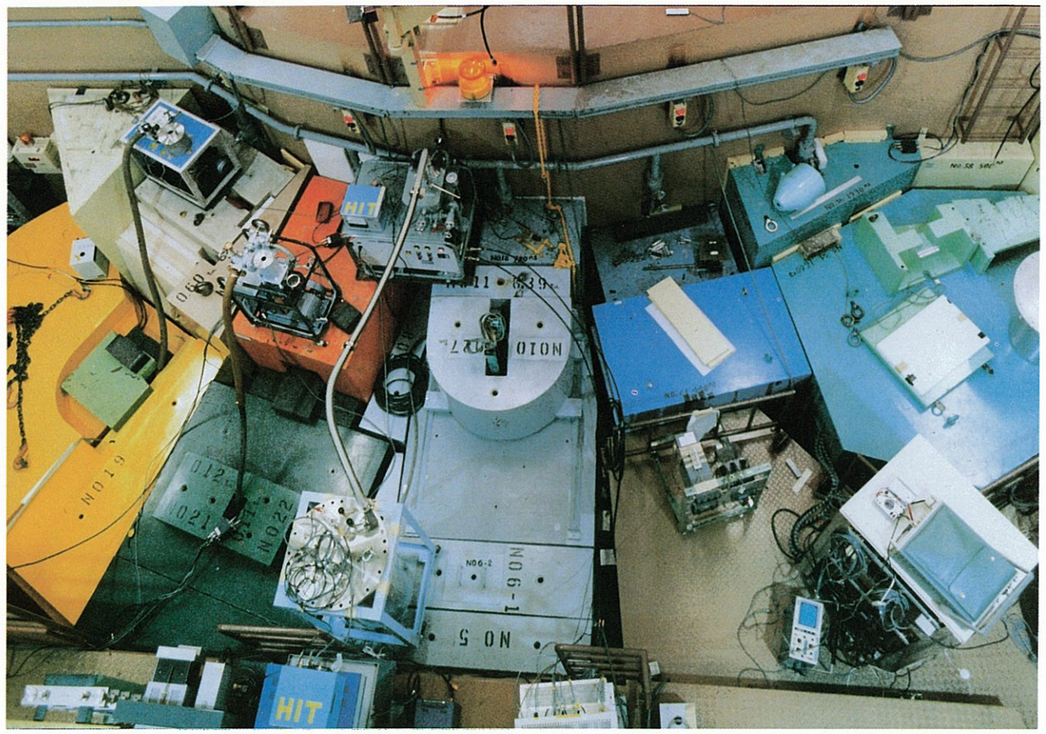

MAX, MRP, HIT, WIT, FOX

Neutron Scattering Experimental Area

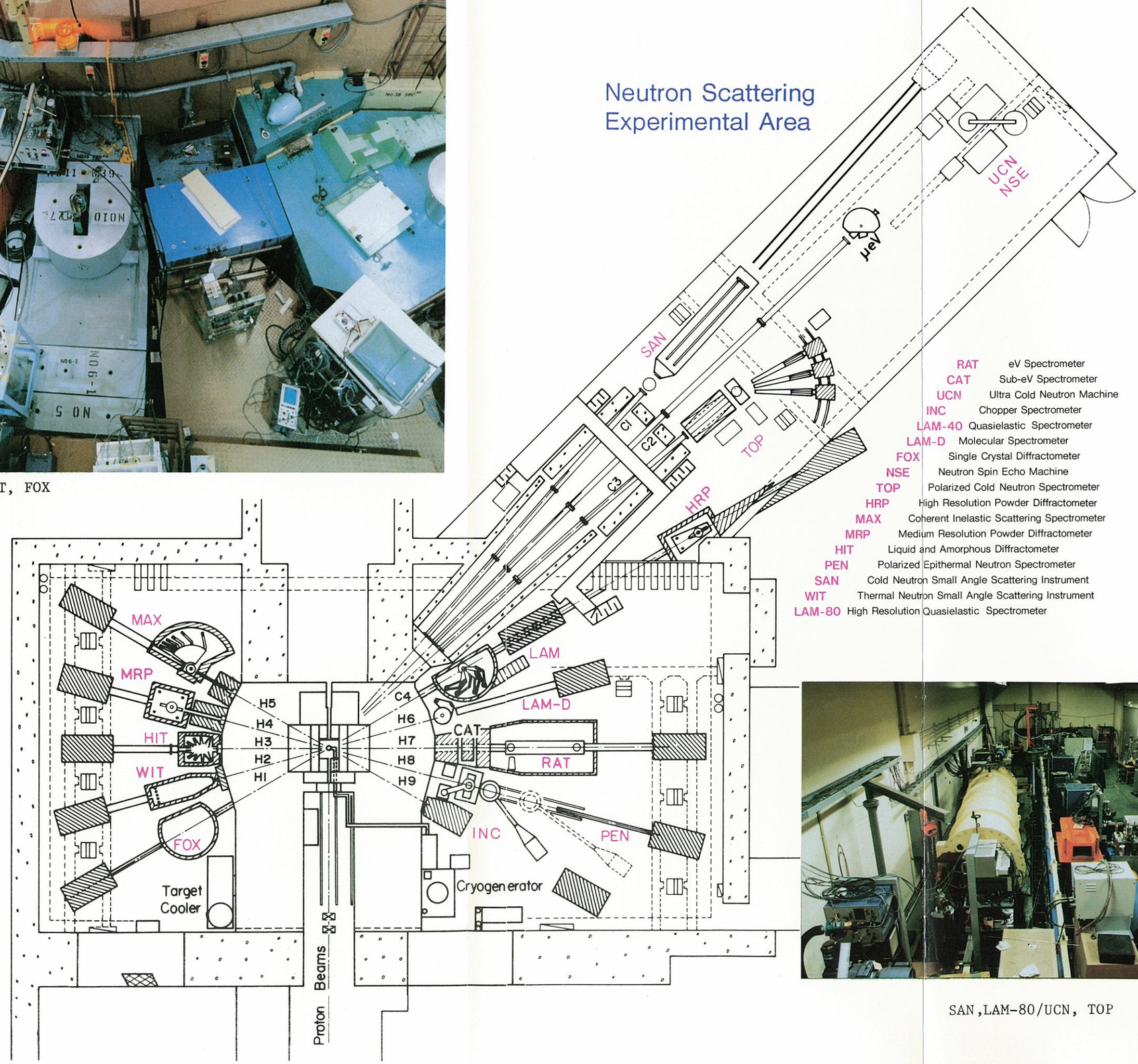

RAT eV Spectrometer
CAT Sub-eV Spectrometer
UCN Ultra Cold Neutron Machine
INC Chopper Spectrometer
LAM-40 Quasielastic Spectrometer
LAM-D Molecular Spectrometer
FOX Single Crystal Diffractometer
NSE Neutron Spin Echo Machine
TOP Polarized Cold Neutron Spectrometer
HRP High Resolution Powder Diffractometer
MAX Coherent Inelastic Scattering Spectrometer
MRP Medium Resolution Powder Diffractometer
HIT Liquid and Amorphous Diffractometer
PEN Polarized Epithermal Neutron Spectrometer
SAN Cold Neutron Small Angle Scattering Instrument
WIT Thermal Neutron Small Angle Scattering Instrument
LAM-80 High Resolution Quasielastic Spectrometer

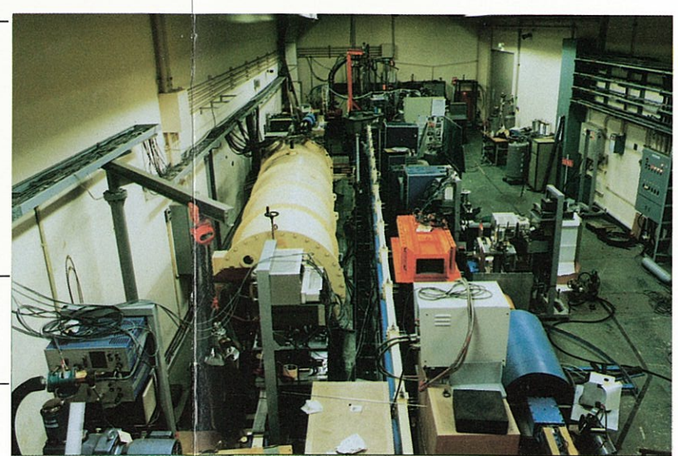

SAN, LAM-80/UCN, TOP

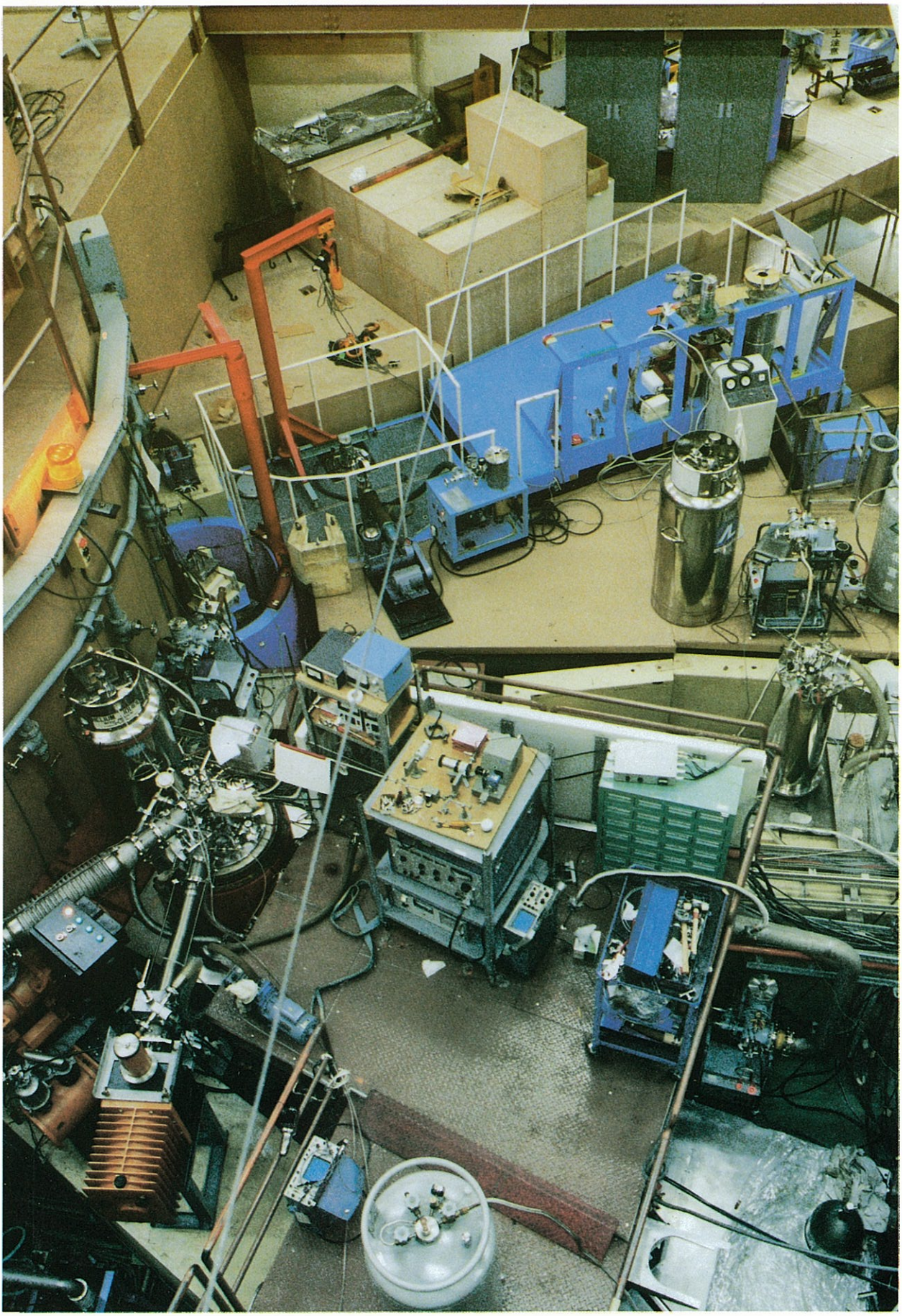

PEN, CAT/RAT, LAM-D, LAM-40

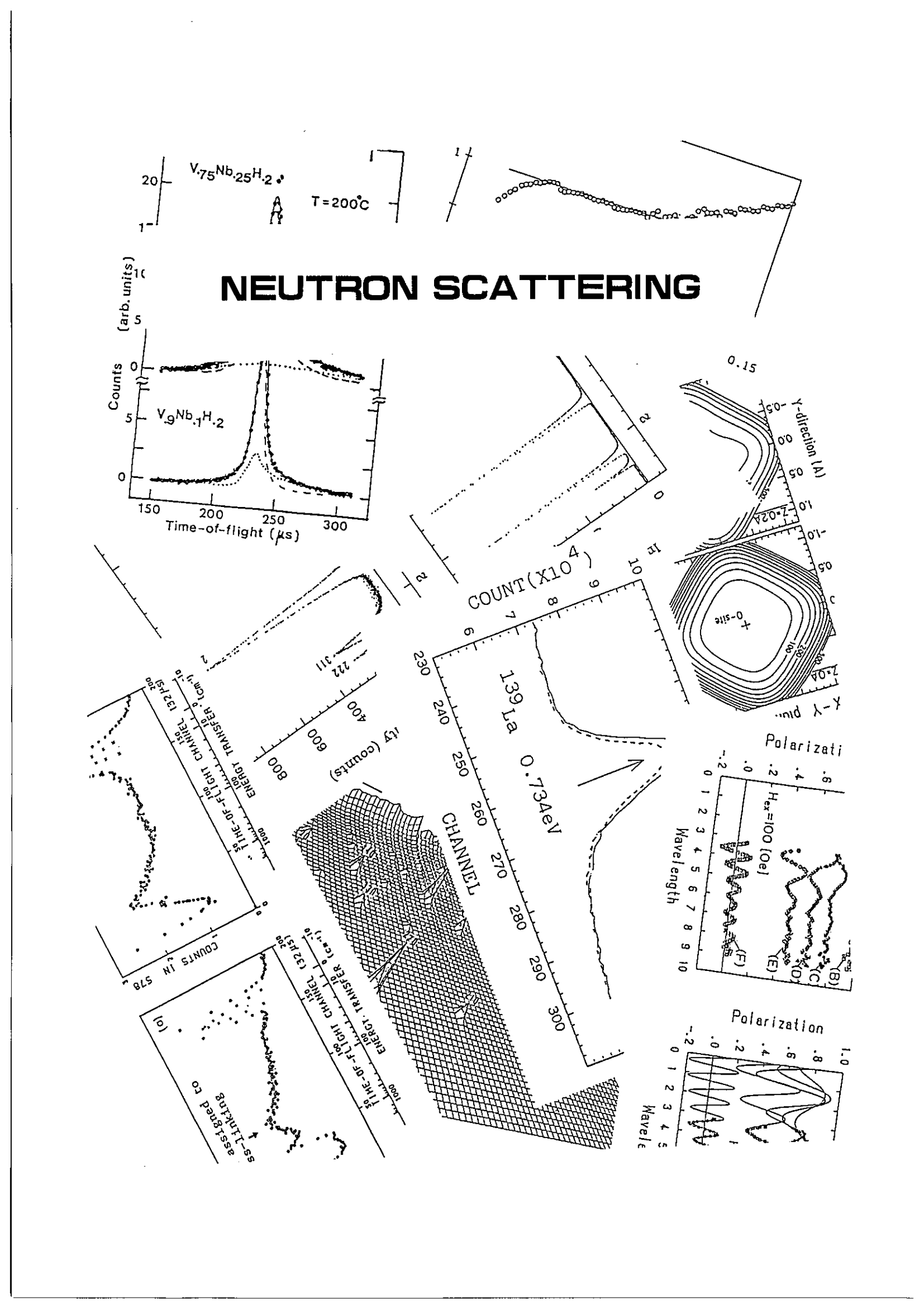
NEUTRON SCATTERING
$V_{.75}Nb_{.25}H_{.2}$
T=200°C
Counts
$V_{.9}Nb_{.1}H_{.2}$
Time-of-flight (μs)
COUNT(X10^4)
139La 0.734eV
CHANNEL
Polarization
Wavelength
Hex=100 (Oe)
Y-direction (A)
X-Y plane
Energy Transfer (cm-1)
Time-of-flight (32 μs)
COUNTS IN 578
assigned to
ss-lattice

CONTENTS

2. Structures of Liquids and Glasses

Neutron Diffraction Study on the γ Modification of Bi_2O_3

H. ASANO, K. KARAHASHI, M. UMINO, T. ISHIGAKI, F. IZUMI*, N. WATANABE**, M. HORIBE+ and N. YAMAMOTO+

Institute of Materials Science, University of Tsukuba, Sakura-mura, Ibaraki 305, Japan
*National Institute for Research in Inorganic Materials, Sakura-mura, Ibaraki 305, Japan
**National Laboratory for High Energy Physics, Oho-machi, Ibaraki 305, Japan
+College of General Education, Kyoto University, Kyoto 606, Japan

Bi_2O_3 is known to exist in four polymorphic modifications α, β, γ and δ. The α form is stable at room temperature, while the others can exist only at high temperatures above 600°C. Accordingly, the crystallographic information on β, γ and δ forms is not fully established. Craig and Stephenson[1] studied the crystal structure of sillenite ($Bi_{25}FeO_{40}$) by single crystal X-ray diffraction and proposed the end compound $Bi_{26}O_{40}$ to be the γ form of Bi_2O_3. Recently, Yamamoto and Horibe[2] prepared γ Bi_2O_3 stabilized by Fe_2O_3 under hydrothermal reaction at 100°C; Fe_2O_3 is soluble in γ Bi_2O_3 up to 80 mole %, whereas $Bi_{25}FeO_{40}$ synthesized in the dry condition exists only in a limited composition. The present work is undertaken to ascertain whether the hydrothermal product belongs to the sillenite structure and to refine the atomic parameters by means of high-resolution powder neutron diffraction.

The experiment was performed by using HRP at room temperature. The sample $Bi_{25.1}Fe_{0.9}O_{40}$ was filled in a cylindrical can (10 mm in diameter) made of 25 μm-thick vanadium foil. The counting time was 40 hours. The obtained data were analyzed by the Rietveld method using a new version of the RIETAN system described elsewhere.[3]

Figure 1 shows a Rietveld refinement pattern of γ $Bi(Fe)_2O_3$. The pattern covers a d-range of 60 - 430 pm and includes 474 reflections. The experimental data are shown by crosses and the solid line represents the Rietveld profile. Markers below the pattern indicate the Bragg positions and Δy_i is the difference between observed and calculated intensities. The crystal system belongs to cubic space group I23 with the lattice parameter

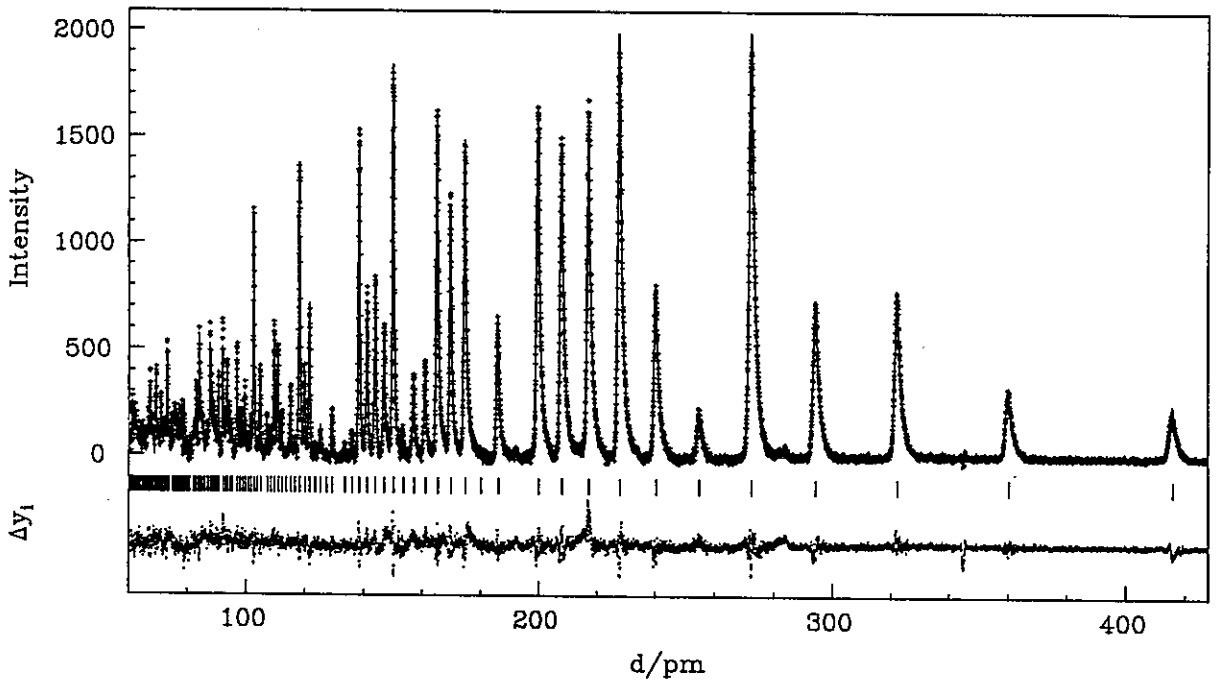

Fig. 1 Neutron diffraction pattern of γ $Bi(Fe)_2O_3$. Background is subtracted.

a = 10.1925 Å. The atomic coordinates are

(0 0 0, 1/2 1/2 1/2) +

24	Bi	in 24f: x y z etc.
2	$Bi_{0.55}Fe_{0.45}$	in 2a: 0 0 0
24	O(1)	in 24f
8	O(2)	in 8c: x x x etc.
8	O(3)	in 8c.

The refined positional and thermal parameters are listed in Table 1. The final R-factors defined by Young et al.[4] are R_{wp} = 8.5, R_p = 5.9, R_B = 4.3 and R_F = 3.9%. Positional parameters of Bi and O agree well with the previous single crystal X-ray work on $Bi_{25}FeO_{40}$.[1] In addition, the oxygen positions have been determined with better accuracy. These results indicate that $Bi(Fe)_2O_3$ synthesized under the wet condition crystallizes in the sillenite structure. Full occupation of Bi in the 2a position is naturally led to the structure of γ Bi_2O_3. On the other hand, cation distribution in Fe-rich samples is of great interest, which is now under investigation.

References

1) D. C. Craig and N. C. Stephenson: J. Solid State Chem. 15 (1975) 1.

2) H. Yamamoto and M. Horibe: unpublished work.

3) F. Izumi, H. Asano, H. Murata and N. Watanabe: in this volume.

4) R. A. Young, E. Prince and R. A. Sparks: J. Appl. Crystallogr. 15 (1982) 357.

Table 1 Crystallographic parameters of $Bi_{25.1}Fe_{0.9}O_{40}$.

	Bi	$Bi_{0.55}Fe_{0.45}$	O(1)	O(2)	O(3)
x	0.1760(4)	0	0.6352(5)	0.6911(7)	0.8924(8)
y	0.3181(3)	0	0.7518(6)	0.6911(7)	0.8924(8)
z	0.0141(4)	0	0.9875(7)	0.6911(7)	0.8924(8)
B	0.8	1.9	1.2	0.9	2.3

Determination of Cation Distribution in $M'M_2Se_4$ with HRP

Akihiko HAYASHI, Yutaka UEDA, Koji KOSUGE, Hideaki MURATA*, Hajime ASANO*
Noboru WATANABE† and Fujio IZUMI‡

Department of Chemistry, Faculty of Science, Kyoto University
Sakyo-ku, Kyoto 606, Japan

* Institute of Materials Science, University of Tsukuba
Sakura-mura Niihari-gun, Ibaraki 305, Japan

† National Laboratory for High Energy Physics
Oho-machi, Tsukuba-gun, Ibaraki 305, Japan

‡ National Institute for Research in Inorganic Materials
Sakura-mura, Niihari-gun, Ibaraki 305, Japan

The Cr_3S_4-structure (Fig. 1) is one of the vacancy-ordered structures found in 3d-transition metal chalcogenides. The structure can be described as the defective NiAs-structure which consists of hcp of chalcogen atoms with the metal atoms occupying the octahedral interstices. The metal vacancies are confined to alternate metal layers and ordered within these layers resulting in $M^fXM^vXM^fX...$ layer stacking, where M^f denotes the metal layer fully occupied with metal atoms and M^v the metal layer half-occupied with metal atoms. So this structure is characterized by two crystallographic sites for metal atoms: one in the M^v layer (2(a) site), and the other in the M^f layer (4(i) site). Hereafter the structure is referred to as $(M)[MM]X_4$, where parentheses and brackets denote the M^v and M^f layers, respectively. For the mixed-metal compounds $M'M_2X_4$ with the Cr_3S_4-structure, it arises as an interest whether a metal-ordered structure or the site preference of each metal exists or not. Chevreton and Andron[1] introduced the two types of metal-ordered structures: (i) normal-type, $(M')[MM]X_4$; (ii) inverse-

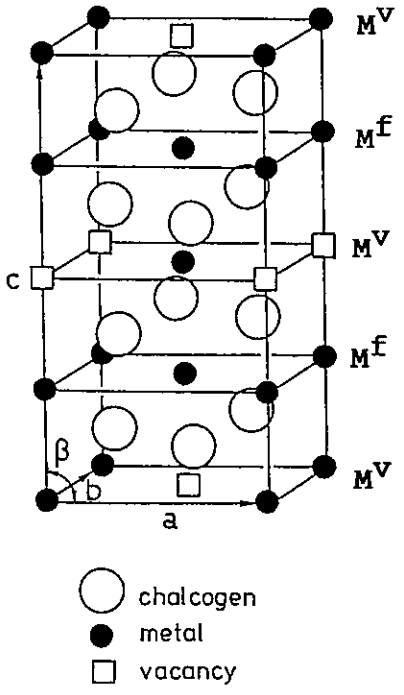

Fig. 1. Cr_3S_4-structure

type, $(M)[M'M]X_4$, on the analogy of those for spinel compound. The determination of the cation distribution for these compounds is indispensable for the interpretation of their various physical properties and chemical bonding. Transition metals M and M' are hardly distinguishable by X-ray diffraction because of their nearly equal scattering factors. So, neutron diffraction is an effective methods for this purpose[2].

Neutron diffraction experiments were carried out on four compounds, $CrTi_2Se_4$, $TiCr_2Se_4$, VTi_2Se_4 and VCr_2Se_4 using high-resolution powder diffractometer HRP[3] at KENS pulsed spallation neutron source. The resolution, $\Delta d/d$, of HRP is about 0.3 %, which is superior to that of a conventional double axis diffractometer by about one order of magnitude. The diffraction data were analyzed by the Rietveld method[4]. The assumption made prior to the refinement is that each atom site is completely occupied, that is, no vacancy exists both on metal and selenium sites. This results in the general formula for the cation configuration in the compound $M'M_2X_4$, $(M'_gM_{1-g})[M'_{1-g}M_{1+g}]X_4$, where g is the occupation factor of M' for the 2(a) site, which is the only parameter to be refined concerning the cation distribution. The occupation factor g and the atomic coordinates were determined through least-squares refinement, together with the overall temperature factor and the unit cell parameters. The obtained cation distribution is given in Table 1. The observed and calculated profiles of the four compounds are shown in Figs. 2 and 3. The experimental data are plotted by dots and the vertical markers indicate Bragg positions. The solid curve overlying the data points is a result of the Rietveld analysis and the difference ΔY between observed and calculated counts is shown by a series of dots in the bottom. As presented in Table 1, the results of the Rietveld analysis revealed that $CrTi_2Se_4$ and $TiCr_2Se_4$ has approximately the normal- and inverse-type metal-ordered structure, respectively. This showed that the Cr ions have a tendency to occupy the M^V site relative to the Ti ions. It was also determined that V ions prefer for M^V sites in VTi_2Se_4 and VCr_2Se_4, though the metal ion distributions in both compounds were rather disordered compared to the ideal one. As the results, the site preference for M^V sites among them is in order V > Cr > Ti.

Table 1. Cation Distribution in $M'M_2Se_4$

Compound	Cation Distribution
$CrTi_2Se_4$	$(Cr_{0.69}Ti_{0.31})[Cr_{0.31}Ti_{1.69}]Se_4$
$TiCr_2Se_4$	$(Ti_{0.16}Cr_{0.84})[Ti_{0.84}Cr_{1.16}]Se_4$
VTi_2Se_4	$(V_{0.60}Ti_{0.40})[V_{0.40}Ti_{1.60}]Se_4$
VCr_2Se_4	$(V_{0.55}Cr_{0.45})[V_{0.45}Cr_{1.55}]Se_4$

In the course of our study of site preference of 3d-transition metals, we proposed that the pseudo-binary system $(M'_xM_{1-x})_3X_4$ serves as a useful tool. For $(Cr_xTi_{1-x})_3Se_4$, anomaly in the compositional dependence of the lattice parameters could be correlated with the selective substitution of metal atoms[5]. The results of the present report support our simplified model that the substitution proceeds according to the site preference of each metal over the whole composition range.

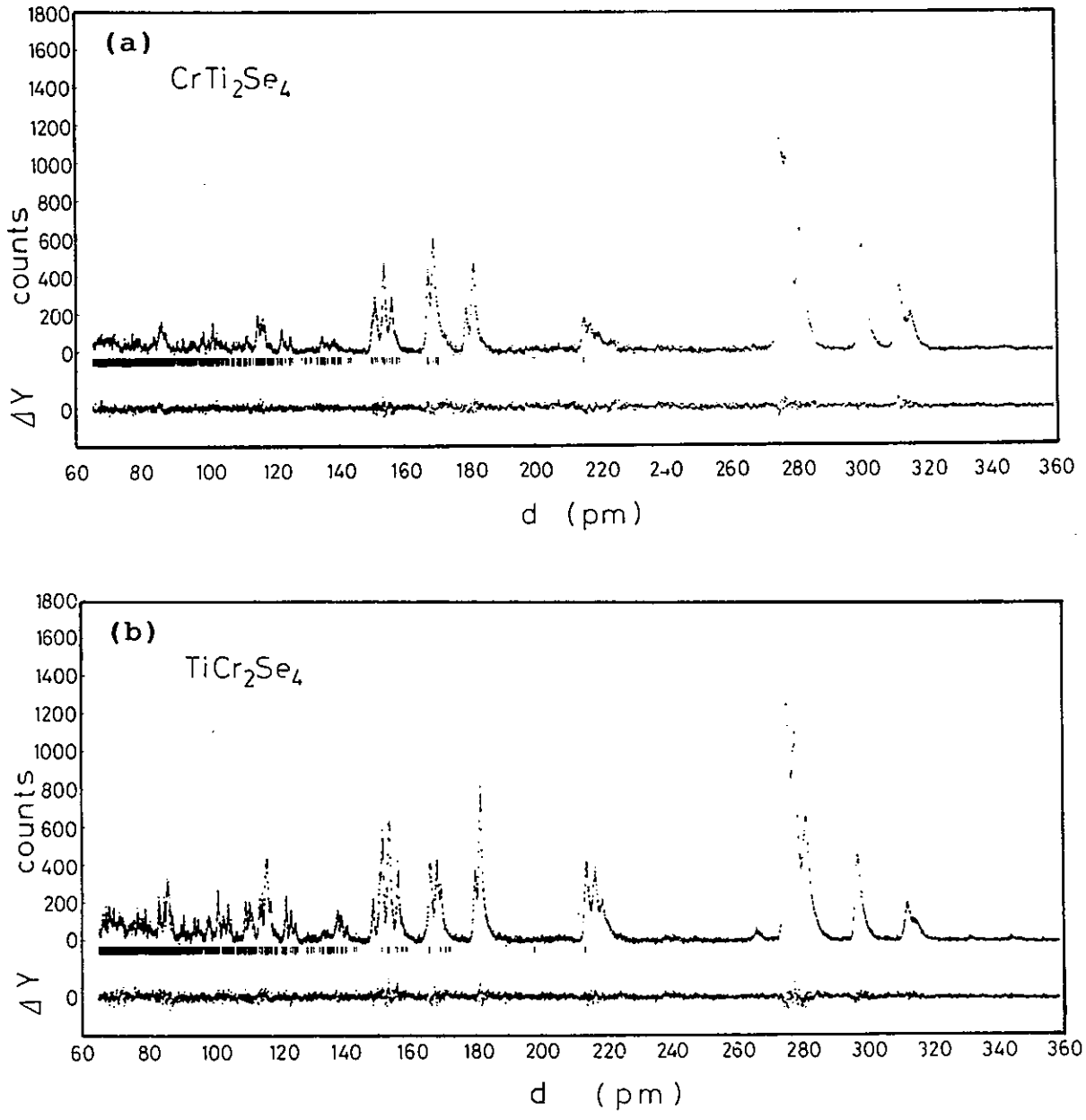

Fig. 2. Observed (dots) and calculated (solid line) neutron diffraction pattern of (a) $CrTi_2Se_4$ and (b) $TiCr_2Se_4$.

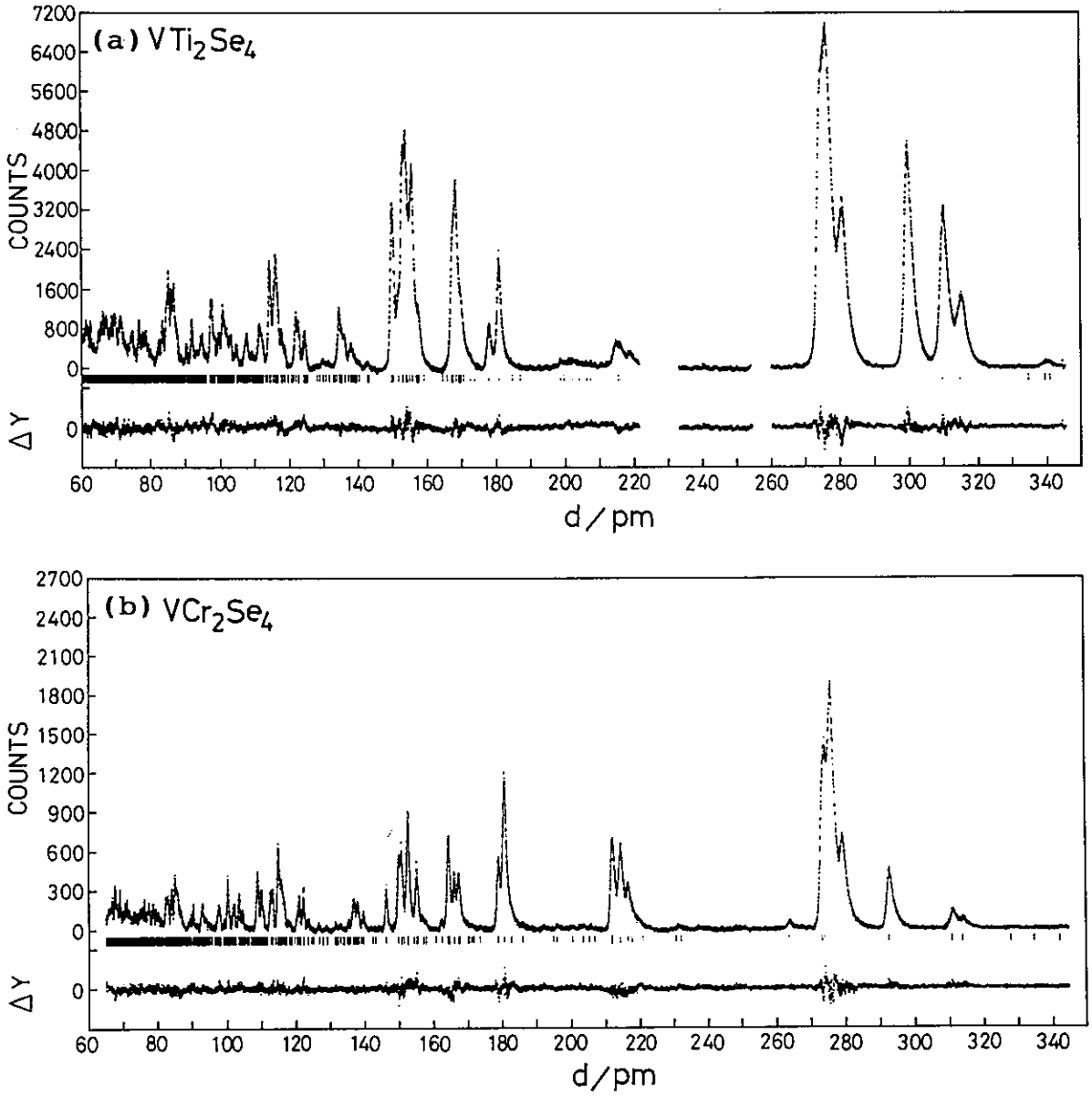

Fig. 3. Observed (dots) and calculated (solid line) neutron diffraction pattern of (a) VTi_2Se_4 and (b) VCr_2Se_4.

References

1) M. Chevreton and B. Andron, C. R. Acad. Sci. Ser. B 264, 316 (1967).

2) K. Adachi, K. Sato and K. Kojima, Mem. Fac. Eng. Nagoya Univ. 22, 253 (1970).

3) N. Watanabe, H. Asano, H. Iwasa, S. Sato, H. Murata, T. Fukiura, S. Tomiyoshi, F. Izumi and K. Inoue, KENS Report-V, KEK Progress Report 84-2, 581 (1982).

4) F. Izumi, J. Cryst. Soc. Jpn. 27, 23 (1985) [in Japanese].

5) Y. Ueda, K. Kosuge, M. Urabayashi, A. Hayashi, S. Kachi and S. Kawano, J. Solid State Chem. 56, 263 (1985).

Crystal and Magnetic Structure of Ce_2Bi and Ce_2Sb

Shigehumi ONODERA, Atsushi ISOBE*, Masahumi KOHGI*

Kazuyoshi YAMADA** , Takashi SUZUKI* and Hajime ASANO***

Sendai National College of Technology, Ayashi
Miyagi-cho Miyagi-gun, Miyagi 989-31, Japan

* Department of Physics,Tohoku University,
Sendai 980, Japan
** Laboratory of Nuclear Science, Tohoku University,
Mikamine, Sendai 980, Japan
*** Institute of Material Science, University of Tsukuba
Sakura-mura, Niihari-gun, Ibaraki 305, Japan

This paper reports preliminary results of the diffraction measurements of Ce_2Bi and Ce_2Sb with medium-resolution powder dif fractometer(MRP). Ce_2Bi and Ce_2Sb have been expected to show the anomalous magnetic properties by c-f mixing. But, there were no systematic studies about physical properties of these materials, because it is difficult to prepare and handle these samples. Recently, Isobe et al succeeded to prepare the single crystal and to measure the susceptibilities and the electrical resistivities of Ce_2Bi and Ce_2Sb. The temperature dependence of susceptibilities of Ce_2Bi and Ce_2Sb are similar to that of antiferromagnetic materials. The magnetic phase transition temperature is 8.38K in Ce_2Sb and 15K in Ce_2Bi. The temperature dependence of the electrical resistivity of the single crystal Ce_2Sb shows a large hysterisis in the temperature range from 30K to 200K, which suggests the first order phase transition. Therefore, it is interesting to investigate the crystal structure , the magnetic structure and the magnitude of the magnetic moment of Ce atoms in these materials.

Fig.1 shows the diffraction pattern for Ce_2Bi at 30K obtained by the detector fixed at a scattering angle of 150 . Fig.2 shows the diffraction pattern for Ce_2Sb at 150K. These two diffraction

patterns are normalized by the incident neutron spectrum and are used for detemination of the crystal structure above a magnetic phase transition temperature. Table 1. shows the calculated intensities and the observed intensities of Ce_2Bi and Ce_2Sb. The observed intensities were estimated separately by the profile fitting technique.[1] The calculated intensities were obtained by the following equation,

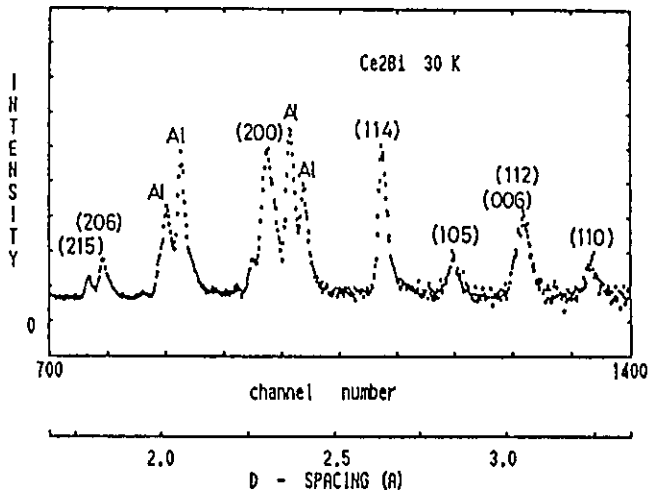

Fig.1 Diffraction pattern for Ce_2Bi at 150 K. Scattering angle is 150 degrees.

$$Ical.= k\cdot|F(h,k,l)|^2\cdot p\cdot\lambda^4$$

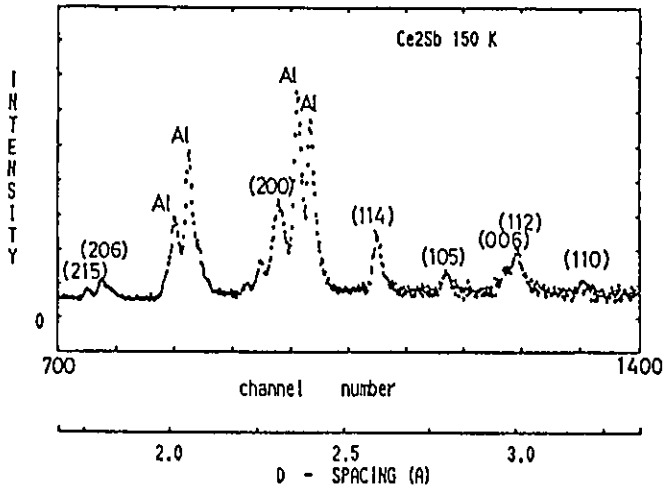

Fig.2 Diffraction pattern for Ce_2Sb at 150 K. Scattering angle is 150 degrees.

where k is a constant of the powder diffractometer, F(h,k,l) the crystal structure factor, p the multiplicity and λ the wave length of neutrons scattered at (h,k,l) reciprocal lattice point. The crystal structure was assumed to be tetragonal and atomic arrangement in Ce_2Bi and Ce_2Sb to be belong to the space group I4/ mmm (D^{17}_{4h}); 4Ce(1) in 4(c), 4Ce(2) in 4(e) with z parameter, 4Bi or 4Sb in 4(e) with z' parameter. The z and z' parameters were determined to minimize the residual between the calculated and the observed intensities. The agreement between the observed and calculated intensities is satisfactory. The obtained values of z and z' in Ce_2Bi are 0.33 and 0.136, z and z' in Ce_2Sb, 0.328 and 0.132 respectively.

Table I. Comparison between observed intensities for Ce compounds and those calculated for the tetragonal crystal structure.

	Ce2Bi		Ce2Sb	
	a=4.615 A , c=18.07 A z=0.330 , z'=0.136		a=4.538 A , c=17.71 A z=0.328 , z'=0.132	
(h,k,l)	Iobs.	Ical.	Iobs.	Ical.
1,1,0	92	135	47	83
1,1,2	226	211	248	261
0,0,6	82	113	103	113
1,0,5	92	89	117	112
1,1,4	359	362	328	334
2,0,6	105	62	118	63
2,1,5	42	28	38	35

Fig.3 shows the diffraction patterns for Ce_2Bi at 5 K and 30 K obtained by the detector fixed at a scattering angle of 30 . In this case, the white back ground and the intensities from the Al cell are subtracted. In the figure, the differnce between these two diffraction patterns is also shown. Two additional lines are observed around (004) and (101) reflections at the d-spacing 4.5 A. The displacement of these lines from the nuclear position is 0.037 A^{-1}. If these lines are magnetic satellites ,the magnetic structure has a long period and the spiral axis is parallel to a-axis by taking into account of the antisymmetric intensities of satellites. As the qther magnetic peak by the ferromagnetic or the antiferromagnetic components could not be observed, the magnetic moments on a-plane are considered to be alined ferromagnetically. The periodicity is estimated to be 36 sheets along a-axis. The magnetic moment of Ce atoms is estimated to be $3.3\mu_B$ by using the magnetic structure described above. The value is comparable to the moment $2.14\mu_B$ of free Ce^{3+} ion and suggests that the Ce atoms in Ce_2Bi have almost the same moment as the free Ce^{3+} ion. The diffraction measurement of Ce_2Sb at 4 K was also performed. The diffraction pattern at 4 K changes drastically as compared with that

at 150 K. This change might correspond to the first order phase transition predicted by the electrical resistivity. However, since there were some inconsistencies between the data at 150 K and 4K, some additional measurements and the detailed analysis based on them are required.

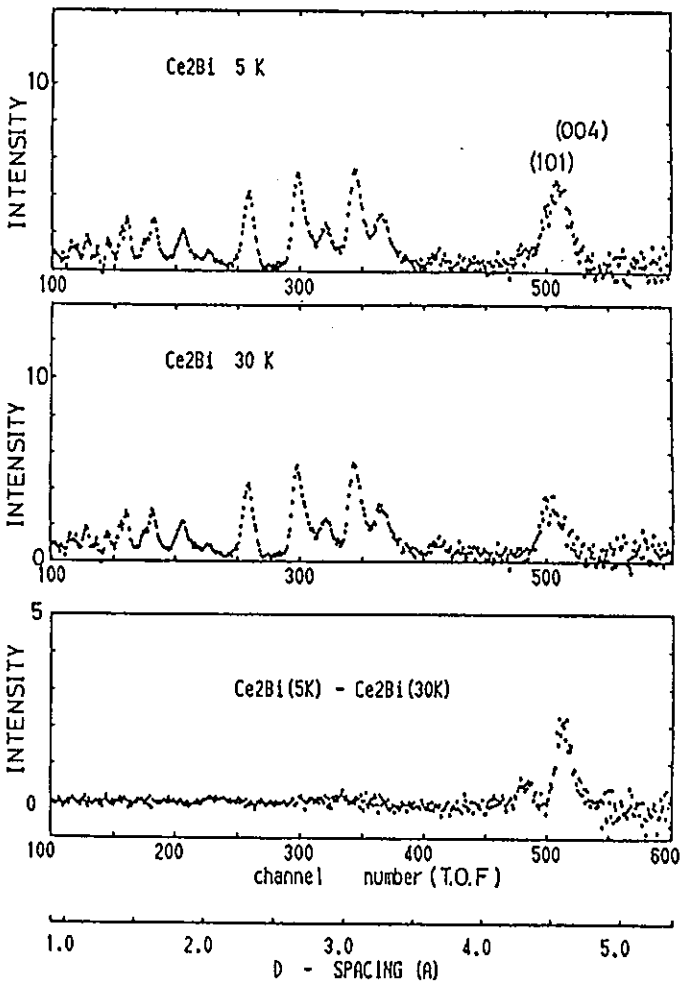

Fig.3 Diffraction patterns for Ce_2Sb at 5 K and 30 K. Scattering angle is 30 degrees. The lowest figure is the difference between the intensities at 30 K and 5 K.

Reference

1) R.B.Von Dreele, J.D.Jorgensen and C.G.Windsor:J.Appl. Cryst. 15(1982) 581

Neutron Diffraction Study of γ-TiD

H. Numakura*$, M. Koiwa*,+, H. Asano† and F. Izumi‡

* The Research Institute for Iron, Steel and Other Metals,
Tohoku University, Sendai 980, Japan
+ Department of Metal Science and Technology,
Kyoto University, Kyoto 606, Japan
† Institute of Materials Science, University of Tsukuba,
Ibaraki 305, Japan
‡ National Institute for Research in Inorganic Materials,
Ibaraki 305, Japan

Introduction

In Fig. 1 is shown the phase diagram of the Ti-H system. Titanium can absorb a considerable amount of hydrogen, and form the δ hydride (f.c.c., CaF_2-type structure) or the ε hydride (f.c.t., $c/a<1$), in which hydrogen atoms occupy tetrahedral sites of the host metal lattices. Recently we have demonstrated that, by electron diffraction and X-ray diffraction, a metastable hydride phase appears in the α+δ region and coexists with both the α titanium and the δ hydride[1,2]; this hydride phase, named γ, has a face-centred tetragonal structure with c/a = 1.09, and is analogous to the γ zirconium hydride in the Zr-H(D) system[3].

Because of its metastable nature, however, it is difficult to obtain a single phase specimen, not to mention a single crystal, of the γ titanium hydride. In order to determine the hydrogen location in the γ hydride, therefore, it is necessary to carry out a powder neutron diffraction experiment with sufficiently high resolution which enables a quantitative analysis of weak diffraction peaks from the γ phase (which is always a minor constituent). In the present note we shall report the result of such an investigation performed on deuterium-loaded specimens using a high-resolution diffractometer HRP[4] in the National Laboratory for High Energy Physics (KEK).

$ Present address: Department of Metal Science and Technology, Kyoto University, Kyoto 606, Japan

Experimental

Powder specimens of Ti-45 at.%D and Ti-60 at.%D were prepared from a commercial purity titanium metal. Both the specimens are composed of three phases, *i.e.*, α, δ and γ with volume ratios (α:δ:γ) being 0.27:0.63:0.10 and 0.03:0.88:0.09, respectively. Neutron diffraction experiments were done using a time-of-flight powder diffractometer HRP at the KENS pulsed neutron source in KEK. Diffraction data were obtained at room temperature, and were analysed by a TOF version of the Rietveld analysis code RIETAN developed by one of the present authors[5].

Results and Discussion

For both the specimens, numbers of diffraction peaks from the γ deuteride were detected although they are much weaker than those of the δ deuteride. Besides the fundamental reflections of the f.c.t. metal lattice, *i.e.*, of indices h,k,l = all even or all odd, extra reflections due to deuterium atoms are observed; the indices of the latter are found to satisfy the condition 'h,k = odd, l = even', *e.g.*, 110, 112, 312 ...etc. The existence of this type of reflections have been recognized in the previous electron diffraction study[1], and so hydrogen atoms have been considered to be ordered in the same way as the γ zirconium deuteride studied by Sidhu *et al.*[3] The structure model of the γ zirconium deuteride proposed by those authors is illustrated in Fig. 2. The present diffraction data show qualitative agreement with this model. Therefore, the structure of the γ phase can be described by the space group $P4_2/ncm$ with the following atomic positions:

4 Ti in 4c: 1/4,1/4,1/4; 3/4,3/4,1/4; 1/4,3/4,3/4; 3/4,1/4,3/4,

4 D in 4b: 0,0,0; 0,0,1/2; 1/2,1/2,0; 1/2,1/2,1/2,

assuming the occupation probability of deuterium to be unity. The space groups $P4_2/n$ and $P4_2/nnm$ are equally possible.

Nevertheless, the diffraction pattern of the γ deuteride exhibits a notable feature that the *hkl*-type reflections have broader widths systematically than *hhl*-reflections. Figure 3 shows a part of the raw diffraction data for a Ti-60 at.%D specimen; to take an example, the 200 reflection from the γ phase is broader than the other reflections from the same phase. Therefore, it is probable that the unit cell of the γ deuteride

is not tetragonal but slightly orthorhombic*, in which the atomic arrangements being essentially the same as Fig. 2. In that case the structure belongs to the space group Ccc2, with the co-ordinates of atoms

(0,0,0; 1/2,1/2,0)+

4 Ti in 4c: 1/4,1/4,z; 1/4,3/4,1/2+z,

4p_D D in 4a: 0,0,z; 0,0,1/2+z,

where z=1/4 for the former and z=0 for the latter, and p_D is the occupation probability of D atoms. The Rietveld analysis based on the above model have shown reasonable agreement between the calculated- and the observed diffraction intensities, with a residual factor R_{wp} being 6.9 %; the two a-axes (strictly, the a-axis and the b-axis) differ by 1 % in length from each other, *i.e.*, a = 0.419 nm, b = 0.423 nm, and c = 0.458 nm. More detailed description of the result of the present analysis will be published elsewhere.

Acknowledgements - The authors are grateful to Professor N. Watanabe for the arrangements for the neutron diffraction experiment. They also wish to thank Mr H. Murata for his technical assistance throughout the study.

References

1. H. Numakura and M. Koiwa, *Acta Metall.* 32, 1799 (1984).
2. H. Numakura, M. Koiwa, H. Asano, H. Murata and F. Izumi, *Scripta Metall.* 20, 214 (1986).
3. S. S. Sidhu, N. S. Satya Murthy, F. P. Campos and D. D. Zauberis, *Adv. Chem. Ser.* 39, 87 (1963).
4. N. Watanabe, H. Asano, H. Iwasa, S. Sato, H. Murata, T. Fukiura, S. Tomiyoshi, F. Izumi and K. Inoue, *KENS Report-V, KEK Prog. Rep.* 84-2, 93 (1984).
5. F. Izumi, *J. Crystallogr. Soc. Japan* 27, 23 (1985).

---

* Higher order reflections, *e.g.*, 400, are expected to be split into two peaks owing to the more improved resolution at lower d-spacings. However, such clear evidence has not been obtained due to the weak intensities.

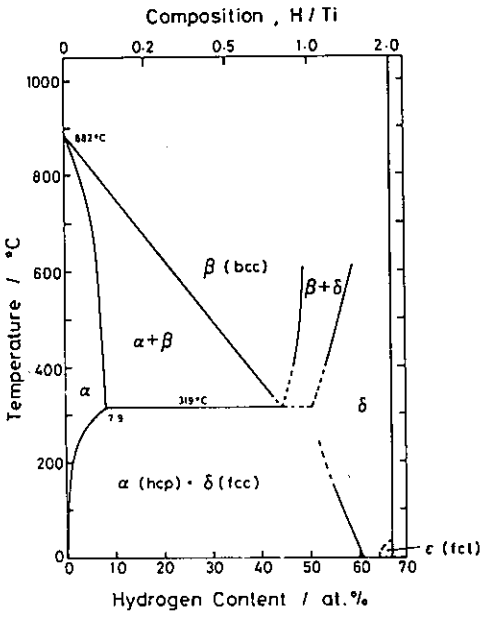

Fig. 1. The phase diagram of the Ti-H system.

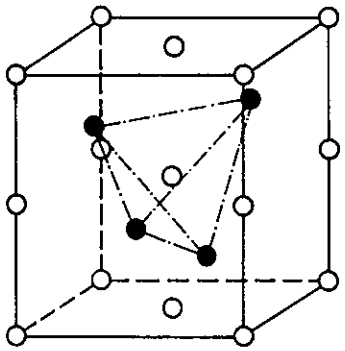

Fig. 2. The tetragonal unit cell of the γ zirconium deuteride (c/a = 1.08). Filled circles indicate positions of the metal atoms and open circles those of deuterium atoms.

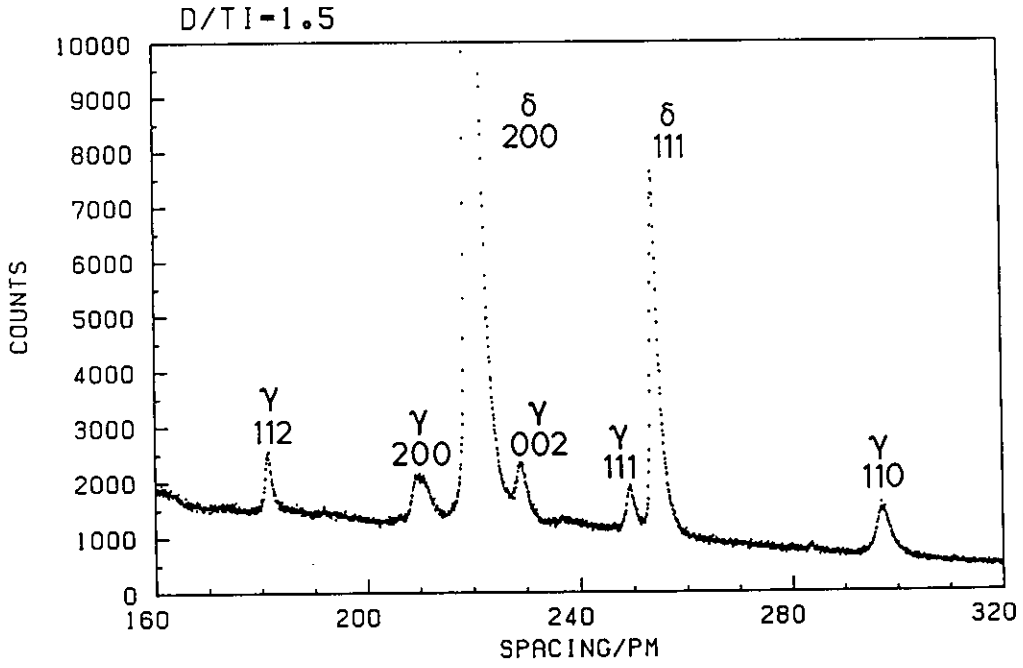

Fig. 3. A part of a TOF powder neutron diffraction pattern of a Ti-60 at.% specimen obtained by HRP. Note the broadness of the 200 diffraction peak from the γ' titanium deuteride.

Low-Temperature Monoclinic Modification of $LaCu_6$ and $CeCu_6$

M. UMINO, H. ASANO, Y. ŌNUKI, T. KOMATSUBARA,
F. IZUMI* and N. WATANABE**

Institute of Materials Science, University of Tsukuba
Sakura-mura, Ibaraki 305, Japan

**National Institute for Research in Inorganic Materials*
Sakura-mura, Ibaraki 305, Japan

***National Laboratory for High Energy Physics*
Oho-machi, Ibaraki 305, Japan

The RCu_6 compound (R = Ce, Pr, Nd, Sm and Gd) crystallizes with an orthorhombic $CeCu_6$-type structure[1] of space group *Pnma*. The crystal structure of $LaCu_6$ has been considered so far to be the same as $CeCu_6$.[2,3] Cirafici and Palenzona[2] reported from single crystal X-ray diffraction that $LaCu_6$ was isomorphic with $CeCu_6$. However, the same authors pointed out that the powder X-ray diffraction pattern of $LaCu_6$ could not fully be accounted for by the $CeCu_6$ structure. In fact, careful examination of the Laue photograph on $LaCu_6$ used in ref. 3) revealed several irrational reflections, which motivated us to reinvestigate the crystal structure of $LaCu_6$.[4]

The crystal structure of $LaCu_6$ was studied by an X-ray precession method and powder X-ray diffractometry in conjunction with the Rietveld analysis. The X-ray precession photographs indicate that the unit cell of $LaCu_6$ is slightly deformed from orthorhombic to monoclinic. From the extinction rule for reflections, it is concluded that the space group is $P2_1/c$. We can rewrite the atomic positions of orthorhombic $CeCu_6$ in terms of the monoclinic space group $P2_1/c$. Using these atomic parameters as initial parameters and taking account of the monoclinic deformation, powder X-ray diffraction data were analyzed by the Rietveld method using the RIETAN system.[5] The determined positional parameters are listed in Table 1. The atomic coordinates of $LaCu_6$ do not differ appreciably from

Table 1. Atomic coordinates of monoclinic $LaCu_6$ and $CeCu_6$.

Atom	Position	x	y	z
La	4*e*	0.262(2)	0.434(1)	0.248(1)
Cu_1	4*e*	0.016(3)	0.192(2)	0.440(2)
Cu_2	4*e*	0.491(3)	0.198(2)	0.434(2)
Cu_3	4*e*	0.246(4)	0.144(2)	0.148(2)
Cu_4	4*e*	0.273(3)	0.748(1)	0.810(2)
Cu_5	4*e*	0.226(3)	0.594(2)	0.540(2)
Cu_6	4*e*	0.246(3)	0.517(2)	0.894(2)
Ce	4*e*	0.257(1)	0.436(1)	0.258(1)
Cu_1	4*e*	0.008(1)	0.188(1)	0.437(1)
Cu_2	4*e*	0.497(1)	0.192(1)	0.432(1)
Cu_3	4*e*	0.242(1)	0.140(1)	0.146(1)
Cu_4	4*e*	0.253(1)	0.757(1)	0.819(1)
Cu_5	4*e*	0.230(1)	0.594(1)	0.562(1)
Cu_6	4*e*	0.248(1)	0.517(1)	0.900(1)

the initial parameters, *i. e.* the atomic positions in orthorhombic $CeCu_6$. Accordingly, it is concluded that the crystal structure of $LaCu_6$ is a slight modification of orthorhombic $CeCu_6$ accompanied by monoclinic deformation and minor shift of the atomic positions. The refined lattice parameters are $a = 0.5143$ nm, $b = 1.0204$ nm, $c = 0.8144$ nm and $\beta = 91.49°$. Final R-factors are $R_{wp} = 3.3$, $R_p = 2.5$ and $R_B = 7.2$ %.

Recently, it was found that monoclinic $LaCu_6$ transforms to orthorhombic at about 500 K.[6] In addition, Ōnuki *et al.*[7] showed in a pseudobinary system $La_{1-x}Ce_xCu_6$ that the stable form at room temperature is monoclinic in $x = 0 - 0.28$ and orthorhombic for $x > 0.28$. It is likely that the monoclinic-orthorhombic transition temperature lowers with increasing Ce concentration and tends to 168 K in $CeCu_6$ suggested by the anomaly of elastic constants.[8]

Preliminary X-ray powder diffraction on $CeCu_6$ at 89 K showed an appearance of the monoclinic symmetry.[7] However, X-ray powder diffractometry of $CeCu_6$ as well as $LaCu_6$ suffered from a considerable preferred orientation effect. Accordingly, we performed high resolution neutron powder diffraction using HRP at 65 K in order to determine the

crystal structure of monoclinic $CeCu_6$.[8] The obtained diffraction data were anlyzed by the RIETAN system. Figure 1 shows the Rietveld refinement pattern of $CeCu_6$ at 65 K. The diffraction pattern covers a d-range from 60 to 300 pm and includes 1979 reflections. Final structural parameters are listed in Table 1. The atomic coordinates of monoclinic $CeCu_6$ are almost identical with those of $LaCu_6$, which indicates that two substances are isomorphic. It is also evident that these atomic positions do not differ appreciably from those determined for orthorhombic $CeCu_6$.[1] The refined lattice parameters are $a = 0.5080$ nm, $b = 1.0121$ nm, $c = 0.8067$ nm and $\beta = 91.36°$. Final R-factors are $R_{wp} = 6.7$, $R_p = 5.1$ and $R_B = 3.8$ %.

In conclusion, we determined the crystal structure for low-temperature forms of $LaCu_6$ and $CeCu_6$ to be monoclinic with space group $P2_1/c$. The structure is derived from orthorhombic $CeCu_6$ by monoclinic deformation and minor shift of the atomic positions.

References

1) D. T. Cromer, A. C. Larson and R. B. Roof, Jr. : Acta Crystallogr. 13(1960)913.
2) S. Cirafici and A. Palenzona : J. Less-Common Metals 53(1977)199.
3) Y. Ōnuki, Y. Shimizu and T. Komatsubara : J. Phys. Soc. Jpn. 53(1984)1210.
4) H. Asano, M. Umino, Y. Hataoka, Y. Shimizu, Y. Ōnuki, T. Komatsubara and F. Izumi : J. Phys. Soc. Jpn. 54(1985)3358.
5) F. Izumi : J. Cryst. Soc. Jpn. 27(1985)23 [in Japanese].
6) Y. Endoh : private communication.
7) Y. Ōnuki, Y. Shimizu, M. Nishihara, Y. Machii and T. Komatsubara : J. Phys. Soc. Jpn. 54(1985)1964.
8) T. Suzuki, T. Goto, A. Tamaki, T. Fujimura, Y. Ōnuki and T. Komatsubara : J. Phys. Soc. Jpn. 54(1985)2367.
9) H. Asano, M. Umino, Y. Ōnuki, T. Komatsubara, F. Izumi and N. Watanabe : J. Phys. Soc. Jpn. 55(1986)454.

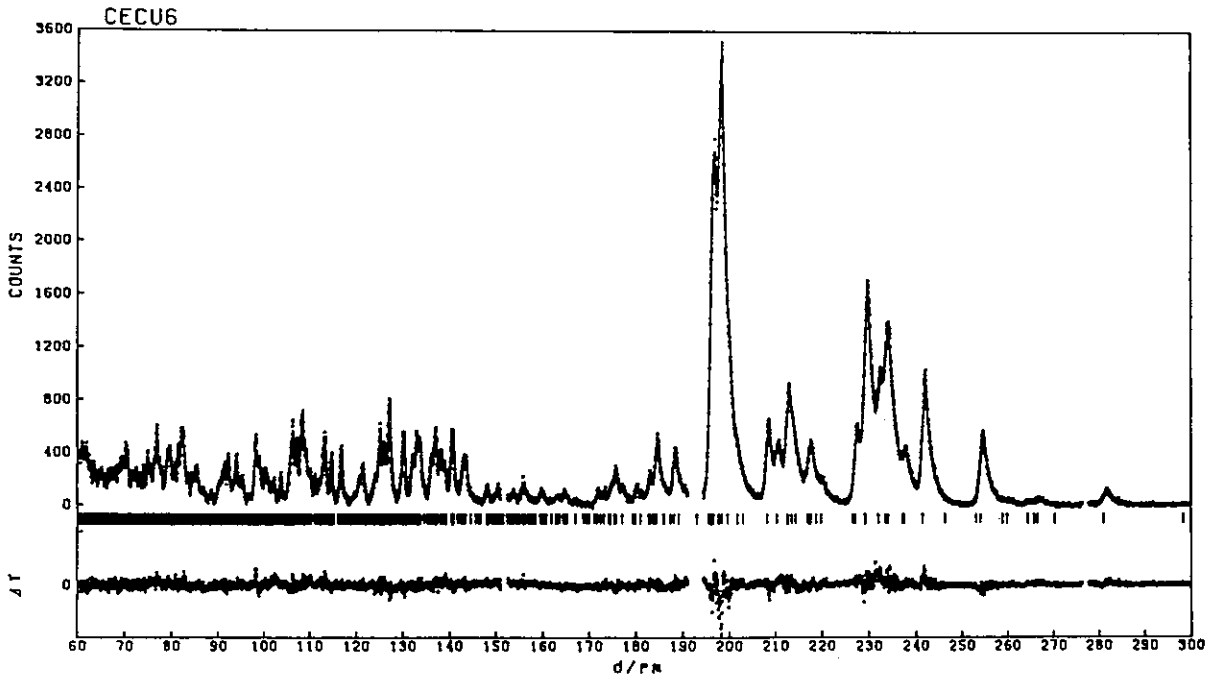

Fig. 1 Neutron diffraction pattern of monoclinic $CeCu_6$ at 65 K

Neutron Diffraction Study of $BaPb_{0.75}Bi_{0.25}O_3$

H. ASANO, K. KARAHASHI, M. UMINO, T. ISHIGAKI, F. IZUMI*, N. WATANABE**, Y. ENDOH[+], M. ODA[‡] and Y. HIDAKA[‡]

Institute of Materials Science, University of Tsukuba, Sakura-mura, Ibaraki 305, Japan

*National Institute for Research in Inorganic Materials, Sakura-mura, Ibaraki 305, Japan

**National Laboratory for High Energy Physics, Oho-machi, Ibaraki 305, Japan

[+]Department of Physics, Tohoku University, Sendai 980, Japan

[‡]Ibaraki Electrical Communication Laboratory, NTT, Tokai-mura, Ibaraki 319-11, Japan

$BaPb_{1-x}Bi_xO_3$ (BPB) crystallizes in a distorted perovskite structure and exhibits superconductivity around x = 0.25.[1] The crystal structure has been studied by several authors[2-4] as a fuction of composition x. Cox and Sleight[2] reported distinct structural changes with x; orthorhombic below x = 0.05, tetragonal in x = 0.05 - 0.35, orthorhombic in x = 0.35 - 0.9 and monoclinic above x = 0.9. On the other hand, Khan et al.[3] and Oda et al.[4] showed that the structure is orthorhombic in the whole composition range up to x = 0.9. Recently, Oda et al.[5] reported occurrence of both tetragonal and orthorhombic structures at x = 0.25 depending on growth condition of the sample. In the present work, crystal structures of tetragonal and orthorhombic samples with x = 0.25 have been investigated by high-resolution powder neutron diffraction.

The experiment was carried out by using HRP at room temperature and 47 K. The sample was filled in a vanadium sample holder. The counting time

was 40 hours. The obtained data were analyzed by the Rietveld method using a new version of the RIETAN system.[6)]

Figure 1 shows the Rietveld refinement patterns of tetragonal and orthorhombic BPB. The structure model for tetragonal BPB (x = 0.3) has been

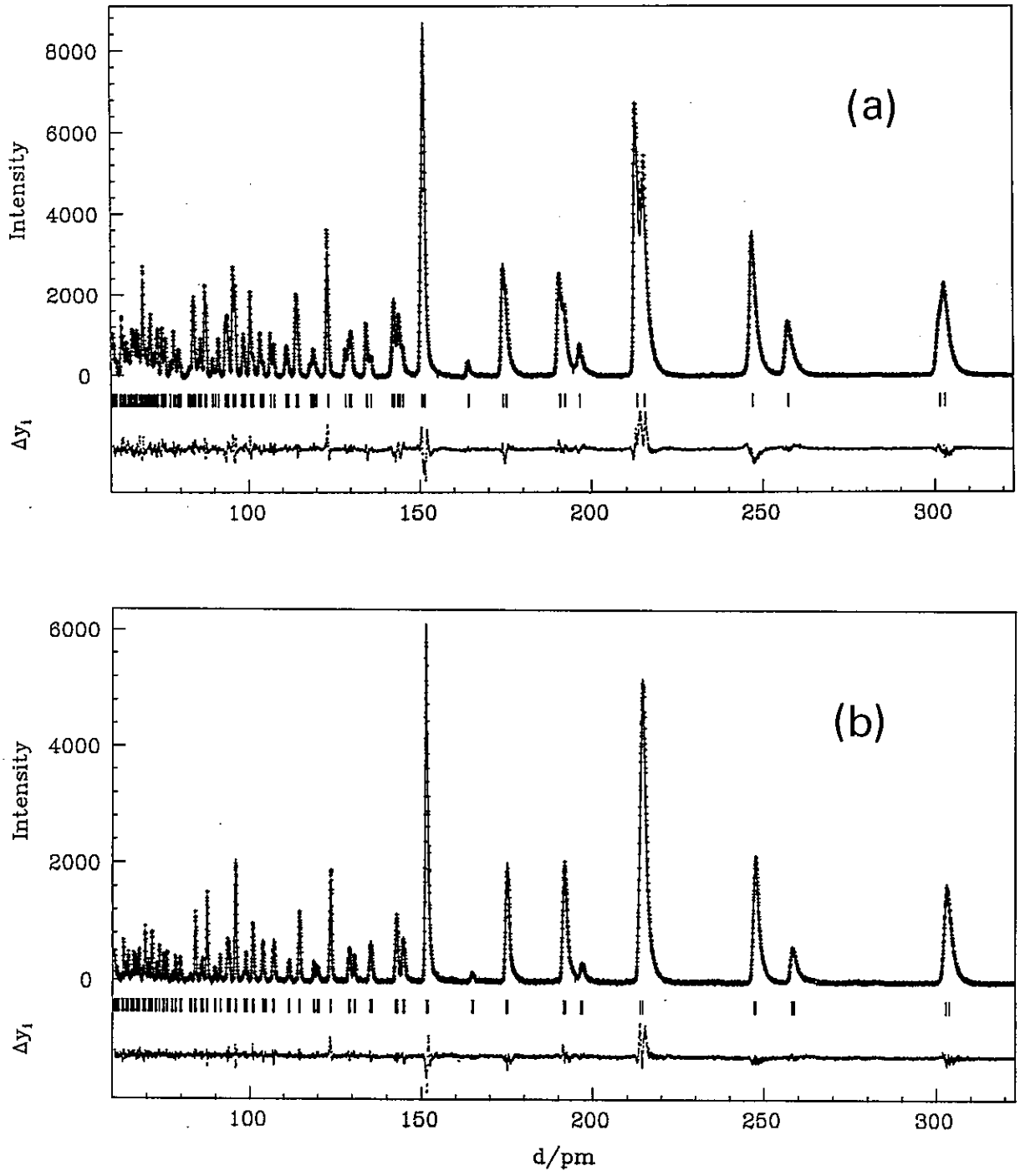

Fig. 1 Neutron diffraction patterns of (a) tetragonal BPB at 47 K and (b) orthorhombic BPB at room temperature.

given in the neutron diffraction work of Cox and Sleight.[2] The crystal system belongs to space group I4/mcm. The atomic coordinates are

4 Ba	in 4b: 0 1/2 1/4
4 $Pb_{0.75}Bi_{0.25}$	in 4c: 0 0 0
8 O(1)	in 8h: x x+1/2 0
4 O(2)	in 4a: 0 0 1/4.

The refined lattice parameters are a = 6.0315(7) and c = 8.6179(9) Å, where a and c relate to the original perovskite structure with a pseudocubic lattice parameter a_o in terms of $a = \sqrt{2}a_o$ and $c = 2a_o$. Final positional and thermal parameters are listed in Table 1. The present results agree with those of Cox and Sleight.[2] Final R-factors are R_{wp} = 9.4, R_p = 7.7, R_B = 5.3 and R_F = 2.6%. The room temperature result on the same sample is also consistent with Table 1.

Table 1 Crystallographic parameters of tetragonal BPB.

	Ba	$Pb_{0.75}Bi_{0.25}$	O(1)	O(2)
x	0	0	0.2121(6)	0
y	0.5	0	0.7121(6)	0
z	0.25	0	0	0.25
β_{11}	0.001(1)	0.000(1)	0.001(1)	0.006(2)
β_{22}	0.001(1)	0.000(1)	0.001(1)	0.006(2)
β_{33}	0.001(1)	0.000(1)	0.003(1)	0.003(1)
β_{12}	-	-	0.002(1)	-

The neutron diffraction result of orthorhombic BPB was analyzed by the structure model for $BaPbO_3$. The crystal system belongs to space group I/mma. The atomic coordinates are

4 Ba	in 4e: 0 1/4 z
4 $Pb_{0.75}Bi_{0.25}$	in 4a: 0 0 0
8 O(1)	in 8g: 1/4 y 1/4
4 O(2)	in 4e: 0 1/4 z.

The refined lattice parameters are a = 6.0583(6), b = 8.5492(8) and c = 6.0756(6) Å, where $a \sim c \sim \sqrt{2}a_o$ and $b = 2a_o$. The refined atomic parameters are listed in Table 2. Final R-factors are $R_{wp} = 8.0$, $R_p = 6.3$, $R_B = 5.2$ and $R_F = 2.5\%$. The present sample is known to undergo structural phase transition to monoclinic at 160 K.[4] Neutron diffraction work on this sample at low temperature is under way and the result will appear soon.

References

1) A. W. Sleight, J. L. Gillson and P.E. Bierestedt: Solid State Commun. 17 (1975) 27.

2) D. E. Cox and A. W. Sleight: Proc. Conf. Neutron Scattering, Gatlinburg (1976) 45.

3) Y. Khan, K. Nahm, M. Rosenberg and H. Willner: phys. stat. sol. (a) 39 (1977) 79.

4) M. Oda, Y. Hidaka, A. Katsui and T. Murakami: Solid State Commun. 55 (1985) 423.

5) M. Oda, Y. Hidaka, A. Katsui and T. Murakami: to appear in Solid State Commun.

Table 2 Crystallographic parameters of orthorhombic BPB.

	Ba	$Pb_{0.75}Bi_{0.25}$	O(1)	O(2)
x	0	0	0.25	0
y	0.25	0	0.977(1)	0.25
z	0.497(3)	0	0.25	0.044(2)
β_{11}	0.014(4)	0.005(2)	0.009(3)	0.022(6)
β_{22}	0.001(1)	-0.001(1)	0.004(1)	0.000(1)
β_{33}	0.003(3)	0.006(2)	0.005(3)	0.011(3)
β_{13}	-	-	-0.002(1)	-
β_{23}	-	0.001(1)	-	-

Structural Study of Single Crystal $BaPb_{1-x}Bi_xO_3$(x=0.25) by Neutron Diffraction

A. MASAKI, M. ISOBE*, F. P. OKAMURA*, N. NIIMURA**, H. HORIUCHI***, H. TAKAGI, S. UCHIDA, K. KITAZAWA, S. TANAKA and A. KATSUI****

Department of Applied Physics, Faculty of Engineering,
University of Tokyo, Hongo, Tokyo 113, Japan

*National Institute for Research in Inorganic Materials,
Sakura-mura, Ibaraki 305, Japan

**Laboratory of Nuclear Science, Tohoku University, Sendai 982, Japan

***Mineralogical Institute, Faculty of Science,
University of Tokyo, Hongo, Tokyo 113, Japan

****Ibaraki Electrical Communication Laboratory, NTT,
Tokai-mura, Ibaraki 319-11, Japan

$BaPb_{1-x}Bi_xO_3(0\leq x\leq 1)$ has distorted perovskite-type structure. It shows the superconductivity at the highest temperature among the non-transition metal compounds at x=0.25, whereas at about x=0.35, it exhibits a metal-semiconductor transition.[1-3] Electron-phonon interactions are considered to contribute largely to these properties.[4] In order to investigate the phonon modes for such strong coupling system, e.g. breathing mode phonons, it is essential to know the displacement of oxygen atoms in the structure. Neutron diffraction method is more favorable than X-ray diffraction method for the precise determination of the displacement, since all of the constituent elements other than oxygen, namely Bi, Pb and Ba, are heavy elements. Cox and Sleight[5] reported that the crystal symmetry of the compound varies with x; orthorhombic (x=0-0.05), tetragonal (x=0.05-0.35), orthorhombic (x=0.35-0.9) and monoclinic (x=0.9-1), and that the deviation from the ideal perovskite structure comes from nearly rigid rotations of oxygen octahedra. As a preliminary crystal chemical study on this system, structure of the crystal with composition x=0.25, was investigated. The

specimen crystal was grown from the melt of PbO_2, Bi_2O_3 and $BaCO_3$ with excess PbO_2 and Bi_2O_3 as a solvent. Intensity measurement was carried out on a single crystal of size 1x1x2mm, using a four-circle diffractometer (FOX) at KENS. The spectrometer equipped with a one-dimensional PSD of ^{6}Li-glass scintillators connected with TOF technique enables the two-dimensional data collection on a reciprocal plane passing through the origin.[6] The observed intensities on { h k 0 } * plane are given in Fig. 1. In the range of wavelength 0.2-6.35A and that of 2θ:6-160°, 276 reflections in total were obtained. As a trial, the structure model by Cox and Sleight[5] was refined and it converged with the residual R about 0.12. The atom parameters thus obtained are given in Table 1.

Further analysis is now in progress to obtain detailed structural information.

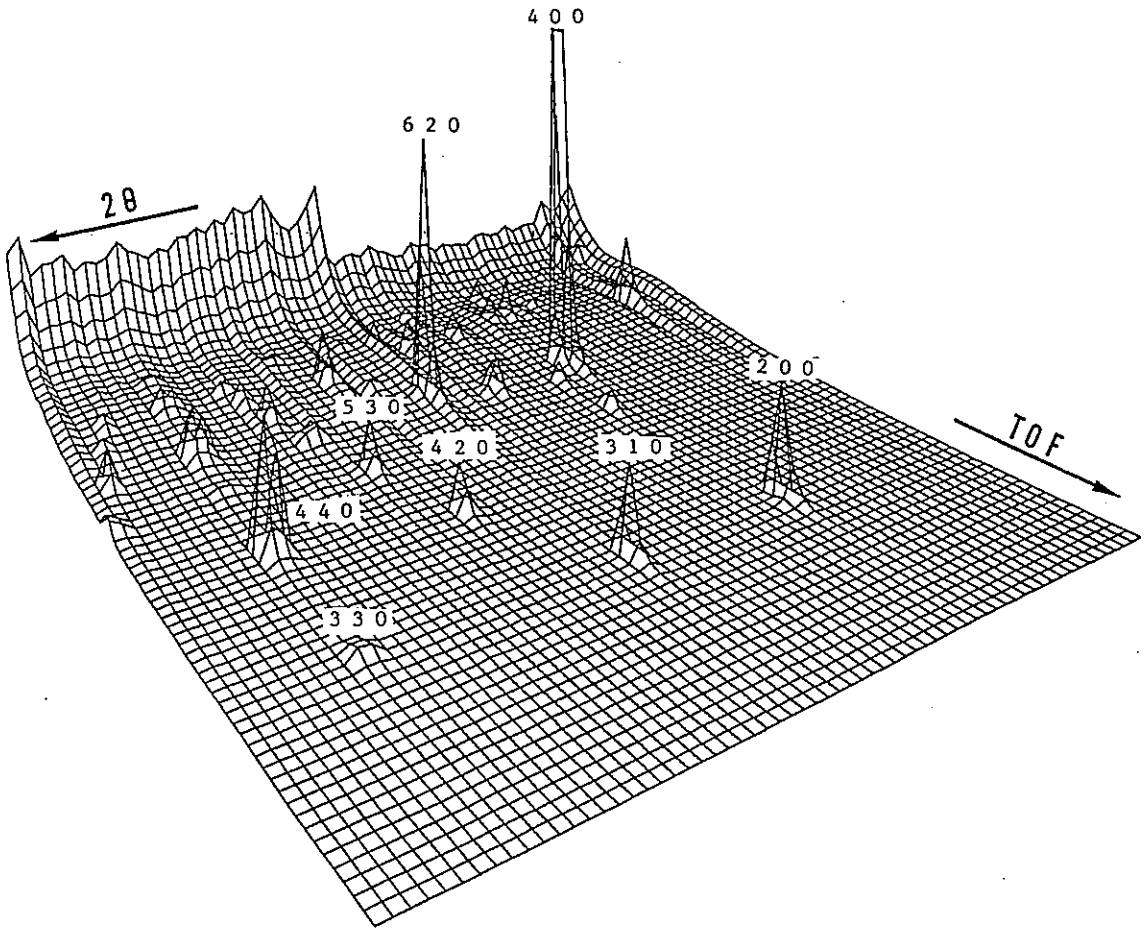

Fig. 1. TOF Spectrum of $BaPb_{0.75}Bi_{0.25}O_3$ on { h k 0 }* plane

Table 1. Atomic coordinates and thermal parameters

	X	Y	Z	β_{11}	β_{22}	β_{33}	β_{12}	β_{13}	β_{23}
Ba	0.511(2)	0	1/4	0.005(1)	0.009(3)	0.0026(5)	0	0	0
Pb-Bi	0	0	0	0.0057(7)	0.003(2)	0.0015(3)	0	-0.0001(8)	0
O(I)	0.028(1)	0	1/4	0.008(2)	0.018(7)	0.0025(7)	0	0	0
O(II)	1/4	1/4	-0.012(2)	0.019(2)	0.020(4)	0.007(1)	-0.015(2)	0	0

References

1) A. W. Sleight, J. L. Gillson and P. E. Bierestedt: Solid State Commun. 17 (1975) 27.

2) T. D. Thanh, A. Koma and S. Tanaka: Appl. Phys. 22 (1980) 205.

3) D. E. Cox and A. W. Sleight: Acta Crystallogr. Sect. B35 (1979) 1.

4) T. Itoh, K.Kitazawa and S. Tanaka: J. Phys. Soc. Jpn. 53 (1980) 2668.

5) D. E. Cox and A. W. Sleight: Proc. Conf. Neutron Scattering, Gatlingburg (1976) 45.

6) N. Niimura, K. Yamada, T. Kubota, M. Isobe, F. P. Okamura, I. Kawada, A. Masaki and H. Horiuchi: KENS-Report VI (1987).

A profile shape function for TOF powder diffraction using cold neutron sources

Fujio IZUMI, Hajime ASANO*, Hideaki MURATA*, and Noboru WATANABE**

National Institute for Research in Inorganic Materials
Sakura-mura, Niihari-gun, Ibaraki 305, Japan

* Institute of Materials Science, University of Tsukuba
Sakura-mura, Niihari-gun, Ibaraki 305, Japan

** National Laboratory for High Energy Physics
Oho-machi, Tsukuba-gun, Ibaraki 305, Japan

A high-resolution powder diffractometer (HRP) at KENS utilizes neutrons from a solid methane moderator at 20 K. Peak shapes measured on the HRP depend primarily on the wavelength of neutron; that is, epithermal and thermal neutrons afford nearly symmetric, sharp peaks whereas cold neutrons give rise to a long trailing tail to each broad peak. Therefore, profile shape functions designed for moderators at room temperature[1),2)] and at 108 K[3)] cannot be used, without any modification, for the least-squares fitting of Bragg peaks in the whole t (time-of-flight: TOF) region.

In previous work[4)], a profile shape function proposed by Von Dreele *et al.*[2)] was modified by adding two asymmetric Lorentz functions near the peak position and at the decaying tail. Rietveld refinements based on this function yielded fairly satisfactory results. However, it contains variable profile parameters as many as 29; a simpler function has been roundly desired.

The cold moderator at KENS was altered from a grooved type to a flat one in 1985 with a result that both peak shapes and resolutions in diffraction patterns measured on the HRP changed appreciably. The present investigation has aimed at developing a new profile shape function suitable for the Rietveld analysis and pattern decomposition of powder diffraction data taken on the HRP at the present stage.

Cole and Windsor[1)] represented the peak shape obtained with thermalized neutrons by a function (hereinafter called the CW function) which consists of three separate regions: (1) a Gauss function with a

standard deviation σ_1, (2) another Gauss function with a standard deviation σ_2, and (3) a decaying exponential function with a decay constant γ. The peak position, t_k, of the kth reflection lies at the joint of the two Gauss functions having the same peak height.

Preliminary calculations showed that peak shapes in thermal and cold neutron regions could be adequately approximated by the CW function but that those in a transient region deviated markedly from it. Then, a more flexible profile shape function, $G(\Delta t_{ik})$, was devised which is the summation of two CW functions, $g_1(\Delta t_{ik})$ and $g_2(\Delta t_{ik})$, in a $(1-R):R$ ratio:

$$G(\Delta t_{ik}) = A[(1-R)g_1(\Delta t_{ik}) + Rg_2(\Delta t_{ik})] \tag{1}$$

$$t_i < t_k \qquad g_1(\Delta t_{ik}) = g_2(\Delta t_{ik}) = \exp\left(-\frac{\Delta t_{ik}^2}{2\sigma_1^2}\right) \tag{2}$$

$$t_k < t_i < t_k + \gamma_1\sigma_2^2 \qquad g_1(\Delta t_{ik}) = \exp\left(-\frac{\Delta t_{ik}^2}{2\sigma_2^2}\right) \tag{3}$$

$$t_i > t_k + \gamma_1\sigma_2^2 \qquad g_1(\Delta t_{ik}) = \exp\left(\frac{\gamma_1^2\sigma_2^2}{2} - \gamma_1\Delta t_{ik}\right) \tag{4}$$

$$t_k < t_i < t_k + \gamma_2\sigma_2^2 \qquad g_2(\Delta t_{ik}) = \exp\left(-\frac{\Delta t_{ik}^2}{2\sigma_2^2}\right) \tag{5}$$

$$t_i > t_k + \gamma_2\sigma_2^2 \qquad g_2(\Delta t_{ik}) = \exp\left(\frac{\gamma_2^2\sigma_2^2}{2} - \gamma_2\Delta t_{ik}\right) \tag{6}$$

$$A^{-1} = c\sigma_1 + c(1-R)\sigma_2\mathrm{erf}\left(\frac{\gamma_1\sigma_2}{\sqrt{2}}\right) + \frac{1-R}{\gamma_1}\exp\left(-\frac{\gamma_1^2\sigma_2^2}{2}\right) + cR\sigma_2\mathrm{erf}\left(\frac{\gamma_2\sigma_2}{\sqrt{2}}\right) + \frac{R}{\gamma_2}\exp\left(-\frac{\gamma_2^2\sigma_2^2}{2}\right) \tag{7}$$

where $\Delta t_{ik} = t_i - t_k$, t_i is the TOF at the ith channel, A is the normalization factor, and $c = (\pi/2)^{1/2}$. Functions $g_1(\Delta t_{ik})$ and $g_2(\Delta t_{ik})$ have common standard deviations: σ_1 at $t_i < t_k$ and σ_2 at $t_i > t_k$, but they differ in decay constant: γ_1 for $g_1(\Delta t_{ik})$ and γ_2 for $g_2(\Delta t_{ik})$ ($\gamma_1 < \gamma_2$). Since eqs. (1)-(7) include the pure CW function as a special case ($R = 0$), they can be used for the profile fitting of powder diffraction patterns obtained with neutrons from both ambient and cold moderators.

Suitable empirical functions to express the wavelength dependence of the profile parameters (σ_1, σ_2, γ_1, γ_2, and R) are still required in Rietveld analysis. Of these five parameters, the decay constant of the long-time exponential tail, γ_2, proved to be almost invariable regardless of the wavelength, as is theoretically defensible[3]. The value of γ_2 is believed to depend not on the particle size or strain of a sample but only

on the neutron moderation process[1]. Once γ_2 has been determined by the Rietveld analysis of standard samples, it may be held fixed at the refined value in other refinements.

We have found that the following equations can adequately approximate the dependences of the other profile parameters on the wavelength of neutron:

$$\sigma_1 = \sigma_{11} + \sigma_{12} d_k \tag{8}$$

$$\sigma_2 = \sigma_{21} + \sigma_{22} d_k^{2.5} \tag{9}$$

$$\gamma_1 = \gamma_{11} \exp(-\gamma_{12} d_k^2) + \gamma_{13} \tag{10}$$

$$R = 1 - \exp\left(-R_1 d_k^{R_2}\right) \tag{11}$$

In eqs. (8)-(11), d_k denotes the interplanar spacing, which is, of course, proportional to the wavelength. It is interesting to note that the first term in eq. (10) is Gaussian and that eq. (11) has just the same form as so-called Avrami's equation to express conversion ratios in phase transformation.

Equations (1)-(11) were implemented in a computer program, RIETAN, for the Rietveld analysis and simulation of TOF neutron diffraction patterns[5], and structures of Si and α-Al_2O_3 were refined with this program. Figure 1 shows the neutron profile fit and difference pattern for α-Al_2O_3. The solid lines are the calculated intensities, crosses overlaying them are observed intensities, and Δy_i is the difference between observed and calculated intensities. The short vertical lines mark the positions of possible Bragg reflections. The intensity data in TOF ranges where Bragg reflections of a vanadium container appeared were excluded in the refinements. The agreement between the calculated and observed intensities was most satisfactory, and quite low R factors[6] could be obtained: $R_{wp} = 7.5\%$, $R_p = 5.4\%$, $R_I = 1.4\%$, $R_F = 1.2\%$ for Si and $R_{wp} = 7.1\%$, $R_p = 4.9\%$, $R_I = 1.8\%$, $R_F = 1.7\%$ for Al_2O_3. The resulting positional and isotropic thermal parameters for the two standard samples agreed very closely with literature data. The introduction of anisotropic thermal parameters hardly lowered the R factors.

The structures of metal hydrides, organic and inorganic compounds are now being refined with the current version of RIETAN described above. Preliminary reports on these Rietveld refinements will be published in this volume.

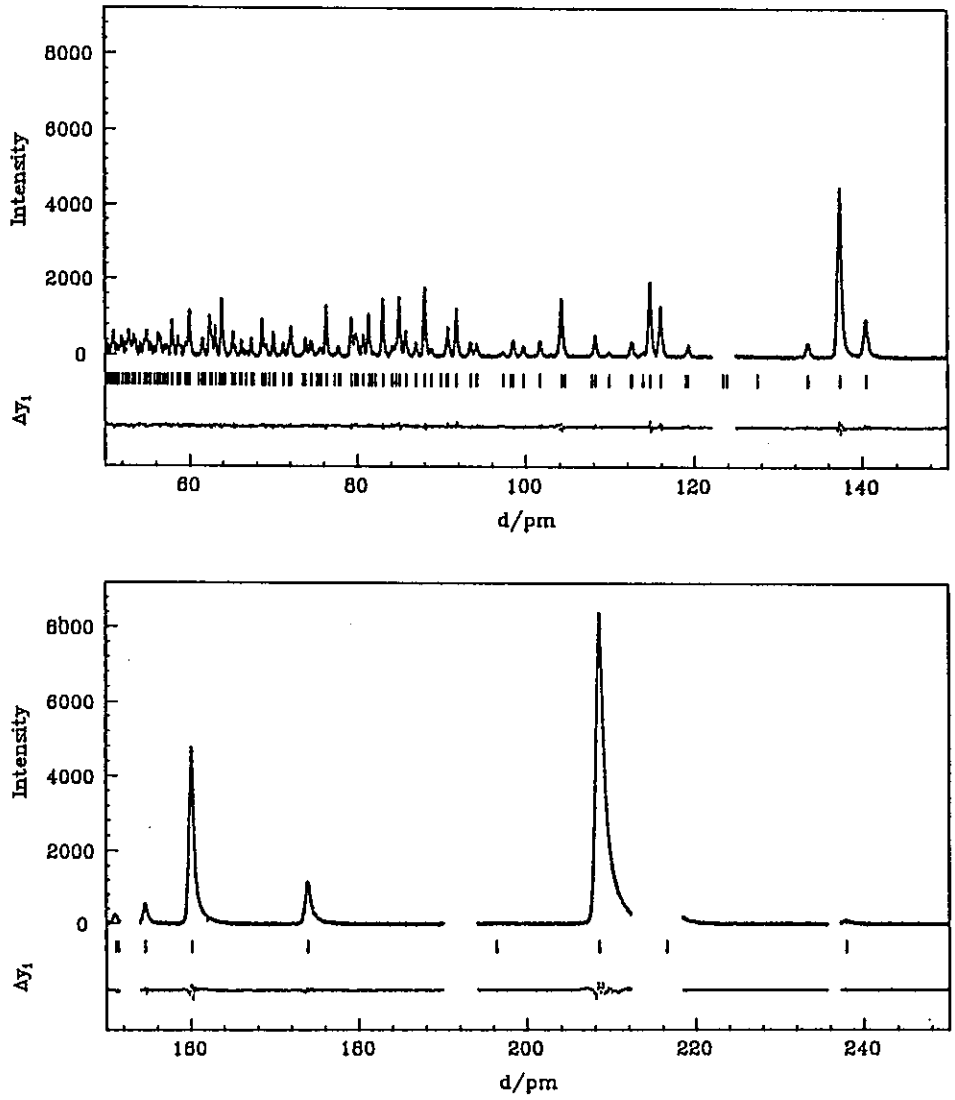

Fig. 1. Rietveld refinement patterns for α-Al_2O_3.

References

1) I. Cole and C. G. Windsor, *Nucl. Instrum. Methods*, 171, 107 (1980).

2) R. B. Von Dreele, J. D. Jorgensen, and C. G. Windsor, *J. Appl. Crystallogr.*, 15, 581 (1982).

3) J. M. Carpenter, R. A. Robinson, A. D. Taylor, and D. J. Picton, *Nucl. Instrum. Methods Phys. Res., Sect. A*, 234, 542 (1985).

4) H. Asano, M. Umino, Y. Onuki, T. Komatsubara, F. Izumi, and N. Watanabe, *J. Phys. Soc. Jpn.*, 55, 454 (1986).

5) F. Izumi, *Nippon Kessho Gakkai Shi*, 27, 23 (1985).

6) R. A. Young, E. Prince, and R. A. Sparks, *J. Appl. Crystallogr.*, 15, 357 (1982).

Method of Analysis of Pulsed Neutron Diffraction Pattern in the Study of Cold-worked Powder

T.Kamiyama, S.Tomiyoshi, T.Shinohara, H.Asano*, H.Yamamoto and N.Watanabe**
The Research Institute for Iron, Steel and Other Metals Tohoku University, Sendai, Japan
* Institute of Materials Science, Tsukuba University, Ibaraki, Japan
** National Laboratory for High Energy Physics, Ibaraki, Japan

High resolution time-of-flight (TOF) neutron diffraction has become of new importance in the study of the defect structure where detailed analysis of the diffraction profiles is necessary. However, the instrumental resolution function is distinctly asymmetric, and the profile function proposed is useless in the cases where the sample affects the peak shape by crystallite size, strain and others. So, we have developed a new method which incorporates of size, strain and other defects analysis into the profile-refinement method. All contributions of the defects and the instrumental resolution are expressed in terms of Fourier coefficients, and the inverse Fourier transforms of those product represent the calculated profiles.

In the TOF powder diffractometry, the effect of strain on the width of the profile can be given by $\Delta\lambda = \varepsilon_{hkl}\lambda$. ($\varepsilon_{hkl}$ is the effective strain along a <hkl> direction.) If the strain $\langle\varepsilon_n\rangle$ obeys a Gaussian distribution, the Fourier coefficient of strain A^D_n is given by,

$$A^D_n = \exp(-2\pi^2 l^2 n^2 \langle\varepsilon_n^2\rangle) \quad . \qquad (1)$$

where n is the harmonic number of the Fourier coefficient and is related to the average distance normal to the reflecting planes, and l the order of the diffraction peak.[1] Adler and Houska[2] gave the equation,

$$\langle\varepsilon_n^2\rangle^{1/2} = |n|^r \langle\varepsilon_1^2\rangle^{1/2} \quad . \qquad (2)$$

If r=-1/2, eq. (1) becomes $A^D_n = \exp(-2\pi^2\langle\varepsilon_1^2\rangle l^2|n|)$, which is the Fourier transform of a Lorentzian. If one takes r=0, each column undergoes uniform strain with $\varepsilon_n = \varepsilon_1$ for each pair of cells. This gives long-range strain and eq. (1) then

becomes $A_n^D = \exp(-2\pi^2\langle\varepsilon_l^2\rangle l^2 n^2)$, which is the Fourier transform of a Gaussian. Therefore, we expect that the strain broadened profile is the convolution of Gaussian and Lorentzian. In general, reflections with different (hkl) have different line widths. Following Rothman and Cohen[3], we express the orientational dependence of the effective strain ε_{hkl} by,

$$\varepsilon_{hkl}=A\Gamma+B \ , \qquad (3)$$

where $\Gamma=(h^2k^2+k^2l^2+l^2h^2)/(h^2+k^2+l^2)^2$. B is the effective strain along <1 0 0>, which satisfies $\Gamma=0$. A is usually negative and represents the elastic anisotropy of the crystal.

The effect of crystallite size on the width of the profile in the TOF diffractometry is $\Delta\lambda\simeq\lambda^2/(2D_{hkl}\sin\theta)$, where D_{hkl} is effective crystallite-size along <hkl> direction. For the analysis of the crystallite-size effect, profile is often approximated by a Lorentzian.[4] Therefore, the Fourier coefficient for the crystallite-size effect is $A^S=\exp(-|n|/D)$. If the reduction of coherent domain size is ascribed to faults like small angle boundaries or stacking faults, this domain size must be anisotropic. To express plane-like, needle-like and spherical crystallines, we consider a spheroidal body as a crystalline.

We must also consider the effects of the stacking faults (SF) and anti-phase domain boundaries (APB). The main effect is broadening of the fundamental and superstructure reflections in the case of SF, and the superstructure peaks in the case of APB.

The observed profile h(s) arises from a convolution of the true one f(s) and instrumental one g(s). Using F(t) and G(t)(Fourier transforms of f(s) and g(s)), one can express the observed profile h(s) by,

$$h(s)=\int g(x)f(s-x)dx=\int F(t)G(t)\exp(2\pi its)dt, \qquad (4)$$

where $F(t)=A^S\ A^D_{Gauss}\ A^D_{Lorentz}\ A^{APB}$.

The calculated intensity $Y_{cal}(t)$ is determined from,

$$Y_{cal}(t)=ki(t)A(T)(\sum|F_j|^2 m_j d_j^4 h_j(t)+y_b(t)), \qquad (5)$$

where i(t) is the incident intensity, A(t) the absorption factor, F_j structure factor, m_j multiplicity, d_j d-spacing, $h_j(t)$ profile function. Least-squares refinement is achieved by minimizing $\Delta = \sum w_i(Y_{cal}(t)-Y_{obs}(t))^2$.

As an example of the above method, we chose Pd_2MnSn, which shows large reduction in magnetization by cold-working.[5] Figures 1,2 and 3 show the results of fitting. Excellent fits between the observed and calculated values were obtained. A detailed discussion will be reported elsewhere.

References

(1) B.E.Warren: X-ray Diffraction (Addison-Wesley Publishing Company 1968)

(2) T.Adler and C.R.Houska: J.Appl.Phys.50(1979)3282

(3) R.L.Rothman and J.B.Cohen: Adv. X-ray Anal.12(1969)208

(4) Th.H.de Keijser, E.J.Mittemeijer and H.C.F.Rozendaal: J.Appl.Cryst.16(1983)309

(5) T.Shinohara,K.Sasaki,H.Watanabe, H.Sekizawa and T.Okada: J.Phys.Soc.Jpn.50(1981)2904

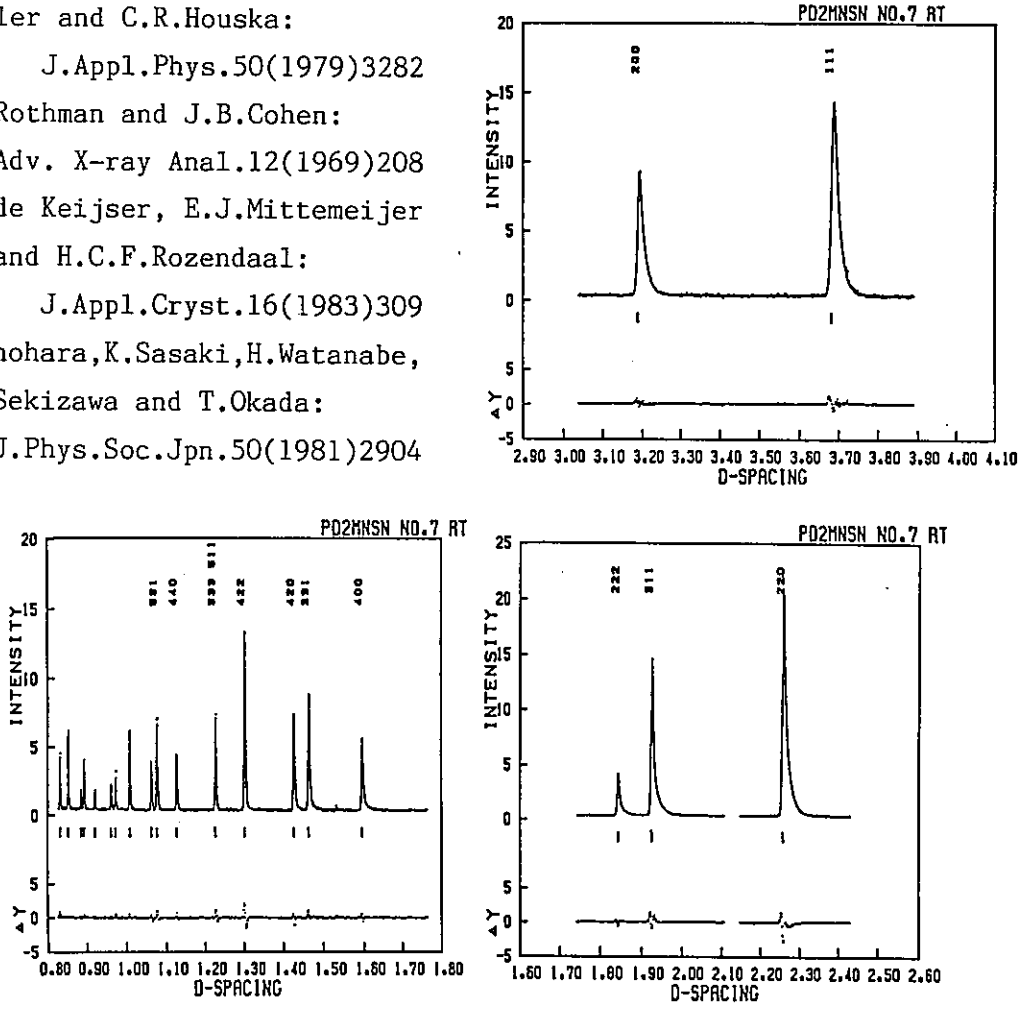

Fig. 1. Profile refinement patterns of Pd_2MnSn annealed at 840°C. The observed data are indicated by the dots; the calculated pattern is shown as the solid line overlying them.

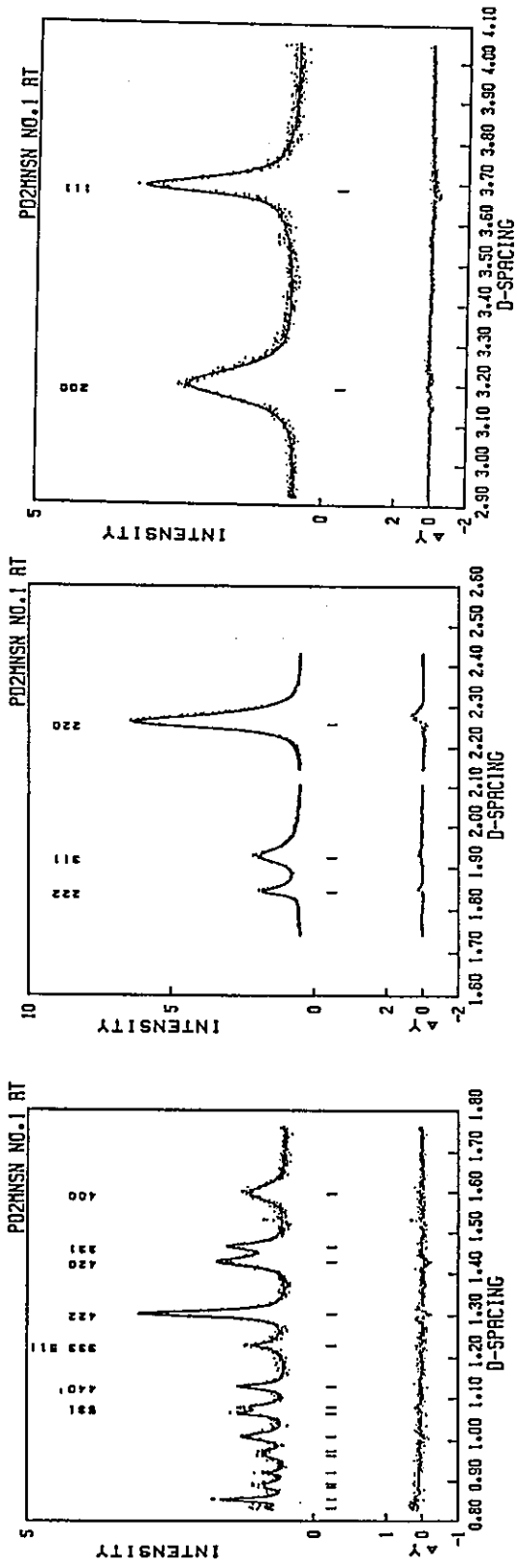

Fig. 2. Diffraction patterns of Pd_2MnSn after cold-working.

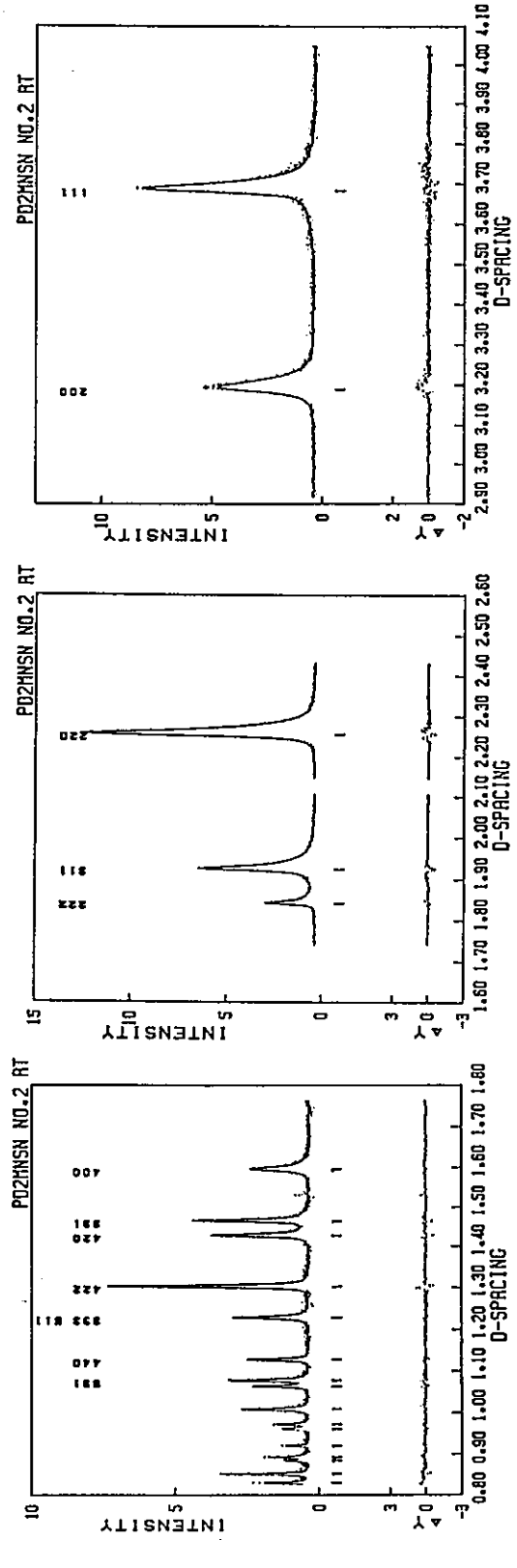

Fig. 3. Diffraction patterns of Pd_2MnSn annealed at 300°C.

Structure of Molten (Li-K)Cl and (Li-Na-K)Cl Mixtures of the Eutectic Composition Studied by Pulsed Neutron Diffraction

Akira ENDOH, Toshio YAMAGUCHI, Yusuke TAMURA, Osamu ODAWARA, Isao OKADA, Hitoshi OHTAKI and Masakatsu MISAWA*

Department of Electronic Chemistry, Tokyo Institute of Technology, Nagatsuta, Midori-ku, Yokohama 227, Japan

*National Laboratory for High Energy Physics, Oho-machi, Tsukuba-gun, Ibaraki 305, Japan

Although the structure of pure ionic melts has been investigated by means of X-ray or neutron diffraction, only a few studies on the structure of mixed ionic melts has been carried out. This is mainly due to difficulties of separating the partial distribution functions from the total distribution function especially in the case of mixed melts.

In previous studies, we performed X-ray diffraction measurements on molten (Li-K)Cl[1] and (Li-Na-K)Cl[2] mixtures of the eutectic composition ((Li-K)Cl : 58.8 - 41.2 mol % ; (Li-Na-K)Cl : 53.5 - 8.6 - 37.9 mol %) and the data were analysed with the aid of molecular dynamics (MD) simulations. By modifying the Tosi-Fumi pair potentials[3], the structure functions $s \cdot i(s)$ and the radial distribution functions G(r) derived from the MD simulations could well reproduce those obtained from the X-ray diffraction method.

In the present study, we have performed Time-of-Flight (TOF) neutron diffraction measurements on molten (Li-K)Cl and (Li-Na-K)Cl mixtures of the eutectic composition using a pulsed spallation neutron source in order to compare the results with those obtained from MD simulations and to investigate Li^+-Cl^- interactions, which were difficult to detect by means of X-ray diffraction, in the melts.

Alkali metal chlorides of reagent grade were dried in a vacuum oven at about 430 K for one day and mixed in the eutectic composition by weighing. The mixtures were melted and stirred sufficiently in a crucible before pouring into a Pyrex tube. After cooling the melts in a desiccator the solidified samples were taken out from the tubes, transferred into quartz sample cells with 0.4 mm wall thickness, 10 mm in inner diameter and 70 mm in height, and sealed in vacuo. Neutron scattering measurements of the melts were performed by using the High Intensity Total scattering

spectrometer (HIT). The sample cell was heated with two infrared lamps facing each other. The temperature was kept at 668 K for (Li-K)Cl and 625 K for (Li-Na-K)Cl.

Figures 1 and 2 show the structure factors S(Q) of (Li-K)Cl and (Li-Na-K)Cl, respectively. In both systems, the S(Q)'s calculated from the MD simulations were in good agreement with those obtained from the neutron diffraction experiments. The total correlation functions H(r) (= G(r) - 1) were obtained by conventional Fourier transformation of the $Q\cdot(S(Q) - 1)$ values and shown in Figures 3 and 4 for (Li-K)Cl and (Li-Na-K)Cl, respectively. With respect to the H(r) functions, the partial values $h_{ij}(r)$ ($\sum h_{ij}(r) = H(r)$) of the predominant interactions in the systems, which are functions derived from the MD simulations, are also shown in the figures. The H(r) functions obtained by the neutron diffraction experiments have still quasi peaks around 240 pm. Improvement in evaluating the H(r) functions from the S(Q) values obtained by the experiments is now in progress. As seen in Figures 3 and 4, the first peak gave a negative contribution to the H(r) around 240 pm for both melts, corresponding to the Li^+-Cl^- interaction expected from the negative scattering length of the Li nucleus. In the case of the X-ray diffraction method, this interaction is difficult to be observed due to small atomic scattering factor of Li atom. The second peak appeared around 380 pm in both melts is assignable to the interaction between Cl^- ions bound to the central Li^+ ion. A discernible shoulder around 320 pm is ascribed to the K^+-Cl^- interaction. In the case of the (Li-Na-K)Cl mixture, a rather clearly resolved Na^+-Cl^- interaction in the simulations, which was difficult to be detected by the X-ray diffraction method, could not be observed by the present neutron diffraction method.

References

1) I. Okada, H. Okano, H. Ohtaki and R. Takagi, Chem. Phys. Lett., 100, 436 (1983).

2) A. Endoh, T. Yamaguchi, I. Okada and H. Ohtaki, Nippon Kagaku Kaishi, submitted for publication.

3) M. P. Tosi and F. G. Fumi, J. Phys. Chem. Solids., 25, 45 (1964).

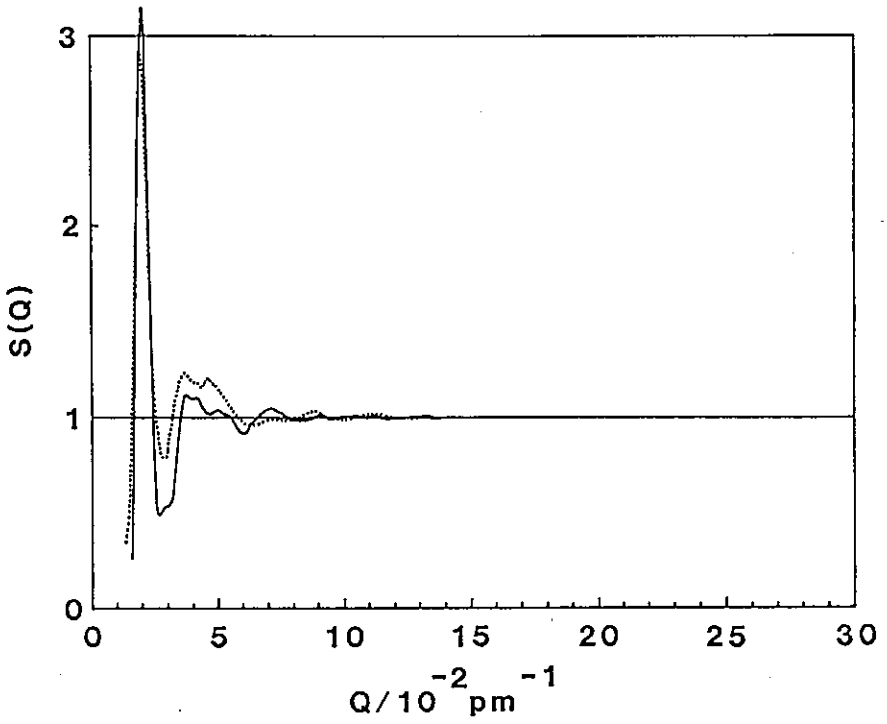

Figure 1. Structure factor obtained by the neutron diffraction (dots) and MD (solid line) for (Li-K)Cl melt.

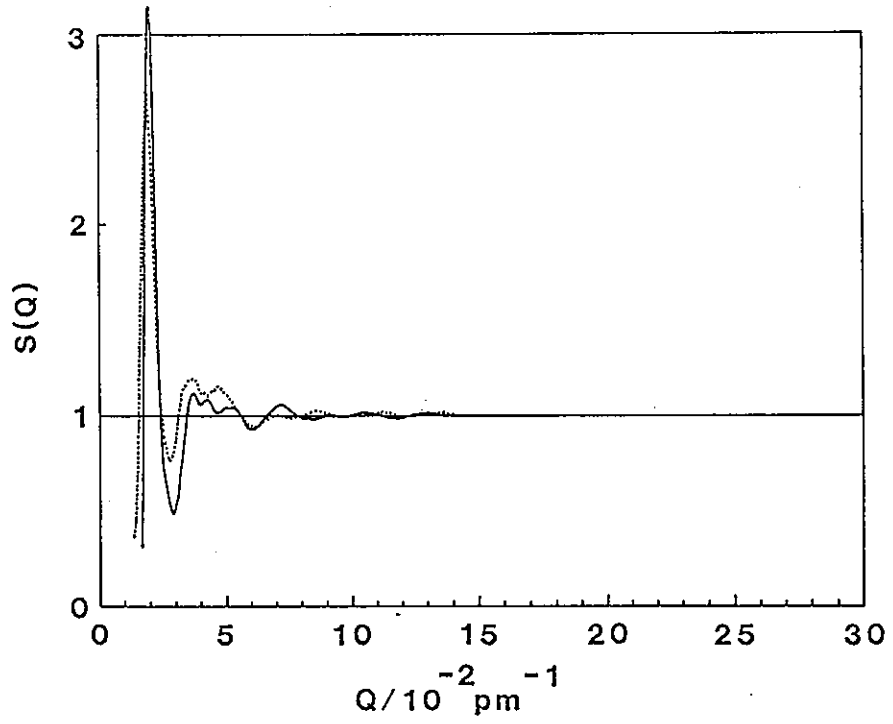

Figure 2. Structure factor obtained by the neutron diffraction (dots) and MD (solid line) for (Li-Na-K)Cl melt.

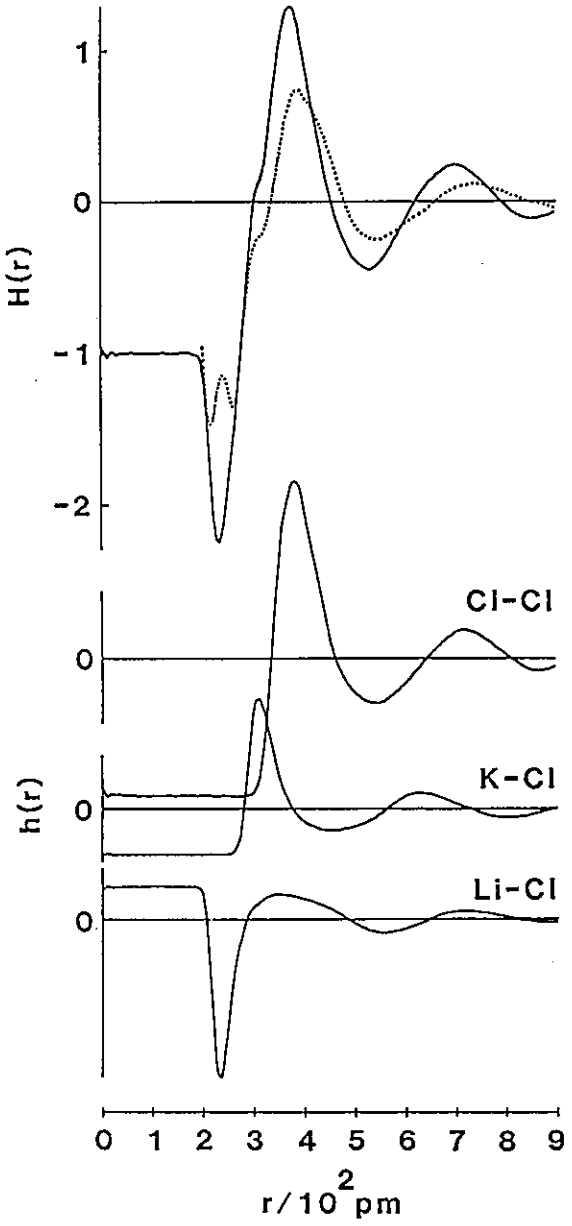

Figure 3. Total correlation function H(r) and the partial values h(r) for (Li-K)Cl melt. (dots : neutron diffraction, solid line : MD)

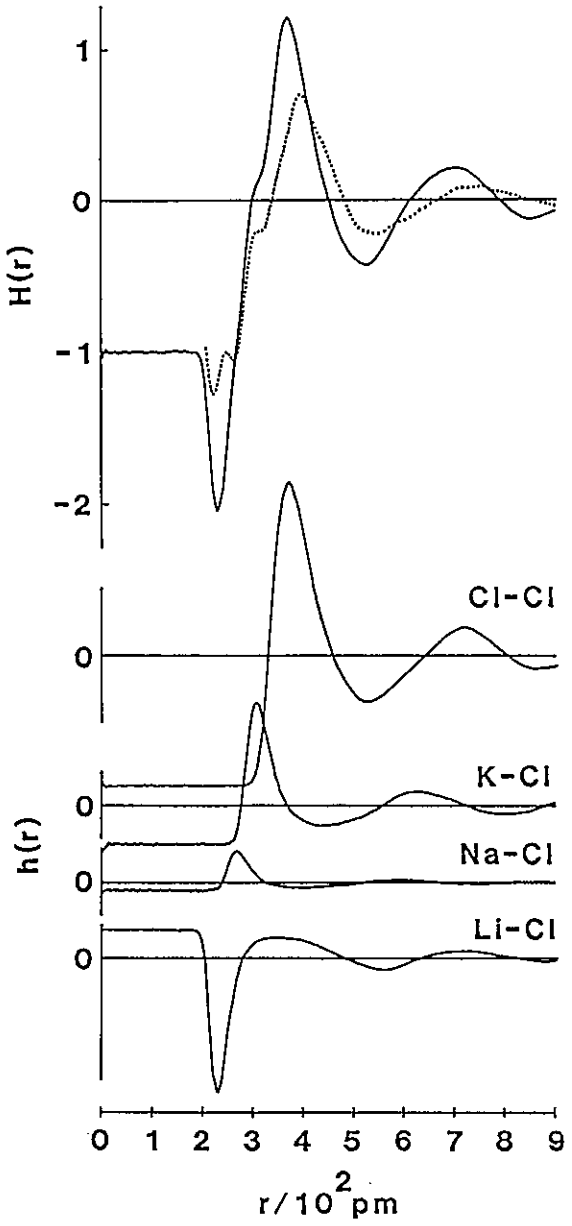

Figure 4. Total correlation function H(r) and the partial values h(r) for (Li-Na-K)Cl melt. (dots : neutron diffraction, solid line : MD)

Hydration Structure of Trivalent Metal Ions by Means of Neutron Diffraction using Isomorphous Substitution

Toshio Yamaguchi*, Yusuke Tamura, Hitoshi Ohtaki and Masakatsu Misawa†

Department of Electronic Chemistry, Tokyo Institute of Technology,
Nagatsuta, Midori-ku, Yokohama 227, Japan
†National Laboratory for High Energy Physics, Oho-machi,
Tsukuba 305, Japan

1. Introduction

The hydration energy of ions in solution depends on the orientation of water molecules in the coordination sphere as well as the hydration number. The hydration number of ions in solution has successfully been determined by X-ray diffraction and Extended X-ray Absorption Fine Structure (EXAFS) methods, but information for the orientation of water molecules in the first hydration sphere is available only by the neutron diffraction method. In particular, the isotopic substitution method, which utilizes the difference in the scattering amplitude of nuclei, has been proved to be very effective in uniquely extracting information of ion-water interactions in several electrolyte solutions [1-4].

In the present study, we propose an isomorphous substitution method, which is also capable of obtaining similar structural information as in the isotopic substitution method. We measured aqueous perchlorate solutions of iron(III) and chromium(III), of which ionic radii are very similar with each other, in order to determine the hydration structure, especially the orientation of water molecules in the first hydration sphere of trivalent metal ions.

2. Experimental

Iron(III) and chromium(III) perchlorates were recrystallized three times from light water and then the light water in the solutions was replaced with heavy water by repeated boiling and dilution with heavy water. The final content of light water in the sample solutions was determined by the infrared spectroscopy. A small amount of deuterized perchloric acid was added to the solutions in order to avoid hydrolysis of the metal ions. The composition of the sample solutions measured is given in Table 1.

Neutron diffraction measurements were performed with HIT at National Laboratory for High Energy Physics (KEK). The sample solutions were sealed into a Ti−Zr null alloy cell with 0.3 mm thickness, 8 mm inner diameter and 50 mm height. The measured data were

*Present address: Department of Chemistry, Faculty of Science, Fukuoka University, Nanakuma, Jonan-ku, Fukuoka 814-01

corrected for absorption, multiple scattering, and then normalized to the absolute unit by using scattering data from a vanadium rod.

3. Isomorphous Substitution Method

In the present system, the total structure factor $S(Q)$ is expressed in terms of ten partial structure factors; $S_{MO}(Q)$, $S_{MD}(Q)$, $S_{XO}(Q)$, $S_{XD}(Q)$ from ion-water interactions, $S_{MX}(Q)$, $S_{MM}(Q)$, $S_{XX}(Q)$ from ion-ion interactions, and $S_{OO}(Q)$, $S_{OD}(Q)$, and $S_{DD}(Q)$ from water-water interactions. Since the structure of both solutions containing metal ions with similar ionic radius can be assumed to be identical with a good approximation, their algebraic difference $\Delta_M(Q)$ can be expressed as

$$\Delta_M(Q) = A[S_{MO}(Q)-1]+B[S_{MD}(Q)-1]+C[S_{MX}(Q)-1]+D[S_{MM}(Q)-1], \quad (1)$$

$$A = 2c_O c_M b_O b_M \Delta b_M,$$

$$B = 2c_D c_M b_D b_M \Delta b_M,$$

$$C = 2c_X c_M b_X b_M \Delta b_M,$$

$$D = c_M^2(b_{Fe}^2 - b_{Cr}^2),$$

with $\Delta b_M = b_{Fe} - b_{Cr}$ and $Q = 4\pi\sin\theta/\lambda$. c_α and b_α are the atomic fraction and the scattering length of atom α, respectively. The $\Delta_M(Q)$ is Fourier transformed into the radial distribution function $G_M(r)$ as

$$G_M(r) = \frac{1}{2\pi^2 r\rho_N}\int_{Q_{min}}^{Q_{max}} Q\Delta_M(Q)\sin(Qr)dQ, \quad (2)$$

where ρ_N is the number density, Q_{max} and Q_{min} the upper and lower limits of the Q values obtainable in the experiments.

4. Results and Discussion

Figures 1 and 2 show the experimental $\Delta_M(Q)$ obtained at the scattering angle $2\theta = 25°$ and $G_M(r)$, respectively.

It is seen from Fig. 2 distinct peaks appeared at 204 and 265 pm and broad peaks were observed at 400 − 550 pm in the $G_M(r)$. The first and the second peaks were assignable to M−O and M−D interactions within hydrated M(III) ion. The coordination number of M(III) calculated by

$$N_{M\alpha} = c_\alpha \rho \int 4\pi r^2 g_{M\alpha}(r)dr, \quad (3)$$

was 6.2 for the M-O interactions. On the basis of the geometry of a water molecule (r_{OD}=98 pm, <DOD=104.7°), the tilt angle Θ (see Fig. 2), of water molecules coordinated to M(III) was found to be 38±10°. The present result is compared with the previous findings for other ions in Table 2.

The degree of orientation of hydrated water molecules of Fe(III) estimated by the present measurement, which should be the same as that of Cr(III) according to the present assumption, is similar to the angle of water molecules in the hydration shell of other metal ions, i.e. the lone-pair orbitals of water molecules are practically oriented towards the metal ions. The tilt angle of water molecules in the hydration shells of Nd(III) and Dy(III) seems to be slightly smaller than that of Fe(III) and Cr(III). This may be due to the shorter Fe(III)− and Cr(III)−O distances than the Nd(III)− and Dy(III)−O ones, which lead to an increase in repulsion between the water molecules in the coordination sphere. The second neighbor Fe(III)−O interactions appeared around 420 pm as a broad peak. The first and the second hydration spheres are clearly separated in the present system, which is in contrast with the case of silver(I) ion [2].

References

[1] G. W. Neilson, Physica, **120B**, 325 (1983) and references therein.

[2] M. Sandström, G. W. Neilson, G. Johansson, and T. Yamaguchi, J. Phys. C. Solid State Physics, **18**, L115 (1985).

[3] A. H. Narten, and R. L. Hohn, J. Phys. Chem., **87**, 3193 (1983).

[4] B. K. Annis, R. L. Hohn, and A. H. Narten, J. Chem. Phys., **82**, 2086 (1985).

Table 1 Composition of the sample solutions and sample parameters

Solution	Fe(III)	Cr(III)
Ionic radius(pm)	64.5	61.5
Scattering length b_M(10^{-12} cm)	0.954	0.3635
Concentration(mol dm^{-3})		
M^{3+}	1.63	1.64
D^+	2.25	2.28
ClO_4^-	7.14	7.20
D_2O	41.4	41.8
H_2O	0.4	0.4
Number density $10^6\rho_N$(atoms pm^{-3})	0.098	0.099

Table 2 The hydration structure of metal ions determined by the neutron diffraction method

Ion	m/mol kg^{-1}	r(M-O)/pm	r(M-D)/pm	Θ/deg	N	Ref.
Li(I)	3.57	195	255	40±10	5.5	1
Ag(I)	3.71	241	297	45±10	4.1	2
Ca(II)	2.80	239	302	34±9	6.4	1
Ni(II)	3.01	207	267	42±8	5.8	1
Fe(III)	1.63	204	268	38±10	6.2	This work
Nd(III)	2.85	248	313	24±4	8.5	3
Dy(III)	2.38	237	304	17±3	7.4	4

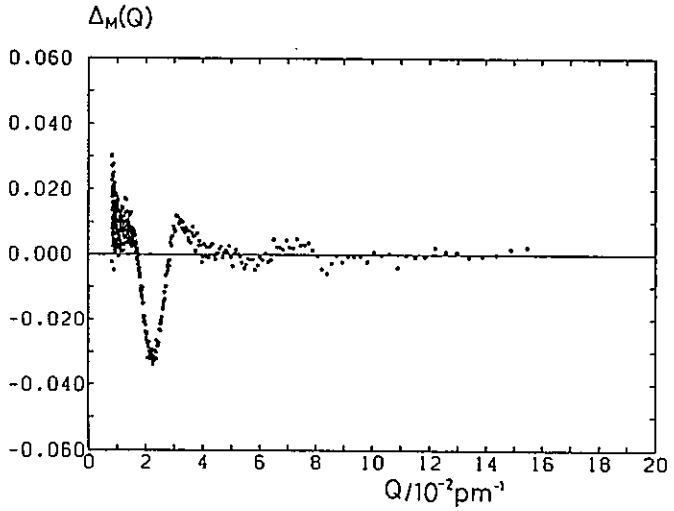

Fig. 1 $\Delta_M(Q)$ derived from 1.63 molar solutions of $Fe(ClO_4)_3$ and $Cr(ClO_4)_3$ in D_2O

Fig. 2 $G_M(r)$ obtained by Fourier transform of $\Delta_M(Q)$ in Fig. 1

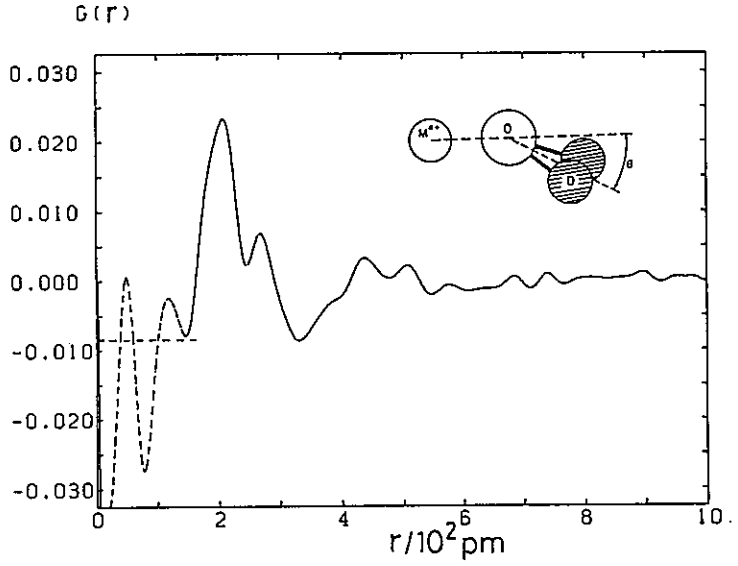

Structure of Liquid Water in the Temperature Range of 25 - 200 °C by the Neutron Diffraction Method

Toshio Yamaguchi*, Yusuke Tamura, Hitoshi Ohtaki,
Susumu Ikeda† and Masakatsu Misawa†

Department of Electronic Chemistry, Tokyo Institute of Technology,
Nagatsuta, Midori-ku, Yokohama 227, Japan
†National Laboratory for High Energy Physics, Oho-machi,
Tsukuba 305, Japan

1. Introduction

X-Ray and neutron diffraction methods have so far played an important role in investigation of the structure of liquid water. Narten *et al.* measured X-ray scatterings from liquid water in the temperature range of 4 - 200 °C [1]. Gorbaty *et al.* performed X-ray diffraction measurements at 25 - 500 °C at 1 kbar and at 1 - 2000 bar at 20 °C [2,3]. These X-ray investigations have given oxygen-oxygen positional correlation in liquid water in the wide temperature and pressure ranges. The neutron diffraction method has an advantage in obtaining information of the position of deuterium atoms, which helps, together with the oxygen-oxygen correlation from X-ray scattering measurements, to reveal orientational correlations of water molecules in the liquid state. Neutron scattering experiments of liquid D_2O were carried out at −14.5 - 79 °C by Dore *et al.* [4], and at 15 - 95 °C by Ohtomo *et al.* [5]. Recently, Whalley *et al.* [6] succeeded in neutron measurements of liquid D_2O in the pressure range of 0.06 - 15.6 kbar at 85 °C.

In the present study, we constructed a Ti-Zr null alloy cell for liquid samples and measured neutron scatterings from liquid D_2O in the temperature range 25 - 200 °C.

2. Experimental

Liquid D_2O (D content 99.95 %) was purchased from Canada Merck. The sample was sealed into a Ti-Zr null alloy cell with the dimension of 8 mm inner diameter, 50 mm height, and 0.3 mm wall thickness. Neutron scattering measurements were carried out with HIT at

*Present address: Department of Chemistry, Faculty of Science, Fukuoka University, Nanakuma, Jonan-ku, Fukuoka 814-01

KEK (National Laboratory for High Energy Physics). The experimental data were corrected for absorption, multiple scattering, and then normalized to the absolute units by comparing with scatterings from a vanadium rod.

3. Results and Discussion

Figure 1 shows the structure factor $S(Q)$ at each temperature. There appeared the first peak around 0.02 pm^{-1}, a hump around 0.04 pm^{-1}, and broad peaks centered at 0.08 and 0.14 pm^{-1} (not shown in the figure). With increasing temperature, the height of the first peak decreased, but the position of the peak remained practically unchanged. The hump also decreased with temperature and became flat at 200 °C. This hump has been found to correlate with orientational correlation of water molecules in the liquid [3-6]. We analyzed the $S(Q)$ functions at different temperatures by employing the following nearest-neighbor model.

In the case of randomly oriented water molecules, the total structure factor $S(Q)$ can be expressed by eq. (1):

$$S(Q) = f_1(Q) + f_{2U}(Q)[S_{OO}(Q)-1] \tag{1}$$

Here, $f_1(Q)$ denotes the form factor of one water molecule written by

$$f_1(Q) = 1+\frac{4b_O b_D}{3<b>^2}\frac{\sin(Qr_{OD})}{Qr_{OD}}\exp(-\frac{<(\Delta r)^2>}{2}Q^2) + \frac{2b_D^2}{3<b>^2}\frac{\sin(Qr_{DD})}{Qr_{DD}}\exp(-\frac{<(\Delta r)^2>}{2}Q^2) \tag{2}$$

with $<b> = (b_O+2b_D)/3$. $f_{2U}(Q)$ represents the form factor for the random orientation,

$$f_{2U}(Q) = \frac{1}{3<b>^2}[\, b_O+2b_D\frac{\sin(Qr_{OD})}{Qr_{OD}}\exp(-\frac{<(\Delta r)^2>}{2}Q^2)\,]^2, \tag{3}$$

where $S_{OO}(Q)$ is the oxygen-oxygen structure factor derived from X-ray scattering method.

When N pairs of nearest-neighbor water molecules are orientated as shown in Fig. 2, the structure factor $S(Q)$ may be written as

$$S(Q) = S_0(Q) + \Delta S(Q). \tag{4}$$

The first term corresponds to the structure factor for randomly orientated water molecules. The second term represents the contribution from N pairs of water molecules orientated as shown in Fig. 2, and is given by

$$\Delta S(Q) = N[\, f_{2C}(Q) - (\, f_{2U}(Q) - \frac{b_O^2}{3<b>^2}) \, F_{OO}(Q) \,], \tag{5}$$

Here,

$$F_{OO}(Q) = \frac{\sin(Qr_{OO})}{Qr_{OO}} \exp(-\frac{<(\Delta r)^2>}{2} Q^2), \tag{6}$$

and

$$f_{2C}(Q) = \sum\sum \frac{b_i b_j}{3<b>^2} \frac{\sin(Qr_{ij})}{Qr_{ij}} \exp(-\frac{<(\Delta r)^2>}{2} Q^2). \tag{7}$$

A variety of orientations were tested for the observed $S(Q)$, and the most likely configuration and the number of nearest-neighbors were obtained. Figure 3 shows the final results for liquid water at 25 and 200 °C. The experimental $S(Q)$ function at 25 °C was well reproduced with N=3.0 and the angle Φ=37°, whereas at 200 °C a model of N=1.5 and Φ=37° gave the best fit. These results indicate that about three normal hydrogen bonds are formed at room temperature, but with increasing temperature these hydgrogen bonds are gradually broken.

Although the result obtained from the present calculations seems to be reasonable, the model structure assumed for the orientational configuration of the water molecules (Fig. 2) may to be too simple to interplete the $S(Q)$ functions over the whole Q range measured at different temperatures, because the tilted water molecule is not twisted in this model. A more generalized model structure of orientation of water molecules will be examined to obtain more reliable information for the positional correlation of water molecules in the liquid state.

The analysis of the neutron scattering data in the real space is now in progress in terms of the radial distribution function.

References

[1] A. H. Narten and H. A. Levy, J. Chem. Phys., **55**, 2263 (1971).
[2] Yu. E. Gorbaty and Yu. I. Dem'yanets, Russ. J. Struct. Chem., **24**, 716 (1983).
[3] Yu. E. Gorbaty and Yu. N. Demianets, Mol. Phys., **55**, 571 (1985).
[4] I. P. Gibson and J. C. Dore, Mol. Phys., **48**, 1019 (1983).
[5] N. Ohtomo, K. Tokiwano, and K. Arakawa, Bull. Chem. Soc. Jpn., **55**, 2788 (1982).
[6] A. Y. Wu, E. Whalley, and G. Dolling, Mol. Phys., **47**, 603 (1982).

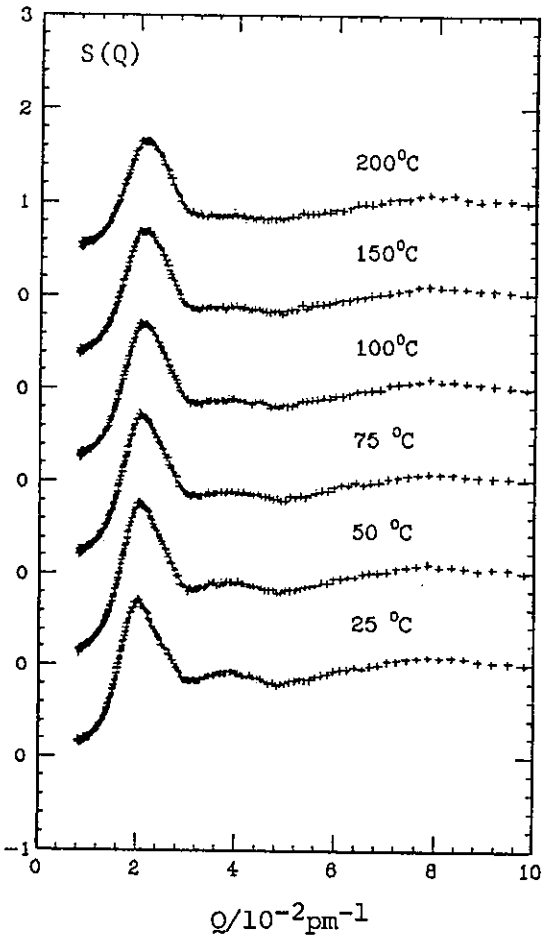

Fig. 1 Structure factors S(Q) of liquid D_2O at various temperatures.

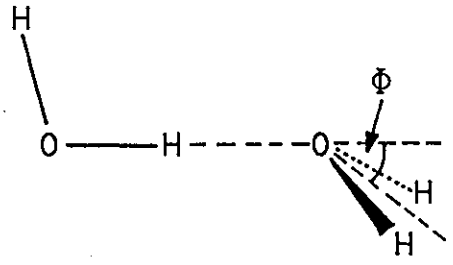

Fig. 2 Configuration of a water dimer.

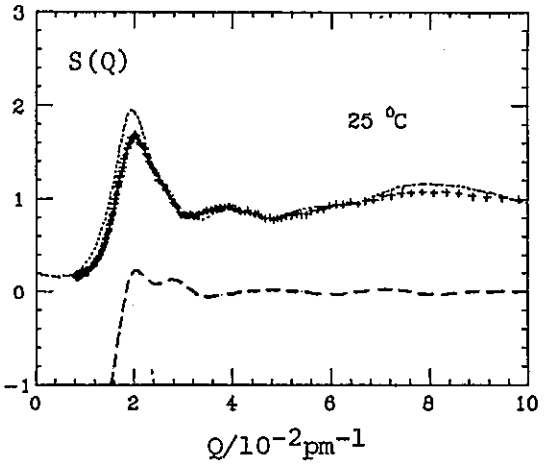

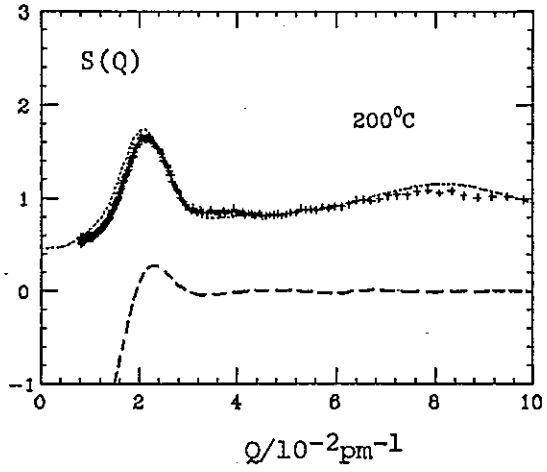

Fig. 3 Structure functions S(Q) of liquid D_2O at 25 and 200 °C. Crosses and dotted lines show, respectively, the experimental and calculated values by eq. (4) based on the model described in the text and in Fig 2, together with $F_{OO}(Q)$ values (broken line) obtained by means of X-ray diffraction [1].

Structural Analysis of Molten NaSCN and KSCN by The Neutron Diffraction Method

Toshio Yamaguchi*, Yusuke Tamura, Hirosuke Matsui, Isao Okada,
Hitoshi Ohtaki and Masakatsu Misawa†

Department of Electronic Chemistry, Tokyo Institute of Technology,
Nagatsuta, Midori-ku, Yokohama 227, Japan
†National Laboratory for High Energy Physics, Oho-machi,
Tsukuba 305, Japan

1. Introduction

Thiocyanate ion (SCN^-) can bind with metal ion *via* both sulfur and nitrogen atoms. Therefore, it seems interesting to investigate the structure of molten NaSCN and KSCN to see which site can preferably interact with alkaline metal ions in the liquid state. We also plan to perform molecular dynamics simulation of molten NaSCN with a rigid SCN moiety, and thus the reliable structural information on SCN^- ion in the molten system is needed.

In the present study, we measured neutron scattering from molten NaSCN and KSCN to determine the structure of SCN^- ion in both melts and also to examine the coordination of SCN^- ions to the cations.

2. Experimental

Powder NaSCN and KSCN were dried in a vacuum oven and then sealed in a quartz tube with the dimension of 10 mm inner diameter, 50 mm height, and 0.5 mm wall thickness. Neutron scattering measurements were performed on HIT of the National Laboratory for High Energy Physics (KEK). The temperature of the samples were (563 ±1) K and (523 ±1) K for molten NaSCN and KSCN, respectively. The counters for scattered neutrons were arranged at the scattering angles (2θ) of 8°, 13°, 23°, 30°, 50°, 90°, and 150°. The experimental data were corrected for absorption, multiple scattering, the Placzek effect, and subsequently normalized to the absolute units by a comparison of the scattering of a vanadium rod with the same dimension.

3. Results and Discussion

The structure factor $S(Q)$ can be defined by

$$S(Q) = (\sum c_i b_i)^{-2}[(d\sigma/d\Omega)_{obs} - \sum c_i b_i^2 + (\sum c_i b_i)^2], \quad (1)$$

*Present address: Department of Chemistry, Faculty of Science, Fukuoka University, Nanakuma, Jonan-ku, Fukuoka 814-01

where $(d\sigma/d\Omega)_{obs}$ is the observed differencial cross-section, and Q the scattering vector $(=(4\pi/\lambda)\sin\theta)$. c_i and b_i denote the mole fraction and the scattering length of the i-th atom, respectively. The $S(Q)$ is Fourier transformed into the radial distribution function $D(r)$,

$$D(r) = 4\pi r^2\rho_0 + \frac{2r}{\pi}\int Q[S(Q)-1]\sin(Qr)dQ, \tag{2}$$

where ρ_0 is the mean density. The resulting $S(Q)$ and $D(r)$ are shown in Figs. 1 and 2, respectively.

In the $D(r)$ of both melts, peaks appeared at 115 and 165 pm, which are assignable, respectively, to the C−N and C−S interactions within SCN^- ion. The structural parameters of SCN^- ion were determined by a least-squares fitting procedure, in which the function U

$$U = \sum_{Q_{min}}^{Q_{max}} [i(Q)_{obs}-i(Q)_{calc}]^2, \tag{3}$$

was minimized. The theoretical structure function $i(Q)_{calc}$ $(= S(Q)-1)$ can be expressed by

$$i(Q)_{calc} = \sum_i\sum_j c_i b_i b_j \frac{\sin(Qr_{ij})}{Qr_{ij}}\exp(-\gamma_{ij}Q^2). \tag{4}$$

Here r_{ij} and $2\gamma_{ij}$ stand for the distance between the i- and j-th atoms and the mean square displacement to r_{ij}, respectively. The Q-region used in the fits was $0.09 \leq Q/pm^{-1} \leq 0.30$. The final results are given in Table 1, together with those obtained for crystals by the X-ray and neutron diffraction methods. The structure of SCN^- is very similar in both melts and is close to that found in the corresponding crystal structures [1,2]. The C−S distance is much shorter than expected for a single C−S bond, while the C−N bond length is close to that of a triple bond.

In the $D(r)$ of molten NaSCN, three peaks were observed at 243, 283 and 319 pm. The peak at 243 pm was consistent with the one found for the Na−N contact in the crystal of NaSCN, thus assinged to be due to the Na−N interaction in the melt. As in the crystal structure, the peak around 283 pm corresponds to the Na−S interaction. The non-bonding N···S interaction also contributes in part to this peak.

It has been found that SCN^- ion coordinates to metal ions through the S atom with the bond angle <S−M···N = 38° − 41° (<M−S−C = 102° − 106°) for Hg^{2+} and Cd^{2+} ions in H_2O [3] and in DMF [4], while it binds through the N atom with Cd^{2+} and Zn^{2+} ions with the angle <N−M···S = 17° − 20° (<M−N−C = 145° − 149°) (*i.e.*, almost linear bonding of M−N−C−S) in the same solvents. These types of bonding of SCN^- ion to metal ions may usually occur due to the electronic structures of the S and N atoms within SCN^- ion.

Potential minima appear at the positions shown in Fig. 3 around SCN^- ion according to the *ab initio* calculations by using the 3-21G basis set [5]. Therefore, we can assume that Na^+ ion interacts with SCN^- ion in the melt with a similar manner as shown in Fig. 4. Some Na^+ ions can also come to the positions above and below the plane of the picture. If we accept the local structure of the melt mentioned above, the peaks found in the radial distribution function curves given in Fig.2 can be reasonably explained as indicated in the figure.

In the $D(r)$ of molten KSCN two peaks appeared at 278 and 315 pm. From a comparison between structure data found in crystal and in the melt, the former peak was ascribed to the K−N contact and the latter to the K−S interaction. Assignments of the peaks found in the radial distribution curve (Fig. 2, below) can be made according to the model structure given in Fig. 4 (below), which is similar to that of the NaSCN melt. Detail discussions on the coordination structure of SCN^- to Na^+ and K^+ ions will be examined later by employing molecular dynamics simulations.

References

[1] J. W. Bats, P. Coppens, and Å. Kvick, Acta Crystallogr., **B33**, 1534 (1977).
[2] C. Akers, S. W. Peterson, and R. D. Willett, Acta Crystallogr., **B24**, 1125 (1968).
[3] T. Yamaguchi, K. Yamamoto, and H. Ohtaki, Bull. Chem. Soc. Jpn., **58**, 3235 (1985).
[4] T. Takamuku, K. Ozutsumi, T. Yamaguchi, S. Ishiguro, and H. Ohtaki, unpublished data.
[5] H. Matsui, Master Thesis, Tokyo Institute of Technology, (1986).

Table 1 Structures of NaSCN and KSCN in melts and in crystals (distance in pm)

NaSCN	Neutron melt	Neutron crystal[1)]	KSCN	Neutron melt	X-Ray crystal[2)]
S−C	165	164.3	S−C	163	168.9
C−N	118	117.4	C−N	115	114.9
S−N	283	281.7	S−N	278	283.8
Na−N	243	242.2	K−N	278	297.4
Na−S	283	289.1	K−S	315	327.2
Na−C	319	319.3			
<SCN	180	179.1	<SCN	180	178

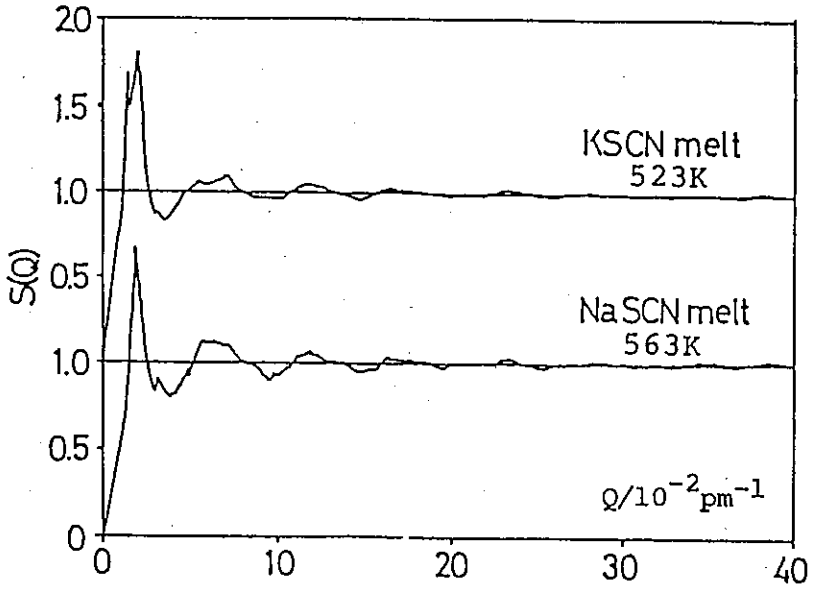

Fig. 1 Structure factors of NaSCN and KSCN melts.

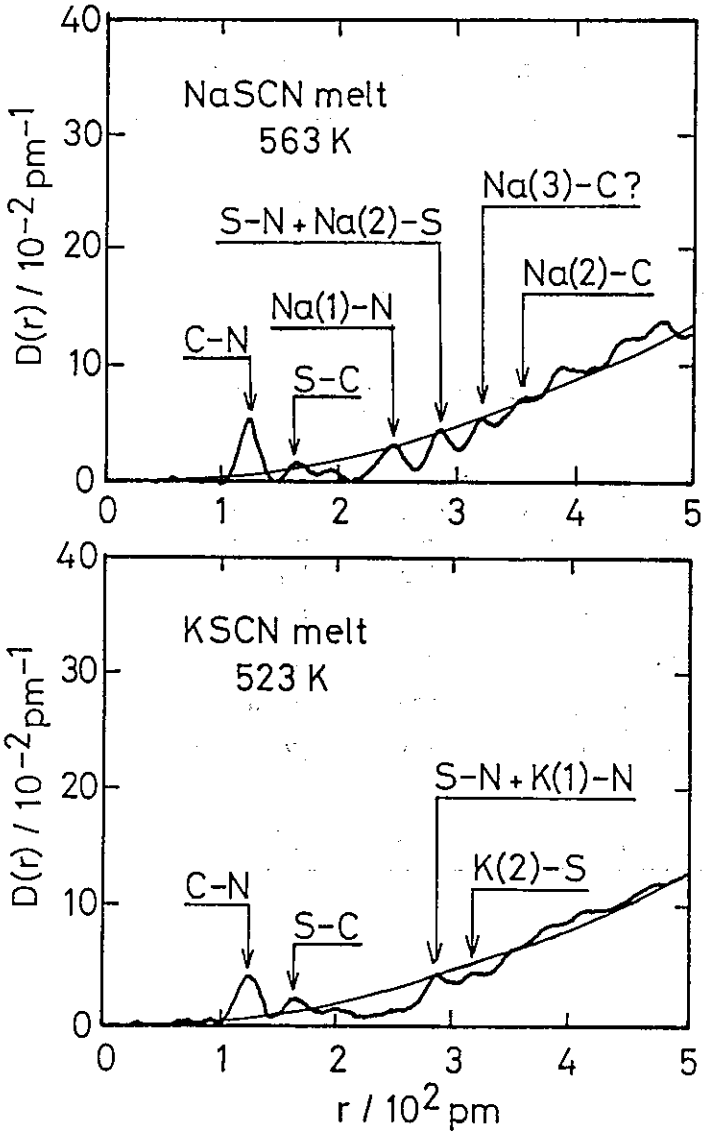

Fig. 2 Radial distribution functions of NaSCN and KSCN melts.

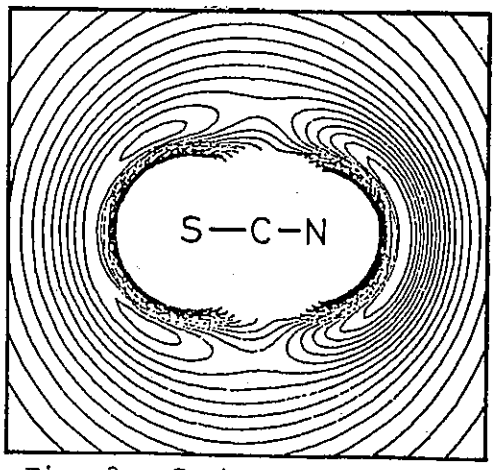

Fig. 3 Contour energy map derived from *ab initio* calculation of Na^+-SCN^- dimer. The contour interval is 20 KJ/mol.

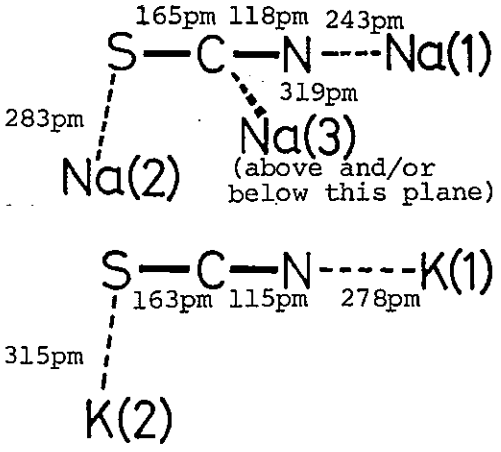

Fig. 4 Coordination of Na^+ and K^+ to SCN^- ion.

A Neutron Diffraction Study on Molten $LiAlCl_4$

Yasuo KAMEDA, Kazuhiko ICHIKAWA, *Takaaki MATSUMOTO,
**Masakatsu MISAWA and **Noboru WATANABE

Department of Chemistry and *Department of Nuclear Engineering
Hokkaido University, Sapporo 060, Japan
**National Labolatory for High Energy Physics, Oho-machi,
Tsukuba-gun Ibaraki 407, Japan

The $AlCl_4^-$ species is dominant in molten $LiAlCl_4$ in the Raman spectroscopic study[1], and the splitting in the anti-symmetric stretching band is interpreted in terms of the lowering of T_d symmetry for $AlCl_4^-$. The ^{27}Al NMR study in $AlCl_4^-$ for molten $LiCl+AlCl_3$ mixture has been reported by using the inversion recovery method[2]. The temperature dependence of the ^{27}Al spin-lattice relaxation rate is interpreted in terms of the electric quadrupolar interaction and the rotational motion of $AlCl_4^-$. The geometry of $AlCl_4^-$ has been investigated by using X-ray diffraction technique[3]. The three partial pair distribution functions g_{AlAl}, g_{AlCl} and g_{ClCl} were obtained from the neutron diffraction measurements using Cl isotope substitution method[4]. However, the intermolecular structure around Li^+ in the chloroaluminate melt is not yet known.

In this paper, we report the distribution function $\overline{G}_{Li}(r)$ around Li^+ and the intramolecular parameters of $AlCl_4^-$. They were determined from the observed coherent differential scattering cross sections in molten $^{6,7}LiAlCl_4$ and $^{7}LiAlCl_4$.

The observed total differential scattering cross section can

be devided into two parts corresponding to self and interference terms. The interference term consists of the two contributions; the intramolecular and intermolecular parts. The intramolecular interference term, which is the scattering from an isolated complex ion $AlCl_4^-$ can be expressed as

$$[d\sigma/d\Omega]_{int}^{intra} = 8b_{Al}b_{Cl}\exp(-\frac{1}{2}l^2_{AlCl}Q^2)\frac{\sin Qr_{AlCl}}{Qr_{AlCl}} + 12b_{Cl}^2\exp(-\frac{1}{2}l^2_{ClCl}Q^2)\frac{\sin Qr_{ClCl}}{Qr_{ClCl}} \quad (1)$$

We worked out an expression for the difference Δ_{Li} between intermolecular interference cross-section, scaled by a molecule formulated by $LiAlCl_4$, between two melts $^7LiAlCl_4$ and $^{6,7}LiAlCl_4$; they were identical in all respects except that the isotopic state of Li was changed. The difference Δ_{Li} consists of only three terms which include Li contributions, i.e.,

$$\Delta_{Li}(Q) = (b_{Li}^2-b'^2_{Li})[a_{LiLi}(Q)-1] + 2b_{Al}(b_{Li}-b'_{Li})[a_{LiAl}(Q)-1] + 8b_{Cl}(b_{Li}-b'_{Li})[a_{LiCl}(Q)-1] \quad (2)$$

The Fourier transform of $\Delta_{Li}(Q)$ gives the distribution function $\bar{G}_{Li}(r)$ around Li^+, i.e.,

$$\bar{G}_{Li}(r) = (b_{Li}^2-b'^2_{Li})[g_{LiLi}(r)-1] + 2b_{Al}(b_{Li}-b'_{Li})[g_{LiAl}(r)-1] + 8b_{Cl}(b_{Li}-b'_{Li})[g_{LiCl}(r)-1] \quad (3)$$

The sample was sealed in a quartz sample cell (10 mm in inner diameter and 0.4 mm in thickness). The pulsed-neutron diffraction measurement of the two $LiAlCl_4$ melts with difference in isotopic

state of Li, $f(^6Li)=0$ and $f(^6Li)=0.54$, was carried out at 190±10°C using the high intensity total scattering spectrometer (HIT).

The two internuclear distances r_{AlCl} and r_{ClCl} and two root mean square displacements l_{AlCl}, and l_{ClCl} for $AlCl_4^-$ were determined by a least squares fit of eqn(1) to the observed interference term of molten $^{6,7}LiAlCl_4$, recorded for the ca. 150°, ca. 91° and ca. 43° detectors, at the high Q region: $r_{AlCl}=2.180\pm0.008$ Å, $r_{ClCl}=3.560\pm0.008$ Å, $l_{AlCl}=0.10\pm0.01$ Å, $l_{ClCl}=0.17\pm0.01$ Å. Figures 1(a) and (b) show the intermolecular interference functions for the two melts $^7LiAlCl_4$ and $^{6,7}LiAlCl_4$ at $2\theta=20.5°$. Figure 1(c) shows the algebraic difference $\Delta_{Li}(Q)$ between 1(a) and (b). The Li-Cl term in $\Delta_{Li}(Q)$ of eqn(2) is dominant and hence $\bar{G}_{Li}(r)$ (see eqn(3)) yielded the distribution of Cl around Li. Figure 2 shows $\bar{G}_{Li}(r)$ obtained by a Fourier transform of $\Delta_{Li}(Q)$ truncated at 10 $Å^{-1}$. The large peak located at 2.72 Å is assigned to the nerest neighbour Li···Cl correlation. The coordination number of Cl atom around Li^+ is found to be 7.7.

References

1) E. Ritter, H. A. Øye, S. J. Cyvin, B. N. Cyvin and P. Cl æboe, J. Inorg. Chem. 1185, 35 (1973)

2) T. Matsumoto and K. Ichikawa, J. Amer. Chem. Soc. 6, 1100 (1982)

3) S. Takahashi, T. Muneta, N. Koura and H. Ohno, J. Chem. Soc., Faraday Trans. II 319, 81 (1985)

4) S. Biggin, S. Cummings, J. E. Enderby and M. Blander, Proc. of the Fifth Intern. Symp. on Molten Salts (Eds., M. L. Saboungi et al., Electrochem. Soc.) 81 (1986).

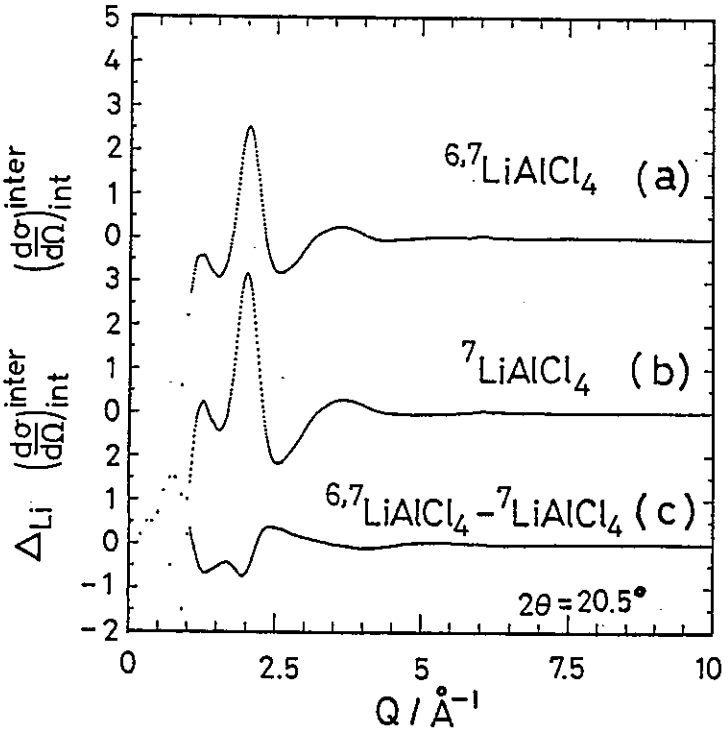

Fig.1 The intermolecular interference cross sections and the difference $\Delta_{Li}(Q)$ for $LiAlCl_4$ melt at 190±10°C

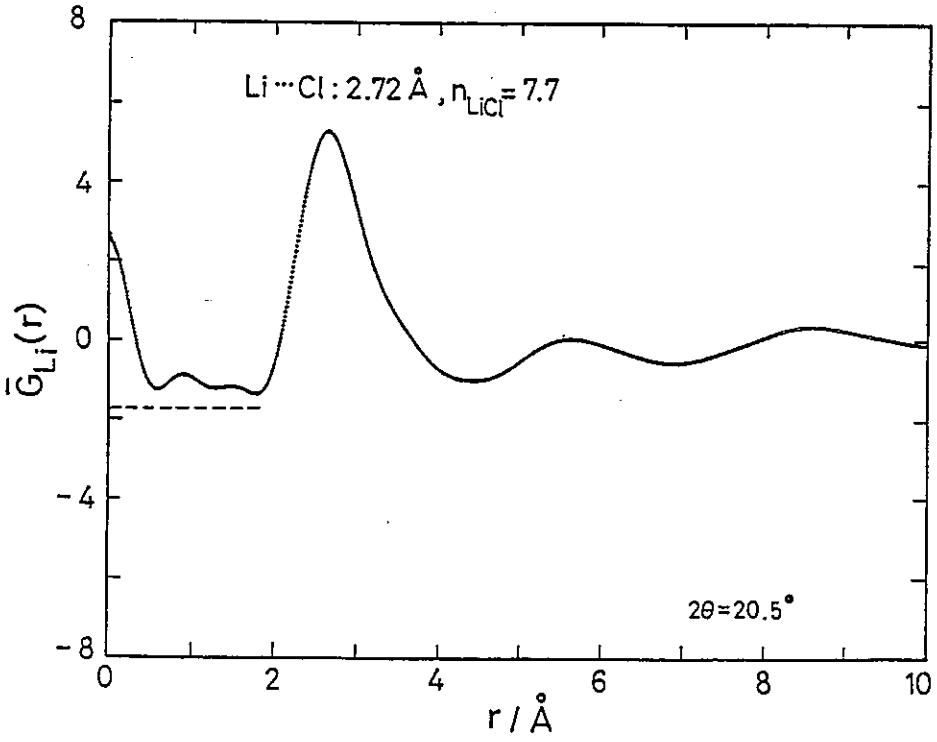

Fig.2 $\bar{G}_{Li}(r)$ for $LiAlCl_4$ melt at 190±10°C

Inelasticity Correction for a Time-of-Flight Neutron Diffraction Data of Heavy Water

Yasuo KAMEDA and Kazuhiko ICHIKAWA

Department of Chemistry, Hokkaido University, Sapporo 060, Japan

In recent years, a great interests for the hydrogen bonded liquids has been increased. Especially, the liquid heavy water has been widely investigated by many authors from the neutron diffraction measurements.[1-6] The time-of-flight neutron diffraction technique has a great advantage to determine the molecular structure in liquid phase, although the inelasticity correction is much difficult for the liquid which contains light nuclei as hydrogen or deuterium. The inelasticity corrections have been tried for the neutron diffraction cross sections measured using the time-of-flight technique.[7-9]

In this paper, we report the inelasticity correction for the diffraction data of heavy water obtained by using a high intensity total scattering spectrometer(HIT)[10].

The observed total scattering cross-section can be devided into the self and the interference terms. The self term including the inelasticity correction can be written as

$$\left(\frac{d\sigma}{d\Omega}\right)_i^{self} \Big/ \overline{b_i^2} = 1-2\frac{\sin^2\theta}{M_i^*}\left\{2(1-\gamma)+(1-\gamma)\frac{d\ln\varepsilon}{d\ln k}\Big|_{k=k_e} - \gamma\frac{d\ln\phi}{d\ln k_\circ}\Big|_{k_\circ=k_e}\right\} \qquad (1)$$

and

$$M_i^* = M_i \Big/ \left\{1-\alpha_i \exp(-\beta_i Q^2)\right\}$$

where $4\pi\overline{b_i^2}$: total scattering cross section of nucleous i

γ : the ratio of the incident and scattered neutron flight path

ε : detector efficiency

ϕ : incident neutron spectrum

k_0, k : wave number of incident and scattered neutron

M_i^* : effective mass of nucleus i for self scattering

α, β : constant calculated by using the molecular geometry and the vibrational frequencies[11]

The intramolecular interference term including the inelasticity correction for i-j atom pair is expressed as follows

$$\left(\frac{d\sigma}{d\Omega}\right)^{intra}_{int\ ij} \Big/ b_i b_j = \exp(-\frac{1}{2}l_{ij}^2Q^2)\frac{\sin Qr_{ij}}{Qr_{ij}} - \frac{\sin^2\theta}{M_{ij}^*}\left[2\left\{2(1-\gamma)+(1-\gamma)\frac{d\ln\varepsilon}{d\ln k}\Big|_{k=k_e}\right.\right.$$

$$\left.\left. -\gamma\frac{d\ln\phi}{d\ln k}\Big|_{k=k_e}\right\}\frac{\sin Qr_{ij}}{Qr_{ij}} + (1-2\gamma)\left(\cos Qr_{ij} - \frac{\sin Qr_{ij}}{Qr_{ij}}\right)\right]\exp(-\varkappa_{ij}Q^2) \qquad (2)$$

where M_{ij}^* : effective mass for interference scattering

$\varkappa_{ij}$: damping factor calculated by using the molecular geometry and the vibrational frequencies[11]

The term of $d\ln\phi/d\ln k$ was determined by the numerical derivatives of the scattering data from the vanadium rod, and the term of $d\ln\varepsilon/d\ln k$ was evaluated by using the absorption coefficient calculated for 20 atom ^{3}He gas, as shown in fig.1.[12]

Figure 2 shows the self-scattering cross-section calculated by using eqn(1) (solid line) and the measured total differential scattering cross-section at the scattering angle of 91° (dots). The charactaristic feature is mainly determined by $d\ln\phi/d\ln k$ in eqn(1). Figure 3 shows the best fit of eqn(2) to the observed intramolecular interference cross sections at the scattering angle of 91° and 150°, respectively. The parameters obtained from 150° data and 91° data are the intramolecular bond lengths in

D_2O molecule, $r_{OD}=0.971\pm0.003$ Å and $r_{DD}=1.55\pm0.02$ Å. The fact that the parameters are in excellent agreement with the values obtained from the data for the steady state reactor[11], shows the validity of our inelasticity correction procedure. Without the inelasticity correction, the r_{OD} value of 0.948 Å for $2\theta=150^\circ$ is too short.

References

1) D.I.Page, J.G.Powles, Mol.Phys. 21,901(1971)

2) A.H.Narten,J.Chem.Phys. 56,5681(1972)

3) G.Walford,J.H.Clarke,J.C.Dore,Mol.Phys. 33,25(1977)

4) J.G.Powles,Mol.Phys. 26,1325(1973)

5) A.K.Soper,R.N.Silver,Phys.Rev.Lett. 49,742(1982)

6) W.E.Theesen,A.H.Narten,J.Chem.Phys. 77,2656(1982)

7) J.G.Powles,Mol.Phys. 36,1181(1976)

8) T.Matsumoto,J.Nucl.Sci. and Tech. 16,401(1979)

9) K.Ichikawa,Y.Kameda,T.Matsumoto and M.Misawa J.Phys.C 17,L725(1984)

10) K.Ichikawa,T.Matsumoto,M.Misawa,N.Watanabe, unpublished data,1982

11) J.G.Powles,Mol.Phys. 42,757(1981)

12) M.Misawa, private communication

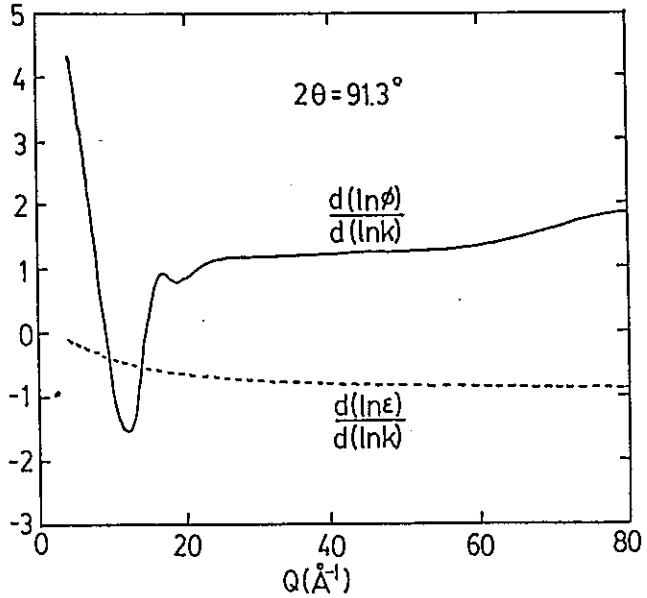

Fig.1 The logalithmic derivatives of the incident neutron spectrum ϕ and the detector efficiency ε for $2\theta=91.3^\circ$

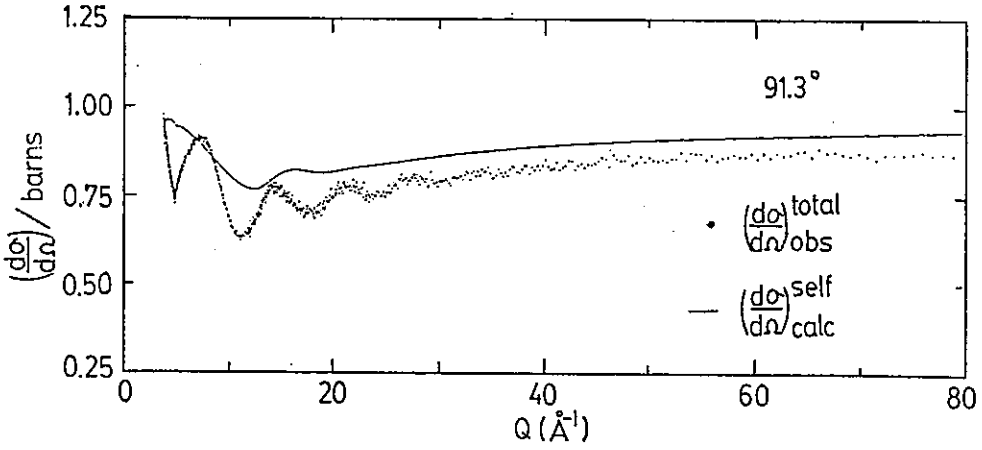

Fig.2 The self scattering cross section calculated by using eqn(1) and the observed total scattering cross section at $2\theta=91.3^{\circ}$

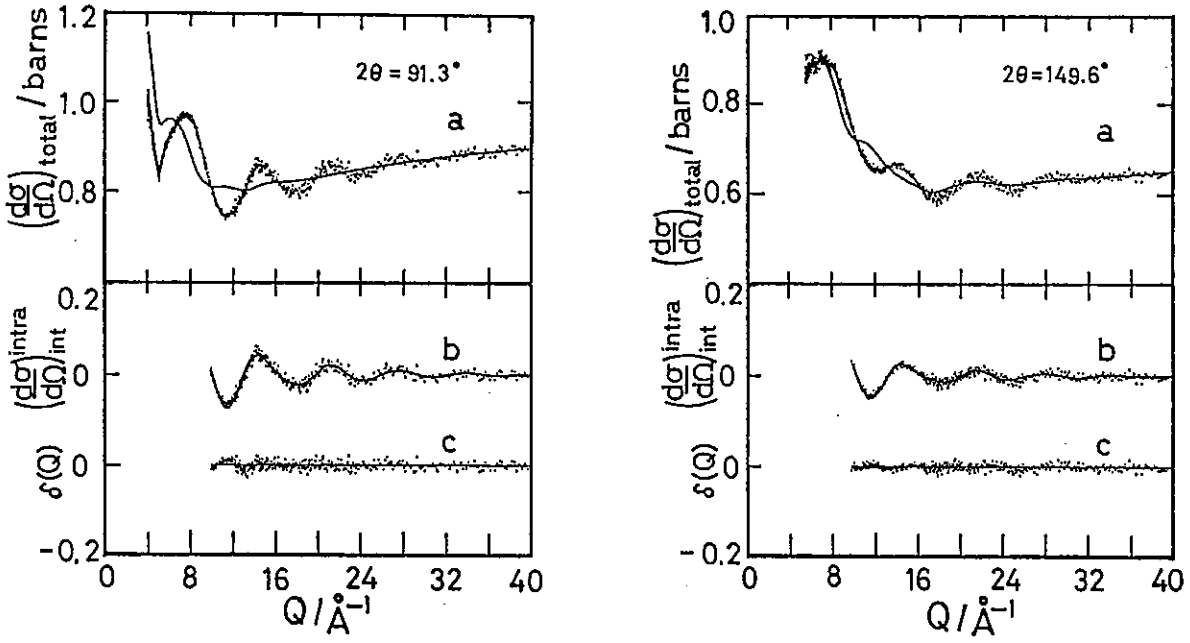

Fig.3 (a)The observed total scattering cross section (dots) and the self scattering contribution (solid line). (b) Subtraction of self term which corresponds to solid line in (a) from total cross section yields the measured intramolecular interference cross section (dots) for $Q>10$ Å^{-1}. The best fit of eqn(2) to the measured (solid line). (c) The residual functions (dots).

Structural study of molten KNO_3 and (2:1) KNO_3-$Ca(NO_3)_2$ mixture by Neutron Diffraction Method

Seiichi FUKUNAGA, Toshio YAMAGUCHI, Yusuke TAMURA, Osamu ODAWARA, Isao OKADA, Hitoshi OHTAKI and Masakatsu MISAWA*

Department of Electronic Chemistry, Tokyo Institute of Technology, Nagatsuta, Midori-ku, Yokohama 227, Japan

*National Laboratory for High Energy Physics, Oho-machi, Tsukuba-gun, Ibaraki 305, Japan

Structures of molten univalent metal nitrates have been investigated by Raman and infrared spectroscopy. These measurements have suggested the presence of specific ionic association between cations and nitrate ions and formation of quasi-crystalline aggregates. Previously, we reported a neutron diffraction study on molten $LiNO_3$, $RbNO_3$, $AgNO_3$, and 1:1 mixture of $LiNO_3$-$RbNO_3$ [1], in which the radial distribution function (RDF) of the molten $AgNO_3$ revealed that about four nitrate ions are bound to a Ag^+ as a monodenate ligand with the shortest Ag-O distance of 240 pm. Further structural details of the other melts have been demonstrated by molecular dynamics simulations in combination with X-ray and neutron diffraction [2].

In the present study, we have measured neutron scattered intensities from molten KNO_3 and 2:1 KNO_3-$Ca(NO_3)_2$ mixture in order to determine the structure of nitrate ions in the melts and also to examine the effect of divalent Ca^{2+} on the structure of the melts.

Commercial KNO_3 and $Ca(NO_3)_2$ of reagent grade were used without further purification. Powder samples were dried in vacuo at about 373 K for 3 days. KNO_3 was sealed in vacuo in a quartz tube with an inner diameter of 10 mm. 2:1 KNO_3-$Ca(NO_3)_2$ mixture was prepared by mixing required amounts of each nitrate at 650 K and subsequent cooling. The mixture was sealed into a quartz cell in the same way as for KNO_3. Neutron scattering measurements of these melts were performed at 633 K on the High Intensity Total scattering spectrometer (HIT). The furnace consisted of two infrared lamps facing each other on both sides of the sample cell.

The structure factor S(Q) can be defined by

$$S(Q)=(I(Q)-\Sigma b_i^2+(\Sigma b_i)^2)/(\Sigma b_i)^2 ,$$

where I(Q) is the normalized observed intensity and b_i the coherent scattering length of the i-th nucleus. Experimental S(Q) of both melts are shown in Fig. 1. The radial distribution function (RDF) is calculated by the conventional Fourier transform,

$$D(r) = 4\pi r^2 \rho_0 + (2r/\pi) \int_{Q_{min}}^{Q_{max}} Q \; i(Q) \sin(Qr) \, dQ ,$$

where ρ_0 denotes the number density, Q_{min} and Q_{max} the lower and upper limits of the momentum transfer Q restricted under the experimental conditions, and i(Q) (= S(Q)-1) the structure function. The RDFs obtained are depicted in Fig. 2.

The first peak observed at 130 pm corresponds to the expected N-O distance within nitrate ion and the second peak around 225 pm is due to the O-O contacts within the nitrate ion. The present results are consistent with those of molten $LiNO_3$, $RbNO_3$, and mixture of $LiNO_3$-$RbNO_3$. The peak around 250 pm can be ascribed to the K-O interactions in the melts from the sum of the effective ionic radius of K^+ (133 pm) and the effective radius of oxygen atom (135 pm). Furthermore, the peak appears in D(r)s of both KNO_3 and KNO_3-$Ca(NO_3)_2$ mixture, thus supporting this assignment. In addition, Ca-O interaction in the mixture is expected to appear around 230 pm from the stand point of their ionic radii, so its peak must overlap with the predominant O-O peak at 225 pm. In order to confirm this, we shall perform a least-squares fitting procedure for S(Q) values, which is now in progress.

The orientation of nitrate ions and the cations seems difficult to be determined only from the present neutron diffraction data, since the M^+-N and M^+-O peaks found in the RDF are not well resolved. We are planning to measure X-ray diffraction of the melts and to further perform molecular dynamics simulations of molten KNO_3 and the mixture to examine more detailed structure of the melts.

References

[1] T. Yamaguchi, Y. Tamura, I. Okada, H. Ohtaki, M. Misawa and N. Watanabe, Z. Naturforsch, 40a (1985) 490.

[2] T. Yamaguchi, I. Okada, H. Ohtaki, M. Mikami and K. Kawamura, Mol. Phys., 58 (1986) 349.

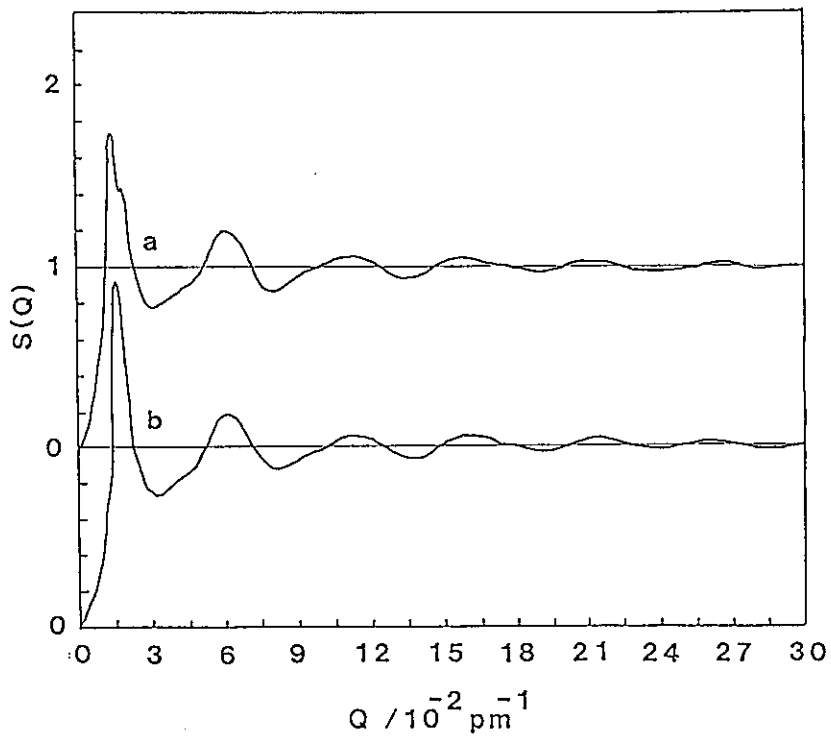

Fig. 1. Structure factors S(Q) of the melts:
(a) KNO_3, (b) 2:1 KNO_3-$Ca(NO_3)_2$

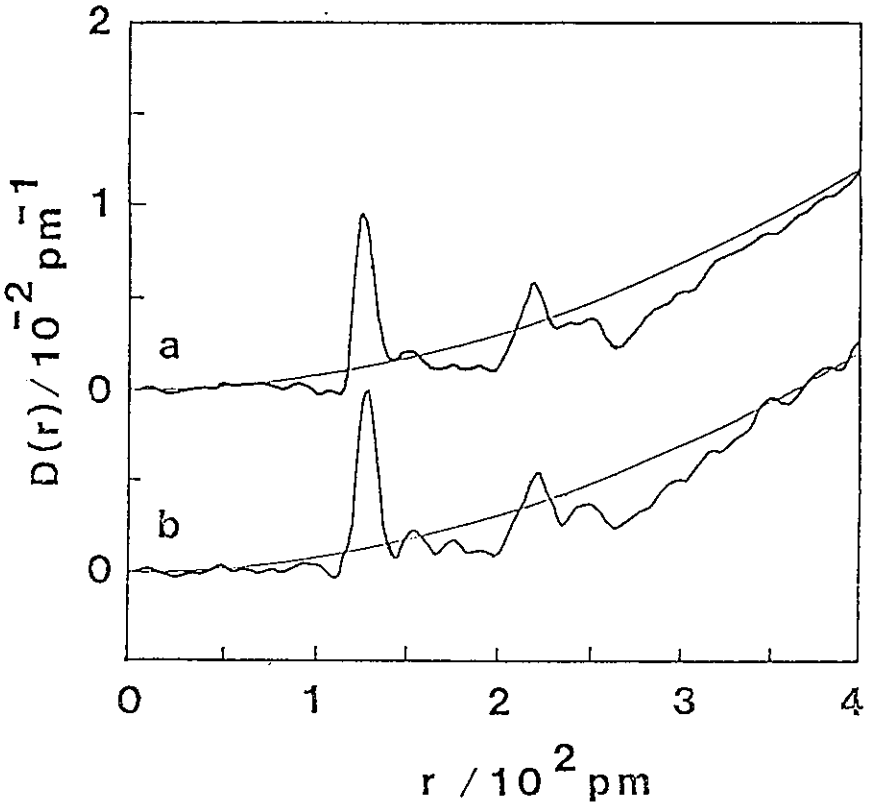

Fig. 2. Radial distribution functions of the melts:
(a) KNO_3, (b) 2:1 KNO_3-$Ca(NO_3)_2$

Neutron Diffraction of As-quenched $Ge_{20}Te_{80}$ Glass near the Glass-Undercooled Liquid Transition

Kazuhiko ICHIKAWA, Yasuo KAMEDA, Quang XU, Takaaki MATSUMOTO*, Masakatsu MISAWA,** and Noboru WATANABE**

Department of Chemistry and *Department of Nuclear Engineering, Hokkaido University, Sapporo 060, Japan
**National Laboratory for High Energy Physics, Oho-Machi, Tsukuba-gun, Ibaraki 405, Japan

Both semiconducting and metallic glasses are now the most interesting materials for the topicses on the thermal relaxation and the microstructure. During quenching the equilibrium liquid state is frozen-in under an irreversible process. A relaxation process towards an equilibrium state occurs with very slow kinetics at temperatures well below its glass transition temperature T_g. A glass-crystal transition takes place, in passing through the undercooled liquid at temperatures well above T_g. Xu and Ichikawa of the authors reported the glass-undercooled liquid transition for the $Ge_{20}Te_{80}$ glass manifested thermally by an abrupt rise in heat capacity C_p and by a λ-form in thermal diffusivity D_T.[1,2] Crystallization of the new phase, which can be easily distinguished from the normal GeTe/Te crystals, was confirmed by X-ray powder pattern and reflected light micrograph at the composition 20at.% Ge-80at%Te suggesting a possible stoichiometry of $GeTe_4$.[2,3]

In this paper we report the pulsed-neutron diffraction data in the glassy $Ge_{20}Te_{80}$ alloy at temperatures near the glass-

undercooled liquid transition and the experimental evidence on the undercooled liquid-crystal transition.

The samples at the composition 20at% Ge-80at% Te metal at 800°C were quenched in saturated aqueous solutions of NaCl at ca. -15°C and solidified to the glassy $Ge_{20}Te_{80}$. The sample was sealed in a quartz sample cell (10 mm inner diameter and 0.4 mm thickness).

The pulsed-neutron diffraction measurement of the as-quenched $Ge_{20}Te_{80}$ glass at 25°C and 130±10°C just below T_g(=155.7±1.0°C) using a high-intensity total scattering spectrometer (HIT). The measurements of the $Ge_{20}Te_{80}$ glass were also carried out at 0.5, 1, 1.5 and 2 hour at 190°C±10°C just above T_g to observe the experimental evidence for the glass-undercooled liquid-crystal transition.

The structure factors S(Q) of the glassy $Ge_{20}Te_{80}$ alloy at three temperatures are shown in fig. 1. The exposure times were 3 hours at 25°C and 130°C±10°C, and 0.5hour at 190±10°C. A first sharp diffraction peak (FSDP) at $Q \sim \mathring{A}^{-1}$ is observed in both glass and undercooled liquid.[4,5] The origin of the anomalous FSDP is based on the presence of large molecular clusters and on the medium-range order among the clusters.[6] Figure 2 shows the total radial distribution functions RDF(r) obtained by a Fourier transform of S(Q) truncated at $Q=32\mathring{A}^{-1}$. The position r_1 of the first peak and the full width at half maximum (FWHM) were obtained with the aid of a least squares fit of a Gaussian function to the first peak in the RDF(r); r_1=2.68Å and FWHM=0.30Å at 25°, 2.68 and 0.34 at 130±10°C and 2.71 and 0.34 at 190±10°C. Both r_1 and FWHM have a systematic change from the glass to the

undercooled liquid. The increase in r_1 took place under the glass-undercooled liquid transition.

The time evolution of S(Q) in fig. 3 shows the crystallization process of the undercooled liquid $Ge_{20}Te_{80}$ at 190±10°C. The neutron diffraction data of S(Q), the measurements of which were carried out at every 30 minutes, demonstrated the strong neutron beam and the good efficiency of the neutron detectors. The crystallization of the undercooled liquid was observed when the 1.5 hour passed at 190±10°C. Because the many peaks produced by the Bragg law were measured in S(Q). The peaks were compared with the diffraction patterns for the crystal which was prepared from the $Ge_{20}Te_{80}$ glass heat treated for 93 hours at 215°C,[3] the GeTe crystal and the Te crystal, as shown in fig. 4. The crystal prepared from the undercooled liquid $Ge_{20}Te_{80}$ showed the new phase which differs little from a possible stoichiometry $GeTe_4$.

1) Q. Xu and K. Ichikawa, J. Phys. Soc. C in press

2) Q. Xu and K. Ichikawa, J. Phys. Soc. C 18, L985 (1985)

3) A. G. Moore, C. Maghrabi and J. M. Parker, J. Mater. Sci. 13, 1127 (1978)

4) F. Betts, A. Bienstock, D. T. Keating and J. P. de Neufville, J. Non-Cryst. Solids 7, 417 (1972)

5) O. Uemura, Y. Sagara, M. Tsushima, T. Kamikawa and T. Satow, ibid. 33, 71 (1979)

6) J. C. Phillips, ibid. 43, 37 (1981)

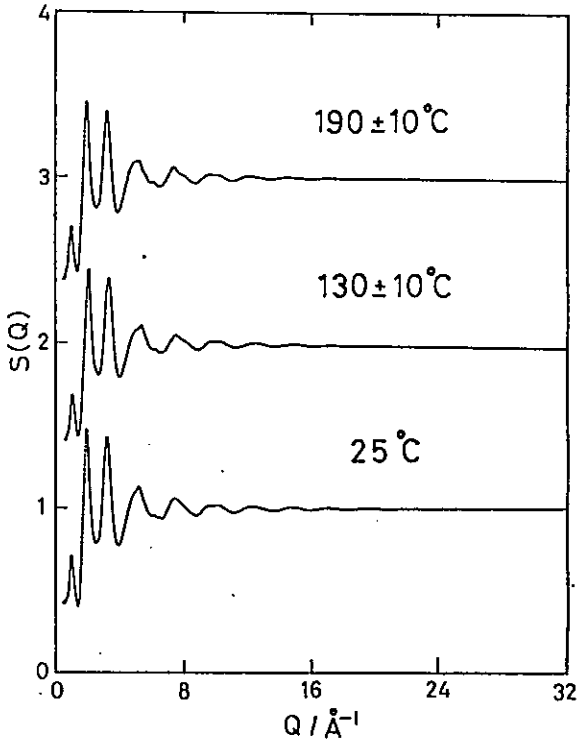

ig.1 S(Q) in the $Ge_{20}Te_{80}$ glass

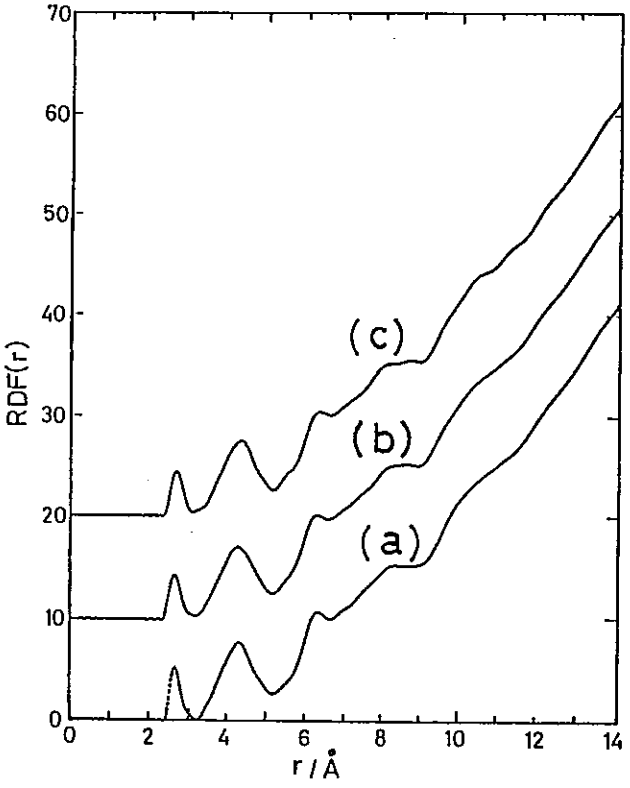

Fig.2 RDF(r) at 25°C(a), 130±10°C (b) and 190±10°C(c)

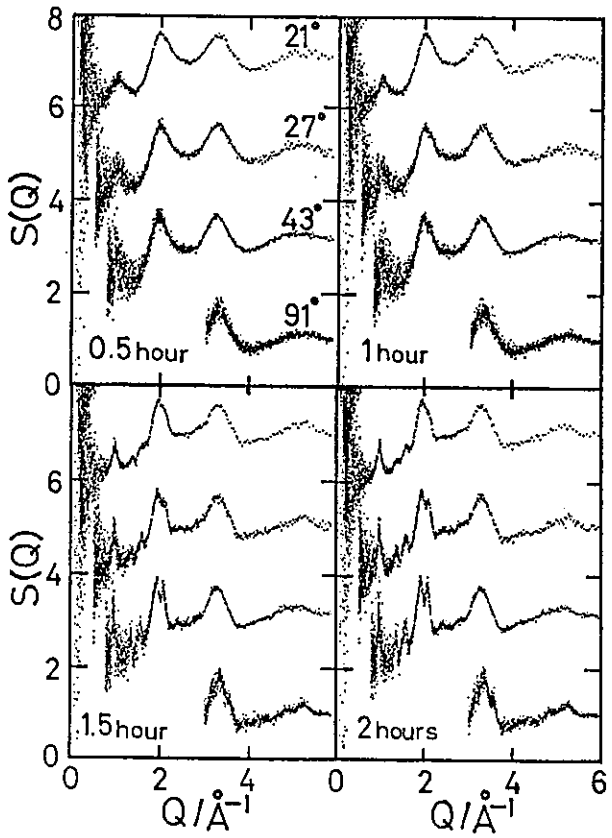

Fig.3 The time evolution of S(Q) at 190±10°C

Fig.4 The comparison among diffraction patterns of the four crystals of Ge-Te system

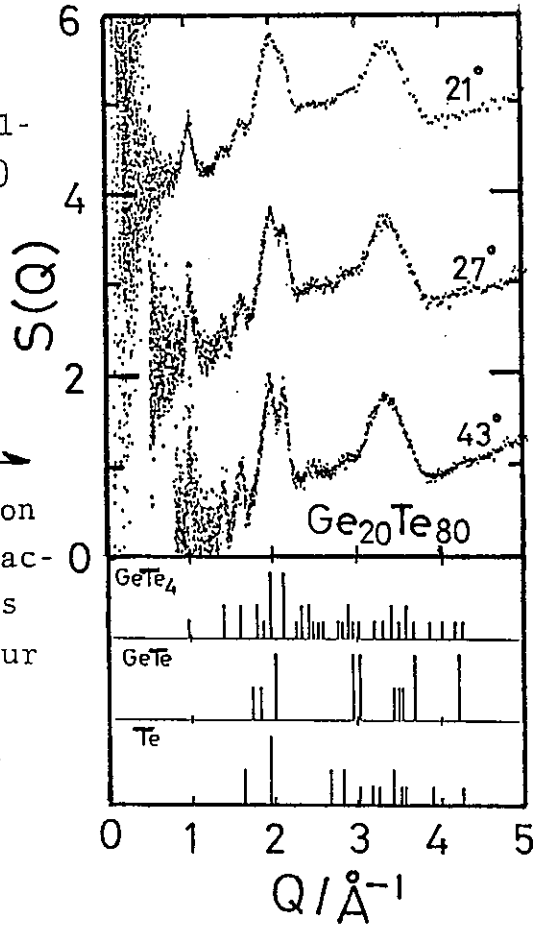

Neutron Diffraction of $2Bi_2O_3.B_2O_3$ Glass

Hiroshi HASEGAWA, Itaru YASUI

Institute of Industrial Science, University of Tokyo
22-1, Roppongi 7 Chome, Minato-ku, Tokyo 106, Japan

One of the noteworthy properties of Bi_2O_3 is high oxygen conductivity. Among four crystal forms of Bi_2O_3, δ-phase, the highest temperature form, shows high oxygen conductivity (10 mho at 800°C). This is stable in the temperature range higher than 730°C. If this high conductivity is realized in lower temperature range, wider applications become possible. There are many studies in this direction[1] and it was proved that addition of some oxides is effective to lower the transition temperature. The more oxide is added to Bi_2O_3, the more stable the δ-phase becomes in low temperature range, but the smaller the conductivity of δ-phase. Therefore, it is hoped to form δ-phase with as small amount of added oxide as possible. Rapid quenching method was tried in our laboratory and it was proved that crystallines obtained by this method showed high ionic conductivity and that the glasses of the same compositions show higher ionic conductivity[2]. To clarify the mechanism of high ionic conductivity of the glasses, structure analysis of the glasses is requested. As one of the important added oxides is B_2O_3, x-ray diffraction analysis of $2Bi_2O_3.B_2O_3$ glass was tried and the structure concerning Bi-atom was clarified, but that concerning the other component B_2O_3 could not be clarified because of small scattering power of B atom for x-ray (scattering factors of B, O, Bi= 5, 8, 83 e.u.). As the structure of the glass is controlled greatly by B atom, the information concerning B atom is requested for complete structure analysis. In neutron diffraction, the diffraction power of B atom is comparable with Bi and O atoms (scattering lengths of B, O, Bi= 0.54, 0.58, 0.85×10^{-12}cm) and more complete structure analysis of this glass may be possible. Therefore, a neutron diffraction measurement of this glass was tried at KEK. This paper reports the results.

Experimental

Sample was prepared from reagent grade of Bi_2O_3 and H_3BO_3. The

mixture was melted at about 850°C for 10min. in a Pt-Rh crucible and quenched dipping the crucible in water. The density determined by an Archimedean method was 7.77g/cm^3. The flakes smaller than 2mm diameter were filled 50mm high in a vanadium cell with thickness 0.025mm, diameter 10mm. The neutron diffraction measurement was carried with the total scattering spectrometer (HIT) installed at the pulsed neutron source (KENS) in KEK. In this measurement, the data at scattering angles 2θ=150°, 91°, 51°, 32°, 25° and 14° were used. Signals were accumulated for 15.5 hours. After correction for the absorption and multiple scattering, they were normalized to S(Q). The normalized data were unified to one S(Q) connecting suitable parts of data for each detecter as shown in Fig.1. The S(Q) was converted to RDF by the Fourier transformation, which was shown in Fig.2 with that from x-ray diffraction. The quality of the data was not very good, because the glass contains 20% of ^{10}B atoms which have very high absorption cross-section, $3837\times10^{-24}cm^2$, but we judged that it was possible to carry out more precise structure analysis of the glass together with x-ray data.

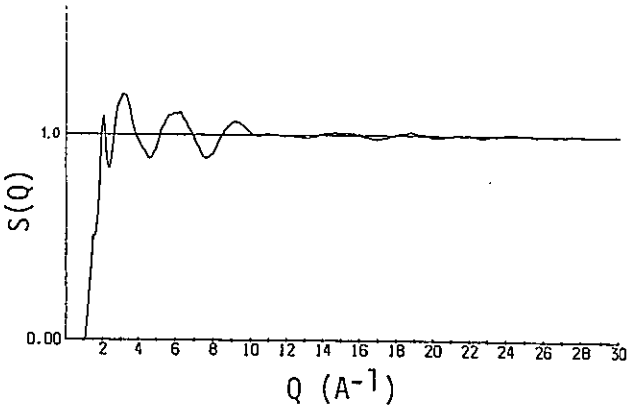

Fig.1 Structure factor of $2Bi_2O_3.B_2O_3$ glass

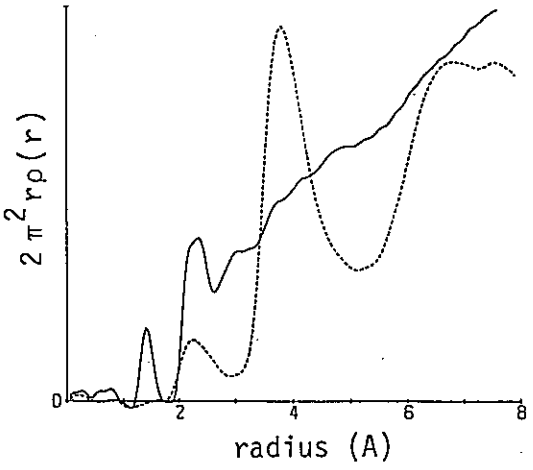

Fig.2 Radial distribution function of $2Bi_2O_3.B_2O_3$ glass. Maxima of y-axis are 10 and 10000 in the case of the RDFs from neutron and x-ray diffraction, respectively. ——— neutron, ----- x-ray

Structure Analysis

The RDF from neutron diffraction is greatly different from that from x-ray diffraction and it is attributed to the difference of relative scattering powers of constituent elements between for neutron and for x-ray diffraction. The RDF from neutron diffraction shows a peak at 1.4A

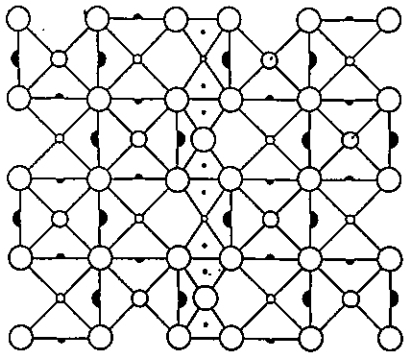

Fig.3 Structure model derived from δ-Bi_2O_3 crystal.
○; oxygen ●; bismuth •;boron

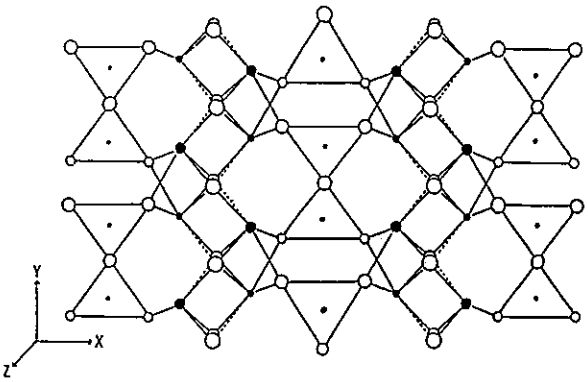

Fig.4 Structure model derived from $Bi_2O_3.GeO_2$ crystal
○ ; oxygen ●; bismuth •; boron

corresponding to the nearest B-O pair which is invisible in the RDF from x-ray diffraction. In the range from 2.0 to 2.5A a peak corresponding to the nearest Bi-O pair is visible both in the RDF from neutron diffraction and that from x-ray diffraction. In the range greater than 3.5A the RDF from neutron diffraction shows only a monotonous increasing line with small jaggedness, while the RDF from x-ray diffraction shows pronounced peaks at 3.8 and 6.5-8A. At longer radius where contributions of many atomic pairs overlap each other, it is natural that the regularity of the structure becomes invisible because of the close neutron scattering powers of constituent elements.

There are several approaches to construct structural models.

1. a model similar to the glass structures of of As or Sb oxide which belongs to V-group as Bi.
2. a model similar to the structure of $PbO-B_2O_3$ glass, for a Bi^{3+} ion has the same electron structure as a Pb^{2+} ion.
3. models similar to crystals based on Bi_2O_3
   a) a model similar to α-, β-, γ-, δ-Bi_2O_3 crystals
   b) a model similar to $Bi_2O_3.GeO_2$ or $Bi_2O_3.SiO_2$ crystal

The approaches 1 and 2 lead to too bulky models compared with the observed density and the approach 3 is, therefore, left. Among Bi_2O_3 crystals (3-a), β-, γ- and δ-phases have a similar structure and α-phase has somewhat different structure. The structure similar to α-phase is not appropriate because a Bi atom is coordinated by eight oxygen atoms in this structure. The structure model deduced from δ-phases (see Fig.3) seems plausible for the glass has as high ionic conductivity as δ-phase. The calculated RDF of this model really showed good agreement with the observed RDF from x-ray diffraction, while the agreement with the RDF

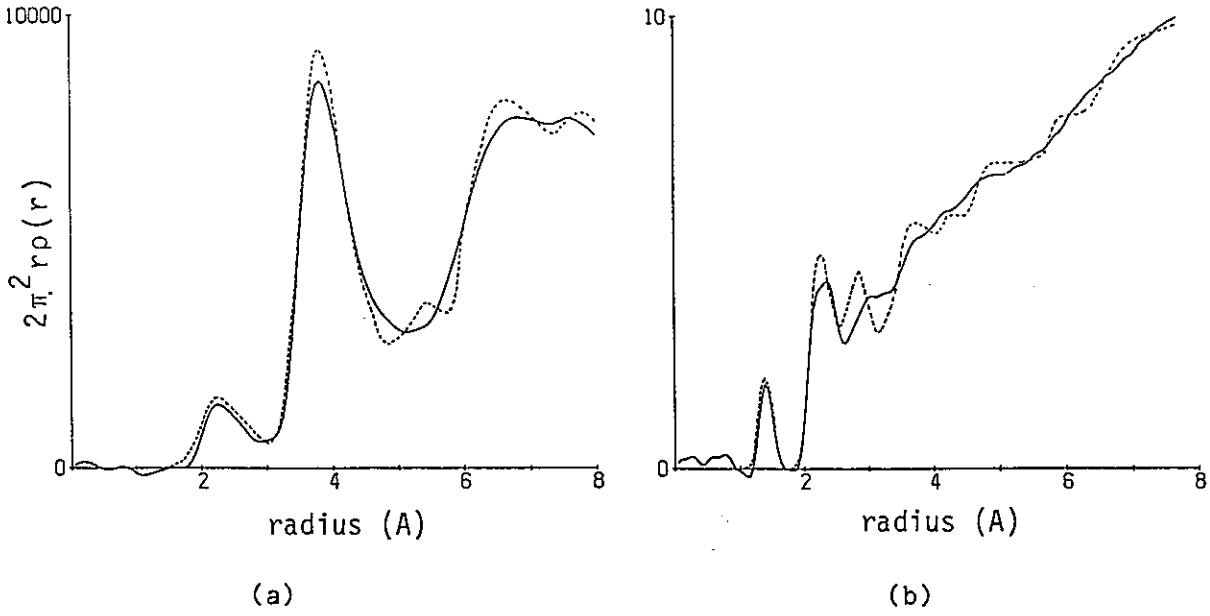

Fig.5 Radial distribution functions for $2Bi_2O_3.B_2O_3$ glass.
(a) x-ray diffraction (b) neutron diffraction
——— observed
---- calculated for the model deduced from $Bi_2O_3.GeO_2$ crystal

from neutron diffraction was poor. Another model deduced from 3-b was examined. This model is shown in Fig.4. This model also showed good agreement with the RDF from x-ray diffraction (see Fig.5-a) but the agreement with the RDF from neutron diffraction was also poor, although the agreement was a little improved (see Fig.5-b). These models and other somewhat different models are now examined. More exact structure analysis will be carried out after re-measurement by use of ^{11}B-enriched sample.

References

1) e.g.,T.Takahashi, T.Esaki and H.Iwahara, J.Appl.Electrochem.,7,31(1977)
2) I.Yasui, H.Hasegawa and T.Kurita, "Formation of ceramic membrane with metastable structure by rapid quenching", Report of grant-in-aid of the Department of Education (1984)

Structure of Ti-32.44at%Zr Neutron Zero Scattering Alloy

Toshiharu FUKUNAGA, Shinobu SHIBUYA, Masakatsu MISAWA*
and Kenji SUZUKI

The Research Institute for Iron, Steel and Other Metals,
Tohoku University, Sendai 980, Japan

*National Laboratory for High Energy Physics, Oho-machi,
Tsukuba-gun Ibaraki 305, Japan

The phase diagram shown in Fig. 1 indicates that Ti-Zr alloy system is isomorphous over all concentration range. If the atomic positions in Ti-Zr crystal alloys are randomly occupied by Ti and Zr atoms, a neutron zero scatterin alloy can be easily obtained at the composition of Ti-32.44at%Zr, because the coherent neutron scattering amplitudes of Ti and Zr atom are -0.3438 and 0.716 $\times 10^{-12}$ cm^{-1} respectively. This alloy is often used as a sample container for neutron scattering experiment. In this paper we report whether Ti and Zr atoms are distributed at random or not in this alloy.

Bhatia-Thornton[1] type total structure factor $S^{BT}(Q)$ of a binary alloy is defined as follows;

$$S^{BT}(Q)= \{\langle b\rangle^2 S_{NN}(Q)+2\langle b\rangle |\Delta b| S_{NC}(Q)+\Delta b^2 S_{CC}(Q)\} \,/\, \langle b^2\rangle \qquad (1)$$

$$\langle b^2\rangle = C_A b_A^2 + C_B b_B^2$$
$$\langle b\rangle = C_A b_A + C_B b_B$$
$$\Delta b = |b_A - b_B|,$$

where $S_{NN}(Q)$, $S_{NC}(Q)$ and $S_{CC}(Q)$ means the number density-number density, concentration-concentration and number density-concentration partial structure factors respectively. C_i and b_i are the concentration and coherent neutron scattering amplitude of an i atom in the alloy.

If Ti and Zr atoms are randomly distributed in Ti-32.44at%Zr neutron zero sacattering alloy, $\langle b\rangle=0$. Therefore, the experimental structure factor $S^{BT}(Q)$ exclusively presents the concentration-concentration structure factor $S_{CC}(Q)/C_A C_B$ as follows;

$$S^{BT}(Q)\,|_{<b>=0} = (\Delta b^2/<b^2>)\, S_{CC}(Q) = S_{CC}(Q)/C_AC_B = 1. \qquad (2)$$

However, as shown in Fig.2, the small oscillation of $S^{BT}(Q)$ is observed up to $Q\sim20$ A^{-1}. This result may not show the perfectly random distribution of Ti and Zr atoms at each lattice position but the existence of a chemical short-range order something like a concentration fluctuation in the crystal state.

The reduced radial concentration correlation function $G_{CC}(r)$ defined as the Fourier transform of $S_{CC}(Q)$, as follows;

$$G_{CC}(r) = (2/\pi)\int_0^\infty Q\,\{S_{CC}(Q)/C_AC_B-1\}\sin Qr\, dQ \qquad (3)$$

A large negative peak located at r=3.02 A is observed in $G_{CC}(r)$ as shown in Fig.3. This presents Ti-Zr pair correlation because the scattering amplitudes of Ti and Zr atom are negative and positive respectively. The Ti-Zr crystal exhibits bcc phase at high temperature and hcp phase at low temperature. The first nearest neighbor atomic distance in both bcc and hcp crystal phases is r $\sim$3.0 A, at which Ti-Ti, Ti-Zr and Zr-Zr pair correlations are located. These results indicate a little preference for Ti-Zr unlike atom pairs in Ti-Zr crystal.

In order to express quantatively the concentration fluctuation of Ti-32.44at%Zr crystal alloy, the Warren chemical short-range order parameter[2] is calculated as follows;

$$\alpha = 1-Z_{AB}/C_BZ = (1/Z)\int_{\Delta r} rG_{CC}(r)\, dr \qquad (4)$$

$0<\alpha<1$: preference for like atom neighbors
$\alpha=0$: statistically random distribution
$-C_A/C_B<\alpha<0$: preference for unlike atom neighbors,

where Z is the total coordination number between the nearest neighbor atoms, Z_{AB} is the coordination number of B atoms surrounding an A atom and Δr is the range of the first peak of the radial distribution function.

The Warren chemical short range oder parameter value is $\alpha=-0.029$ in case of the first nearest neighbor atoms Z=12 (hcp phase) and $\alpha=-0.035$ in case of Z=10 (bcc phase). These α values are close to zero in comparison with the value of $\alpha=-C_{Ni}/C_{Ti}=-0.48$ for a completely ordered alloy which prefers unlike atom in the first nearest neighbor. We may conclude that in spite of the existence of a little preference of Ti-Zr unlike atom pairs Ti and Zr atoms sit-

ting at the crystal lattice point are distributed almost at random in T-32at%Zr neutron zero scattering alloy.

References

1) A. B. Bhatia and D. E. Thornton, Phys. Rev. B2 (1970) 3004.

2) B. E. Warren, B. L. Averbach and B. W. Roberts, J. Appl. Phys. 22 (1951) 1493.

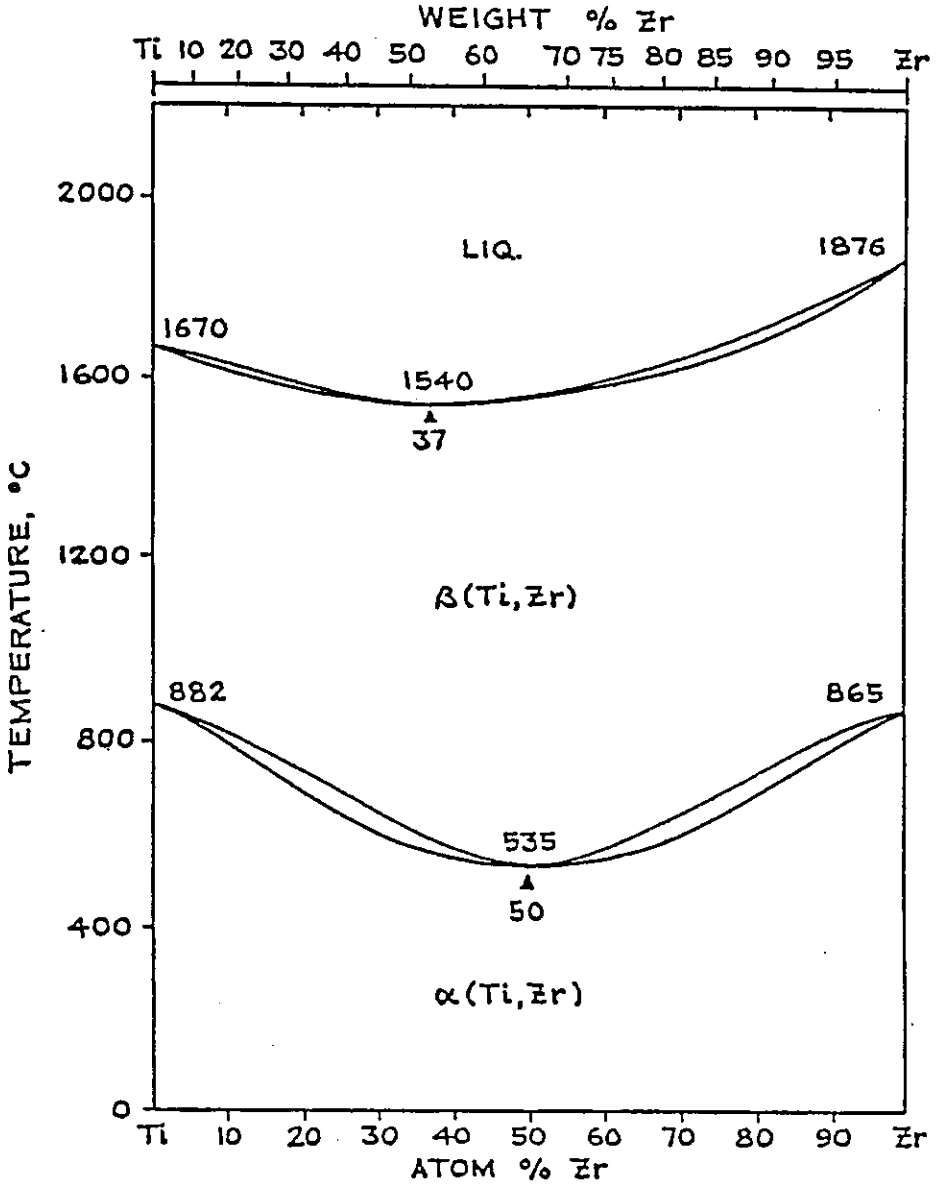

Fig. 1. Phase diagram of Ti-Zr alloy

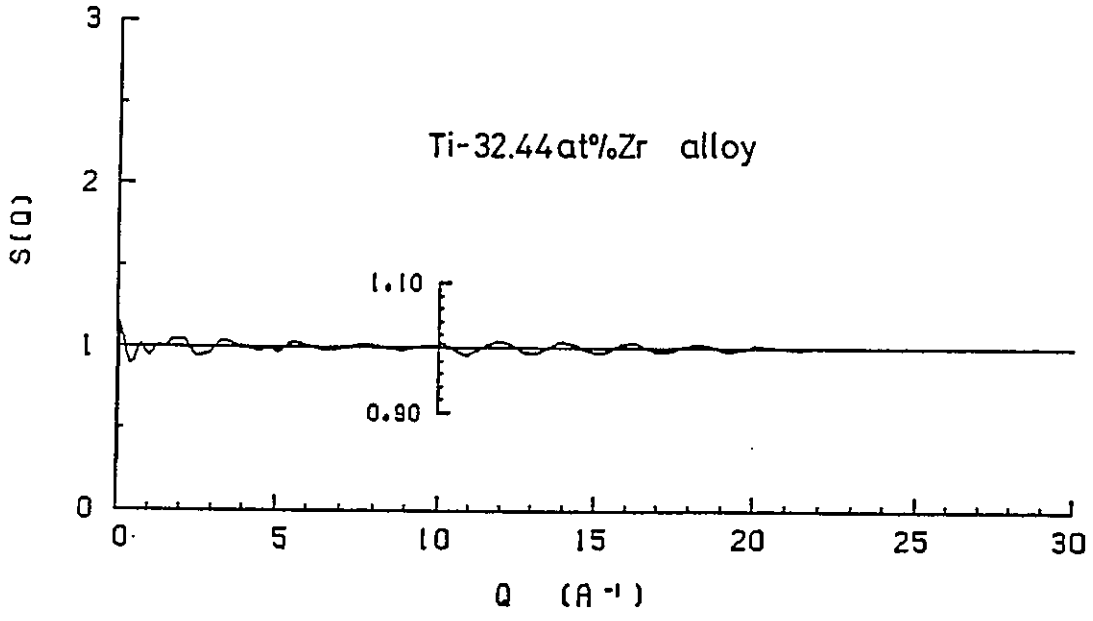

Fig. 2. Bhatia-Thornton type structure factor $S^{BT}(Q)$ of Ti-32.44at%Zr neutron zero scattering alloy

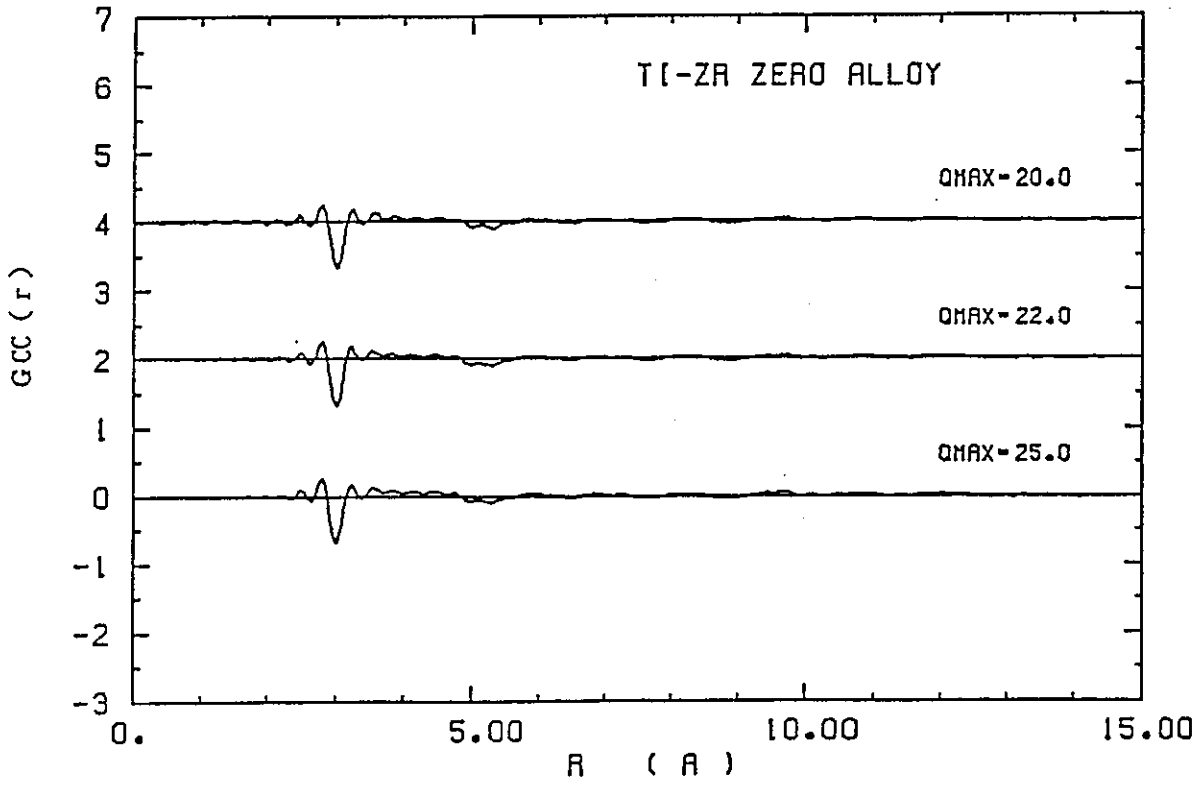

Fig. 3. Reduced concentration-concentration correlation function $G_{CC}(r)$'s of Ti-32.44at%Zr neutron zero scattering alloy

Atomic Structure of Ternary $(Ti,Zr)_{83}Si_{17}$ amorphous alloy

Toshiharu FUKUNAGA, Shinobu SHIBUYA, Masakatsu MISAWA*
and Kenji SUZUKI

The research Institute for Iron, Steel and Other Metals,
Tohoku University, Sendai 980, Japan

* National Laboratory for High Energy Physics, Oho-machi,
Tsukuba-gun Ibaraki 305, Japan

Up to date, much investigation has been reported on the atomic structure of binary metal-metal and metal-metalloid amorphous alloys, that is, the concentration dependence of the total structure and the derivation of the partial structures. However, the structure of a ternary amorphous alloy has been scarcely studied because of the complexity that the total structure is constructed by six partial pair correlations. Many amorphous alloys having characteristic physical or/and chemical properties, which have not been seen in the crystal state, are made from more than three components. It is necessary to know the atomic structure of the ternary amorphous alloys, since the characteristic properties of the amorphous alloys may be due to the atomic arrangements.

In the present report the structures of Zr-Si and Ti-Si binary amorphous alloys and that of Ti-Zr-Si ternary amorphous alloy are described. The interest in these amorphous alloys stems mainly from whether the structure of the ternary amorphous alloy is analogous to a weighted sum of the structures of two binary amorphous alloys or not.

$Zr_{85}Si_{15}$ and $Ti_{83}Si_{17}$ binary and $(Ti,Zr)_{83}Si_{17}$ ternary amorphous alloys were prepared by means of melt spinning technique in an atmosphere of purified argon. (Ti,Zr) means a Ti-32.44at%Zr neutron zero-scattering alloy. The measurements of the neutron scattering intensity from these amorphous alloys were carried out at room temperature in vacuum by using the High Intensity Total scattering spectrometer(HIT).

Figure 1 shows the Bhatia-Thornton type total structure factor $S^{BT}(Q)$'s of $Zr_{85}Si_{15}$ and $Ti_{83}Si_{17}$ binary and $(Ti,Zr)_{83}Si_{17}$ ternary amorphous alloys. The $S^{BT}(Q)$ of $Zr_{85}Si_{15}$ amorphous alloy displays the characteristically high 1st peak and the 2nd peak having a shoulder on high Q side, which have been

generally found in metal-metalloid amorphous alloys. In $Ti_{83}Si_{17}$ amorphous alloy a shoulder of the 1st peak at low Q side of $S^{BT}(Q)$ was observed. These Bhatia-Thornton type $S^{BT}(Q)$'s of $Ti_{83}Si_{17}$ and $Zr_{85}Si_{15}$ amorphous alloys are written by the number density-number density correlation $S_{NN}(Q)$, concentration-concentration correlation $S_{CC}(Q)$ and its cross term $S_{NC}(Q)$ with weighting factors as follows,

$$S^{BT}(Q) = 0.3457\ S_{NN}(Q) - 2.5322\ S_{NC}(Q) + 4.6375\ S_{CC}(Q), \quad \text{for } Ti_{83}Si_{17} \quad (1)$$
$$S^{BT}(Q) = 0.9751\ S_{NN}(Q) + 0.8750\ S_{NC}(Q) + 0.1963\ S_{CC}(Q), \quad \text{for } Zr_{85}Si_{15} \quad (2)$$

From the above equations the shoulder located at the low Q side of the 1st peak in $Ti_{83}Si_{17}$ amorphous alloy is suggested to be due to $S_{CC}(Q)$ because the weighting factor of $S_{CC}(Q)$ of $Ti_{83}Si_{17}$ amorphous alloy is much larger than that of $Zr_{85}Si_{15}$ amorphous alloy.

In the $S^{BT}(Q)$ of $(Ti,Zr)_{83}Si_{17}$ amorphous alloy, no pronounced peak is observed. The amplitude of the oscillation over all Q range is low in comparison with that of $Ti_{83}Si_{17}$ and $Zr_{85}Si_{15}$ amorphous alloys. A synthesized structure factor $S^{*}(Q)$ of $(Ti,Zr)_{83}Si_{17}$ ternary amorphous alloy is defined by the weighted sum of the structure factors of $Ti_{83}Si_{17}$ and $Zr_{85}Si_{15}$ binary amorphous alloys as follows;

$$S^{*}(Q) = 0.6756\ S_{Ti83Si17}(Q) + 0.3244\ S_{Zr85Si15}(Q), \quad (3)$$

where we assume that $S^{BT}(Q)$ of $Zr_{85}Si_{15}$ amorphous alloy is almostly equal to that of $Zr_{83}Si_{17}$ amorphous alloy.

The synthesized $S^{*}(Q)$ has a high 1st peak with a small shoulder at low Q side and 2nd peak with a shoulder at high Q side, of which feature is much diffrent from that of $S^{BT}(Q)$ observed for $(Ti,Zr)_{83}Si_{17}$ amorphous alloy. We should be reminded that Ti-Zr pair correlation is neglected in the synthesized $S^{*}(Q)$. The feature of $S^{BT}(Q)$ observed for $(Ti,Zr)_{83}Si_{17}$ amorphous alloy is analogous to that of Ti-32.44at%Zr neutron zero scattering alloy presented in a previous paper. Moreover, $S^{BT}(Q)$ of $(Ti,Zr)_{83}Si_{17}$ amorphous alloy indicates high scattering intensity at smaller Q region below the 1st peak in comparison with that of the synthesized $S^{*}(Q)$.

Figure 2 shows the reduced radial distribution function G(r) obtained as the Fourier transform of $S^{BT}(Q)$'s shown in Fig.1. The negative peak located at r=2.58 A and the positive peak located at r=3.15 A in G(r) of $(Ti,Zr)_{83}Si_{17}$ amorphous alloy can be assigned to correspond to the Ti-Si and Zr-Si pair cor-

relations respectively from the comparison of the radial atomic distribution functions between $Ti_{83}Si_{17}$ amorphous alloy and Ti_3Si crystalline compound, $Zr_{85}Si_{15}$ amorphous alloy and Zr_2Si crystalline compound. The peak height ratio N/P between the negative(N) peak and positive(P) peak for the experimental G(r) of $(Ti,Zr)_{83}Si_{17}$ amorphous alloy is smaller than that for the synthesized $G^*(r)$, although the negative peak for Ti-Zr pair correlation located at r=3.02 A is ignored in the synthesized $G^*(r)$.

These results indicate that the atomic positions of Ti and Zr atoms in $(Ti,Zr)_{83}Si_{17}$ amorphous alloy are randomly distributed as like in Ti-32.44at%Zr neutron zero scattering alloy, but Si atoms prefer to be combined with Zr atoms to develop the microscopic scale concentration fluctuation due to the difference of the chemical bonding force between Si-Ti and Si-Zr atom pairs in this ternary amorphous alloy. Therefore, it is clearly concluded that the atomic structure of the Ti-Zr-Si ternary amorphous alloy is not analogous to those of the Ti-Si and Zr-Si binary amorphous alloys but shows the characteristic ternary atomic arrangement closely related to the physical and chemical properties.

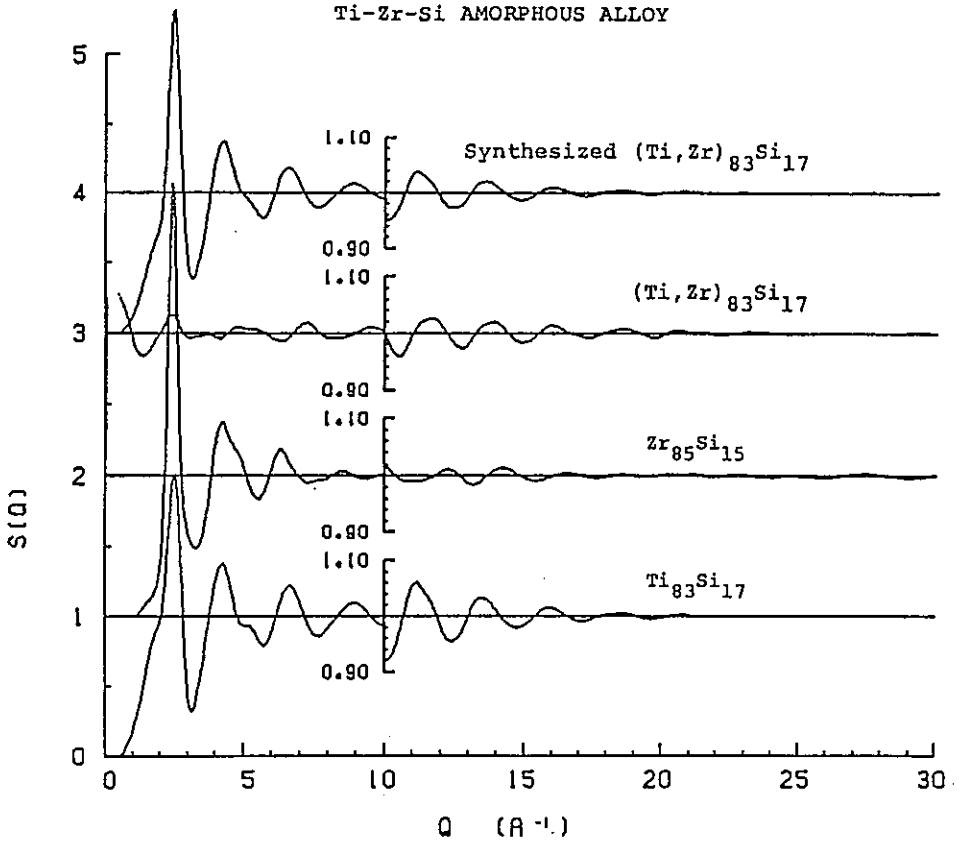

Fig. 1. Bhatia-Thornton type structure factor $S^{BT}(Q)$'s of $Zr_{85}Si_{15}$, $Ti_{83}Si_{17}$ binary and $(Ti,Zr)_{83}Si_{17}$ ternary amorphous alloys, and synthesized structure factor $S^*(Q)$ of $(Ti,Zr)_{83}Si_{17}$ amorphous alloy

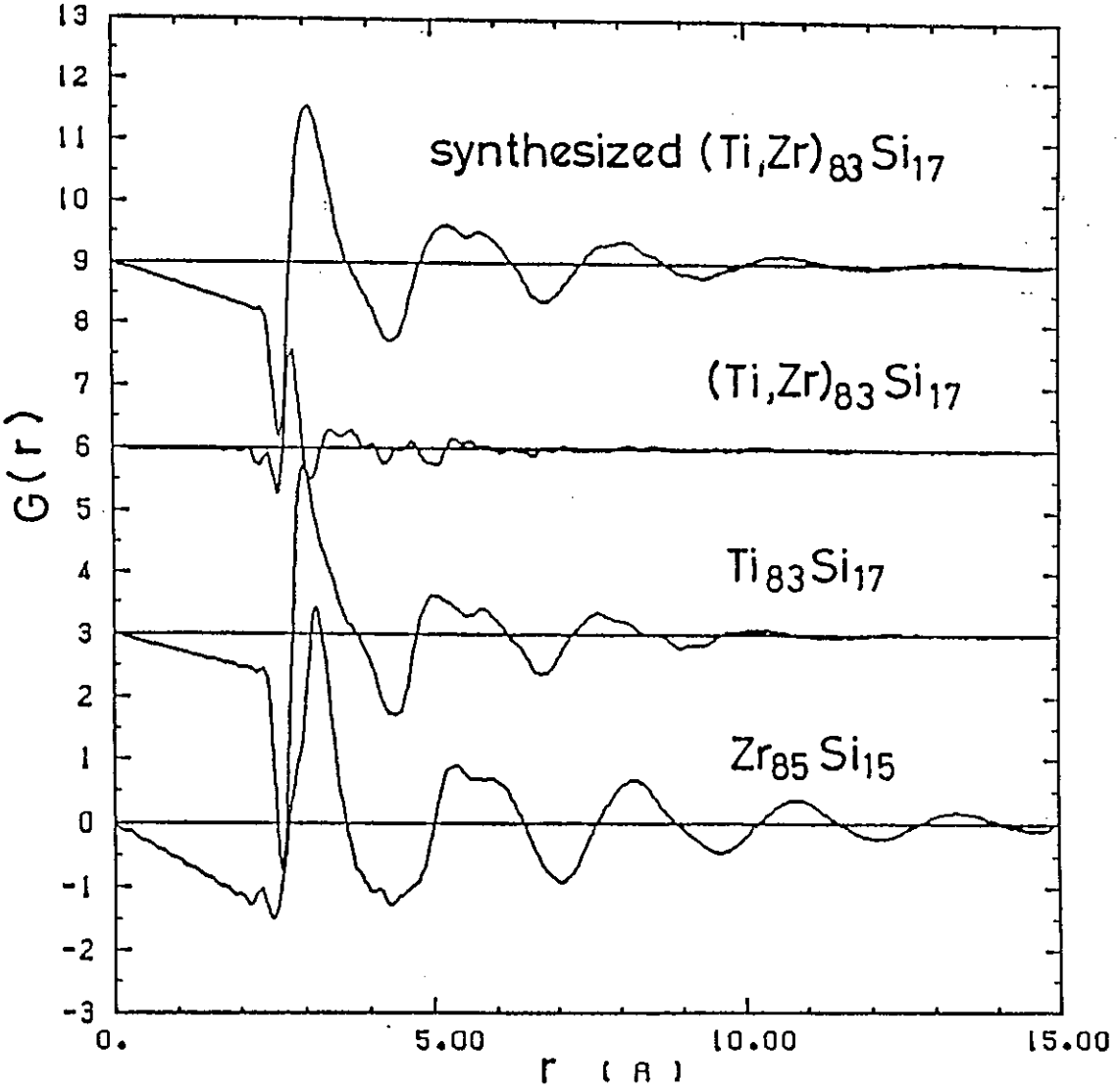

Fig. 2. Bhatia-Thornton type reduced radial distribution function G(r)'s of $Zr_{85}Si_{15}$, $Ti_{83}Si_{17}$ binary and $(Ti,Zr)_{83}Si_{17}$ ternary amorphous alloys, and synthesized reduced radial distribution function $G^*(r)$ of $(Ti,Zr)_{83}Si_{17}$ amorphous alloy

Chemical Atomic Structure of Ternary $(Ti,Zr)_{50}Cu_{50}$ amorphous alloy

Toshiharu FUKUNAGA, Shinobu SHIBUYA, Masakatsu MISAWA*
and Kenji SUZUKI

The Research Institute for Iron, Steel and Other Metals,
Tohoku University, Sendai 980, Japan

* National Laboratory for High Energy Physics, Oho-machi,
Tsukuba-gun Ibaraki 305, Japan

Recently amorphous alloys are being used to manufacture a wide range of commercial components and being investigated for many applications. These amorphous alloys often include more than three different kinds of chemical species. Such a multi-component amorphous alloy system has been known to be very stable even in the non-equilibrium state. However, the structural investigation based on these characteristic properties has not been reported yet, because of the complexity that six pair correlations are contained even in the ternery amorphous alloy.

In this paper we report the structural distinction between metal-metal binary and metal-metal-metal ternary amorphous alloys. It is much interesting to examine how the structure of the ternary amorphous alloy preserves the characteristics of the structure of the binary amorphous alloy.

$Ti_{50}Cu_{50}$, $Zr_{50}Cu_{50}$ binary and $(Ti,Zr)_{50}Cu_{50}$ ternary amorphous alloys were prepared by the rapid quenching from the molten state using single roll technique under Ar gas atmosphere. (Ti,Zr) means Ti-32.44at%Zr neutron zero scattering alloy. The measurement of the neutron scattering intensity from these amorphous alloys were carried out at room temperature in vacuum by using the High Intensity Total scattering spectrometer(HIT).

Figure 1 shows the total structure factor S(Q)'s of $Zr_{50}Cu_{50}$ and $Ti_{50}Cu_{50}$ binary and $(Ti,Zr)_{50}Cu_{50}$ ternary amorphous alloys observed experimentally in this study, and the synthesized $S^*(Q)$ defined as a weighted sum of S(Q)'s of $Zr_{50}Cu_{50}$ and $Ti_{50}Cu_{50}$ amorphous alloys as follows;

$$S^*(Q) = 0.3244\ S_{Zr50Cu50}(Q) + 0.6756\ S_{Ti50Cu50}(Q)\ , \qquad (1)$$

where Ti-Zr pair correlation is neglected. These structure factors were ob-

tained by generalized Bhatia-Thornton definition[1] as follows:

$$S^{BT}(Q) = I(Q)/\langle b^2\rangle$$
$$= \{\langle b\rangle^2 S_{NN}(Q) + 2\langle b\rangle \Sigma b_i S_{NCi} - (1/2)\Sigma(b_i - b_j)^2 S_{CiCj}(Q)\} / \langle b^2\rangle \quad (2)$$

$$\langle b^2\rangle = \Sigma C_i b_i^2$$
$$\langle b\rangle = \Sigma C_i b_i \quad ,$$

where the Bhatia-Thornton partial structure factors $S_{NN}(Q)$, $S_{CC}(Q)$ and $S_{NN}(Q)$ mean the number density-number density correlation , the concentration-concentration correlation and its cross term respectively. b_i and C_i are the coherent neutron scattering amplitude and the concentration of an i atom respectively.

It is interesting to note that the experimental $S^{BT}(Q)$ of $(Ti,Zr)_{50}Cu_{50}$ amorphous alloy is qualitatively similar to the synthesized $S^*(Q)$, which has the prepeak in the vicinity of $Q\sim2$ A^{-1} , the relatively sharp 1st peak and the split 2nd peak, although Ti-Zr pair correlation is completely ignored in the synthesized $S^*(Q)$. However, the small angle scattering intensity observed in the experimental $S^{BT}(Q)$ of $(Ti,Zr)_{50}Cu_{50}$ amorphous alloy can not be found in the synthesized $S^*(Q)$.

Figure 2 shows the reduced radial distribution function G(r)'s obtained as the Fourier transform of $S^{BT}(Q)$'s shown in Fig. 1. The 1st peaks of $Zr_{50}Cu_{50}$ and $Ti_{50}Cu_{50}$ amorphous alloys are located at r=2.77 and r=2.47 A respectively. In the double-headed 1st peak in G(r) of $(Ti,Zr)_{50}Cu_{50}$ amorphous alloy, the splitting corresponds to the 1st peaks in G(r)'s of $Zr_{50}Cu_{50}$ and $Ti_{50}Cu_{50}$ amorphous alloys respectively. However, as shown in Fig. 2, the synthesized $G^*(r)$ has only one peak located at r=2.48 A, in which no peak corresponding to the 1st peak of $Zr_{50}Cu_{50}$ amorphous alloy is observed. These peak positions are not affected by Ti-Zr pair correlation because the interatomic distance between Ti and Zr atoms is 3.02 A. These results may indicate that the short-range atomic arrangement is changed due to the stronger affinity of the Cu-Zr pair correlation than other correlations. Such a difference of chemical bond among constituent atoms in ternary amorphous alloy promotes the frustration of the chemical atomic arrangement and causes the the concentration fluctuation, which allows us to observe the small angle scattering intensity as shown in Fig. 1.

Reference

1) J. Bletly, Z. Naturforsch, 31a (1976) 960.

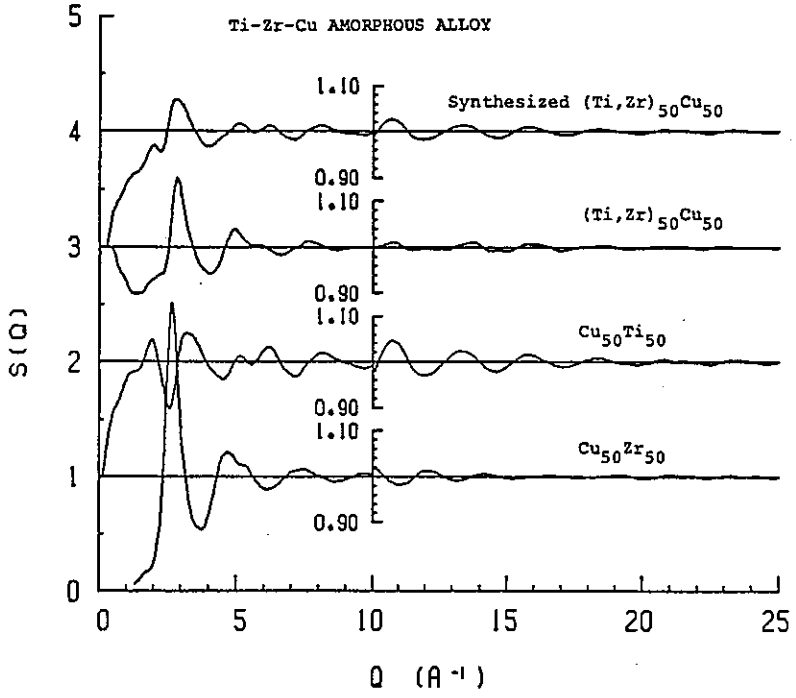

Fig. 1. Bhatia-Thornton type structure factor $S^{BT}(Q)$'s of $Zr_{50}Cu_{50}$, $Ti_{50}Cu_{50}$ binary and $(Ti,Zr)_{50}Cu_{50}$ ternary amorphous alloys, and synthesized structure factor $S^{*}(Q)$ of $(Ti,Zr)_{50}Cu_{50}$ amorphous alloy

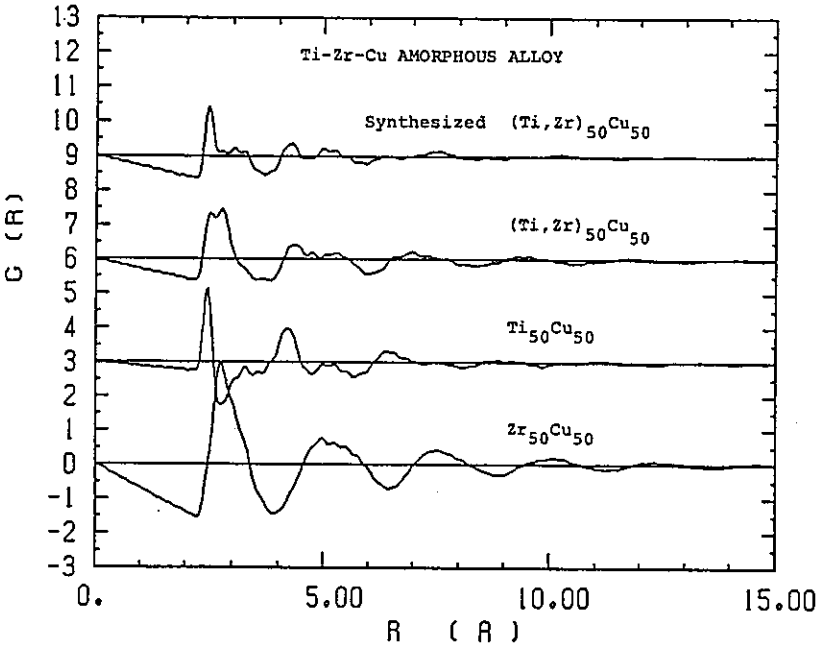

Fig. 2. Bhatia-Thornton type reduced radial distribution function G(r)'s of $Zr_{50}Cu_{50}$, $Ti_{50}Cu_{50}$ binary and $(Ti,Zr)_{50}Cu_{50}$ ternary amorphous alloys, and synthesized $G^{*}(r)$ of $(Ti,Zr)_{50}Cu_{50}$ amorphous alloy

Chemical frustration in $(Ti,Zr)_XCu_{1-X}$ and $(Ti_YZr_{1-Y})_{0.5}Cu_{0.5}$ ternary amorphous alloys

Toshiharu FUKUNAGA, Masaki ISHII, Masakatsu MISAWA*
and Kenji SUZUKI

The Research Institute for Iron, Steel and Other Metals,
Tohoku University, Sendai 980, Japan

*National Laboratory for High Energy Physics, Oho-machi,
Tsukuba-gun Ibaraki 305, Japan

For ternary alloys, even the simple discription of their structures in terms of pair distribution functions requires six independent partial pair correlations to be determined and detailed investigations are quite difficult. On the other hand, there is an engineering expectation that some usefull knowledge on the amorphous alloy structure will be obtained by increasing the constituent elements in the alloy.

In this study the variation in the structure of the Ti-Zr-Cu ternary amorphous alloy system with the alloy composition was investigated because this system provides a wide glass forming composition range.

$(Ti,Zr)_XCu_{1-X}$ (X=0.3, 0.5, 0.7) and $(Ti_YZr_{1-Y})_{0.5}Cu_{0.5}$ (Y=0.33, 0.5, 0.6756) amorphous alloys were prepared by rapid quenching from the molten state using single roll technique under Ar gas atmosphere. (Ti,Zr) means a Ti-32.44at%Zr neutron zero scattering alloy. The measurement of the neutron scattering intensity from these amorphous alloys were carried out at room temperature in vacuum by using the High Intensity Total scattering spectrometer (HIT).

Figure 1 shows the Bhatia-Thornton type total structure factor $S^{BT}(Q)$'s of $(Ti,Zr)_XCu_{1-X}$ (X=0.3, 0.5, 0.7) ternary amorphous alloys. The $S^{BT}(Q)$ of $(Ti,Zr)_{0.3}Cu_{0.7}$ amorphous alloy has a prepeak at $Q\sim1.8$ A^{-1}, a high 1st peak and splitting 2nd peak. The amplitudes of thses peaks become small and the position of the 1st peak moves to the low Q side with decreasing Cu concentration. On the contrary, the small angle scattering intensity becomes larger with decreasing Cu concentration. The $S^{BT}(Q)$'s of $(Ti_YZr_{1-Y})_{0.5}Cu_{0.5}$ amorphous alloys are shown in Fig. 2, of which features are not drastically changed. However, the small angle scattering intensity becomes larger with

decreasing Zr concentration.

These results suggest that the concentration fluctuation due to the rearrangement of constituent atoms in ternary amorphous alloys, as mentioned in previous papers, is changed with the chemical composition of the alloys. The variation in the small angle scattering intensity with the alloy concentration implies that the concentrated Cu and Zr regions appear in Ti-Zr-Cu ternary system alloys. Especially, in case of the low concentration of both Zr and Cu atoms the small angle scattering intensity is remarkable. In case of the higher concentration of either Zr or Cu atom the small angle scattering intensity becomes smaller, because the highly concentrated atoms are so widely spread in all regions of Ti-Zr-Cu amorphous alloy that the concentration fluctuation disappear.

Figures 3 and 4 show the reduced radial distribution function G(r) defined as the Fourie transform of total $S^{BT}(Q)$'s shown in Figs. 1 and 2. In $(Ti,Zr)_{X}Cu_{1-X}$ amorphous alloys both of the oscillation and splitting of the 1st peak in G(r)'s are drastically changed with Cu concentration. The low r side of the 1st peak corresponding to the Cu-Cu pair correlation in $Cu_{0.5}Ti_{0.5}$ binary amorphous alloy decreases in height with increasing Cu concentration. However, the high r side peak of the split 1st peak, which corresponds to the Cu-Zr pair correlation in $Cu_{0.5}Zr_{0.5}$ binary amorphous alloy, remains nearly constant in all Cu concentrations.

The split 1st peak in the G(r) of$(Ti_{0.6756}Zr_{0.3244})_{0.5}Cu_{0.5}$ amorphous alloy changes to the single peak in G(r) of $(Ti_{0.33}Zr_{0.67})_{0.5}Cu_{0.5}$ amorphous alloy. This single peak position corresponds to that of the Cu-Zr pair correlation in Cu-Zr amorphous alloy. It is much interesting to note that the affinity of the Cu-Zr pair correlation is remarkably strong in Ti-Zr-Cu ternary amorphous alloys. These results in r space are consistent with the change in the small angle scattering intensity in Q space.

The variation of the composition in ternary amorphous alloys provides more detailed information of the atomic arrangement. The concentration fluctuation due to the chemical frustration in ternary amorphous alloys occurs according to the change in the alloy composition. This chemical frustration caused by the difference between the chemical bond strengths of atomic pairs may be closely connected to realize the physical and chemical properties in ternary amorphous alloys.

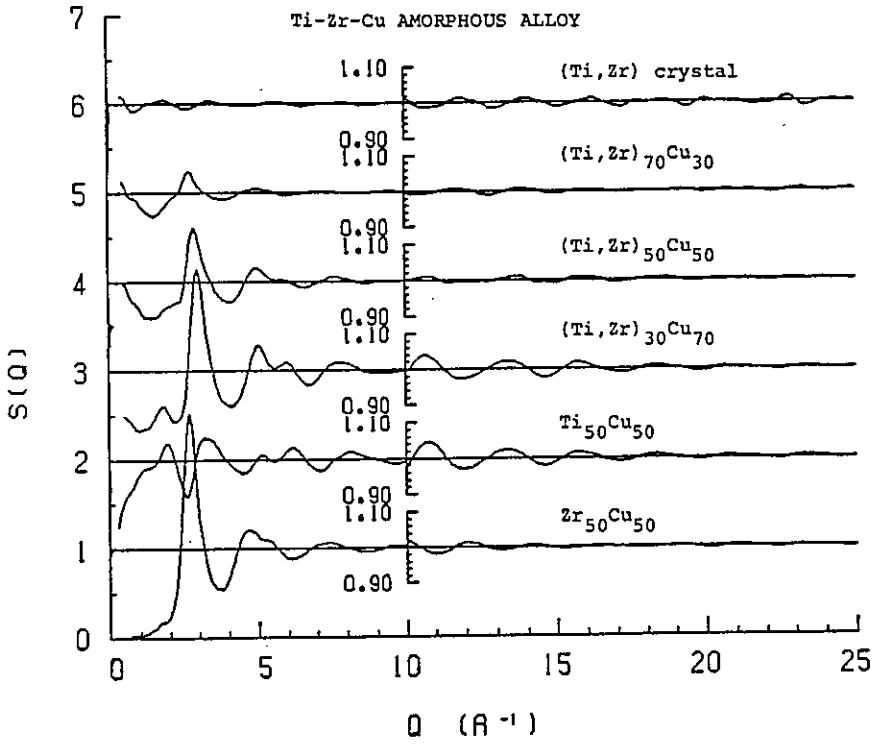

Fig. 1. Bhatia-Thornton type structure factor $S^{BT}(Q)$'s of $Zr_{0.5}Cu_{0.5}$, $Ti_{0.5}Cu_{0.5}$ binary and $(Ti,Zr)_XCu_{1-X}$(X=0.3, 0.5, 0.7) ternary amorphous alloys, and concentration-concentration correlation structure factor $S_{CC}(Q)$ of (Ti,Zr)=Ti-32.44at%Zr neutron zero scattering alloy

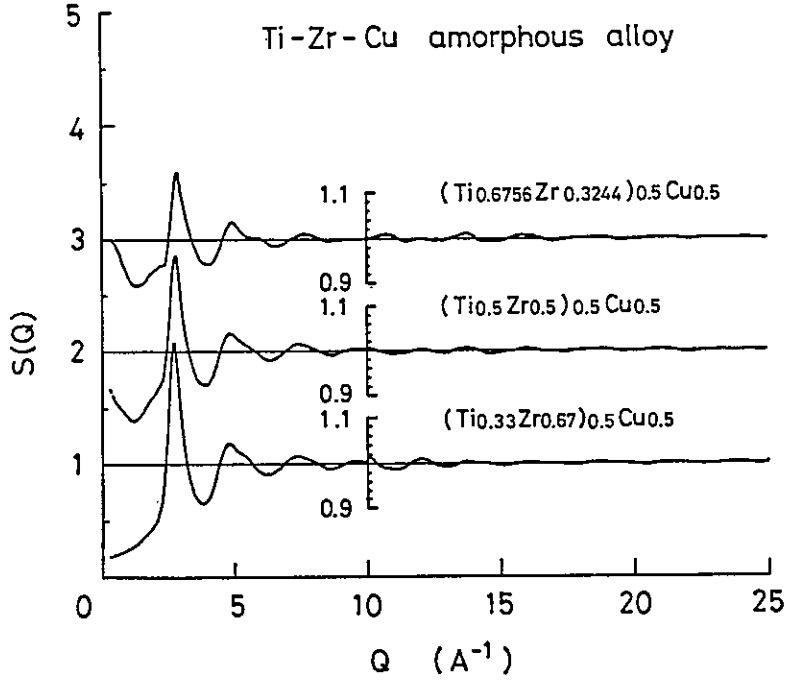

Fig. 2. Bhatia-Thornton type structure factor $S^{BT}(Q)$'s of $(Ti_YZr_{1-Y})_{0.5}Cu_{0.5}$ (Y=0.33, 0.5, 0.6756) ternary amorphous alloys

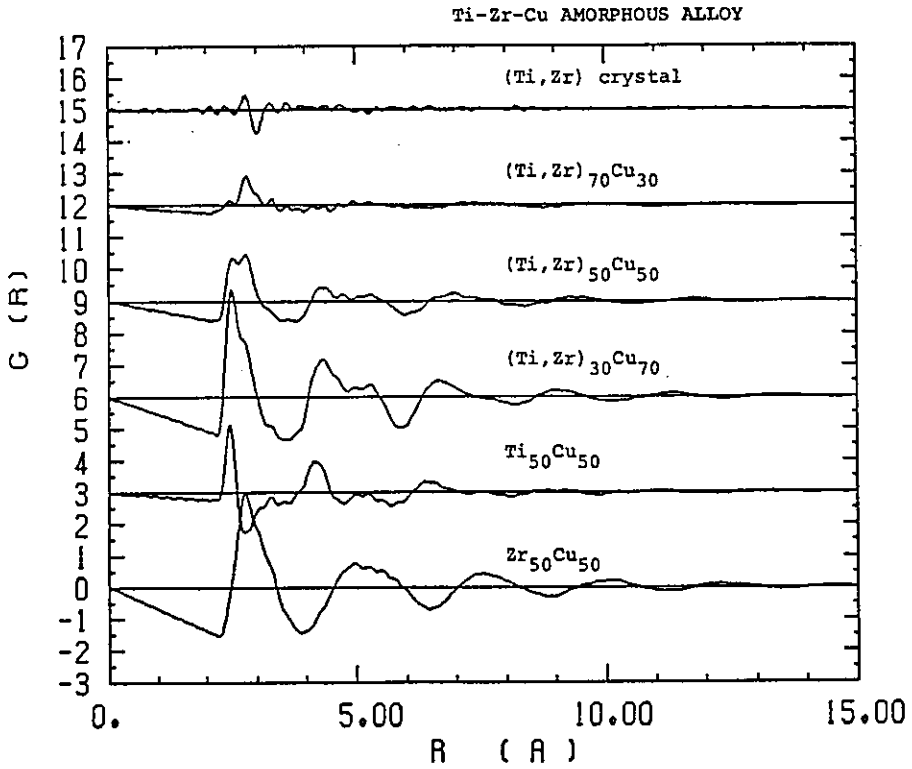

Fig. 3. Bhatia-Thornton type reduced radial distribution function G(r)'s of $Zr_{0.5}Cu_{0.5}$, $Ti_{0.5}Cu_{0.5}$ binary and $(Ti,Zr)_XCu_{1-X}$(X=0.3, 0.5, 0.7) ternary amorphous alloys, and reduced concentration-concentration correlation function $G_{CC}(r)$ of (Ti,Zr)=Ti-32.44at%Zr neutron zero scattering alloy

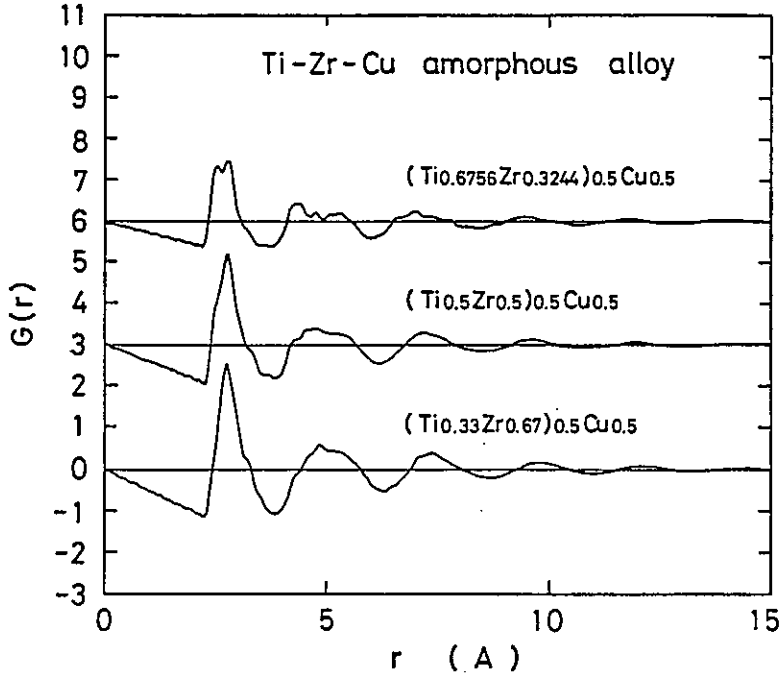

Fig. 4. Bhatia-Thornton type reduced radial distribution function G(r)'s of $(Ti_YZr_{1-Y})_{0.5}Cu_{0.5}$(Y=0.33, 0.5, 0.6756) ternary amorphous alloys

Atomic Arrangement of CVD Amorphous (Si_3N_4)-B

Toshiharu FUKUNAGA, Takashi GOTO, Masakatsu MISAWA*,
Toshio HIRAI and Kenji SUZUKI

The Research Institute for Iron, Steel and Other Metals,
Tohoku University, Sendai 980, Japan

*National Laboratory for High Energy Physics, Oho-machi,
Tsukuba-gun Ibaraki 305, Japan

An amorphous Si_3N_4 is more uniform than a crystal Si_3N_4 because of no grain boundary and lattice defect. Therefore, amorphous Si_3N_4 films have been used as a dielectric layer in electronics components. Recently the electrically conductive amorphous Si_3N_4-C , Si_3N_4-Ti and Si_3N_4-B composites were prepared by using chemical vapor deposition(CVD) method. It is very interesting to investigate the position of C, Ti and B atom in the structure of amorphous Si_3N_4-(C, Ti or B) composites in comparison with that of the amorphous Si_3N_4. In this paper the structural difference between the amorphous Si_3N_4 and Si_3N_4-B composite is described.

The amorphous Si_3N_4 was prepared by a CVD process, in which $SiCl_4$ vapor, NH_3 gas and H_2 gas were heated at 700~900 ℃. For the preparation of the amophous (Si_3N_4)-B composite $SiCl_4$ vapor, NH_3 gas, H_2 gas and B_2H_6 5vol% + H_2 95vol% mixture gas were used as source gases and the deposition temperature was at 1100 to 1300 ℃. The amorphous Si_3N_4-B composite used in this experiment contains 8 at%B atoms. The structures of these amorphous solids were measured at room temperature in vacuum by using the High Intensity Total scattering spectrometer (HIT).

The total structure factor S(Q)'s of the amorphous Si_3N_4 and Si_3N_4-B composite are shown in Fig. 1. The oscillations of both S(Q)'s are obseved up to Q~45 A^{-1}. This means the strong bonding between Si and N atom and the high regularity of the topological short-range atomic arrangement in the amorphous state.

Figure 2 shows the enlarged features of S(Q)'s in low Q region. It is very interesting to note that the small angle scattering intensity is observed in S(Q) of amorphous Si_3N_4, but not observed in S(Q) of amorphous Si_3N_4-B composite. Misawa et al.[1] represented previously that the small angle scat-

tering intensity in amorphous Si_3N_4 was caused by voids with average diameters of about 10 A. This result suggests that the voids observed in amorphous Si_3N_4 are ocuppied by the amorphous BN. However, the small angle scattering intensity is not observed for amorphous Si_3N_4-B composite because of the average neutron coherent scattering amplitude of amorphous BN (b_C=0.733 x 10^{-12} cm) and Si_3N_4 (b_C=0.713 x 10^{-12} cm) are almostly equal each other.

Figures 3 and 4 show the radial distribution functions (RDF) obtained as the Fourier transform of S(Q)'s for amorphous Si_3N_4 and Si_3N_4-B composite. The truncation Q_{max} values are 45, 40, 35 and 30 A^{-1} respectively. The 1st peak located at r=1.74 A represents the Si-N correlation in the amorphous Si_3N_4. The second peak at r=3.15 A contains both Si-Si and N-N correlations. These relations have been reported by Aiyama et al.[2] by the comparison between the RDF of amorphous Si_3N_4 and the atomic configuration of Si_3N_4 crystal. In amorphous Si_3N_4-B composite a small peak located at r=1.46 A is observed beside the main peak at r=1.74 A as shown in Fig. 4. The B-N bond length is 1.446 A in the BN crystal structure being built of hexagonal layers of the same kind like graphite. Therefore, it can be concluded that the small peak at r=1.46 A observed in amorphous Si_3N_4-B composite means B-N bond length in the amorphous(turbostratic) BN.

The existence of B-N bonding in the amorphous Si_3N_4-B composite has been detected by the measurement of XPS[3]. Moreover, the experimental densities of amorphous Si_3N_4-B have been reported to be in good agreement with the calculated values represented by the linear combination of the densities of the CVD amorphous Si_3N_4 and BN[4]. These results reported in previous papers and the information of the structure in this work clearly indicate that the amorphous Si_3N_4-B is composed of amorphous Si_3N_4 and turbostratic BN.

References

1) M. Misawa, T. Fukunaga, K. Niihara, T. Hirai and K. Suzuki, J. Non-Cryst. Solids 34 (1979) 313.

2) T. Aiyama, T. Fukunaga, K. Niihara and K. Suzuki, J. Non-Cryst. Solids 33 (1979) 131.

3) T. Goto and T. Hirai, to be published.

4) T. Hirai, T. Goto and T. Sakai, "Emergent Process Methods for High Technology Ceramics", ed. by R. F. Davis, H. Palmour III and P. L. Porter, Materials Science Research, Vol. 17, Plenum Press, p. 347-358, (1984).

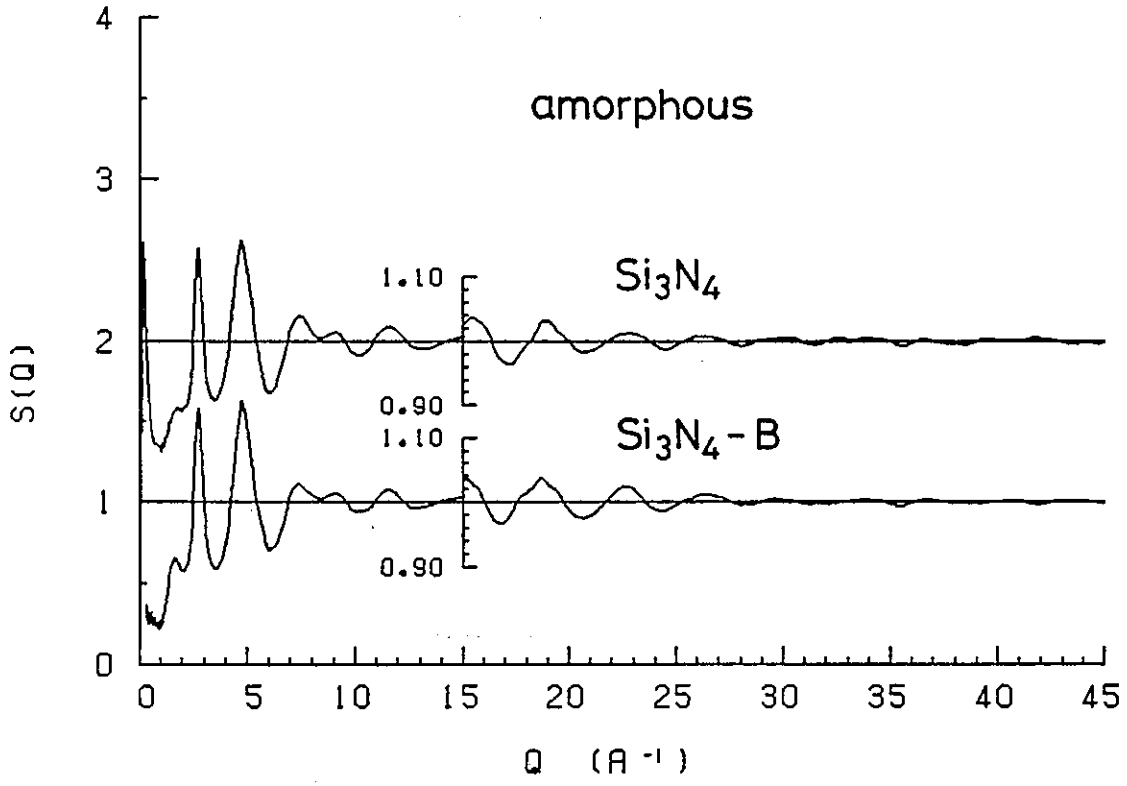

Fig. 1. Structure factor S(Q)'s of CVD amorphous Si_3N_4 and (Si_3N_4)-B composite

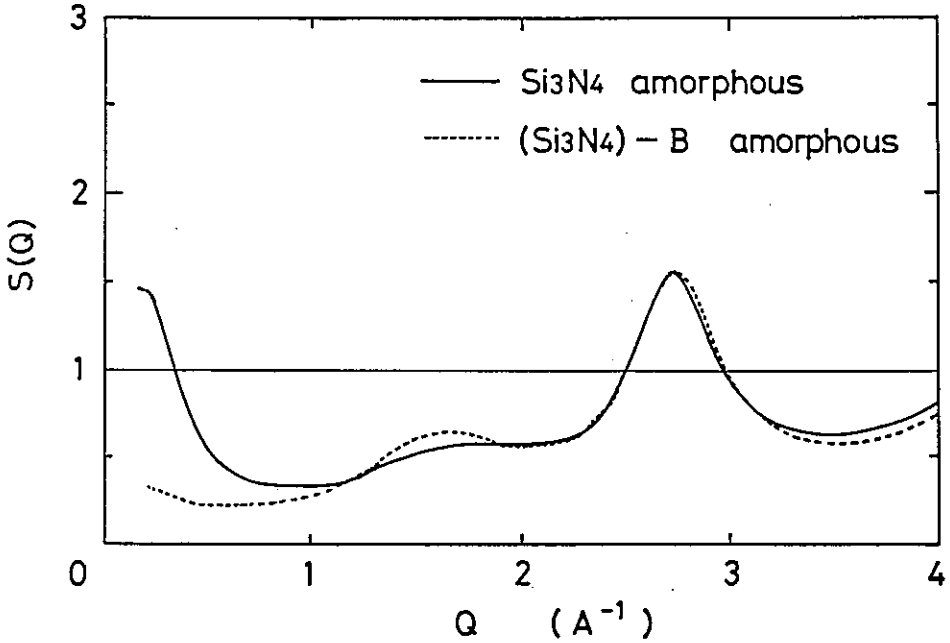

Fig. 2. S(Q)'s of CVD amorphous Si_3N_4 and (Si_3N_4)-B composite in low Q region.

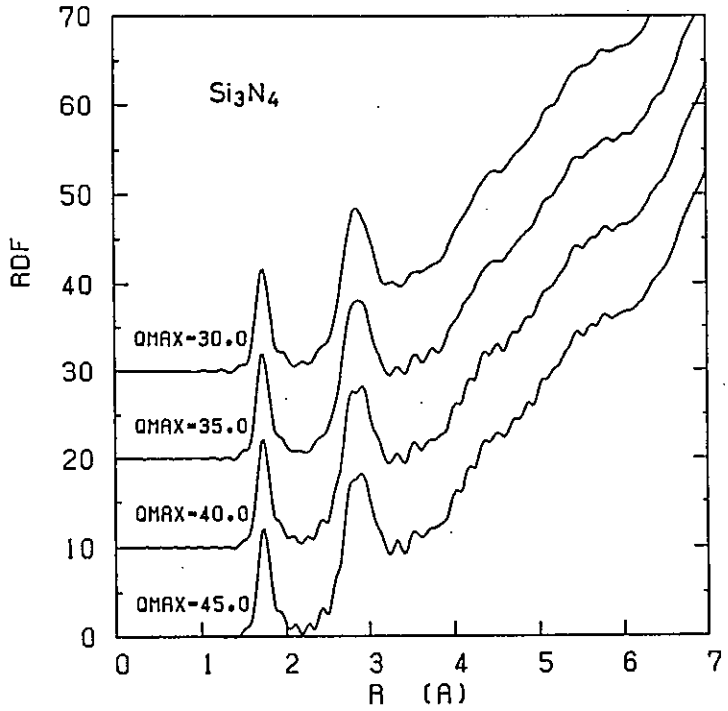

Fig. 3. Radial distribution functions of amorphous Si_3N_4.

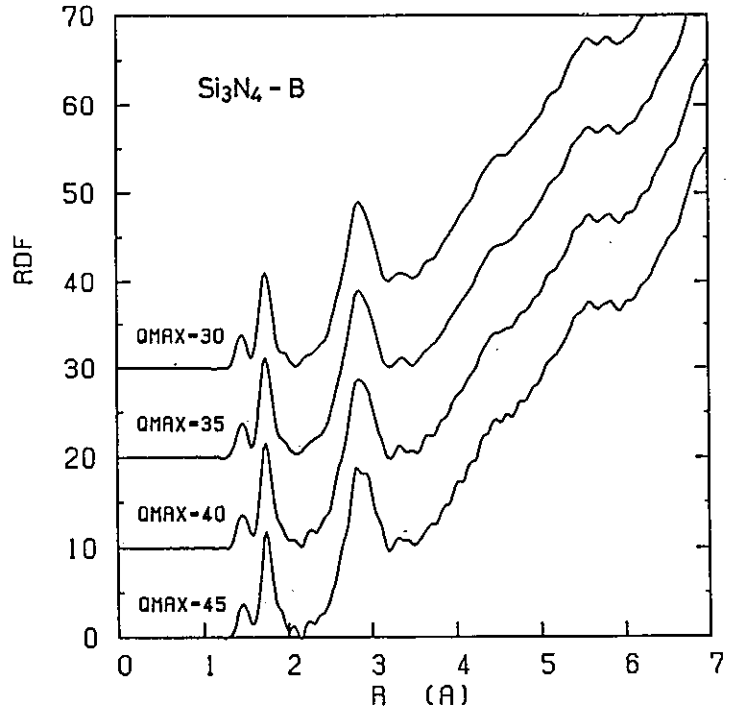

Fig. 4. Radial distribution functions of amorphous (Si_3N_4)-B composite.

Small Angle Scattering Study of Al-Y-D Amorphous Alloys

Noriyuki HAYASHI, Toshiharu FUKUNAGA*, Michihiro FURUSAKA**
and Kenji SUZUKI*

Department of Materials Science and Technology, Technologycal University of Nagaoka, Nagaoka 940-21, Japan

* The Research Institute for Iron, Steel and Other Metals, Tohoku University, Sendai 980, Japan

** Physics Department, Tohoku University, Sendai 980, Japan

It has been found out that as quenched, annealed and hydrogenated amorphous alloys revealed a small angle scattering.[1)2)3)4)5)] In a previous work,[6)] we studied the hydrogen atom environment in Al-Y-D amorphous alloys with a High Intensity Total scattering spectrometer(HIT) installed at KENS. Small angle scattering appeared gradually with increasing D concentration at the Q range from 0.1 to 1 A^{-1} of the structure factors S(Q) of Al-Y-D amorphous alloys. The intensity of the small angle scattering increased monotonically with decreasing the values of Q and the pattern of that was not dependent on alloy composition before absorbing D atoms. According to the results of the previous work[6)] and a X-ray small angle scattering experiment[7)] at the Q range from 0.1 to 1 A^{-1}, it was guessed that the fluctuation of the D atoms distribution occurred in Al-Y-D amorphous alloys with absorbing D atoms.

In this study we measure precisely the small angle neutron scattering for Al-Y-D amorphous alloys at the Q range from $5X10^{-3}$ to $6X10^{-1}$ A^{-1}. The small angle scatterings for $Al_{.33}Y_{.67}D_X$(X=0, .25, .70 and 1.07) and $Al_{.50}Y_{.50}D_X$(X=0, .30 and .56) amorphous alloys were measured at room temperature with a Small Angle Neutron scattering spectrometer(SAN) installed at KENS. Sample preparations were explained in the references 6) and 7) in detail.

A new and precise information concerned with the small angle scattering for Al-Y-D amorphous alloys was obtained. The results of the small angle scattering measurement for Al-Y-D amorphous alloys are shown in Fig. 1 and Fig. 2. Independent of the alloy composition and D concentration, the

intensity monotonically increases towards lower Q at the range from $5X10^{-3}$ to about $2X10^{-2}$ A^{-1}. This may be due to the fluctuation of the metal atoms distribution. Furthermore, two peaks appear at the positions of different values of Q according to the alloy composition before absorbing D atoms. The peak situates at $Q \simeq 0.2$ A^{-1} in $Al_{.33}Y_{.67}D_{1.07}$ amorphous alloy. On the other hand, those situate at $Q \simeq 0.03$ A^{-1} in $Al_{.50}Y_{.50}D_{.30}$ and $Al_{.50}Y_{.50}D_{.56}$ amorphous alloys. On the basis of the results of the present and previous[7] works, the former peak can be regarded as the fluctuation of the D atoms distribution. On the contrary, there is a possibility that the latter one originates from the fluctuation of not simply D but metal atoms distribution.

The small angle scattering curves for Al-Y-D amorphous alloys are shown in log-log scale in Fig. 3 and Fig. 4. The small angle scattering curve for $Al_{.33}Y_{.67}D_{1.07}$ amorphous alloy deviates slightly from the Q^{-3} relation at the higher Q side of the peak, while those for $Al_{.50}Y_{.50}D_{.30}$ and $Al_{.50}Y_{.50}D_{.56}$ amorphous alloys show clearly that. Moreover, in $Al_{.50}Y_{.50}D_{X}$ amorphous alloys the curves of the small angle scattering are close to the Q^{-3} relation at the Q range from 10^{-2} to 10^{-1} A^{-1}.

More detailed studies of the relation between the small angle scattering and the fluctuation of the D and metal atoms distribution in Al-Y-D amorphous alloys are being carried out.

References

1) E. Nold, S. Steeb, P. Lamperter and G. Rainer-Harbach, J. Physique Coll., 41 (1980) C8-186.
2) B. Boucher, ibid., C8-135.
3) B. Boucher, P. Chieux, P. Convert and M. Tournarie, J. Phys. F, 13 (1983) 1339.
4) K. Osamura, S. Ochiai and S. Takayama, J. Mater. Sci., 19 (1984) 1917.
5) P. Goudeau, A. Naudon, B. Rodmacq, P. Mangin and A. Chamberd, J. Physique Coll., 46 (1985) C8-479.
6) N. Hayashi, T. Fukunaga, N. Watanabe and K. Suzuki, KENS Report-V, KEK Internal (1984) p.36.
7) N. Hayashi, Doctor Thesis, Tohoku Univ.,(1986). (in Japanese).

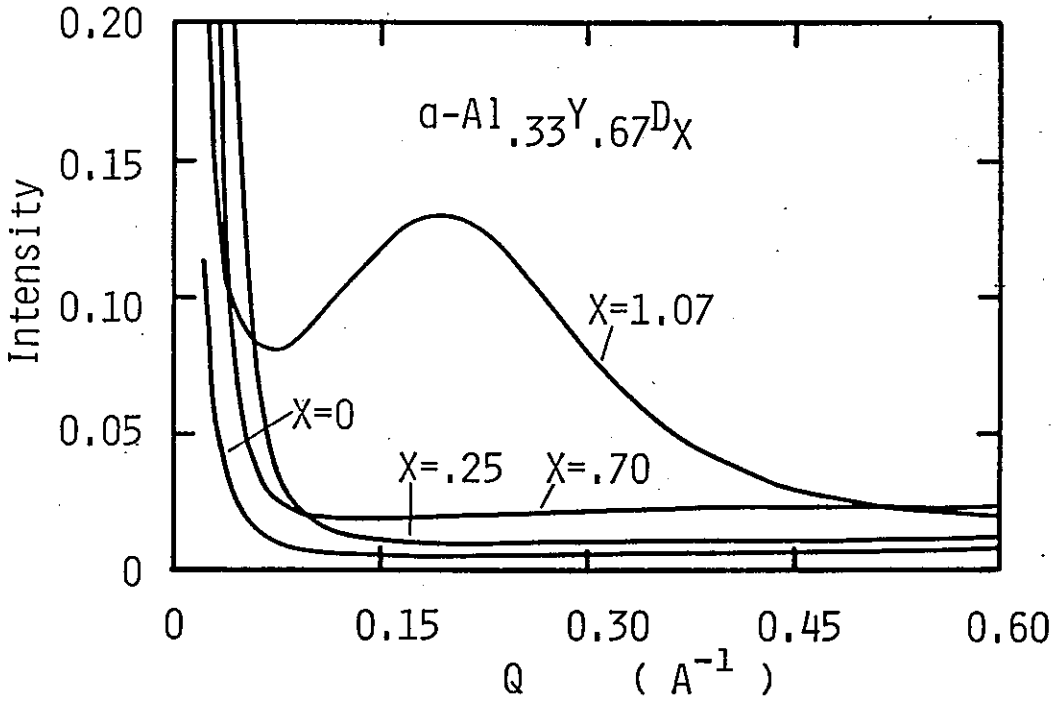

Fig. 1. Scattering functions for $Al_{.33}Y_{.67}D_X$ amorphous alloys.

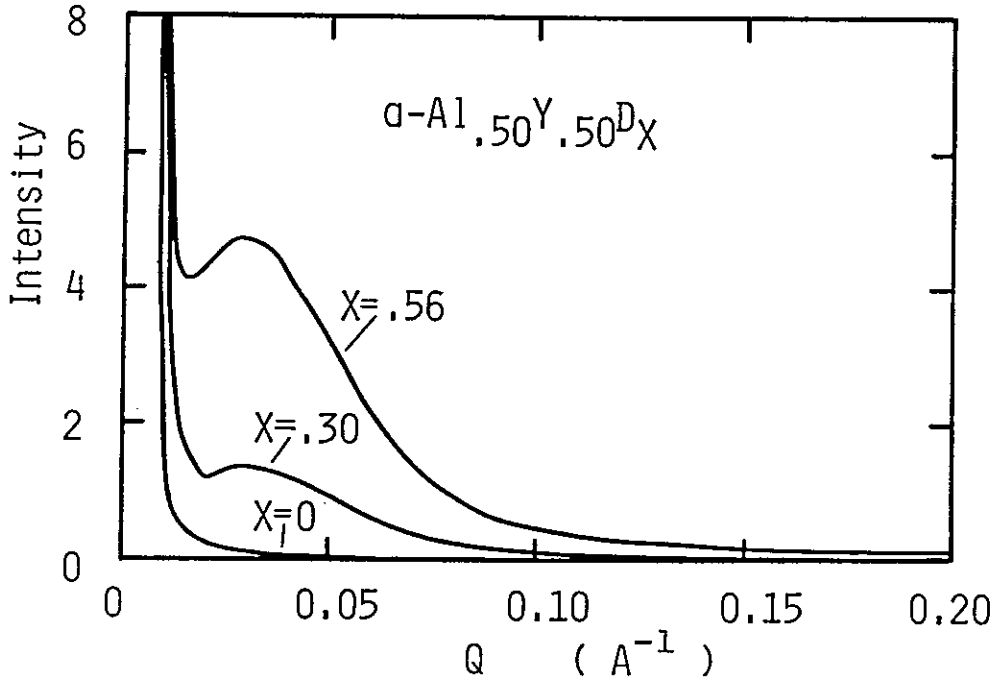

Fig. 2. Scattering functions for $Al_{.50}Y_{.50}D_X$ amorphous alloys.

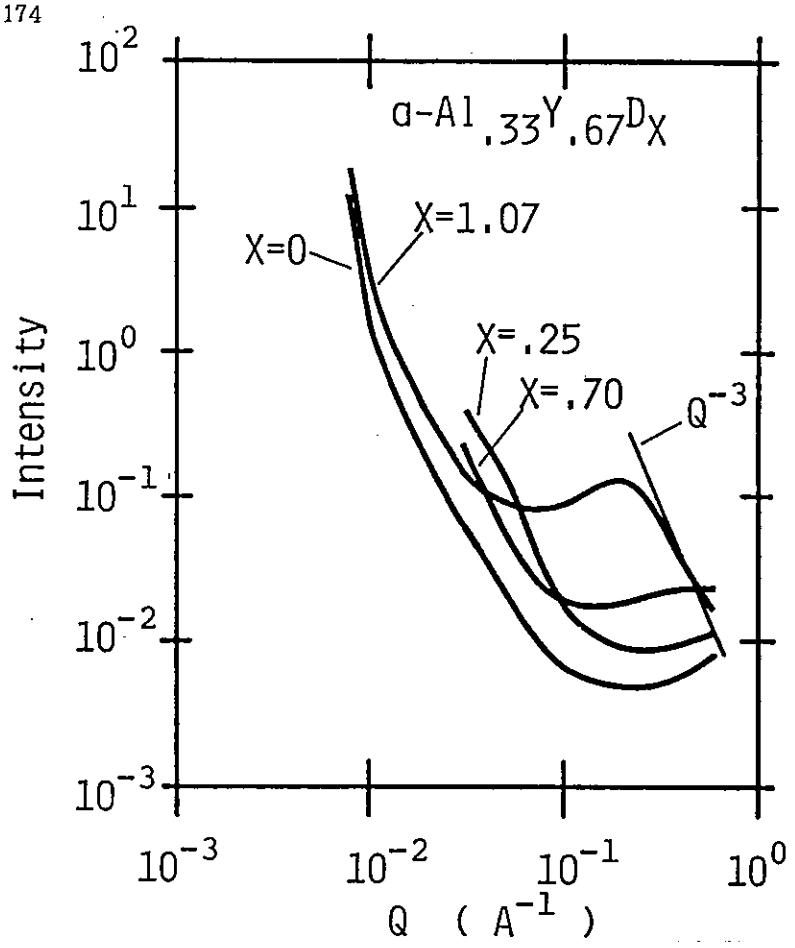

Fig. 3. Log-log plots of scattering functions for $Al_{.33}Y_{.67}D_X$ amorphous alloys.

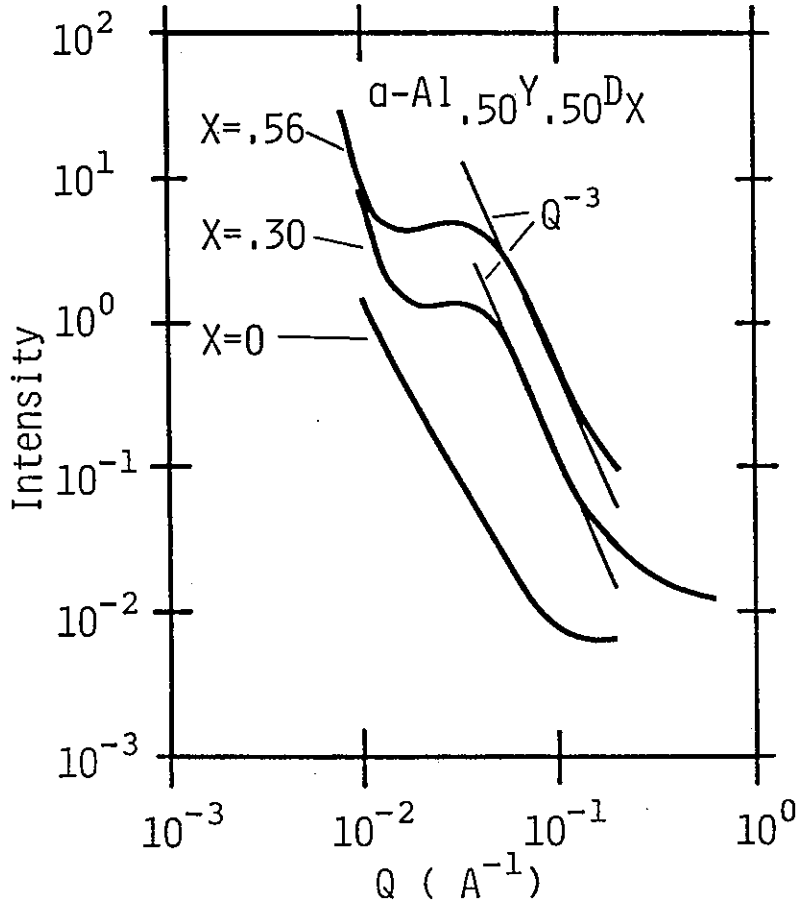

Fig. 4. Log-log plots of scattering functions for $Al_{.50}Y_{.50}D_X$ amorphous alloys.

Small Angle Scattering of Polarized Neutrons from an $Fe_{65}{}^{62}Ni_{35}$ Invar Alloy

Takayoshi TAKEDA, Shigehiro KOMURA, Toshio MIYAZAKI,
Yasuo ENDOH* and Shin'ichi ITOH*

Faculty of Integrated Arts and Sciences, Hiroshima University
Hiroshima 730, Japan

*Department of Physics, Faculty of Science, Tohoku University
Sendai 980, Japan

Our previous experiment by means of small angle neutron scattering from $Fe_{65}Ni_{35}$ invar alloy[1,2] has established that there is a magnetic inhomogeneous structure inherent to this alloy. In order to account this fact we have proposed a model[3] in which local fluctuation of chemical composition gives rise to the magnetic inhomogeneous structure; Ni-rich local regions tend to be ferromagnetic and Fe-rich regions paramagnetic. Although this model explains well the structure function of the alloy, there was no direct evidence which supports the correlation of magnetic inhomogeneous structure with the fluctuation of the chemical composition. A small angle scattering experiment at room temperature using polarized neutrons from $Fe_{65}{}^{62}Ni_{35}$ was performed to demonstrate the correlation and the result suported the proposed model though there was a severe depolarization of polarized neutrons in the samples[4].

In this experiment, we used the time-of-flight polarized neutron spectrometer TOP[5] at KENS and performed the small-angle scattering from the improved sample. The sample, which had been used in the previous

experiment, were heat-treated in pressure of 1000 kgf/cm^2 at 1320 ℃ for one hour in order to reduce the depolarization of polarized neutrons in the sample which is defined by $D = 1 - P/P_0$ where P_0 and P are polarization of neutrons before and after the transmission through the sample. The depolarization in the sample was 6 % for neutron wave length $\lambda = 3$ Å and 14 % for $\lambda = 9$ Å at room temperature and it decreases more with in-creasing temperature T. We measured the small angle scattering cross section $d\Sigma/d\Omega(Q)$ from $Fe_{65}{}^{62}Ni_{35}$ with neutron spin up ($\uparrow$) and down ($\downarrow$) and with the sample magnetization perpendicular to the scattering vector Q at the various temperatues T from 293 to 550 K. From these cross section we obtaind the following quantities:

$$\left(\frac{d\Sigma}{d\Omega}\right)_{sum} = \frac{1}{2}\left\{\left(\frac{d\Sigma}{d\Omega}\right)_{\uparrow} + \left(\frac{d\Sigma}{d\Omega}\right)_{\downarrow}\right\} = \left(\frac{d\Sigma}{d\Omega}\right)_{diff} + S_{bb}(Q) + S_{pp}(Q), \qquad (1)$$

$$\left(\frac{d\Sigma}{d\Omega}\right)_{sub} = \frac{1}{2}\left\{\left(\frac{d\Sigma}{d\Omega}\right)_{\uparrow} - \left(\frac{d\Sigma}{d\Omega}\right)_{\downarrow}\right\} = S_{bp}(Q)\ , \qquad (2)$$

where $(d\Sigma/d\Omega)_{diff}$ is the contribution from the diffuse scattering, $S_{bb}(Q)$ and $S_{pp}(Q)$ are nuclear and magnetic structure functions, respectively. $S_{bp}(Q)$ is the interference structure function between nuclear and magnetic scattering; it is defined by the Fourier transform of the space-correlation function $G_{bp}(\vec{r})$ between the deviations of the nuclear and magnetic scattering amplitude density $\rho_b(\vec{r})$ and $\rho_p(\vec{r})$ from their respective average values $\bar{\rho}_b$ and $\bar{\rho}_p$. The correlation function $G_{bp}(r)$ is given by,

$$G_{bp}(\vec{r}) = \frac{1}{V}\int\left(\rho_b(\vec{r}') - \bar{\rho}_b\right)\left(\rho_p(\vec{r}+\vec{r}') - \bar{\rho}_p\right) d^3\vec{r}'\ , \qquad (3)$$

where V is the volume of sample and the integration is performed over the

volume. Since the nuclear scattering amplitudes are $b_{Fe} = 0.954 \times 10^{-12}$ cm and $b_{Ni(62)} = -0.87 \times 10^{-12}$ cm, we expect that in $Fe_{65}{}^{62}Ni_{35}$ the value of $\rho_b(\vec{r}) - \overline{\rho_b}$ at Fe-rich regions is positive and that at Ni-rich regions is negative. Since in our model we assume that Ni-rich regions are ferromagnetic, the forward magnetic scattering amplitudes at Q = 0 in the regions are $p_{Fe} = 0.755 \times 10^{-12}$ cm and $p_{Ni} = 0.162 \times 10^{12}$ cm, and since Fe-rich regions are paramagnetic, $p_{Fe} = p_{Ni} = 0$ in the regions. Thus it follows that $\rho_p(\vec{r}) - \overline{\rho_p} > 0$ at Ni-rich regions and $\rho_p(\vec{r}) - \overline{\rho_p} < 0$ at Fe-rich regions, and that $G_{bp} < 0$ for small r and $S_{bp} < 0$ for small Q. We obtained the following results:

The scattering cross section $(d\Sigma/d\Omega)_{sub}$ is negative and its absolute value gradually decreases with increasing T and vanished at 550 K. This results supports our previously proposed model. On the other hand, the cross section $(d\Sigma/d\Omega)_{sum}$ increases with increasing T below 450 K and decreases above 450 K. From the fact that $(d\Sigma/d\Omega)_{sub}$ decreases with increasing T though $(d\Sigma/d\Omega)_{sum}$ increases, it is considered that the paramagnetic regions expand with increasing T and start to cover the Ni-rich regions($\rho_b(\vec{r}) - \overline{\rho_b} < 0$) as well as the Fe-rich regions ($\rho_b(\vec{r}) - \overline{\rho_b} > 0$); the paramagnetic regions which are caused by cooperative phenomena grow beyond the extent of the fluctuation of the chemical composition.

References

1) S.Komura, G.Lippmann and W.Schmatz:J.Appl.Cryst.7(1974)233.

2) S.Komura, G.Lippmann and W.Schmatz:J.Magn.Magn.Mat.5(1977)123.

3) S.Komura and T.Takeda: J.Magn.Magn.Mat. 10(1979)191.

4) S.Komura, T.Takeda and Y.Endo: J.Magn.Magn.Mat.50(1965)69.

5) Y.Endoh, Y.Sasaki, H.Ono, S.Mitsuda and S.Ikeda:Physica 120B(1983)45.

Neutron Depolarization Studies on Spin Glass Properties in $Fe_{0.7}Al_{0.3}$*

Setsuo.MITSUDA** and Yasuo.ENDOH

Department of Physics,Tohoku University
Sendai 980

$Fe_{0.7}Al_{0.3}$ is well known to show the re-entrant spin glass behavior[1,2]. It becomes ferromagnetic below Tc≈400 K,then superparamagnetic below T_{inv}≈170 K and finally freezes into spin glass below T_g≈90 K. In order to understand the magnetic state in the spin glass and superparamagnetic phase of this system,neutron depolarization measurement was carried out by using polychromatic polarized neutrons. We have confirmed that our polycrystal sample shows the similar temperature dependence of magnetization to the previous data[1,2] by magnetization measurement as shown in fig.1. Note that phase transition temperatures of this system are very sensitive to the chemical composition.

The wavelength dependence of polarization transmitted through the disk plate of $Fe_{0.7}Al_{0.3}$ is shown at several designated temperatures in fig.2. An appreciable oscillatory behavior with respect to neutron wavelength was obserbed except for (A),(B) in the case of Zero Field Cooling (Z.F.C.). The wavelength dependence of polarization $P(\lambda)$ was fitted to the following empirical formula.

$$P(\lambda)=C_1+C_2EXP[-C_3\lambda^2]*COS(C_4\lambda+C_5) \qquad (1)$$

Temperature dependence of fitted parameters are shown in fig.3. Oscillatory behavior with respect to neutron wavelength corresponds to the precessing motion of neutron polarization vector around a steady internal field B(r) over distance L. Then parameter C_4 is expressed following form

$$C_4[Å^{-1}]=4.63X10^{-2}\int_0^{L[cm]} B(r)[Oe]dr \qquad (2)$$

In the case of analysis[3] based on ferromagnetic domain theory,L gives mean domain size. Using the saturation magnetization M_S determined by magnetization measurement at room temperature,L is determined to be nearly equal to the sample thickness d(0.045 cm). This fact suggests that

ferromagnetic domain state disappear under the external magnetic field H_{ex}=100 [Oe] and neutron polarization vector follows local magnetization adiabatically . Therefore parameter C_4 gives field integral over sample thickness. Damping behavior of oscillation which is characterized by parameter C_3 results from the distribution of C_4 with respect to the neutron beam passage. In the case that this distribution is Gaussian ,width ΔC_4 is expressed by following equation

$$\Delta C_4=\sqrt{2C_3} \quad (3)$$

As seen in magnetization data (fig.1) ,the difference between Z.F.C and F.C. processes was also observed in depolarization. At the temperature (A),(B) in the case of Z.F.C. ,depolarization was negligible. The fact strongly supports the appearence of the glass state where local magnetization disappear by randomly frozen spin state. On the other hand,C_4 becomes finate at the same temperature (A),(B) in the case of F.C.. This means that spin glass state was broken under the finate external magnetic field.

As shown in fig.2,C_4 decreases and $\Delta C_4 / C_4$increases as the temperature is decreased from T_{inv} . This fact seems to be consistent with the picture [2] in the temperature range $T_{inv}>T>T_g$ that finate ferromagnetic cluster size is reduced as decreasing temperature. Note that neutron polarization vector is not affected by paramagnetic reigon surrounding finate ferromagnetic clusters.

Authors thank prof. H.Yoshizawa and Mr.S.Itoh for their helpful discussion.

* A part of Doctor thesis of Setsuo.Mitsuda presented to Department of physics,Tohoku University

* *present address
Institute For Solid State Physics,Tokyou University
Roppongi,Minato-ku,Tokyou 106 ,Japan

Reference

(1) R.D.Shull,H.Okamoto and P.A.Beck :Solid State Commu. 20,863(1978)
(2) K.Motoya,S.M.Shapiro and Y.Muraoka:Phys.Rev.B28(1983)6183
(3) S.Mitsuda and Y.Endoh :J.Phys.Soc.Jpn 54(1985)1570

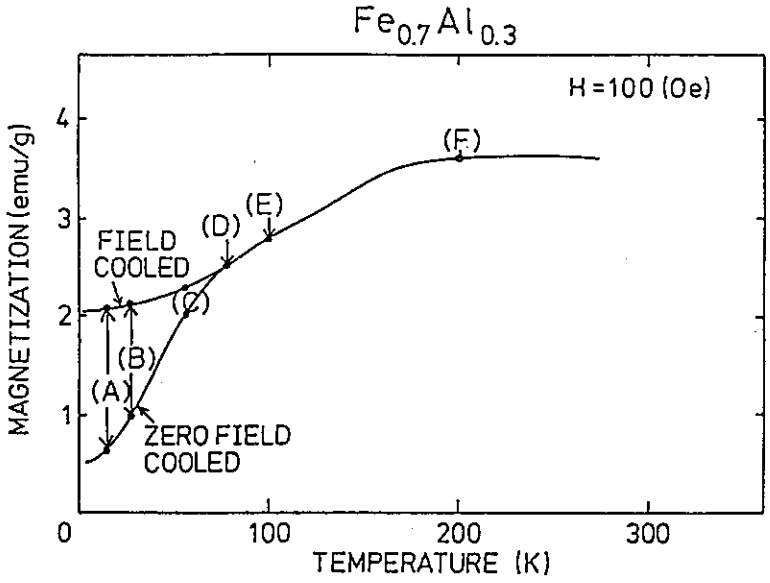

Fig.1

Temperature dependence of magnetization of $Fe_{0.7}Al_{0.3}$ at H_{ex}=100 Oe Inserted mark (A)-(F) represent temperatures at which depolarization measurement was done.

(A)14.5 K (B)28K (C)57K (D)77K (E)100K (F)200K

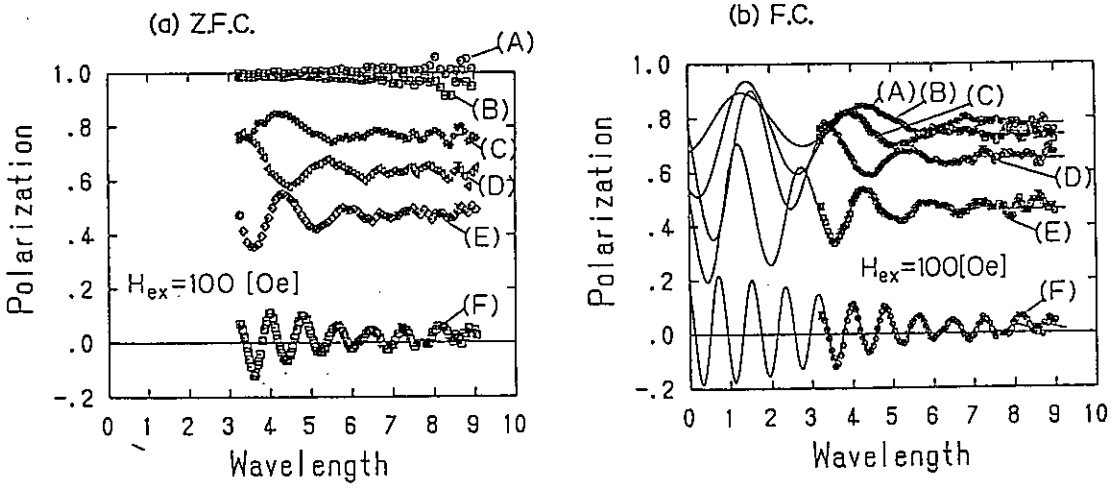

Fig.2

Polarization of the neutron beam transmitted through disk plate of $Fe_{0.7}Al_{0.3}$ is plotted against the neutron wavelength for several temperatures.

(a)Z.F.C. The sample was cooled to 14 K without the external magnetic field and measured with the external magnetic field of 100 Oe increasing temperature. (b) F.C. The sample was measured with the external magnetic field of 100 Oe cooled from room temperature.

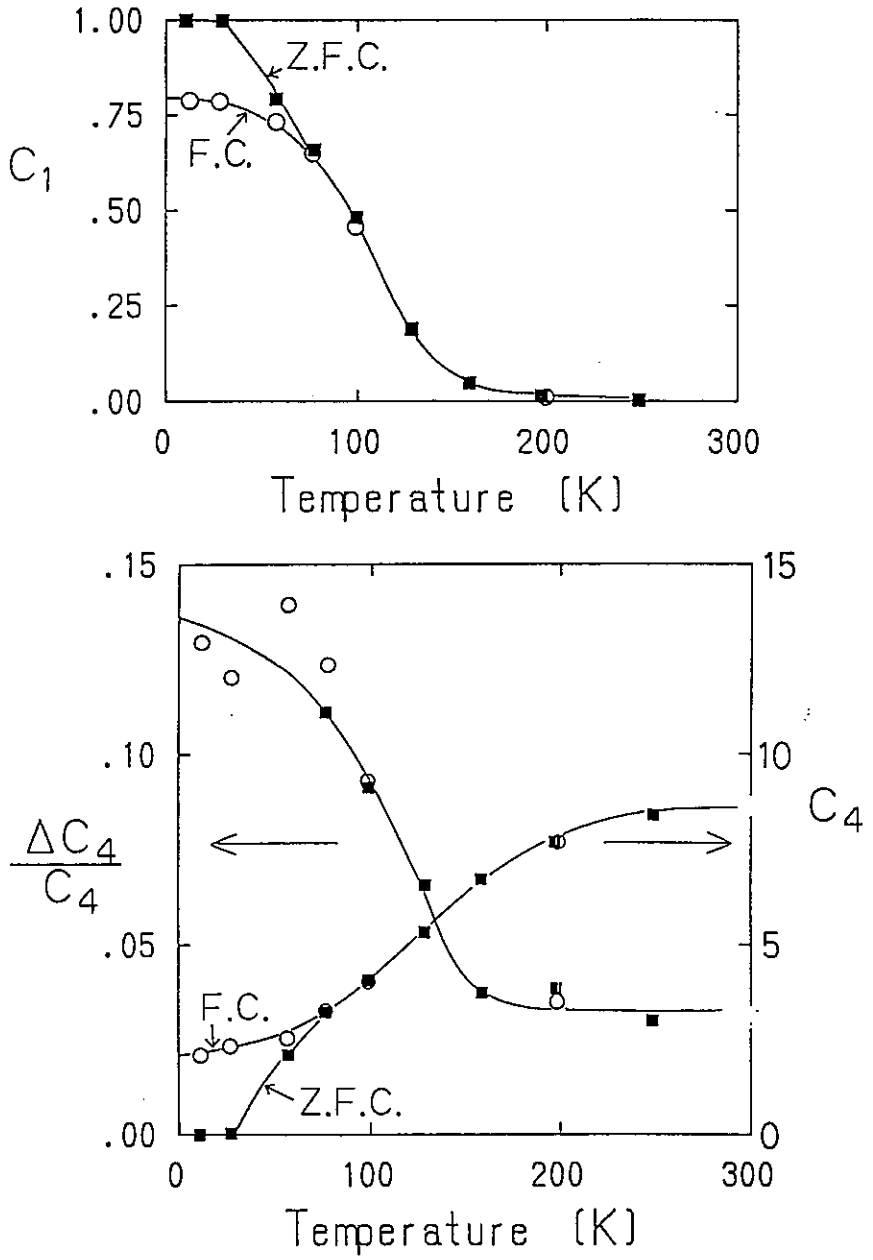

Fig.3
Temperature dependence of fitted parameters C_1, C_4, $\Delta C_4 / C_4$

Polarized Neutron Studies from Co Ferrofluid

Shin'ichi ITOH, Yasuo ENDOH and Roger PYNN

Department of Physics, Tohoku Univ. Sendai 980
Insitut Laue Langevin, Grnoble 38052 Cedex, France

We carried out depolarization measurements of polarized beams transmitted through the ferrofluid. We developed a method of the wavelength dependence of depolarization and have demonstrated that this novel method permits to detect the fluctuations of magnetization straightforwardly[1]. Experimental details together with description of fundamentals were presented in the paper by Mitsuda and Endoh[2], and thus this note reports another demonstration for application to ferrofluids. Neutron measurements were performed on the TOP spectrometer and the supplemental bulk magnetization data were taken with the vibration magnetometer at Tohoku University. The ferrofluid used in the present investigation was composed of cobalt particles of nominally about 100A in diameter in dioctylazelate solvent. The volume fraction of Co was 3.6%.

Typical data of neutron depolarization measurements are shown in Fig.1 and 2. The curve(a) in Fig.1 shows the wavelength dependence of depolarization at room temperature (300K) under zero external field. Note that the data are analyzed as the results of polarizability. For instance, the curve(a) depicts negligible depolarization within the statistical error.

The curve (b) and (c) are those of 20K in weak external field of 600e after being cooled at zero field (ZFC) and cooled at 50000e, respectively. The field upon cooling was applied along the neutron beam direction, but it was perpendiculer to the neutron polarization.

The curve(b) shows the exponential decay of polarization with respect to the wavelength ,which was interpreted successfully in terms of depolarization for superparamagnetic substances. The experimental curve was eventually fitted to the following analytical form obtained by a model where superparamagnetic particles are randomly oriented and dispersed in the

solid.

$$P = \exp\left[-1/3(p+3/2\ p^{5/3})\ C^2B^2\bar{\delta}\cdot d\lambda^2\right],$$

where $\bar{\delta}$, d and p are the parameters of particle diameter, neutron path length and effective volume fraction of Co particles, respectively. Then we could reproduce the observed curve by fitting other parameters in the above expression. The difference between curve(a) and (b) should arise in the difference of fluctuation time of the magnetization. The super-paramagnetic particles in the fluid behave just like paramagnetic at room temperature due to the larger frequency.

Fig.2 depicts a series of measurements upon heating from 20K to 300K at the interval of 20K after the field cooling. The polarization increases with increase of temperature, but the larger changes occur around 150K. Correspondingly the results should tell how induced magnetization by the field cooling becomes random from the aligned orientation.

Since the wavelength dependences of polarization can be represented by $\exp(-\alpha^2\lambda^2)$, B should correspond to the integrated magnetic induction being averaged over particles.

$$\alpha^2 = N/2C^2\ B_\perp{}^2\langle\bar{\delta}^2\rangle$$

In the present case, the cooling field was perpendicular to the neutron polarization, and thus the coefficient B is postulated to be proportional to the magnetization. Then the temperature variation of depolarization was related to that of magnetization.

$$\int B_\perp{}^2 = 4\pi Ms \int \langle\cos^2\theta\rangle$$

$$M = Ms\langle\cos\theta\rangle$$

The origin of thermal change of magnetization will be discussed in the separate paper.

REFERENCES

1) S.Mitsuda, H.Fujimoto, Y.Endoh and S.Ikeda, KENS Rpt.P.186(1984).

2) S.Mitsuda and Y.Endoh, J.Phys.Soc.Jpn.54(1985)1570.

3) S.Itoh, Y.Endoh and R.Pynn, to be published.

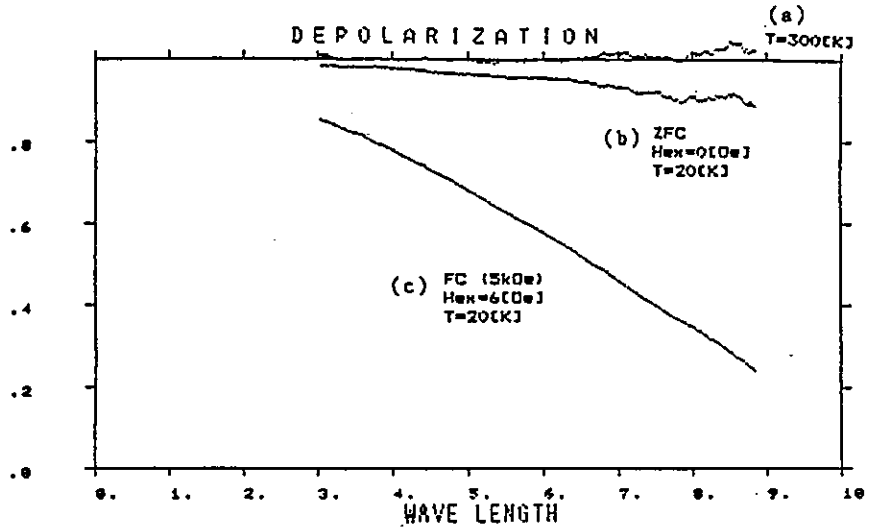

Fig.1 Wavelength dependence of neutron depolarization. ZFC and FC represent that Co ferrofluid was cooled without and with field from 300K down to 20K respectively. Hex means external field at the measurement to align neutron polarization.

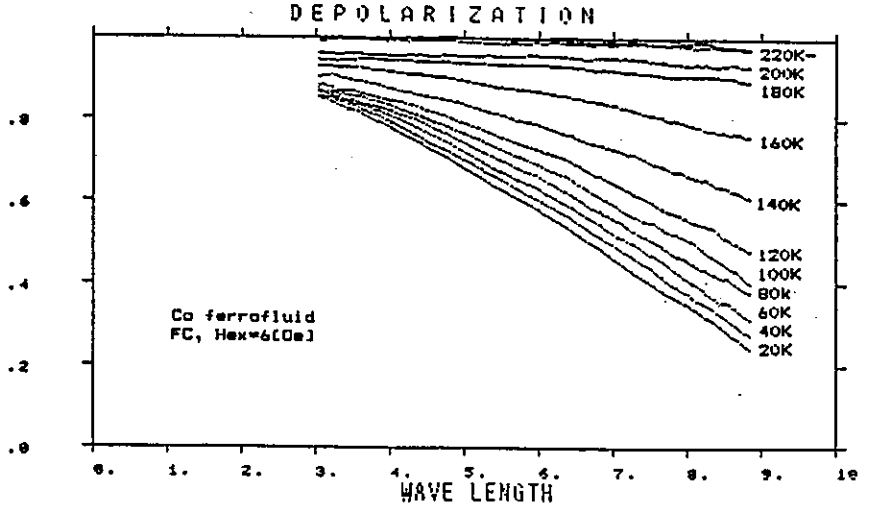

Fig.2 Wavelength dependence of neutron deporization at various temperatures. Co ferrofluid was cooled down to 20K in the field 50000e before starting measurements.

Epi-thermal Neutron diffraction of Sm Compounds

H. Fujimoto, K. Ohyama, M. Kohgi, B. Liu, M. Kasaya,
A. Ochiai, T. Suzuki and Y. Masuda*

Physics department, Tohoku University, Sendai 980
*Laboratory for High Energy Physics, Tsukuba, Ibaraki 305

Sm compounds exhibit a variety of magnetic behaviors depending on the relative positions of the f-levels to the valence or conduction bands as well as on the magnitude of mixing effect. Some compounds show the valence fluctuating or dense Kondo like phenomena. Therefore the determination of their magnetic structures and excitations is of importance for the study of such phenomena. Unfortunately, natural Sm contains about 14% of strongly neutron absorbing isotope ^{149}Sm, and the experiment by utilizing thermal neutrons is not easy to do. However, because of the resonace characters of the neutron absorbing cross section, there are some windows for the neutron scattering experiments at the epi-thermal energy regions, say, near 0.5 eV and above 1 eV.

We performed the epi-thermal neutron diffraction experiments for Sm compounds at the PEN spectrometer at KENS, KEK. The spectrometer is suitable for such measurements because the epi-thermal neutron flux is relatively high at the pulse neutron source and we can utilize highly polarized epi-thermal neutrons by employing the dynamically polarized proton filter method. The details of the spectometer were reported elsewhere.[1)]

We report here the results of the experiments on a single crystal of $SmSn_3$. It has the $AuCu_3$ type crystal structure with the lattice parameter of 4.684Å. It exhibits the dense Kondo like behaviors in the resistivity and susceptibility at low temperatures, and an antiferromagnetic phase transition occurs near 10K, where the triple peaks were observed in the specific heat.[2)] Therefore, the unambiguous determination of the magnetic structure and the magnetic moment of a Sm atom in this material is highly required.

In order to perform such studies, it is necessary to determine experimentally the coherent nuclear scattering length b of Sm at the epi-thermal energy regions, since it may be energy dependent because of the existence of the strongly absorbing levels and no direct measurement of it has ever been reported yet. We tried to determine the scattering length from the measurements of the nuclear Bragg scattering from $SmSn_3$. The sample has a disk shape of about 13 mm in diameter and 5mm in thickness. The coherent scattering lengths at several neutron energies above 400 meV were evaluated from the ratios of integrated intensities of 110 reflections to those of 220 reflections. The ratio at each energy in the TOF scheme is expressed as

$$\frac{I(110)}{I(220)} = \frac{(d_{110})^2}{(d_{220})^2} \cdot \frac{|F(110)|^2}{|F(220)|^2} \equiv 4 \cdot \frac{(b^r_{Sm} - b_{Sn})^2 + b^i_{Sm}{}^2}{(b^r_{Sm} + 3b_{Sn})^2 + b^i_{Sm}{}^2} , \qquad (1)$$

where b^r_{Sm} and b^i_{Sm} are the real and imaginary part of the coherent scattering length of Sm, respectively. The coherent scattering length of Sn is expressed simply by b_{Sn} because it is considered to be a real number in the energy regions. Since the absorption correction factors for both reflections are nearly the same in our case, they are omitted in Eq.1. We supposed that the extinction effect is also negligible in these neutron energy regions.

The scattering lengths are expressed theoretically by the Breit-Wigner formula as

$$b = b^r + ib^i , \qquad (2)$$

$$b^r = b_0 + \sum_j \sum_i \frac{\omega_j g_i \lambda_{0i}}{4\pi} \cdot \frac{\Gamma_{ni}(E - E_{0i})}{(E-E_{0i})^2 + (\Gamma/2)^2} , \qquad (3)$$

$$b^i = \sum_j \sum_i \omega_j \frac{g_i \lambda_{0i}}{4\pi} \cdot \frac{\Gamma_n \Gamma/2}{(E-E_0)^2 + (\Gamma/2)^2} , \qquad (4)$$

where b_0 corresponds to the potential scattering, ω_j is the natural abundance of the j-th isotope, i discriminates the resonance levels for each isotope, and $g\Gamma_n$, Γ and E_0 are the resonance absorption parameters.

In fig.1, the obtained coherent scattering lengths of natural Sm are

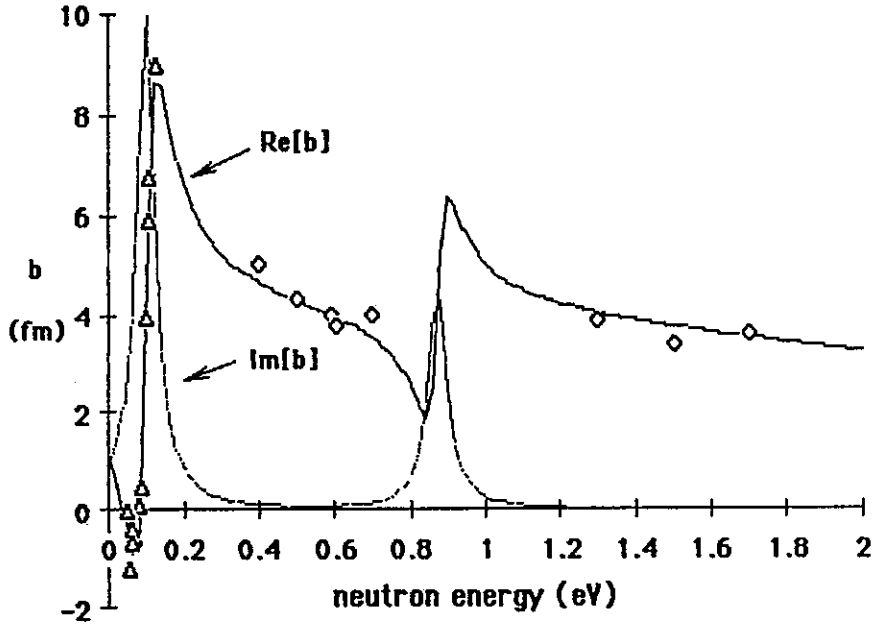

Fig.1 coherent scattering length of natural Sm

plotted, where the imaginary part of the scattering length was neglected in the calculations by the Eq. 1. We also plotted the data at thermal neutron region from D. W. Engel and T. F. Koetzle[3] by triangles. The solid and broken curves in the figure are the calculated real and imaginary parts of scattering lengths based on Eqs. 2-4. The value of b_0 was chosen to be 7.72 fm so as to get best fit to the data. We took into account the resonance levels at 0.097 eV and 0.872 eV of ^{149}Sm and at 8.047 eV of ^{152}Sm. The calculated imaginary part of the scattering length is negligibly small at the regions where we did measurements. It indicates that our assumption of neglecting it in the present data analysis is justified. The agreement between the present values and the theoretical curve for the real part of the scattering length is good within the experimental errors.

Next, we tried to detect the magnetic scattering from $SmSn_3$ at a low temperature. Since it is antiferromagnetic below about 10K, we scanned around the reciprocal lattice points of (0,0,1/4), (1/4,1/4,0), (0,0,1/2), (1/2,1/2,0), (1/2,1/2,1/2), (1/2,1/2,1), (1,1,1/2), and (1/2,1/2,3/2) at 5K by using the energy window around 600 meV. The scan range was about ±15% of the reciprocal vectors. Some points were scanned also at 30K in order to see any difference of neutron counting

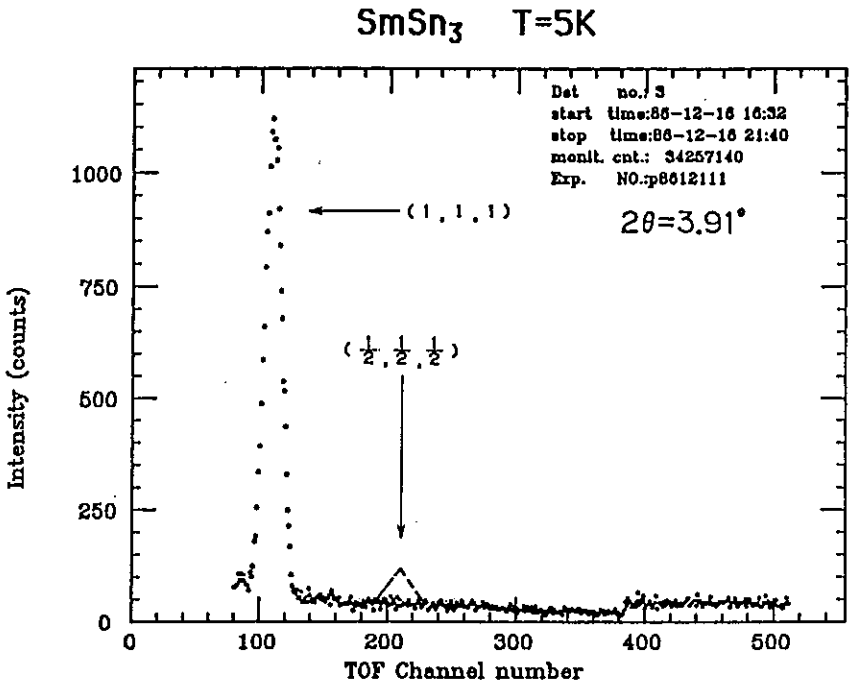

Fig.2 A Typical scan of single crystal of $SmSn_3$ at 5K. Broken curve indicates an estimated magnetic scattering with Sm moment of $0.7\mu_B$.

between below and above the Neel temperature. In Fig.2, we show the scan around (1/2,1/2,1/2) reciprocal lattice point at 5K as a typical example. The broken curve indicates an estimated Bragg scattering if the system has the antiferromagnetic structure of the [1/2,1/2,1/2] type with the magnetic moment per Sm of $0.7\mu_B$, which corresponds to the full moment of the ground multiplet of Sm^{3+}, and with spin direction perpendicular to the scattering vector. As shown in this figure, no trace of magnetic scattering was observed within our experimental accuracy for all points measured. Therefore, we can conclude that, if $SmSn_3$ has an antiferromagnetic structure which gives Bragg scattering at one of the reciprocal lattice points we scanned, the magnetic moment per Sm atom should be much smaller than $0.7\mu_B$, or that its magnetic structure is more complex one than those which we scanned.

References

1) M.Ishida, M.Kohgi, Y.Masuda, S.Hiramatsu, S.Isagawa, Y.Ishikawa, S.Ishimoto, A.Masaike and T.Nakajima: KENS REPORT-IV, KEK Internal 83-4(1983)202; also see Y.Masuda, S.Ishimoto, H.Fujimoto, M.Ishida, Y.Ishikawa, M.Kohgi and A.Masaike: in this Report.
2) M.Kasaya, B.Liu, M.Sera, T.Kasuya, D.Endoh, T.Goto and T.Fujimura: J.Mag.Mag.Mat. 52(1985)289.
3) D.W.Engel and T.F.Koetzle: Acta Cryst. A40(1984)99.

Separation of Spin Wave and Elastic Scattering from a Ferromanget Fe_3Pt Measured with a Pulse Neutron Small Angle Scattering Instrument SAN

*Michihiro FURUSAKA, *Akira YOKOSAWA and **Yoshikazu ISHIKAWA*

Physics Department, Tohoku University, Sendai 980

We have been developing a method to separate spin wave scattering from elastic scattering using small angle scattering instrument at pulse neutron source. The basic idea has been introduced in the previous report.[1] In this paper, improved calculation method and parameter dependence of the calculated scattering function were discussed. The result was applied to the temperature and magnetic field dependence of scattering in Fe_3Pt. It shows very large small angle scattering, but the origin of the scattering had not yet been known.

Integration path of the instrument for the scattering angle θ is expressed as follows. If incident neutron has momentum k_i and energy E_i, the relation of $q(\omega;\theta,k_i)$ and energy transfer $\hbar\omega$ becomes as,

$$q(\omega;\theta,k_i) = k_i\sqrt{2-\frac{\hbar\omega}{E_i}-2\sqrt{1-\frac{\hbar\omega}{E_i}}\cos\theta}\,. \qquad (1)$$

Spin wave dispersion relation $\hbar\omega_q$ and scattering cross section $S(q,\omega)$ were assumed to be,

$$\hbar\omega_q = E_g + Dq^2\,, \qquad (2)$$

$$S(q,\omega) = A(k_i,k_f)\cdot\frac{1}{1-\exp\{-\hbar\omega_q/k_BT\}}\cdot\frac{\Gamma_q^{\,2}}{(\omega_q-\omega)^2+(\Gamma_q^{\,2})^2}\,, \qquad (3)$$

where D is the spin wave stiffness constant, E_g the energy gap, $A(k_i,k_f)$

---

*Present address; Toshiba Co., Saiwaiku, Kawasaki, 210.
**Deceased.

the wavelength dependent constant, and Γ_q the damping factor of the spin wave. The q dependence of Γ_q was assumed to be $\Gamma \cdot q^2$. Small angle scattering intensity I(θ) was obtained by integrating S(q,ω) along the integration path and convoluted by the instrumental resolution. Therefore, the scattering intensity I(θ) is described by three independent parameters; spin wave stiffness constant D, energy gap E_g and inverse of life time Γ.

The E_g dependence of I(θ) by a function of incident wavelength λ is shown in Fig. 1. As shown in the figure, the λ dependence of I(θ) was very sensitive to the energy gap E_g especially in the small θ region (<0.02rad). The calculation showed that I(θ) is also sensitive to the parameter D, but not so sensitive to Γ.

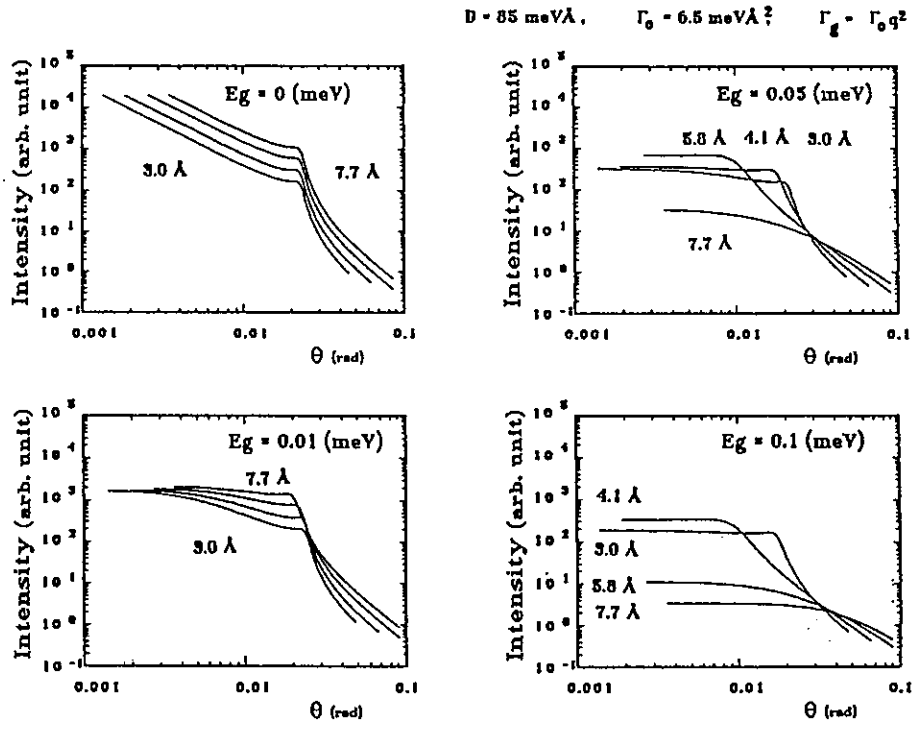

Fig. 1. Energy gap E_g dependence of the spin wave scattering intensity as a function of λ.

The λ obtained from total time-of-flight is very close to the true incident λ because the incident flight path is much longer than the scattering path and the energy transfer is not so large. The elastic scattering and spin wave scattering could be separated by comparing the above calculation and λ dependent scattering intensity obtained by the

experiment. In order to check the validity of this method, elastic scattering from Fe_3Pt alloy at room temperature was compared with the result obtained by triple-axis spectrometer installed at BNL. The instrument installed at cold source was used to obtain as low q as possible, and only the elastic scattering was measured . The result was consistent with our calculation. By this method, we can get scattering down to very low q (about 0.06 nm^{-1}), compared with lowest q attained by the BNL of $q > 0.2$ nm^{-1}.

We have applied this method to the temperature and magnetic field dependence of scattering from Fe_3Pt and spin waves contribution were subtracted from total scattering. One of the typical results with no magnetic field was shown in Fig. 2 in logarithmic scale. Spin wave part was observable only at the high q region of the scattering around 1 nm^{-1} and it was negligible at lower q ($q< 0.2\sim0.3$ nm^{-1}). Since the Curie temperature of this sample is 504K; magnetic critical scattering was observed as shown by q^{-2} dependence at high q region ($q>0.2nm^{-1}$) at high temperature. At lower q region, q^{-4} or higher exponent dependence was observed. This q^{-4} dependence is attributed to the scattering from sharp domain boundaries. It was shown from a simple model calculation that if the size of the domains are not completely random, q dependence becomes

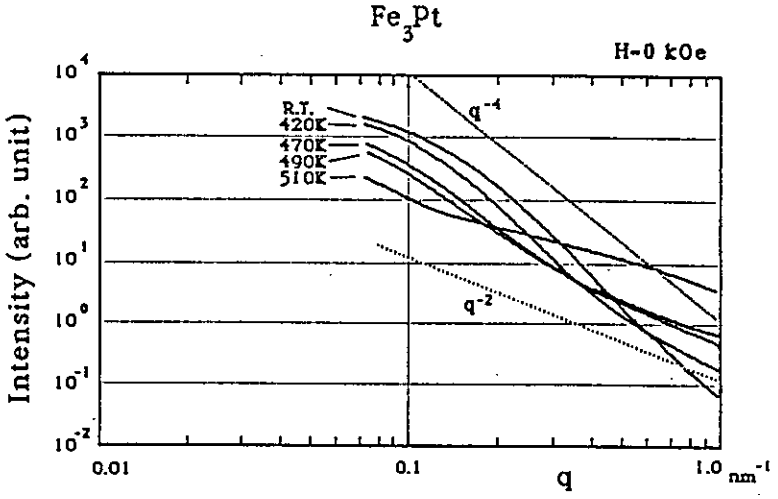

Fig. 2. Small angle scattering from Fe_3Pt with no magnetic field. Spin wave scattering contribution have been removed. Doted lines showed the q^{-2} and q^{-4} dependence.

steeper than q^{-4}, as shown in room temperature sample.

The same analysis has been done for the sample under the magnetic field (11.6kOe). By applying the magnetic field, the scattering intensity was uniformly dropped by almost 2 orders of magnitude as shown in Fig. 3. It is independent of the direction of the applied field. The remaining weak scattering was mainly attributed to the magnetic critical scattering from the q^{-2} dependence. Beside this scattering, there remained the q^{-4} dependent scattering even when the magnetic field of 11.6kOe was supplied at room temperature.

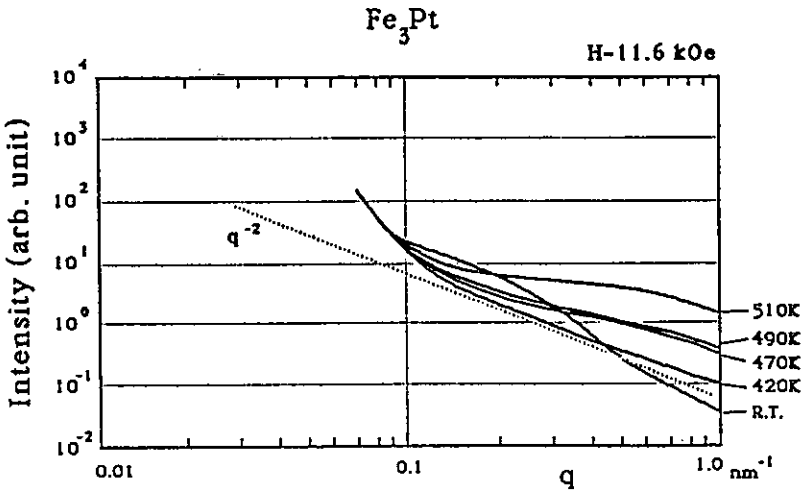

Fig. 3. Small angle scattering from Fe_3Pt with magnetic field. Spin wave scattering contribution have been removed. Doted line showed the q^{-2}.

These results were compared with TEM studies.[2] TEM images from the sample at room temperature showed normal magnetic domains of the size of 10μm order. Inside the normal magnetic domains, "tweed pattern" (about 10~20nm) was detected. Deduced from the contrast of defocussing image, this pattern was attributed to be the modulations of spin direction. This structure is consistent with our small angle scattering results. The detailed analysis of the present data is in progress.

References

1) M. Furusaka, Y. Ishikawa and S. Onodera: KENS Report-V (1984) 67.
2) D. Watanabe: private communication.

Low Energy Peaks in Neutron Spectra from Various Amorphous Solids

Kazuhiko INOUE, Keisuke KAJI*, Toshiji KANAYA*,
Susumu IKEDA+, Masatoshi ARAI+ and Masakatsu MISAWA+

Depertment of Nuclear Engineering, Hokkaido University,
Sapporo, 060 Hokkaido, Japan

* Institute for Chemical Research, Kyoto University,
Uji, 611 Kyoto-fu, Japan

+ National Laboratory for High Energy Physics,
Tsukuba, 305 Ibaraki-ken, Japan

Low energy neutron scattering spectra from several amorphous solids were measured by using the LAM-40. The scattering samples are amorphous bulk polymers, epoxy resin and inorganic amorphous solid, B_2O_3 [1~6]. The LAM-40 spectrometer has a useful performance for the measurement of spectral shape in the energy transfer region from about 0.2 meV to several meV [1]. The spectral shape of elastic scattering has a exceptional sharp rise at left-hand siede of the elastic peak. In this energy transfer region the S/N ratio is extreamly good. We found low energy peaks at about 2 meV. In some of the samples, such peaks were only observed at lower temperatures and the Lorentzian-like quasielastic peaks having peak centers placed at zero energy transfer were observed as alternative ones at higher temperatures. For the vitreous germania Leadbetter and Litchinsky found a peak at 13 cm^{-1} in the neutron spectra and assigned the peak to resonance vibrations associated with structural defects as yet unidentified [7].

Figure 1 shows the spectra from poly(butadiene) obtained at four temperatures from 100 K to 260 K for two scattering angles, 40° and 104°. At lower temperatures, the intensities on the down-scattering side are evidence for a low energy broad peak around 2 meV. The spectral shape of broad peak turns to the ordinary Lorentzian-like quasielastic peak shape as the temperature increases. Similar feature of spectral shape and its dependence on temperature were observed on poly(isoprene), amorphous poly(ethylene) and others. Similar results were obtained concerning the evidence of broad peak on epoxy resin, benzoic acid and B_2O_3 at ambient temperature [5~6].

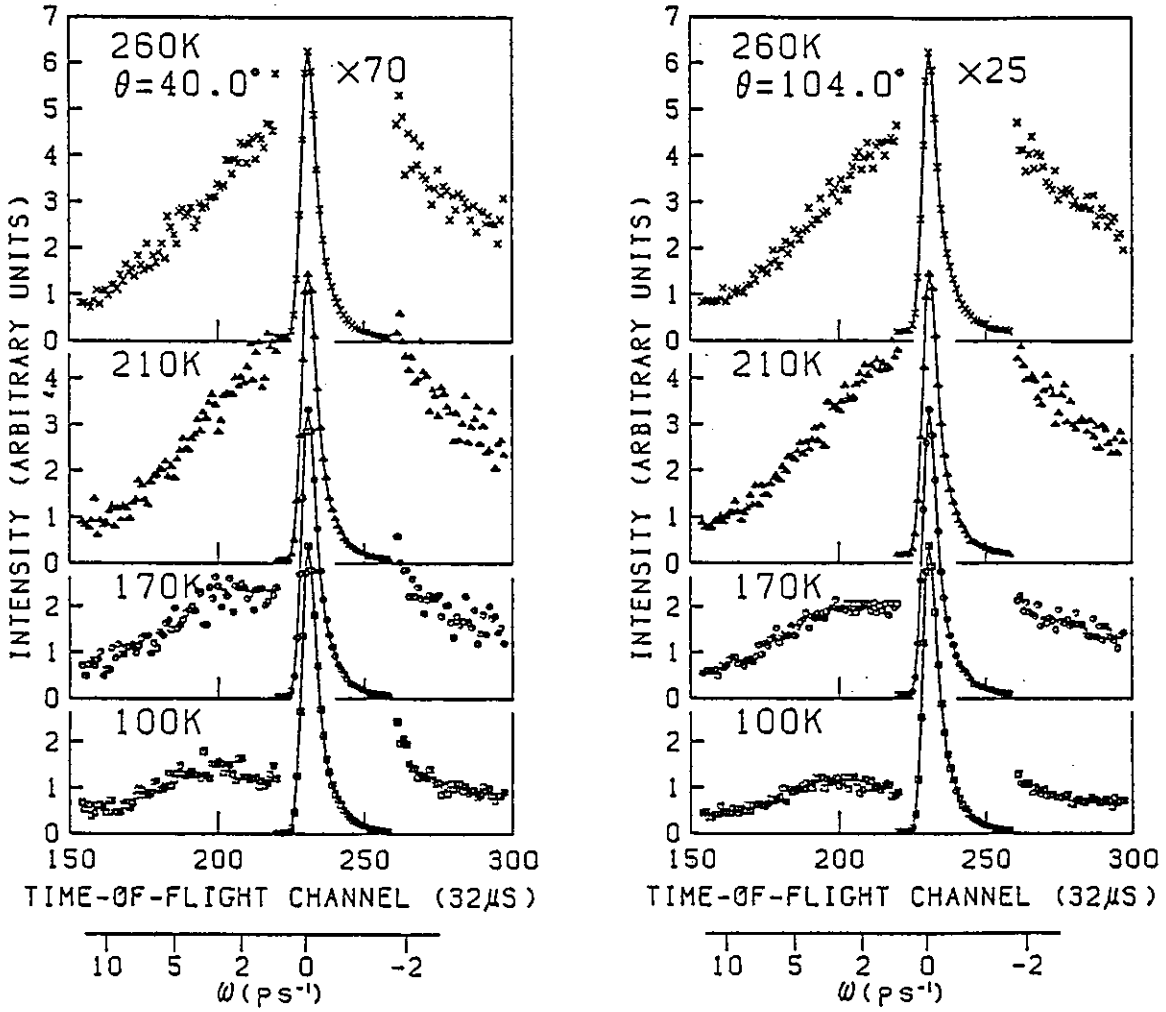

Fig. 1. Typical neutron scattering spectra from poly (butadiene) measured by the LAM-40 spectrometer.

However, for these samples, the quasielastic peak was not measured. Remarkable result was obtained for the crystalized poly(ethylene). In this case, at low temperature, the evidence of broad peak around 2 meV was not observed [2]. This fact suggests strongly that the low energy broad peak concerns the amorphous structure.

The measured scattering in amorphous polymers is then explained by assuming the return trip motions at lower temperatures and the jumping random motions at higher temperatures. The incoherent intermediate scattering function of hydrogen atoms in polymers is given by [7]

$$I_{inc}(Q,t) = N^{-1} \sum_{n=1}^{N} \langle \exp\{-iQ\, r_n(0)\} \exp\{iQ\, r_n(t)\} \rangle, \qquad (1)$$

where <...> means the ensemble average and N is the number of hydrogens in the typical atom groups which have various chain conformations. We assume

that at low temperatures a typical chain changes its conformation to other comformation by the return trip through the intervening potential barrier and then continues round motions. At higher temperatures the conformation of the typical chain would be changed to another by the random forces due to the thermal fluctuations in the surrounding structure and would conduct consecutive random jump motions.

A computer simulation calculation for $I_{inc}(Q,t)$ were carried out by using above model. The dynamical variable, $\exp\{iQ\, r_n(t)\}$, was treated in the classical fashion. We assumed that the variable was approximately expressed by a cyclic function accompanying fluctuations. Preliminary results of power spectrum for various ratios of the average return period, τ, amd the average waiting time for fluctuation of period, α', are illustrated in Fig. 2. From the calculated power spectra and the observed neutron spectra we obtained time constants, τ, α' and the average waiting time of random forces, α. The preliminary results are given in Table 1.

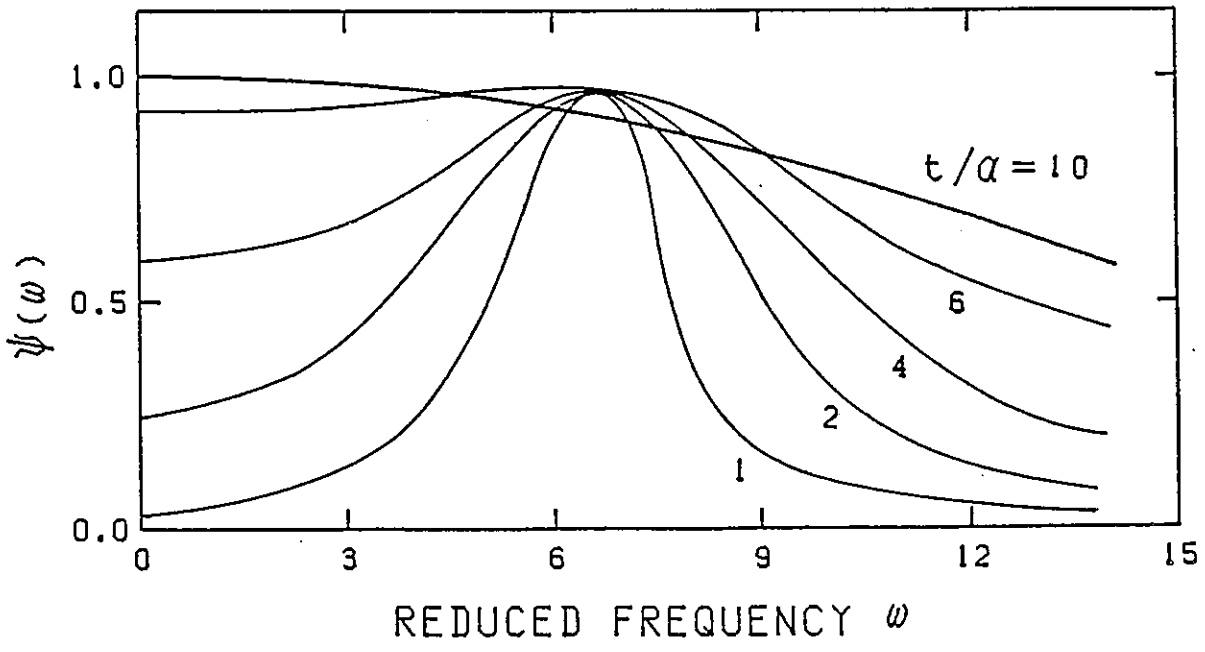

Fig. 2. The power spectra of return and random motions for various ratios of average waiting time of fluctuation and return period.

Table 1. Time constants of return and random motions

T(K)	τ (10^{-12}sec)	α' (10^{-12}sec)*	α (10^{-12}sec)
100	2.1	1.1	
260			0.4

* α' is the average waiting time for fluctuations of period.

These results indicate that there might be low-laying additional excitations due to conformation changes of atom groups in amorphous polymers. From observed neutron data, for other amorphous solids described above, it can be concluded that similar situations concerning the additional exitation modes also evidently exist.

References

1) K. Inoue et al., Nucl. Instr. and Meth., A238(1985)401.
2) T. Kanaya et al., in this report.
3) M. Arai, in this report.
4) T. Kanaya, in this report.
5) K. Kaji, in this report.
6) M. Misawa, to be published.
7) A. J. Leadbetter and D. Litchinsky, Discus. Faraday Soc., 50(1970)62.
8) T. Springer, Springer Tracts in Modern Physics, Vol.64 (Springer-Verlag, Berlin, 1972).

A LOW ENERGY PEAK IN BENZOIC ACID CRYSTALS MEASURED BY NEUTRON SCATTERING

Keisuke KAJI, Soichi HAYASHI, Toshiji KANAYA, and Kazuhiko INOUE*

Institute for Chemical Research, Kyoto University,
Uji, 611 Kyoto-fu, Japan
*Department of Nuclear Engineering, Hokkaido University,
Sapporo, 060 Hokkaido, Japan

The neutron spectra of various amorphous solids in a range of energy transfer between 0.2 and 10 meV were measured at low temperatures by using the LAM-40 spectometer. The observed spectra for all the investigated samples showed a broad peak around a few meV, which was considered to be characteristic of amorphous solids including polymers and inorganic glasses[1] since crystals did not show the peak.[2] The origin of this peak is one of the recent debating problems in connection with low temperature properties of amorphous solids.[3] We show here that even crystals also give such a low energy peak if they have local dynamic disorders.

It is known that carboxylic acids form hydrogen-bonded dimers in the crystalline state where the carboxylic protons transfer between the two tautomeric structures:

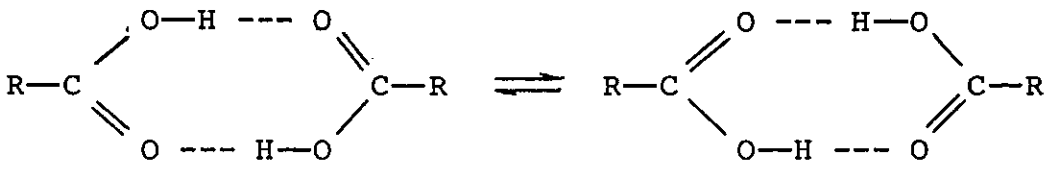

For benzoic acid crystals the jump frequency of the carboxylic protons between the two tautomeric positions was estimated to be about $3 \times 10^{10} s^{-1}$ at ambient temperature from NMR measurements.[4] In such a case where the local dynamic disorders exist it is interesting to know whether the low energy peak at a few meV as seen in the amorphous solids appears.

Commercial deuterated benzoic acid crystal powder was solved in light water, and recrystallized slowly to obtain the crystals hydrogenated only in the carboxylic groups (BA-d_5). Neutron scattering measurements of this BA-d_5 crystal powder were carried out with the LAM-40 spectrometer at ambient temperature. The observed time-of-flight (TOF) spectra at several scattering angles are shown in Fig. 1. A broad inelastic peak on the left side of the very strong elastic peak is seen; the peak energy is between 3 and 4 meV. This suggests that the excitation at a few meV is not due to the frequency distributions peculiar to the static structures of amorphous solids, e.g., expected from a fracton model[5] in which it is assumed that the amorphous solids assume a fractal structure and the cross-over from phonon to fracton occurs at a characteristic length.

References

1) K. Inoue, et al., in this report.
2) T. Kanaya, et al., in this report.
3) W. A. Phillips (editor), "Amorphous Solids-low temperature properties", (Topics in current Physics Vol.24), Springer, 1981.
4) S. Nagaoka et al., Chem. Phys. Lett., 80, 580 (1981).
5) B. Derrida, et al., Phys. Rev., B29, 6645 (1984).

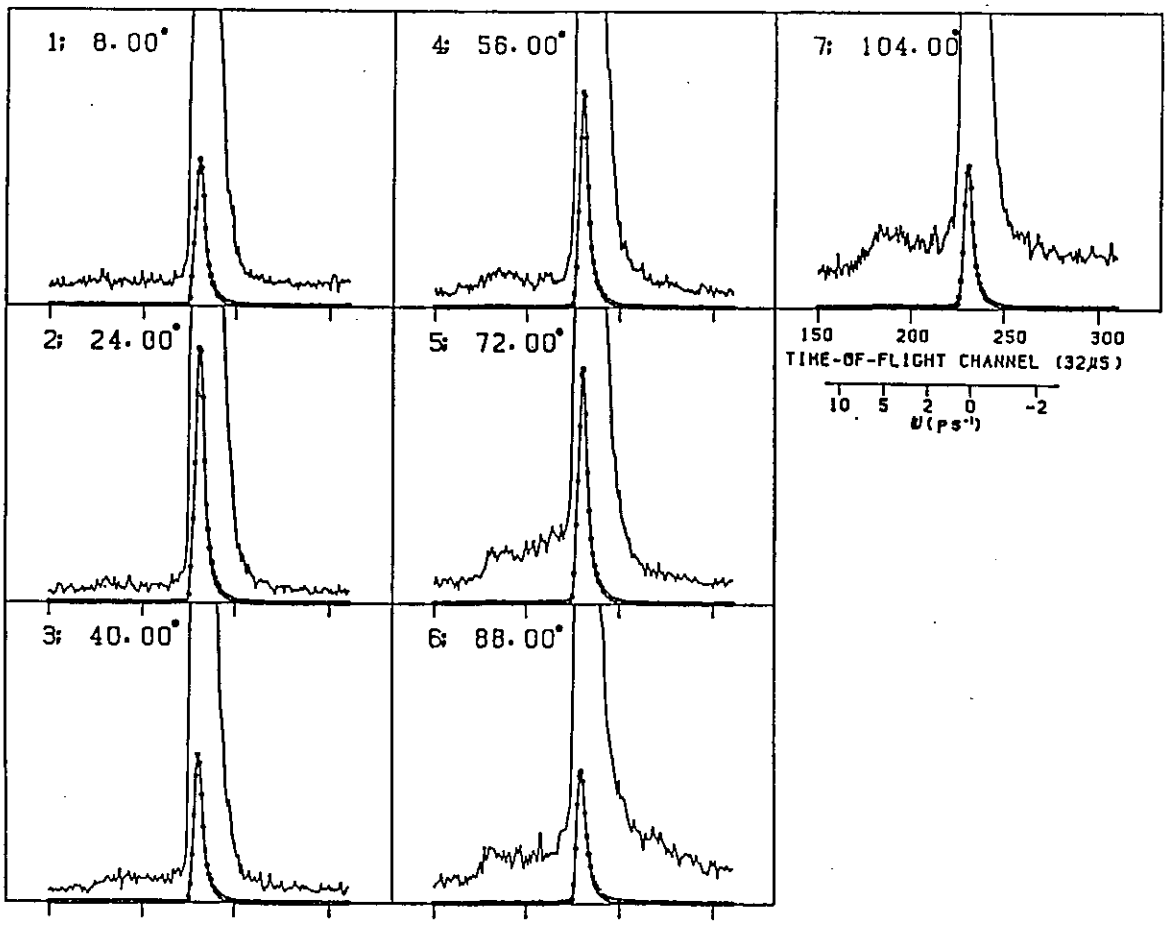

Fig. 1 Neutron time-of-flight spectra for various scattering angles from partly deuterated benzoic acid crystals (BA-d_5) measured at ambient temperature with the LAM-40 spectrometer.

Low Energy Excitation Measurement on Epoxy Resin

Masatoshi ARAI , Kazuhiko INOUE*, Toshiji KANAYA**

National Laboratory for High Energy Physics
Oho-machi, Tsukuba-gun, Ibaraki 305, Japan

*Faculty of Nuclear Engineering, Hokkaido University
Sapporo 060, Japan

** Institute for Chemical Research, Kyoto University,
Uji, Kyoto-ku 611, Japan

It is well known that non-crystalline materials have universal properties such as exhibited by the thermal conductivity, having plateau around 10K, and the specific heat, having contribution proportional to temperature linearly at low temperature[1,2,3]. The thermal properties at low temperature less than 1K is described with two level-tunneling states model[4,5]. With using usual kinetic theory we infer that the mean free path of phonon exhibits a precipitous drop to less than an atomic spacing above the frequency corresponding to 10K. Thus the usual phonon seems no longer a satisfactory description of the vibrational properties of the amorphous systems.

recent theories [6,7,8] suggest that the vibrations of a random material on a sufficiently short length-scale should be described as "fractons" instead of the more conventional phonons . The theory predicts the existence of a cross-over frequency at which the vibrations change from phonon to fracton character.

In order to clarify the mechanism of dynamics on random materials, we have done a series of preliminary inelastic neutron scattering experiment in LAM-40 at 230, 180, 120, 70 and 10K.

Epoxy-resins are cross-linked amorphous polymers. The large content of hydrogen makes them ideal candidates for measurements of vibrational densities of states by incoherent inelastic neutron scattering. The specimens were in the form of cylinder 80 mm long and 0.15 mm thick, which is expected to give multiply scattered neutron intensity less than 5 %.

Figure 1 shows a typical examples of measured intensity at 180 K. In the figures the final energies for each detectors, 2θ=8, 24, 40, 56, 72, 88 and 104 are shown and the corresponding momentum transfer at elastic position are 0.21, 0.62, 1.04, 1.39, 1.74, 2.06 and 2.33 A^{-1}. As you see in the figure there is a shoulder or sub-peak at about 2 meV independent to momentum transfer as reported in Ref. 9 and 10.

The data were analyzed using following equation

$$\left(\frac{d^2\sigma}{d\Omega dE}\right)=\frac{N\,\sigma i\,kf}{8\pi\,M\,ki}\exp\{-2W(q)\}\{b\,\frac{q^2}{\omega}(n(\omega)+1)\,Z(\omega) + a\,(n(\omega)+1)\,\omega\beta\,\frac{q^2D}{\omega^2+(q^2D)^2}\} \qquad (1)$$

Here we take $Z(\omega)=\omega^2$ and $D=\omega\exp(-E\beta)$. The former is description for usual acoustic phonon and the latter is corresponding to a kind of diffusion or migration with phonon frequency ω.

In amorphous materials there would be sites where atoms can tunnel through a energy barrier at low temperature. At finite temperature a atom or a group of atoms in a double well potential would migrate to unoccupied sites with activation energy. And this probability should be proportional to the frequency of the phonon with which atoms vibrate in the potential (phonon-assisted migration). It is natural to consider that there are distributions in energy gap E in amorphous materials, at which phonon is absorbed and turns into migration. Therefore the properties corresponding to energy transfer $\hbar\omega$ reflects the certain energy gap E.

To find the distribution of E and the fraction factor "a" and "b" for phonon and migration, a set of data at the same energy transfer having different momentum transfer were used to solve the eq. (1) having three unknown variables, instead of usual fitting.

As you see in Fig. 2 where the observed density of states are displayed with identical marks and calculated one with lines, the eq. (1) fairly holds in wide range of energy transfer.

The Fig.3 (a) shows "a", phonon part, and (b) shows "b", phonon-assisted migration part. The "a" has a plateau less than 2meV and decrease gradually increasing energy transfer. While the "b" increases toward 2meV and has plateau above this energy. Here is a cross-over from phonon character to phonon-assisted migration character at about 2meV.

Phonons pumps up migration and die away gradually at higher energy. The physical picture on fracton would be a kind of localized motion of atoms like migration in a double well potential, absorbing and emitting phonons. Further measurement is, however, necessary to conclude this picture using several kinds of amorphous materials.

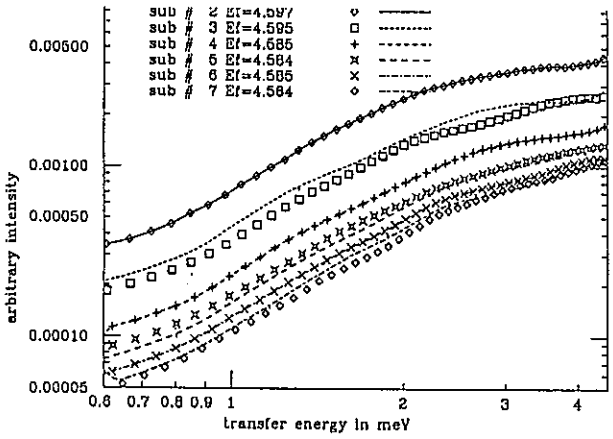

Fig. 2 Observed density of state plotted with marks and Calcurated one with lines.

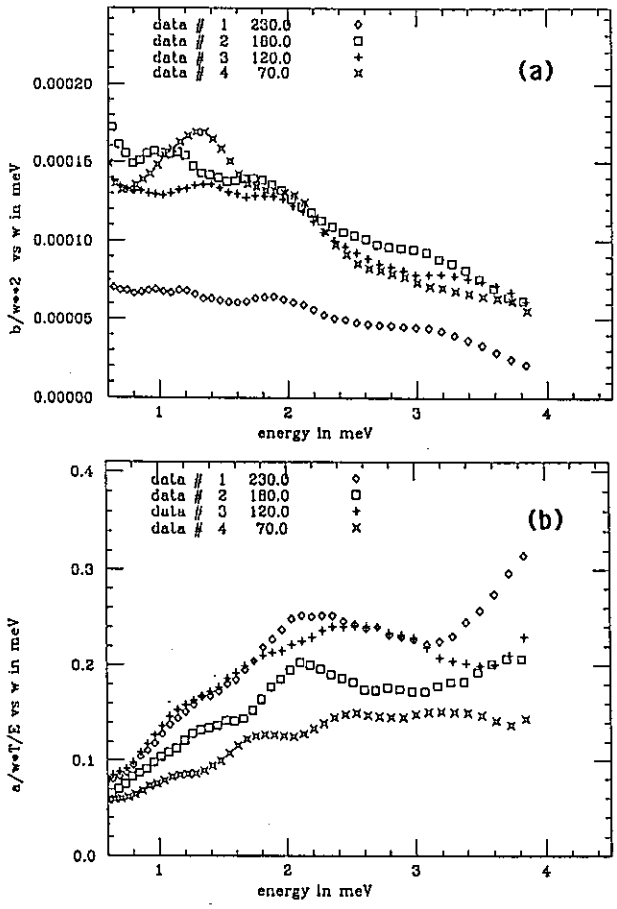

Fig. 3 Separated phonon part (a) and phonon-assisted migration part (b)

References

1) S. Kelham and H. M. Rosenberg, J. Phys . C. 14 (1981) 1737
2) M. P. Zaitlin and A. C. Anderson, Phys. Rev. B, 12 (1975) 4475
3) R. C. Zeller and R. O. Pohl, Phys. Rev. B 4 (1971) 2029
4) W. A. Philips, J. Low Temp. Phys. 7 (1972) 351
5) P. W. Anderson, B. I. Halperin and C. M. Varma, Phil. Mag. 25(1972) 1
6) S. Anderson and R. Orbach, J. de Phys. (Paris) Lett. 43 (1982) L-625
7) S. Alexander, C. Laermans, R. Orbach and H. M. Rosenberg, Phys. Rev. B 28 (1983) 4615
8) P. H. Tua, S. J. Putterman and R. Orbach, Phys. Lett. 98A (1983) 357
9) A. J. Leadbetter and D. Litchinsky, Discuss. Faraday Soc. 50 (1970) 62
10) H. M. Rosenberg, Phys. Rev. Lett. 54 (1985) 704

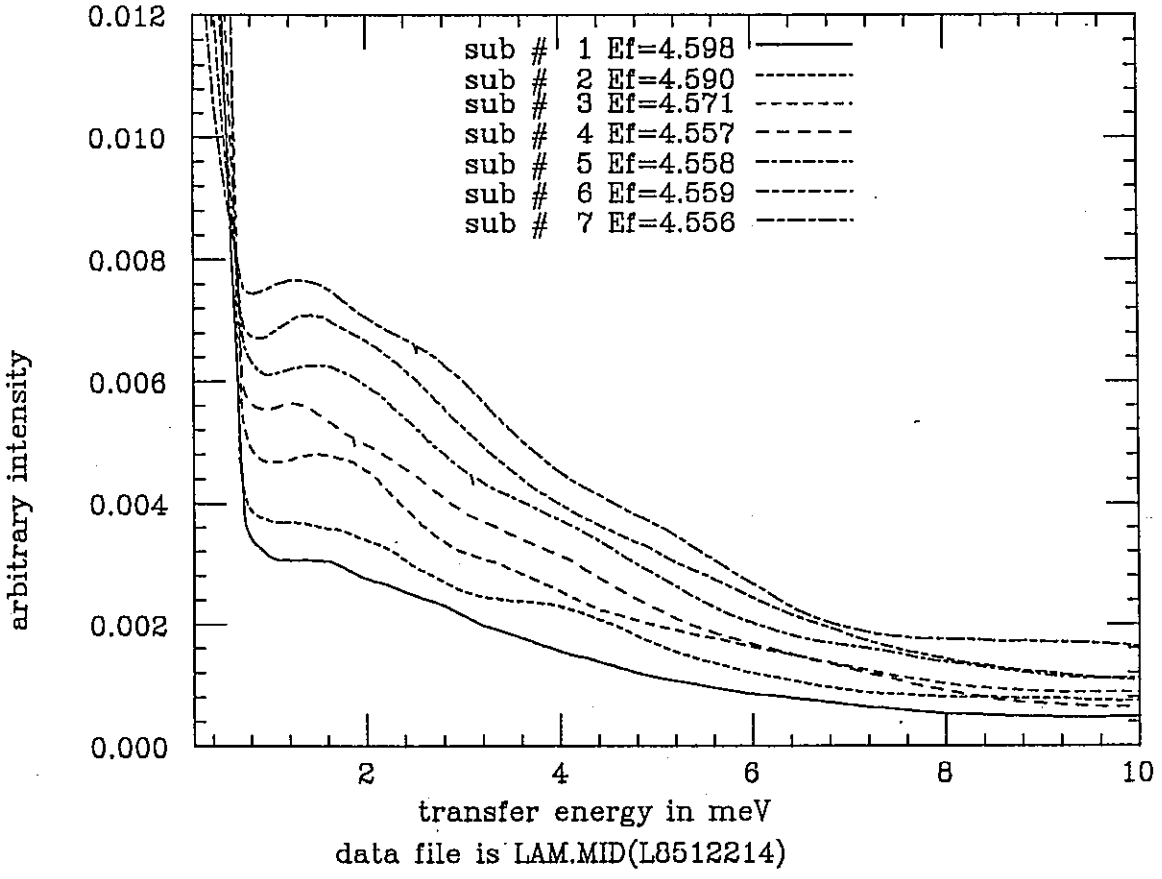

Fig. 1 S(q,w) measured at 180K

Low Energy Excitations in Semicristalline and Crystalline Polyethylenes and in Amorphous and Semicrystalline Polystyrenes

Toshiji KANAYA,[a] Susumu IKEDA,[b] Keisuke KAJI,[a]
and Kazuhiko INOUE [c]

a) Institute for Chemical Research, Kyoto University, Kyoto 611, Japan
b) National Labolatory for Hight Energy Physics, Oho-cho, Tsukuba-gun, Ibaraki-ken 305, Japan
c) Department of Nuclear Engineering, Hokkaido University, Sapporo 060, Japan

Low energy excitations in semicrystalline and crystalline polyethylenes and in amorphous and semicrystalline polystyrenes have been investigated by neutron inelastic scattering in the energy range below 10 meV at 10 K. Neutron scattering measurements were carried out with the time-of-flight (TOF) spectrometer LAM-40 installed at KENS. The Q-range covered by this spectrometer is 0.2-2.7 A^{-1} and the energy resolution is ca. 100 μeV. The degree of crystalinity of the semicrystalline polyethylene used in this study is less than 44 %. The crystalline polyethylene has a degree of crystalinity of more than 96 % which was confirmed by the broad line NMR spectroscopy. The amorphous and semicrystalline polystyrenes are atactic and isotactic, respectively. The former is commercially available and the latter was synthesized by the anionic polymerization method using the Ziegler-Natta catalysis and the degree of crystalinity is ca. 50%.

Fig. 1 shows the observed TOF spectra of the semicrystalline and crystalline polyethylenes. An anomalous broad peak is observed at ca. 2.5 meV in the spectrum of the semicrystalline polyethylene. The shape of the spectra dose not depend on Q. This phenomenon is observed in a number of disordered materials, such as rubbers and amorphous polymers at low temperatures below ca. 100 K,[1),2)] cross-linked polymers at room temperatures,[3),4)] and inorganic glass[5)]. On the other hand, the crystalline polyethylene shows no such broad peaks. Therefore, we conclude that the anormalous broad peak is characteristic to the amorphous polymers. Both the amorphous and semicrystalline polystyrenes also show

such peaks in the TOF spectra (Fig. 2). The peak for the amorphous polystyrene is slightly higher in energy and lower in intensity than that of the semicrystalline one. This may be due to the difference of the degree of crystalinity between the amorphous and semicrystalline polystyrenes.

The amplitude weighted density of states was calculated from the observed TOF spectra using the following equation.

$$\frac{d^2\sigma_{inc}}{d\Omega dE} = \frac{k'}{k} \left(\langle b^2\rangle - \langle b\rangle^2\right) \frac{Q^2}{2M} (n_s+1)\, e^{-2W}\, N\, \frac{g(\omega)}{\omega} \qquad (1)$$

where k and k' are the wave vectors of the incident and scattered neutrons, respectively. b is the scattering length of the hydrogen atom, M its mass, n_s+1 the Bose-Einstein population factor, and e^{-2W} the Debye-Waller factor. In this calculation, the spectra were normalized by the total scattering intensity and the energy range for the calculation was limited above 0.5 meV to avoide the contamination from the tail of the elastic peak. In Fig. 3, $g(\omega)/\omega^2$ is plotted for the semicrystalline and crystalline polyethylenes. It was found that the density of states $g(\omega)$ for the crystalline polyethylene (Fig. 3(b)) is proportional to the square of the energy transfer $\hbar\omega$. This means that $g(\omega)$ of the crystalline polyethylene can be described by the Debye theory. On the other hand, $g(\omega)$ of the semicrystalline polyethylene has the excess excitations compared with that of the crystalline one. This phenomenon is strongly related with the characteristic feature of specific heat of amorphous materials.[6] Then, we calculated specific heat C_v for the both polyethylenes and plotted C_v/T^3 as a function of temperature in Fig. 4. The semicrystalline polyethylene shows the excess specific heat compared with the crystalline one and the peak appears at ca. 6 K in C_v/T^3 vs. T.

1) T. Kanaya et al., in this report.
2) K. Inoue et al., in this report.
3) T. Kanaya et al., in this report.
4) M. Arai, in this report.
5) M. Misawa, in this report.
6) "Amorphous Solids - Low Temperature Properties", (Topics in Current Physics 24), ed. W. A. Phillips, Springer Verlag Berlin, 1981.

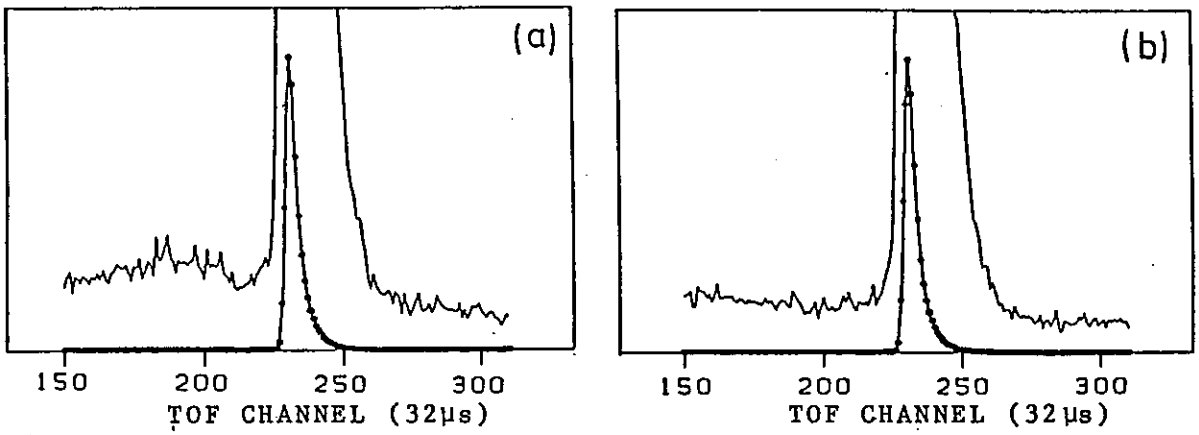

FIg. 1. TOF spectra of semicrystalline (a) and crystalline (b) polyethylenes measured by LAM-40 at 10 K (Q=2.3 A^{-1}). Upper curves are expamded ones by a factor 99.

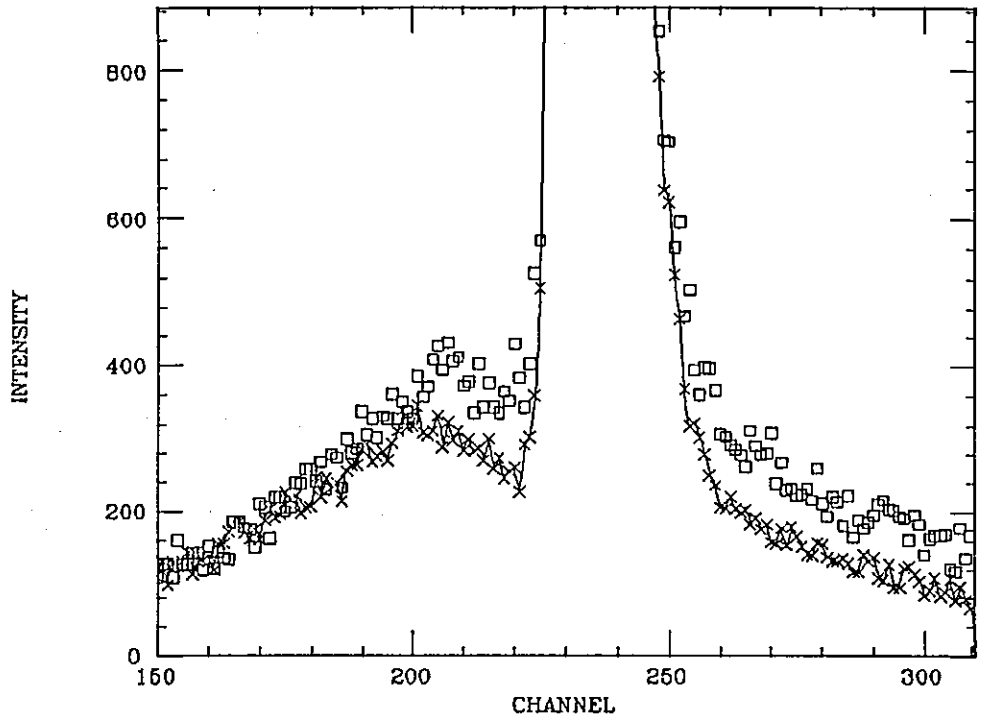

Fig. 2. TOF spectra of amorphous and semicrystalline polystyrenes measured by LAM-40 at 10 K (Q=2.1 A^{-1}). (X): amorphous polystyrene. (□): semicrystalline polystyrene.

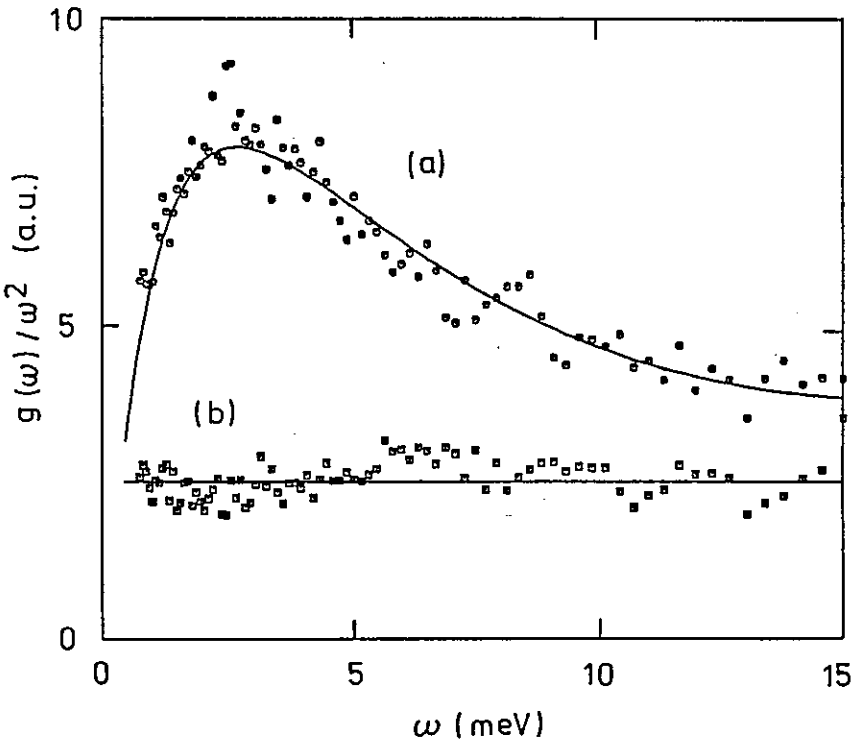

Fig. 3. Calculated density of states of semicrystalline (a) and crystalline (b) polyethylenes at 10 K ($Q=2.3\ A^{-1}$). In the figure, $g(\omega)/\omega^2$ is plotted against ω.

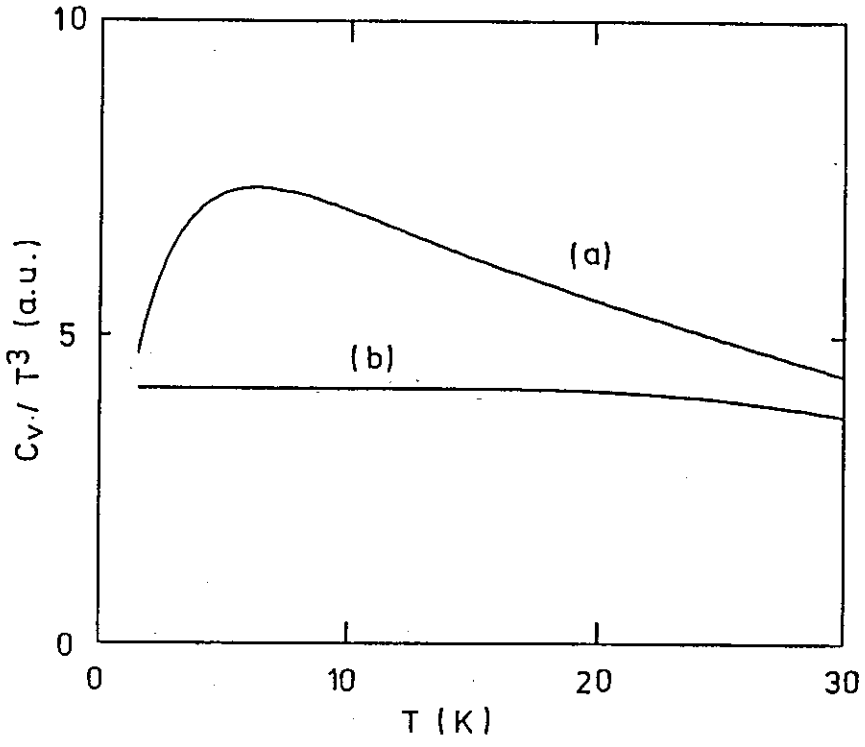

Fig. 4. Specific heat C_v calculated from the density of states in Fig. 3 for semicrystalline (a) and crystalline (b) polyethylenes. In the figure, C_v/T^3 is plotted against T.

Phonons in Layered Semiconductor InSe

Kazuaki Imai and Yutaka Abe*

Department of Electronic Engineering, Hokkaido Institute of Technology, 006 Sapporo

*Department of Nuclear Engineering, Hokkaido University, 060 Sapporo

InSe is one of III-VI layered-type compound semiconductors. The layer consists of four-fold sheet of Se/In/In/Se with rigid bonds, and the inter-layer bondings are those of weak van der Waals type. Special features of the lattice dynamics of these layer compounds are mainly related to the anisotropy in the interatomic forces.

The purpose of our experiments in KEK is to investigate the phonon distribution function and the anisotropic phonon dispersion in InSe, and this paper reports the result of our first attempt of neutron scattering experiment in InSe using LAM-D spectrometer.

At first, in order to obtain global features of the neutron scattering in our specimens, rather than detailed quantitative investigation, we used the powder of InSe , which has been annealed at 470 C for 3 days in order to reduce the large strain introduced during the pulverizing process.

Fig. 1. is the primary experimental result of the neutron scattering in powdered InSe. Four inelastic peaks, 10, 50, 70, and 200 cm^{-1}, were observed.

In powdered InSe, the premitive cell includes two layers, and it is considerd that the low frequency peak around 10 cm^{-1} is due to the E-mode acoustic phonons. Actually, the folded acoustic E branch has been observed at 16 cm^{-1} in the Raman scattering experiment[1]. The broad peak around 50 cm^{-1} might be due to the low-energy optical phonons, but its half width is too large to assign the detailed phonon structure.

There exist large background noise in the scattering spectrum, which indicates further improvement is necessary for the reduction of the background noise.

We have succeeded to grow a large single crystal of InSe in our laboratory using the non-stoichiometric Bridgeman method[2]. We are now trying to find the optimum conditions for the neutron scattering experiments with InSe.

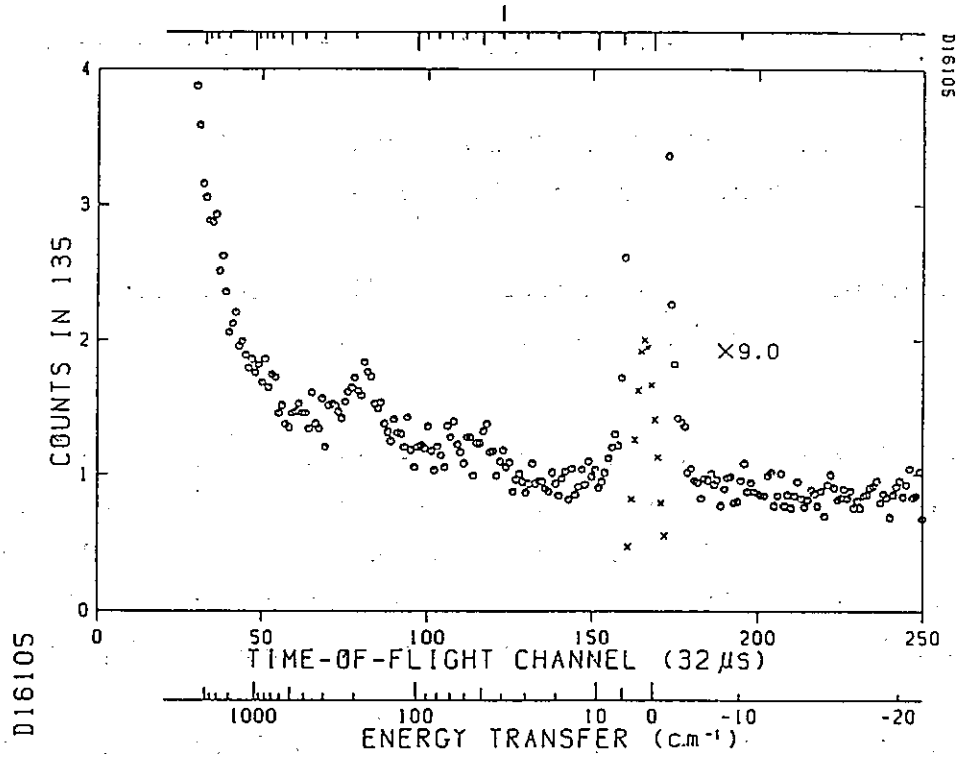

Fig. 1. Spectrum of neutron scattering in powdered InSe.

The experiments on cooled specimen will be one of the possible break-through for the further proceeding of our subject.

We would like to express our gratitude to Prof. K. Inoue and Dr. Nishida for their kind support for the present experiment.

References

1) N. Kuroda and Y. Nishina, Solid State Commun. 28 (1978) 439.
C. Carlone, S. Jandle and H. R. Shanks, phys. stat. sol.(b) 103 (1981) 123.
2) K. Imai, K. Suzuki, T.Haga. Y. Hasegawa and Y. Abe, J. Cryst. Growth 54 (1981) 501.

On Computer Code, Pulse Performance and Improvement of Instrument in LAM-80

Kazuhiko INOUE, Koji NISHIDA, Hirokatsu IWASA,
Takashi AKABA and Fujio HIRAGA

Depertment of Nuclear Engineering, Hokkaido University,
Sapporo, 060 Hokkaido, Japan

The LAM-80 is a high resolution time-of-flight analyser type spectrometer having the special feature of a wide energy window[1]. To utilize thoroughly the features of the instrument we devised computer codes for data analysis, performed detailed measurement of pulse structure of cold neutrons from the pulsed cold source via guide tube and conducted some improvement of device.

The measured spectrum is compared with calculated one in the data analysis by using QUESA80 code. The time-of-flight spectrum of scattered neutrons is actually expressed as a form of double integrals with respect to the incident and scattered neutron energies, E_1 and E_2. In QUESA80 code, however, integration for the time-of-flight spectrum, $\eta(t,\theta)$, is simply performed as follows

$$\eta(t,\theta)=\text{const.}\int Y(t,\epsilon)\ S(Q^*,\epsilon)d\epsilon\,, \tag{1}$$

where $S(Q^*,\epsilon)$ is the scattering function, $\epsilon=E_1-E_2$, t is the neutron flight time, Q^* is the average scattering vector and $Y(t,\epsilon)$ is the effective resolution function given by

$$Y(t,\epsilon)=\int \Phi(E_2+\epsilon, t-\frac{l_2}{\sqrt{2E_2/m}})(\frac{E_2}{E_2+\epsilon})^{1/2} R(E_2)dE_2\,. \tag{2}$$

Here $\Phi(E,t)$ is the neutron flux as a function of energy and time when the neutoron with energy E impinges on the sample at the time t and R(E) is the resolution of analyser.

For data analysis of quasielastic scattering, it is essential that multiple scattering corrections be assesed as accurately as possible by considering energy transfer and angular dependency. CYSMUS and K2 codes were written for the multiple scattering calculations. Details of the data

analysis method for the LAM-80 are described in other reports[2-4].

Information about neutron pulse structure is necessary to calculate the effective resolution function, $Y(t,\epsilon)$. Figure 1 shows a preliminary data of pulse structure of cold neutrons from pulsed source at the outlet of 30 m guide tube. Figure 2 depicts the spectrum from vanadium and it is used to confirm the acculacy of the calculated effective resolution function in the case of $\epsilon=0$. As seen from Eqs. (1) and (2), $Y(t,0)$ has a pulse shape which equals exactly to the one of elastically scattered neutrons.

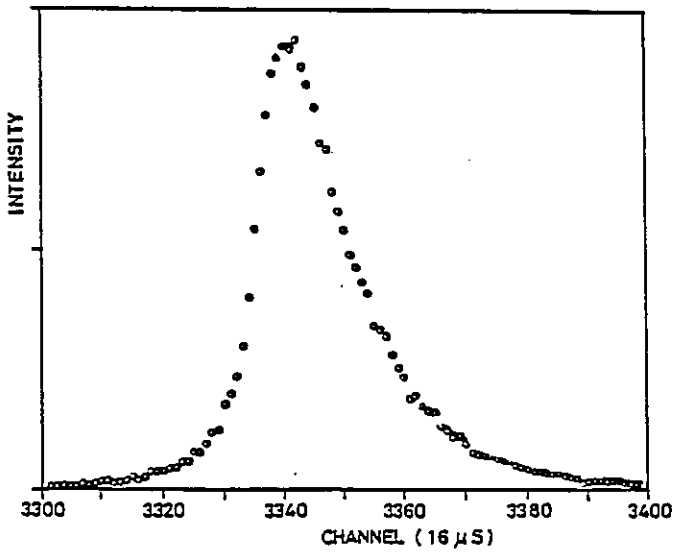

Figure 1 Pulse structure at the place of LAM-80.

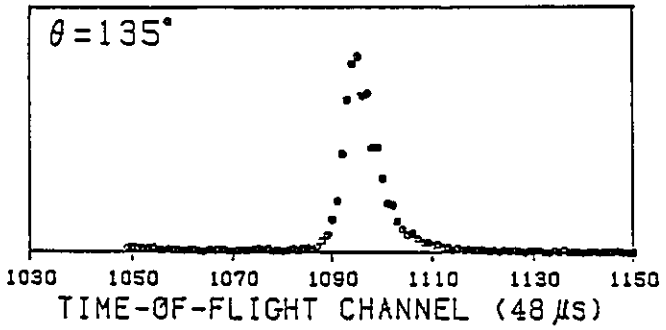

Figure 2 Scattered spectrum from vanadium.

Four analyser mirrors were housed in an evacuated container, which is capable of rotating so that the scattering angle can be changed. But the region of scattering angles were somewhat restricted. From the experiences during the period of operations up to now, we felt the necessity of measurements for various scattering angles which might be settled freely and have small intervals. Then we decided to improve the evacuated container, the turntable and collimaters. The configulation of the new LAM-80 is illustrated in Figure 3. The scattering angles can be selected freely from 10° to

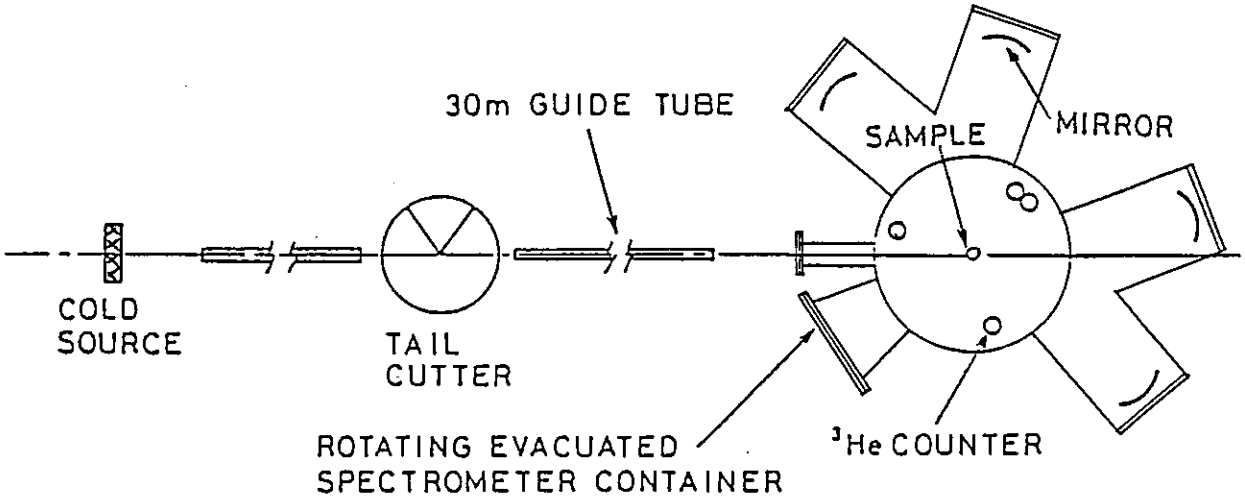

Figure 3 Layout of the LAM-80.

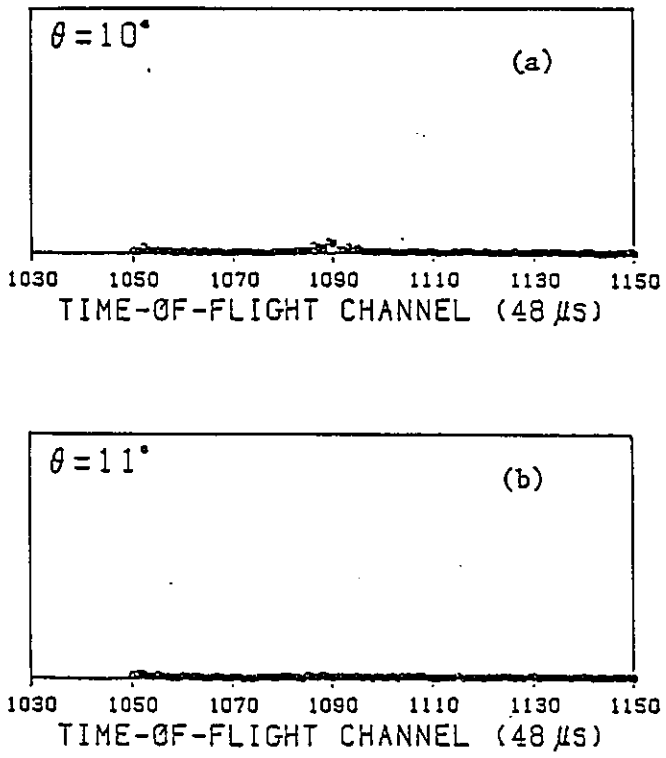

Figure 4 (a) Observed background spectrum at scattering angle of 10° (b) Observed background spectrum at scattering angle of 11°.

135°, and S/N ratio is improved.

The choice of lowest scattering angle is restricted by the spurious neutrons scattered from the structure of analyser mirror and the cadmium inner shield. Figure 4(a) illustrates background spectrum at scattering angle of 10°. As seen in the figure there is a spurious peak. A background

spectrum at scattering angle of 11° is shown in Figure 4(b) and then there is not any spurious signals. The spurious neutrons at scattering angle of 10° is completely removed by adopting screen and improved collimater. But the scattering angles smaller than 10° are not feasible.

References

1) K. Inoue et al., Nucl. Instr. and Meth., A238(1985) 401.
2) K. Inoue, Bull. Facul. Eng. Hokkaido Univ. 98(1980)77.
3) K. Inoue, Bull. Facul. Eng. Hokkaido Univ. 112(1983)83.
4) K. Inoue, Bull. Facul. Eng. Hokkaido Univ. 124(1985)49.

The Investigation of Hydrogen Diffusion in V with Interstitial Traps by Quasielastic Neutron Scattering

Yasuaki SUGIZAKI, Sadae YAMAGUCHI and Kazuhiko INOUE*

Department of Nuclear Engineering, Tohoku Univ., Sendai 980
*Department of Nuclear Engineering, Hokkaido Univ., Sapporo 060

Numerous investigations have been demonstrated that the hydrogen solubility in transition metals and its self-diffusion constant are strongly change by the presence of small amounts of interstitial impurities. These observations can be naturally explained by the assumption that impurities act as trapping centers for the dissolved hydrogen. The influence of traps is of great technological importance for all problems where hydrogen solubility or hydrogen diffusion play a role, e.g. hydrogen embrittlement, hydrogen strage, or fusion reactor wall design. Here we report investigations of the diffusion of hydrogen in vanadium with oxygen interstitials by quasielastic neutron scattering. The aim of the investigation is an atomistic understanding of the trapping and its influence on diffusion.

The quasielastic neutron scattering experiments were performed on three different powder samples, namely (I) $VO_{0.02}H_{0.02}$, (II) $VO_{0.04}H_{0.03}$ and (III) $VH_{0.03}$. They were prepared by the reaction between vanadium metals with or without oxygen impurities and hydrogen gas in a Sievert's type apparatus. In order to perform reliable background substraction, identical samples without hydrogen loading were prepared. The quasielastic neutron scattering spectra were measured by the LAM-40 spectrometer in the wave number range $0.2 < Q < 2.5\ A^{-1}$. The spectra of sample (I) were measured for temperatures between 293 and 473K.

Figure 1 shows quasielastic spectra of $VO_{0.04}H_{0.03}$ and $VH_{0.03}$ samples. The spectrrum of $VO_{0.04}H_{0.03}$ consists of a broad and a narrow quasielastic compornent. We interpreted the scattering data, therefore, by a two step diffusion model[1]; the hydrogen atoms can be trapped with a mean trapping time τ_o in the vicinity of the impurity, while the mean time between trapping event is denoted by τ_1. The scattering function $S(Q,\omega)$ for the two step diffusion model can be calculated in terms of the self-correlation function of the "trapped state" and of the "freely diffusing state". This yields:

$$S(Q,\omega) = A\frac{\Gamma_1/\pi}{\Gamma_1^2+\omega^2} + (1-A)\frac{\Gamma_2/\pi}{\Gamma_2^2+\omega^2} \qquad (1)$$

where Γ_1, Γ_2 and A, (1-A) is the widths and the weights of the two components in the quasielastic spectrum, respectively. Obviously, $S(Q,\omega)$ is a superposition of two Lorentzian-shaped components and their intensities are related to the thermal population of the two possible "states" of the diffusing hydrogen.

We analyzed the scattering data by using a statistical data analysis technique developed by Inoue[2]. This technique consist of procedures for curve fitting of the spectra and hypothesis testing of the scattering model. An example of the analysis is shown in Fig. 1 as the solid lines. The experimental data can be fitted well to the superposition of two Lorenzian-shaped components.

Figure 2 present the measured Q-dependence of the half-width of the broad and narrow components in the quasielastic spectrum for $VO_{0.04}H_{0.03}$. The Q-dependence for $VH_{0.03}$ is also exhibited in the figure for comparison. Detailed analysis of the data at elevated temperature are now in progress. The preliminary results for two representative temperatures are shown in Table 1.

Table 1

Specimen	Temp.	$1/\tau_o(\mathrm{sec}^{-1})$	$1/\tau_1(\mathrm{sec}^{-1})$
$VO_{0.04}H_{0.03}$	293 K	10.1×10^{10}	8.20×10^{10}
$VO_{0.04}H_{0.03}$	433 K	40.6×10^{10}	12.3×10^{10}

From the quasielastic width at small Q, the effective diffusion constant D_{eff} was determined from the relation: $\Gamma_{broad} = D_{eff}Q^2$ which can be written as

$$D_{eff} = 4.7\times10^{-4}\exp(-70\ \mathrm{meV}/k_BT).$$

Obviously the observed D_{eff} is smaller than the self-diffusion coefficient in the undisterbed lattice.

References

1) D. Richter and T. Springer: Phys. Rev., 18B (1978) 126.

2) K. Inoue: Bull. of Faculty of Engrg. Hokkaido University, 112 (1983) 83.

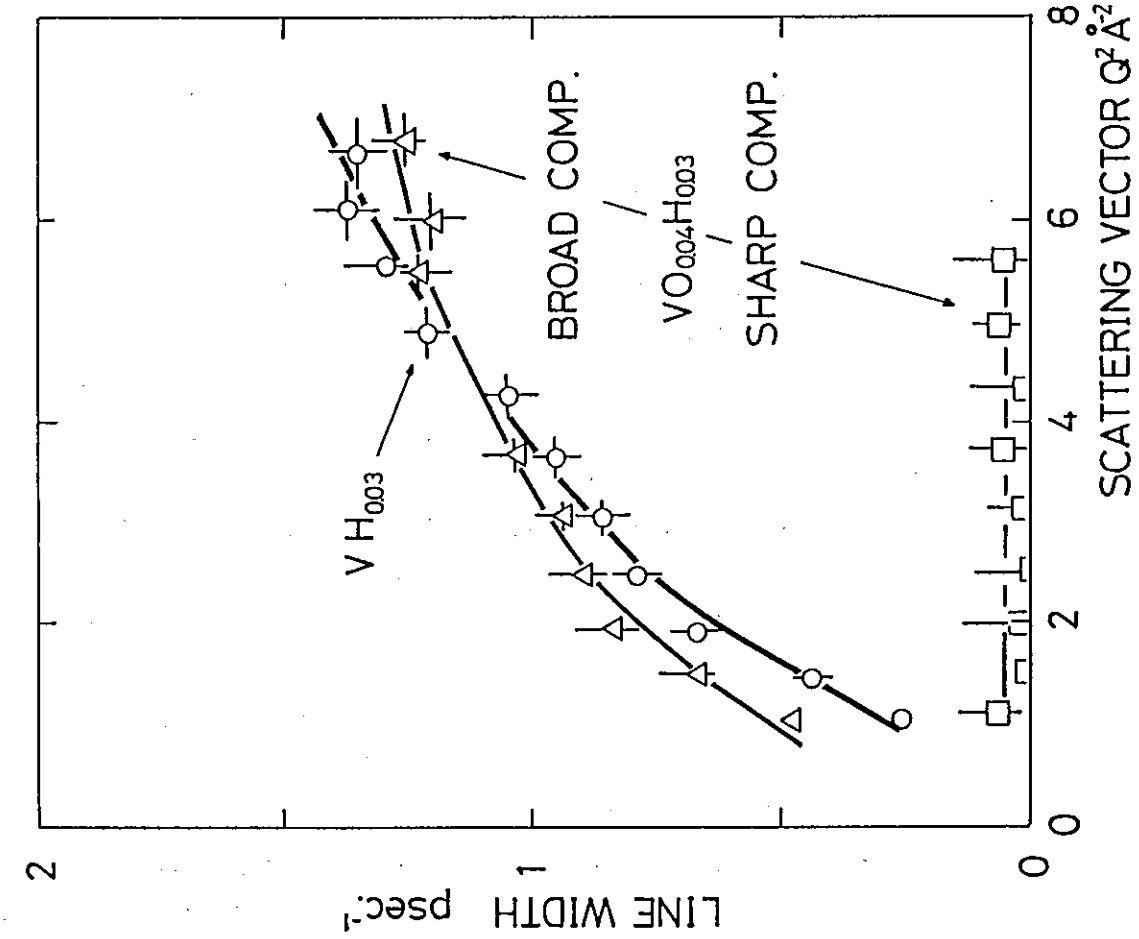

Fig. 2 Effective width of the measured quasielastic spectrum as a function of scattering vector Q.

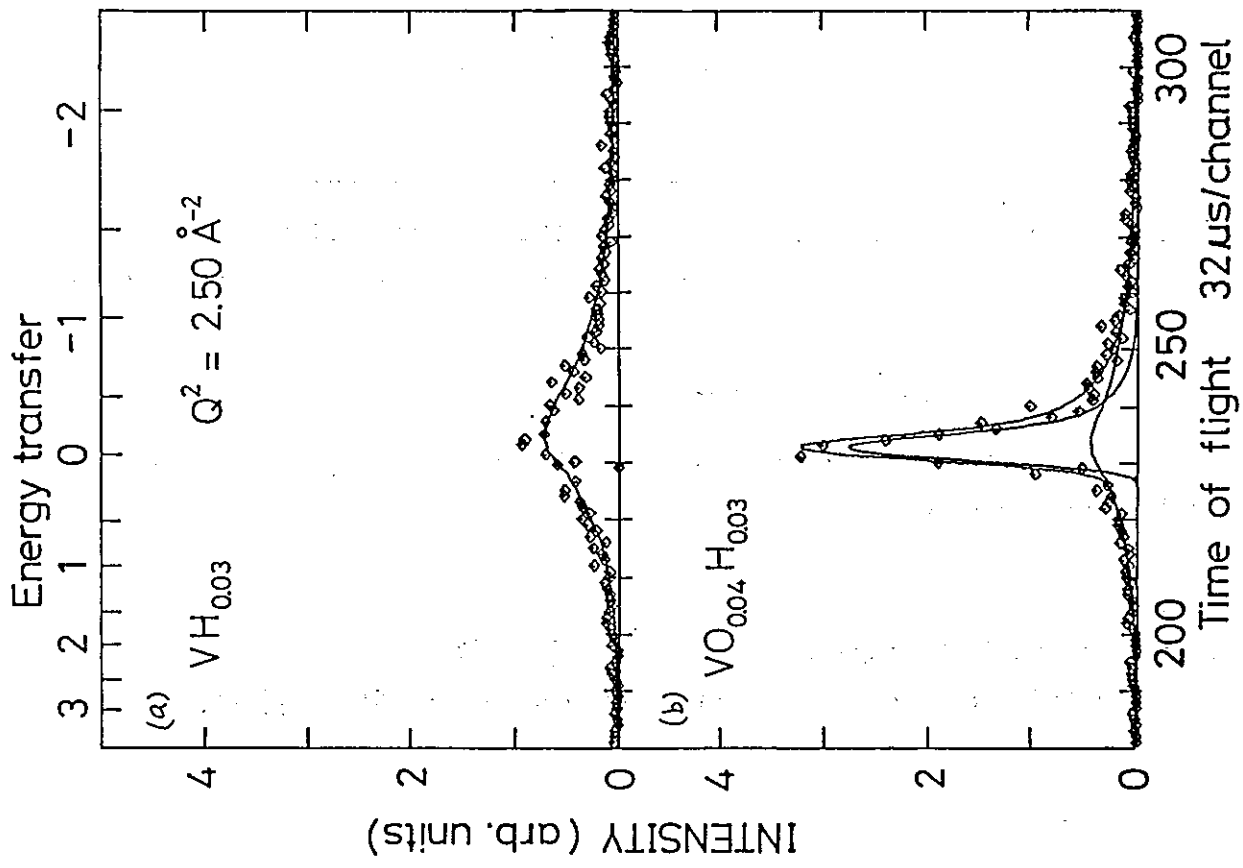

Fig. 1 Quasielastic neutron scattering data of $VH_{0.03}$ and $VO_{0.04}H_{0.03}$.

Quasielastic and Inelastic Scattering by Hydrogen in the Ternary Alloy $V_xNb_{1-x}H_{0.2}$

C.-K. Loong*
National Laboratory for High Energy Physics
Oho-machi, Tsukuba-gun, Ibaraki-ken, 305, Japan

K. Inoue
Department of Nuclear Engineering
Hokkaido University, Sapporo, 060 Hokkaido, Japan

D. Robinson, C. Stassis, and D. T. Peterson
Ames Laboratory-U. S. DOE, and Departments of Physics
and Materials Science and Engineering
Iowa State University, Ames, IA 50011, U. S. A.

The terminal solubility of hydrogen (TSH) in a metal is often found to increase substantially by alloying with another metal solute. In particular, TSH is increased by a factor of three from the pure metal value by the addition of 10 at. % niobium or vanadium. In V_xNb_{1-x} ($0.25 < x < 0.75$) TSH above room temperature is too high to be measured accurately. Although phenomenological models have been proposed by several authors[1-3] to explain these effects, the underlining physical principles are not well understood.

The diffusion of hydrogen in this alloy system is also quite interesting. Recently, measurements[4] of the spin-lattice relaxation times revealed that there may exist different types of hydrogen motion in these alloys depending on the composition. On the other hand, it is surprising to find that H diffusion in this system appeared to behave as a thermally activated process with a single activation energy as

* Permanent address: Argonne National Laboratory, Argonne, IL 60439 U. S. A.

indicated by Arrhenius behavior[3]. Measurements by neutron scattering would, in principle, provide more physical insight into the dynamics of hydrogen in these materials.

We have studied the motion of hydrogen in the alloy system $V_xNb_{1-x}H_y$ (x = 0.1, 0.25, 0.5, 0.75, 0.9; y = 0.2) at ambient and elevated (200° C) temperatures by neutron scattering techniques (see Table I). The acoustic phonons and the local mode vibrations (optical phonons) of hydrogen were investigated by inelastic experiments performed on the LAM-D Crystal-Analyzer Spectrometer. We find (see Fig. 1) an acoustic phonon band below 25 meV characteristic of the host lattice vibrations. The local modes center at energies of about 50, 100 and 140 meV. The large widths associated with the local modes are indicative of a hydrogen potential influenced by a random distribution of surrounding V and Nb atoms.

The diffusion of hydrogen in these alloys was studied by measurements of the quasielastic spectra on the LAM-40 and LAM-80 Spectrometers. We find that the widths of the quasielastic peaks in the intermediate composition range, $0.25 < x < 0.75$, differ significantly from those in either the vanadium-rich or niobium-rich composition (see Fig. 2). The detailed shapes of the spectra are complex probably due to some intriguing diffusion mechanisms. In many cases experimental data can be fitted satisfactorily by a scattering function which consists of two Lorentzians. Detailed data analysis are presently in progress.

References:

1. T. Matsumoto, Y. Sasaki and M. Hihara, J. Phys. Chem. Solids, 36 (1975) 1361.
2. J. F. Miller and D. G. Westlake, Proceedings JIMIS-2, Hydrogen in Metals, p. 153.
3. H. Herro, Ph. D. Thesis, Iowa State University (unpublished).
4. L. Lichty, J. Shinar, R. G. Barnes, D. R. Torgeson and D. T. Peterson, Phys. Rev. Lett. 26 (1985) 2895.

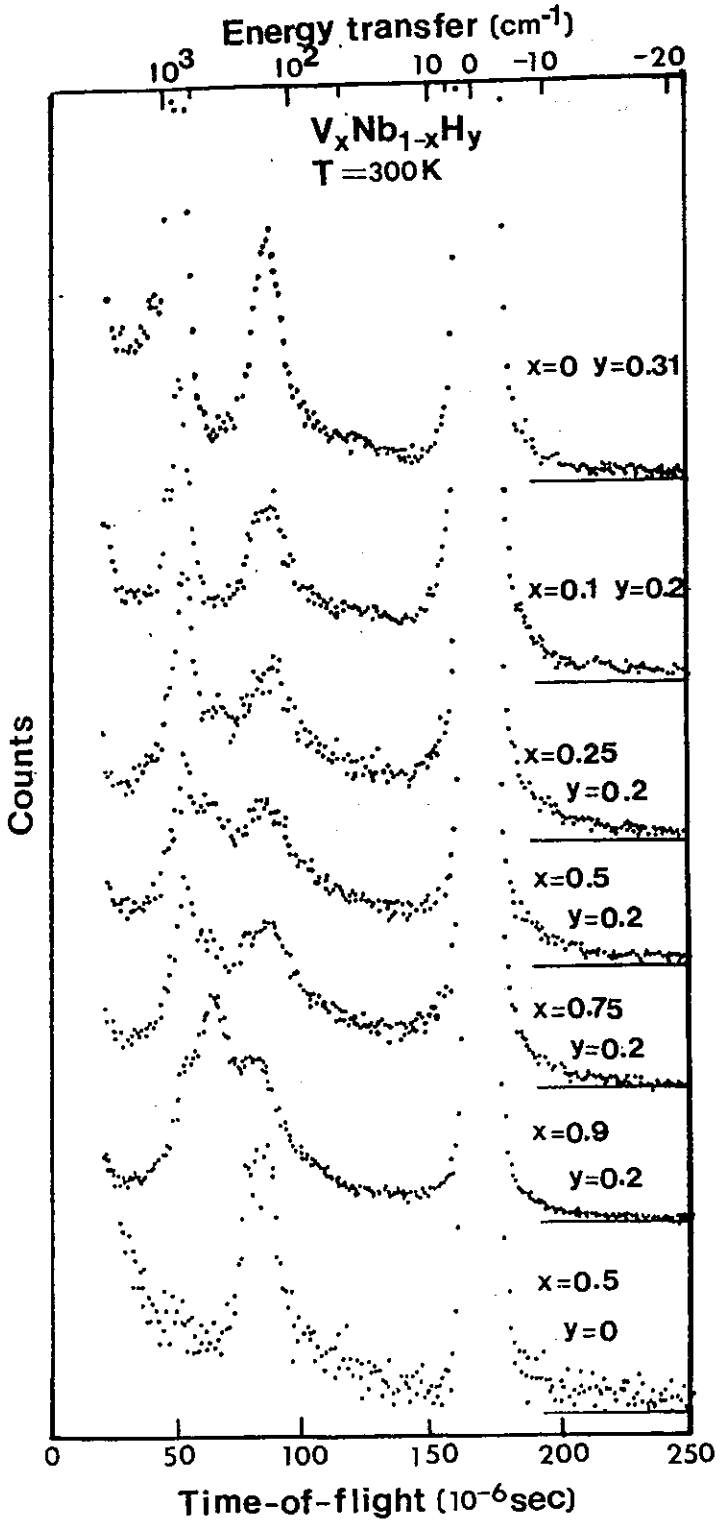

Figure 1.
Time-of-flight spectra of $V_xNb_{1-x}H_y$ alloys obtained by the LAM-D Crystal-Analyzer Spectrometer. Data have not been corrected for the energy dependence of incident neutron spectrum and detector efficiency. They all show an acoustic phonon band below 25 meV. The hydrides also show localized modes centered at about 50, 100 and 140 meV. They may correspond to the vibrations of hydrogen at an O-site and a T-site formed by V and Nb atoms respectively. Data for $NbH_{0.31}$ were obtained by Dr. Ikeda for a different experiment.

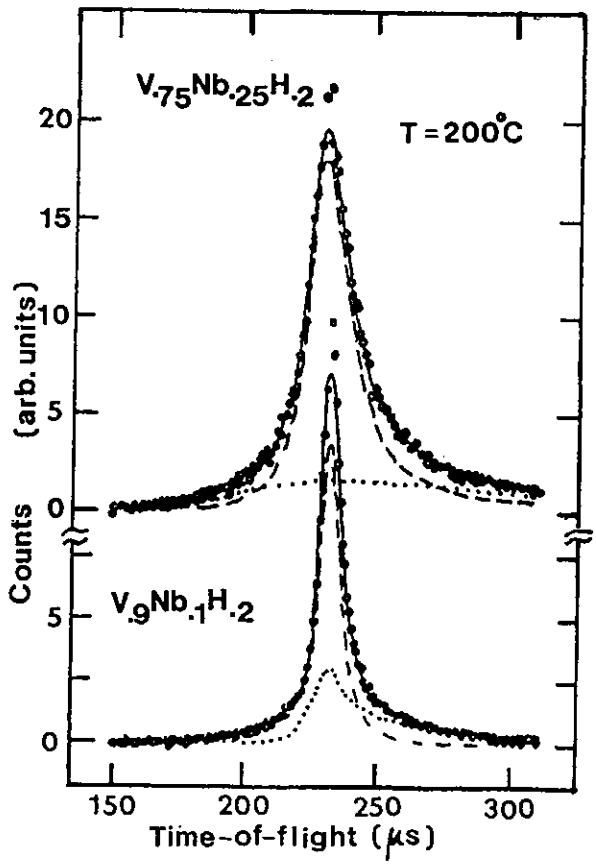

Figure 2. Examples of time-of-flight spectra for the $V_xNb_{1-x}H_{0.2}$ alloys. In many cases the experimental data (circles) can be fitted satisfactorily by a scattering function (solid lines) which consists of two Lorentzian functions (dashed and dotted lines).

LOCAL MODES AND HYDROGEN POTENTIALS IN METAL HYDRIDES

SUSUMU IKEDA AND NOBORU WATANABE

National Laboratory for High Energy Physics
Oho-machi, Tsukuba-gun, Ibaraki-ken, 305, Japan

In the previous papers[1,2] we determined the anharmonic parameter β to a decoupled oscillator approximation from the measured energy spectrum of TiH_2 , $NbH_{0.31}$, $TaH_{0.1}$ and $VH_{0.33}$ and classified their hydrogen potentials into three types. However this approximation was too simple to express an actual hydrogen potential. A more exact approach should be to describe the hydrogen motion as a three-dimentional anharmonic oscillator where the x-, y- and z-motions of the hydrogen are no longer decoupled. In terms of this realistic model we discuss the hydrogen potentials in typical metal hydrides of $NbH_{0.31}$ and $VH_{0.33}$ using the excitaion energies of the local-mode peaks which were measured by CAT spectrometer.[3] Hydrogen atoms in $NbH_{0.31}$ and $VH_{0.33}$ exist at T-site and O-site, respectively. (Figure 1 shows T-site and O-site) J. Eckert et al. introduced a novel Hamiltonian for the hydrogen motions in the T-site and discussed the anharmonic parameters.[4] Here, we added a $C_{6z}z^6$ term to their formulation in order to make a good representation of the z-dependence of the hydrogen potential; we tried to derive the hydrogen potential using the measured excitaion energies, including the higher orders. The Hamiltonian H can be described as

$$\begin{aligned} H &= H_0 + H_1 \ , \\ H_0 &= P^2/2m + m\omega_x^2 X^2/2 + m\omega_y^2 Y^2/2 + m\omega_z^2 Z^2/2 \ , \ and \\ H_1 &= eZ(X^2 - Y^2) + fX^2Y^2 + g(X^2 + Y^2)Z^2 + C_{4z}(X^4 + Y^4) \\ &\quad + C_{4z}Z^4 + C_{6z}Z^6 \ , \end{aligned} \tag{1}$$

where ω_x , ω_y and ω_z are the harmonic frequencies and $\omega_x = \omega_y$ is satisfied for the T-site. It is straight forward to calculate the excitation energy ϵ (lmn) = E(lmn)

- E(000), where E(lmn) is the purturbed energy of the vibrational state corresponding to the (lmn) harmonic level. The l, m and n are the quantum numbers for vibrational excitations in x-, y- and z-motions, respectively. We assumed the following three conditions regarding hydrogen potential V(x,y,z) and the occupation : (1) Hydrogen occupays only a T_1-site, (2) V(x, 0, 3.3/4) has a minimum at the T_2- and T_3-sites and (3) V(0,0,z) has a minimum at the T_1-site and a maximum at the O_1- and O_2-sites. The parameters in the hydrogen potential of $NbH_{0.31}$ were calculated using six experimental values of the excitation energies listed in Table I (with asterisks). These were assigned by the quantum numbers l, m and n in the last column. The calculated parameters of the hydrogen potential in $NbH_{0.31}$ at 30 K are listed in Table III. Measured excitation energies with no asterisks should be compared with the excitation energies ($l+m+n \leq 3$) calculated using the derived potential. The calculated values are listed in the second column of Table I. The agreements with the experimental values are fairly good. It is remarkable that the values of $\hbar\omega_x$ and $\hbar\omega_z$ are close to each other and are almost the same as those of TiH_2 and $ZrH_{1.43}$,[2] in which the hydrogen exists at the T-site of an fcc structure(see Table III). Figure 2 shows four contour maps of the derived hydrogen potential on the planes of y=0, 0.2, 0.4, 0.6 A. In the contour map of y=0, we can see the smallest minimum point at the T_1-site, two minimum points at T_2 and T_3 as apparent from the initial conditions, and two saddle points of about 400 meV around T_1. The smallest minimum point moves from the T_1-site to the left(-z-direction) with increasing y and settles on the plane for z=-0.825 A when y becomes about 0.4 A.

The wave functions ψ_{lmn} were expressed by linear combinations of the harmonic wave function Ψ_{lmn}; their coefficients were determined in this analysis as

$$\begin{aligned} \psi_{000} &\approx \Psi_{000} - 0.007(\Psi_{021} - \Psi_{201}) , \\ \psi_{001} &\approx \Psi_{001} - 0.02(\Psi_{200} - \Psi_{020}) - 0.01(\Psi_{022} - \Psi_{202}) , \qquad (2) \\ \text{and } \psi_{100} &\approx \Psi_{100} + 0.03\Psi_{301} - 0.007\Psi_{121} , \end{aligned}$$

where ψ_{000}, ψ_{001} and ψ_{100} are wave functions of the ground state, the lower first

excited state and the higher first excited state, respectively. ψ_{000} is almost the same as the harmonic wave function Ψ_{000} and is approximately isotropic since ω_x $(= \omega_y) \approx \omega_z$. ψ_{001} is porlarized only to the z-direction, while ψ_{100} is almost polarized along the x-direction with a small porlarization of z-direction (eq.(2)).

In the case of $VH_{0.33}$, we can put $\omega_x = \omega_y$ and $e = 0$ in eq.3 from the symmetry of the O-site. Similarly we calculated the parameters of the hydrogen potential of $VH_{0.33}$ (see Table III). The calculated values of the excitations energies are listed in the second column of Table II. The agreements with the experimental values are also good. Note that the value of $\hbar\omega_z$ is much different from that of $\hbar\omega_x$, contrary to the case of $NbH_{0.31}$. Correspondingly, the hydrogen potential and the ground-state wave function are highly anisotropic. Figure 3 shows contour maps of the derived hydrogen potential on the planes y=0 (Fig.3(a)) and z=0, 0.2, 0.27, 0.29 A (Fig.3(b)). The potential has a narrow bottom with a steep gradient in the z-direction, but a flat bottom with a modest slope in the x-y plane (note that the scale of z-axis in Fig.3(a) is enlarged by three times than that of x-axis). The characteristic feature of the potential shape in the present work is qualitatively consistent with the deuterium density distribution in $VD_{0.51}$ determined by a neutron diffraction.[5] The density distribution is localized in z-direction but expands in x- and y-directions with skirts covering the four neighbouring T-sites.[5] Contour lines above nearly 300 meV exhibit small depressions around x=0 (Fig.3(a)). The minimum point of the potential moves sensitively from O-site onto T-site with increasing z and settles on T-site when z becomes about 0.27 A. These results may correspond to the interpretation that hydrogen atoms in bcc metals tend to prefer O-sites to T-sites as the lattice parameter is reduced and, in particular, vanadium is the borderline in this respect.[6]

REFERENCES

(1) S.Ikeda and N.Watanabe, KENS-report-IV, KEK Internal 83-4(1983) 177

(2) S.Ikeda, N.Watanabe and K.Kai, Physica 120B, (1983) 131.

(3) S.Ikeda and N.Watanabe, J. Phys. Soc.Jpn., (1987) in press.

(4) J.Eckert, J.A.Goldstone, D.Tonks and D.Richter,
Phys. Rev. B27, (1983) 1980.

(5) M.Hirabayashi and H.Asano, Metal Hydrides, Ed. by G.Bambakids,
Plenum Press, N.Y., (1981) 53.

(6) H.Sugimoto and Y.Fukai, Phys. Rev. B22, (1981) 670.

Table I. Measuead and calculated values of local modes of $NbH_{0.31}$ (30 K).

Experimental value(meV)	Calculated value(meV)	Quantum numbers (lmn)
115*	115	(001)
160*	160	(100) (010)
220*	220	(002)
271*	271	(101) (011)
290	316	(003)
323*	323	(200) (020)
345*	345	(110)
400	372	(102) (012)
450	452	(111)
500	489	(300) (030)
500	508	(210) (120)

Table II. Measuead and calculated values of local modes of $VH_{0.33}$ (30 K).

Experimental value(meV)	Calculated value(meV)	Quantum numbers (lmn)
53.5*	53.5	(100) (010)
128*	128	(200) (020)
150*	150	(110)
220*	220	(001)
245	224	(210) (120)
245	223	(300) (030)
266*	266	(101) (011)
380	355	(111)
450*	450	(002)

Table III. Hydrogen potential parameters.

	$NbH_{0.31}$	$VH_{0.33}$	TiH_2	$ZrH_{1.43}$
$\hbar\omega_x(eV)$	0.147	0.0152	0.148	0.147
$\hbar\omega_z(eV)$	0.130	0.218	0.148	0.147
$e(eV/A^4)$	1.246			
$f(eV/A^4)$	30.77	0.565		
$g(eV/A^4)$	-4.23	-1.438		
$C_{4x}(eV/A^4)$	1.373	0.092		
$C_{4z}(eV/A^4)$	-3.807	9.032		
$C_{6z}(eV/A^6)$	2.272			

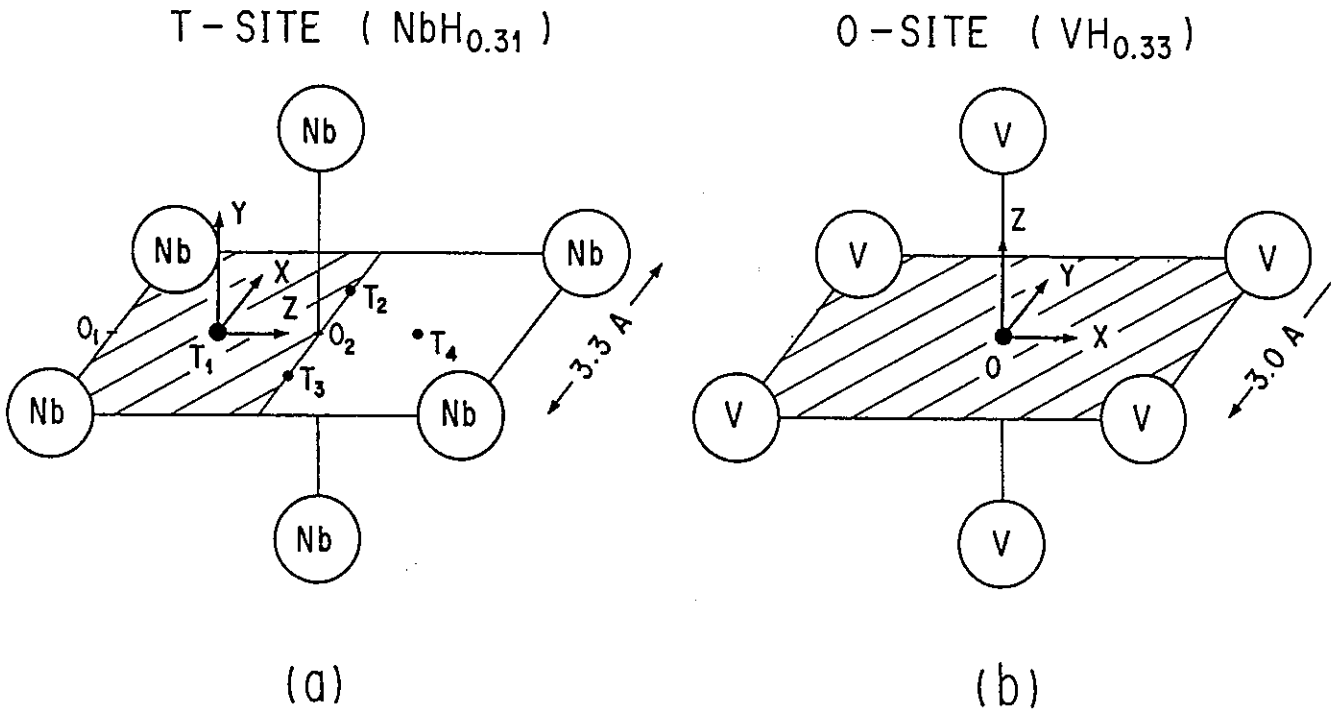

Fig. 1. T-site in $NbH_{0.31}$ (a) and O-site in $VH_{0.33}$ (b).

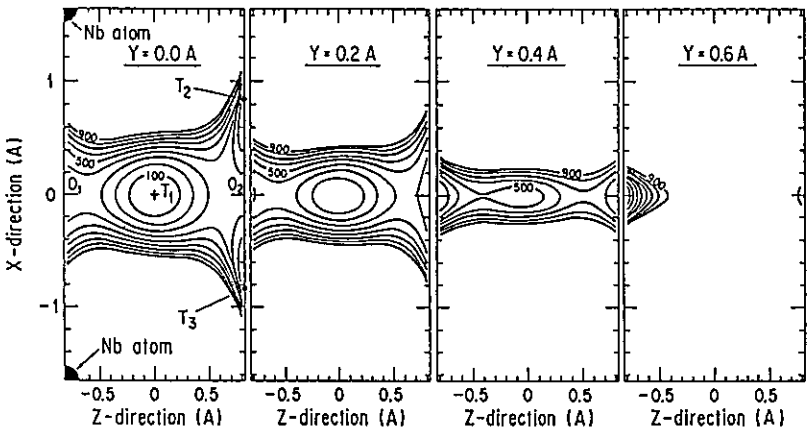

Fig. 2. Contour maps of the hydrogen potential in $NbH_{0.31}$.
Contour lines are 100, 200, 300, 400, 500, 600, 700, 800 and 900 meV.

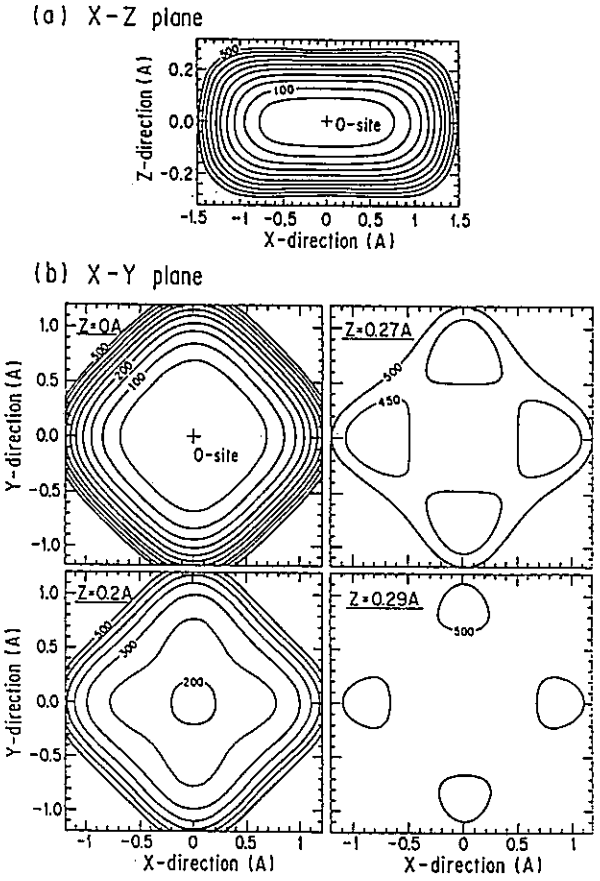

Fig. 3. Contour maps of the hydrogen potential in

Spin Waves in MnP Studied by MAX

Y.Todate , K.Tajima* , T.Miura* and Y.Ishikawa

Department of Physics, Tohoku University,
Sendai 980, Japan

* Department of Physics, Keio University,
Yokohama 223, Japan

The 3d intermetallic compound MnP is ferromagnetic between 291K and 47K and helimagnetic below 47K. Various experimental results such as the ratio of saturation moment to effective paramagnetic moment suggest that MnP exhibits the characteristics of an itinerant electron magnet. In order to investigate the origin of magnetism in MnP more detail the spin dynamics has been studied in wide Q,ω region.

The measurements of the spin-waves in MnP were carried out by MAX at 150K along three principal axes of the orthorhombic MnP structure ; the scans were performed parallel to the a,b-axis through (220) point and also to the c-axis through (022). Examples of neutron spectra obtained are shown in Fig.1(a) and (b). The spectra are converted to a momentum transfer scale. Note that each spectra has different energy transfer scale.

The increase in the neutron source intensity of KENS allowed us to insert the Sollar collimators in order to improve the resolution of the spectrometer. The resolution ($\delta E/E$) ,for example, of the detector of the scattering angle of 40° has been improved to be 0.18 at 20meV energy transfer which is compared with $\delta E/E$ of 0.24 without the collimator.

The spin-wave dispersion relations of MnP have been calculated assuming Heisenberg-type isotropic exchange interactions. Four nonequivarent Mn atoms are contained in a unit cell of the orthorhombic MnP structure. However, for simplicity, 2-sublattice model has been applied by neglecting a

small displacement (0.5%) of Mn atom along the b-axis. The dispersion relations of the 2-sublattice model are given as,

$$\hbar\omega(\mathbf{q}) = 2S(J(0)-J(\mathbf{q})) + 2SJ'(0) \pm |-2SJ'(\mathbf{q})|,$$

where $J'(\mathbf{q})$ is the interaction with different sublattice and the plus and minus sign corresponds to the optical and acoustic branch respectively.

The least squares fitting procedure of the dispersions with experimental results (including low energy transfer data[1),2)] taken by the triple-axis spectrometer TUNS installed at JRR-2) was performed under the condition that the weights were put heavily for lower energy transfer data. As has shown in Fig.2 the satisfactory agreement between experiments and the caluculation could not be obtained even though eighth nearest-neighbour exchange interaction parameters were took into account. The result suggest that the isotropic Heisenberg model is not adequate to the spin waves in MnP and that the itinerant character of d-electrons may be more important for understanding the magnetism of MnP.

References

1) K.Tajima, Y.Ishikawa and H.Obara: J.Magn. & Magn. Mater. 15-18(1980)373.

2) Y.Todate, K.Yamada, Y.Endoh and Y.Ishikawa: J.Phys.Soc.Jpn. (to be published).

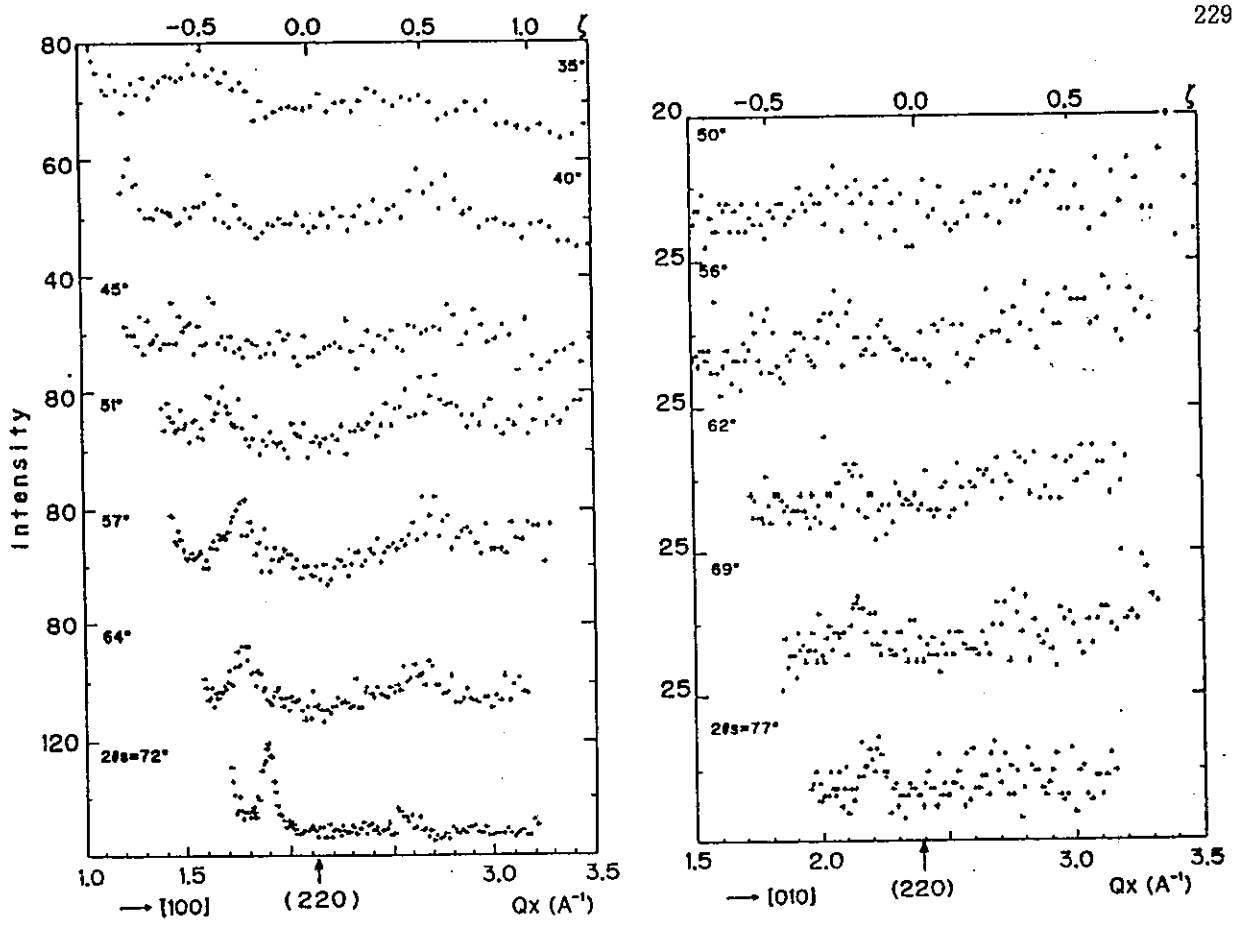

Fig.1 Inelastic neutron scattering spectra along (a) a^*-direction and (b) b^*-dirction.

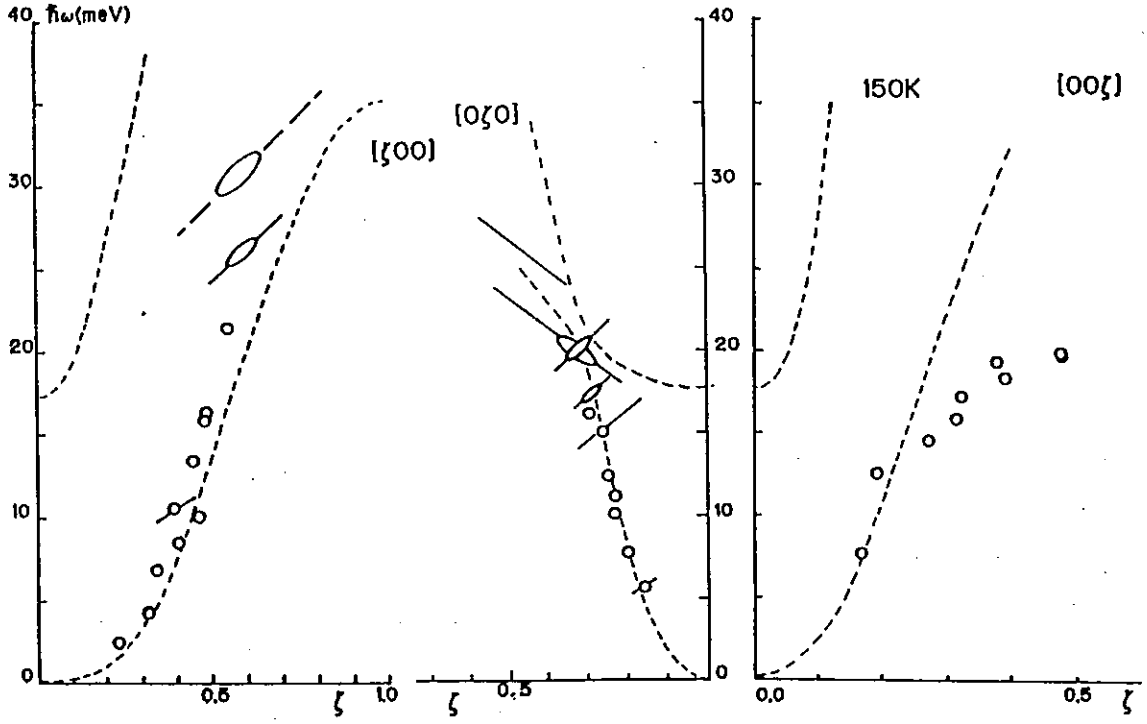

Fig.2 Measured and calculated (broken lines) spin wave dispersions in MnP.

Thermoreversible Gelation of the Polystyrene–Carbon Disulfide System. II. Neutron Quasielastic Scattering

Yoshinobu IZUMI, Yasuhiro MIYAKE, and Kazuhiko INOUE*

Department of Polymer Science, Faculty of Science,
*Department of Nuclear Engineering, Faculty of Engineering,
Hokkaido University, Sapporo 060

In a previous report[1], the dynamic behavior of the gelation of the atactic polystyrene (aPS)–carbon disulfide (CS_2) system has been examined by neutron quasielastic scattering (NQES) method. It was observed that the apparent diffusion coefficient diminished according to a power law $D_{app} \propto (T-t_G)^{0.9}$, where t_G is the temperature in which D_{app} is disappeared.

In the present study, further test of the validity of the above observation has been made by changing the polymer concentration, the sample thickness and using a high resolution quasielastic neutron spectrometer.

Fig. 1 shows the phase diagram of the aPS(MW=9000, M_w/M_n<1.06)–CS_2 system. Open circles denote the points measured by the conventional resolution spectrometer (LAM 40), filled circles denote points measured by the high resolution spectrometer, and half-filled circles denote points measured by two spectrometers. Broken line denotes the gelation curve estimated by Ferry–Eldrige equation based on the data points by Tan et al.[2] The point Q denotes the multicritical point.

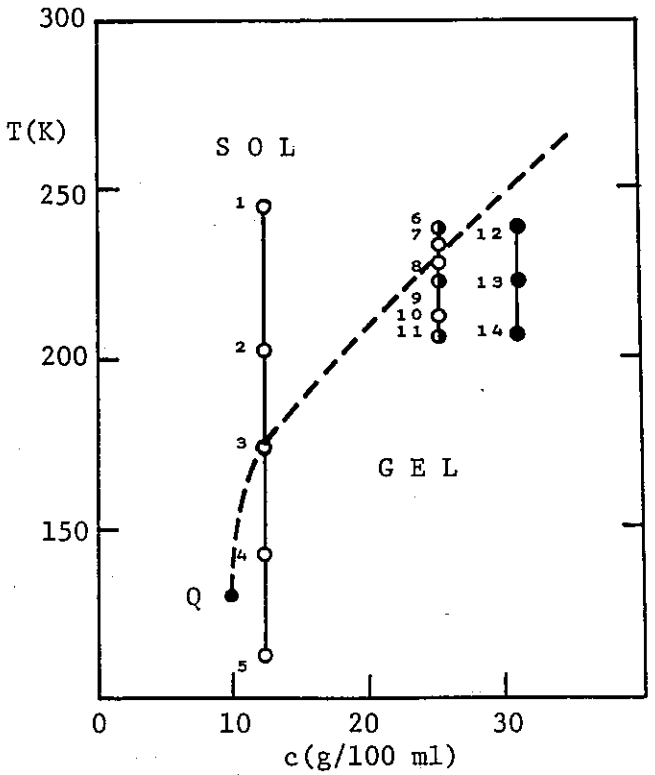

Fig. 1. Phase diagram of aPS(MW=9000, M_w/M_n<1.06)–CS_2 system.

Fig. 2 shows the temperature dependence of the time-of-flight spectra at two different concentrations. There is a distinct difference among these spectra. The spectrum in sol phase like No. 6 is a typical one for a diffusive mode, where the central peak exhibits a clear broadening as the

scattering angle increases. On the other hand, the diffusive mode rapidly decreases in gel phase, such as Nos. 11, 13 and 14.

Analyzing the whole spectra of energy spectrum of scattered neutron, the dynamic behavior of the gelation of polystyrene solution is studied. As we used CS_2 as the solvent, most part of the scattering intensity from the solution can be regarded as due to the proton incoherent scattering in polystyrene. The scattering law is then approximated using two Lorentzians,

$$S_{inc}(q,\omega) \propto \{\delta_d \Gamma_d(q)/(\omega^2+\Gamma_d(q)^2)+\delta_b \Gamma_b(q)/(\omega^2+\Gamma_b(q)^2)\}/\pi,$$

where $\Gamma_d(q)$ and $\Gamma_b(q)$ are the half of the full width at half maximum of the Lorentzian for the diffusive mode of local motion in a polystyrene chain and one for low energy components of the inelastic spectrum, respectively. δ_d and δ_b are these fractions. The detailed analysis of the data of the present system using above scattering law is now in progress.

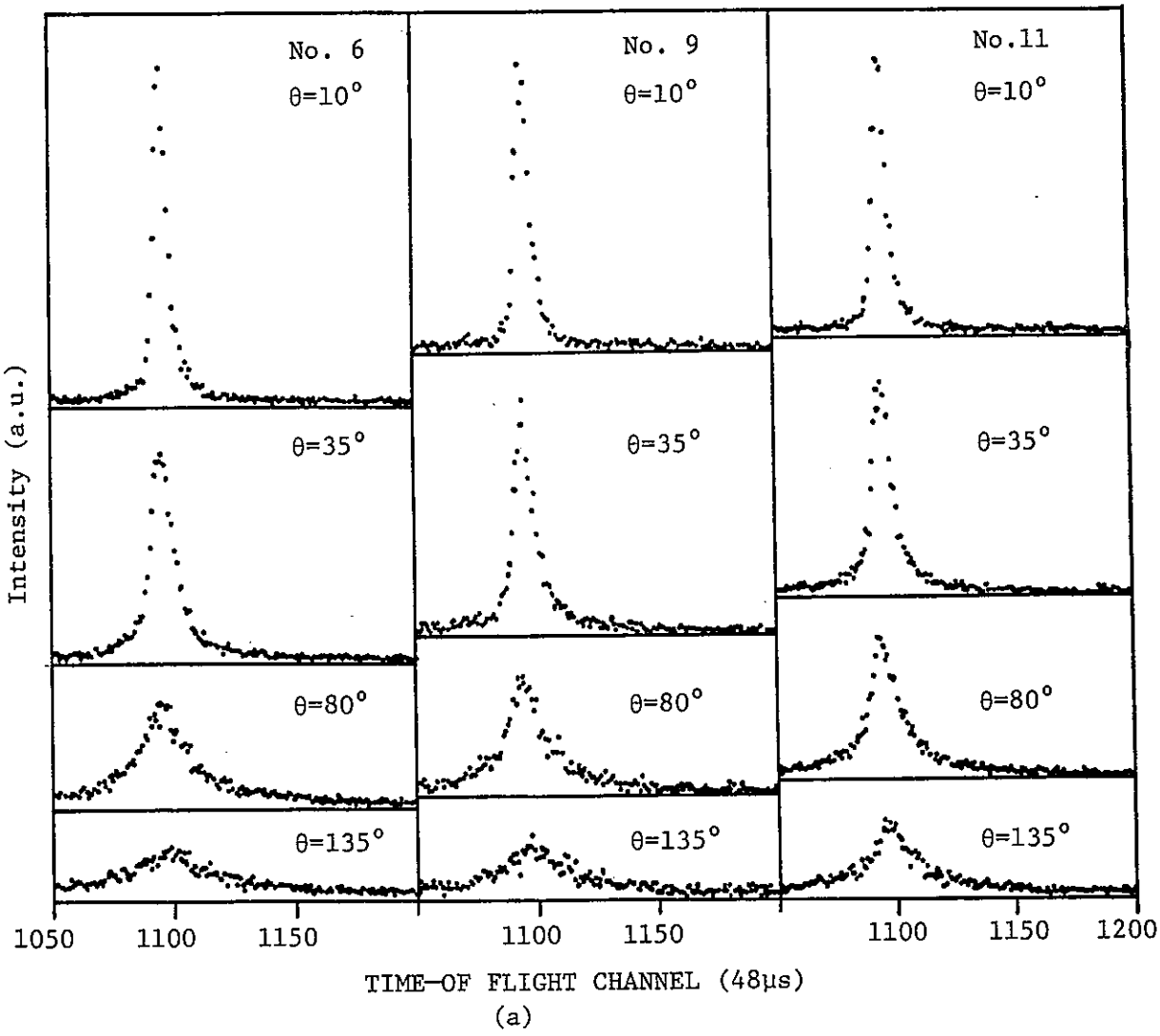

(a)

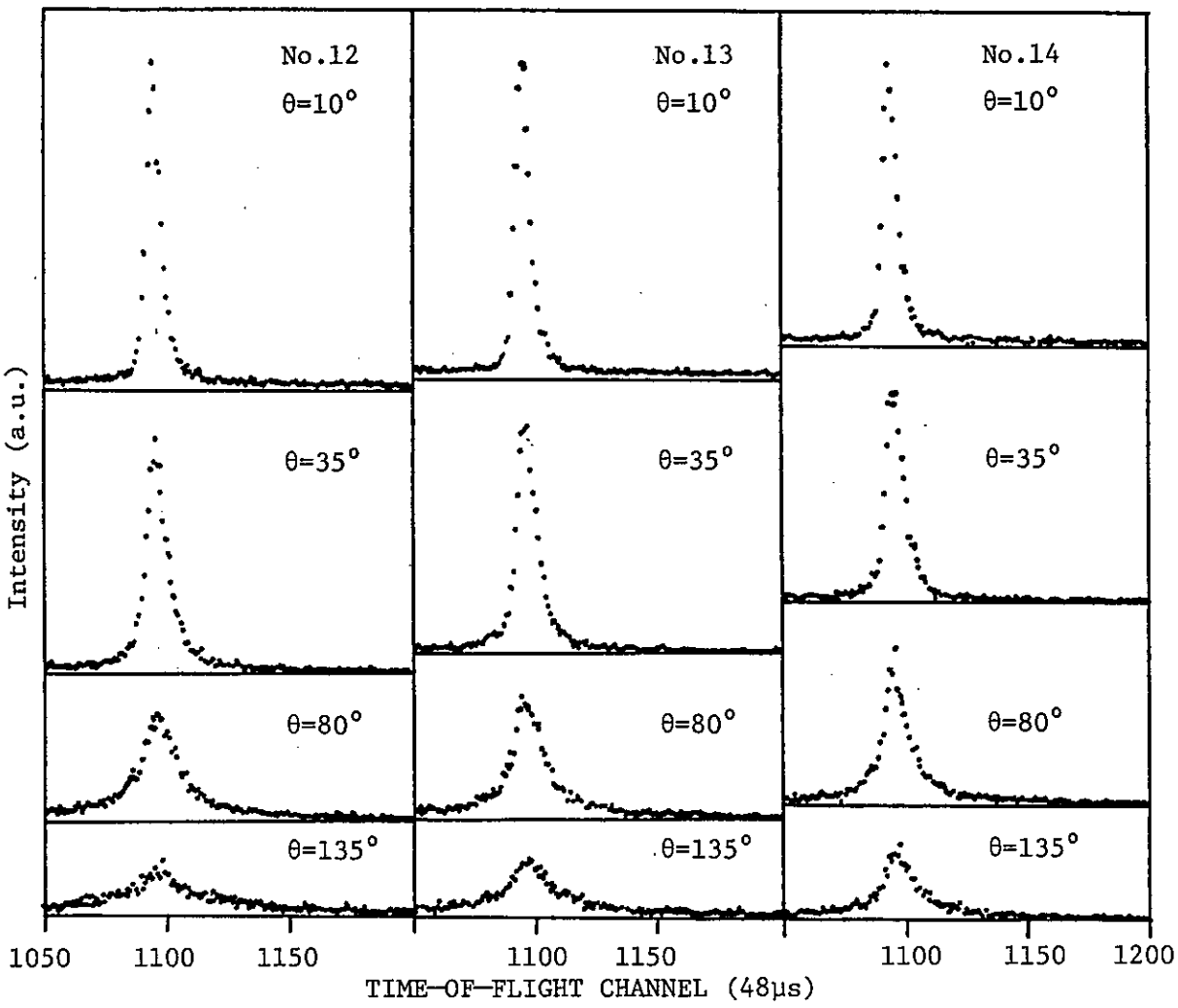

(b)

Fig. 2. Temperature dependence of time-of-flight spectra from aPS-CS_2 solution at two different concentrations.
(a) 25g/100ml, (b) 31g/100ml.
Nos. in Fig. 2 represent those in Fig. 1.

References

1. Y.Izumi, Y.Miyake, and K.Inoue, KENS REPORT — V(1984)135.

2. H.-M.Tan, A.Moet, A.Hiltner, and E.Baer, Macromolecules, 16(1983)28.

Thermoreversible Gelation of the Polystyrene–Carbon Disulfide System. III. Small Angle Neutron Scattering

Yoshinobu IZUMI, Yasuhiro MIYAKE, Michihiro FURUSAKA*,
Hidekazu KUMANO** and Kimio KURITA**

Department of Polymer Science, Faculty of Science,
Hokkaido University, Sapporo 060

*Department of Physics, Faculty of Science,
Tohoku University, Sendai 980

**Faculty of Science and Technology, Nihon University,
Chiyoda-ku, Tokyo 100

Small angle neutron scattering measurement from the atactic polystyrene (aPS)–carbon disulfide (CS_2) system has been paid an attention in conjunction with gelation and multicritical phenomena at a low temperature. The multicritical point is defined as a point, in which the gelation curve meets the phase separation curve at the critical consolute point. Previous scattering results showed that an unusual scattering exponent was obtained, when the system was approached the critical point along the critical isochore[1]. As the exponent value obtained has not been predicted by any existing theory, further test of the above observation has been desired. For this aim, scattering experiments have been made by extending it to lower values of the scattering vector Q and by changing the molecular weight of aPS. At the same time, the effect of the thermal history on the gelation process has also been studied.

The experiments were carried out at the KENS–SAN instrument at KEK[2]. The scattering data represent the excess scattering intensity of aPS–CS_2 solution against the solvent after their transmission corrections. The sample studied possesses the weight concentration of 5.43%. The gelation temperature corresponded to this concentration was 254.5K.

Fig. 1 shows the Q–dependence of the scattered intensity at various temperatures during gelation, in a double log presentation, whose results are consistent with previous results[1]. Contrary to the previous results on the phase diagram[3], the system is not fully reversible, as shown in Fig. 1

(a) and (b). Furthermore, the scattering curve at 300K is represented by the Ornstein-Zernike equation. A representation of the all scattering data in a Guinier plot (log I vs Q^2) indicates that there is no simple characteristic length scale to be deduced from the data and scattering curves of this kind are often analyzed as the scattering from a hypothetical distribution of particles[4]. This approach can be used to represent the present data, but the parameters derived in this fashion do not have any microscopic significance. Instead, we first try to analyze the scattering data by assuming the scattering law from a polydisperse fractals[5]. We next try to analyze the data by a branching theory[6] in conjunction with gelation which is suggested by the Kratky plot as shown in Fig. 2. The detailed analysis of the present data along these lines is now in progress.

References

1. Y.Izumi, Y.Miyake, S.Katano, N.Minagawa and M.Iizumi, Rep.Prog.Polym.Phys. Jpn. 29(1986) in press.
2. Y.Ishikawa, S.Ikeda, M.Furusaka and N.Niimura, KENS REPORT I (1980) 101.
3. H.M.Tan, A.Moet, A.Hiltner and E.Baer, Macromolecules, 16(1983) 28.
4. P.W.Schmidt, J.Appl.Cryst. 15(1982) 567.
5. J.Martin, ibid. 19(1986) 25.
6. M.Gordon, T.Ward and R.Whitney, Polymer Networks, ed. A.Chompff and S. Newman (Prenum Press) New York, 1971, p. 1.

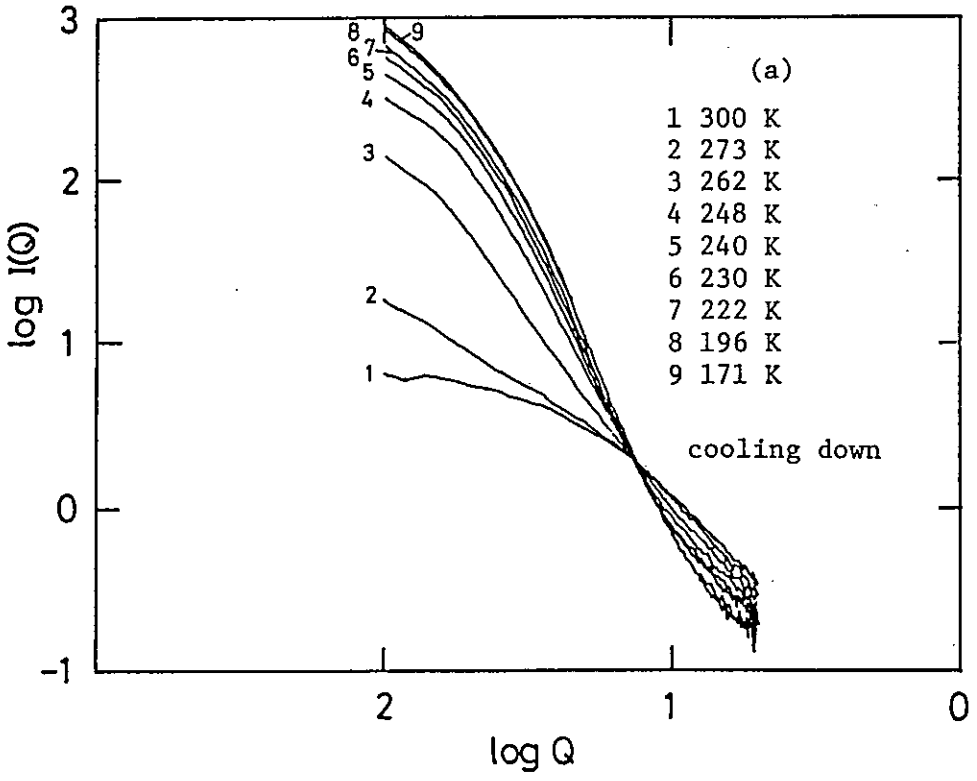

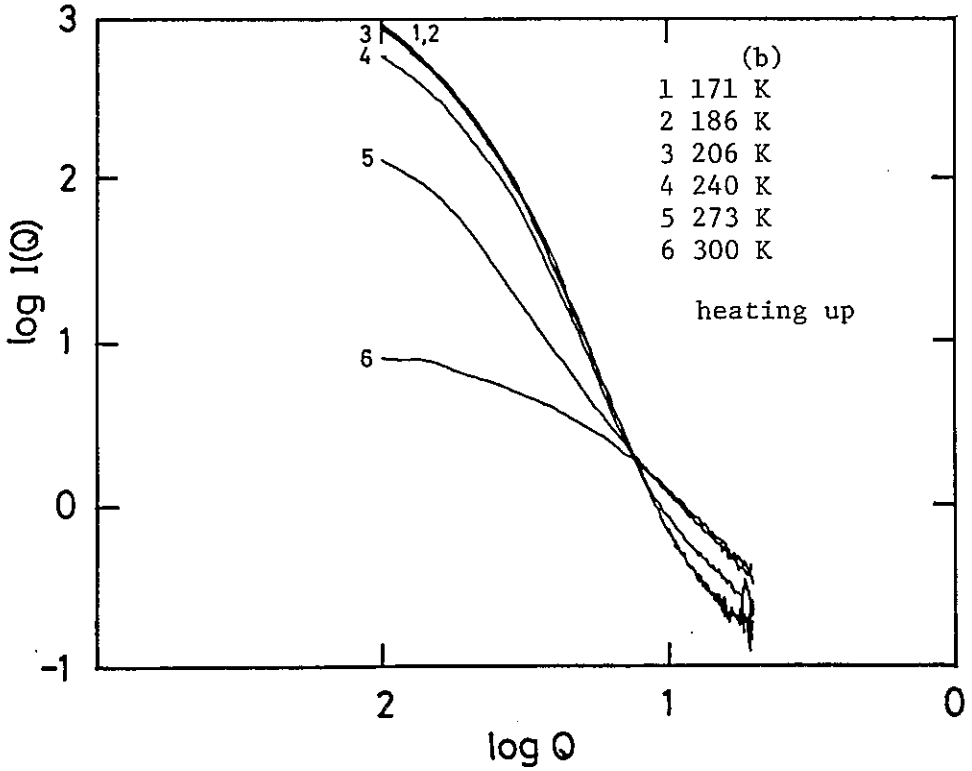

Fig. 1. The scattering curve as a function of Q for various temperatures during gelation. Gelation occurs at T=254.5 K.

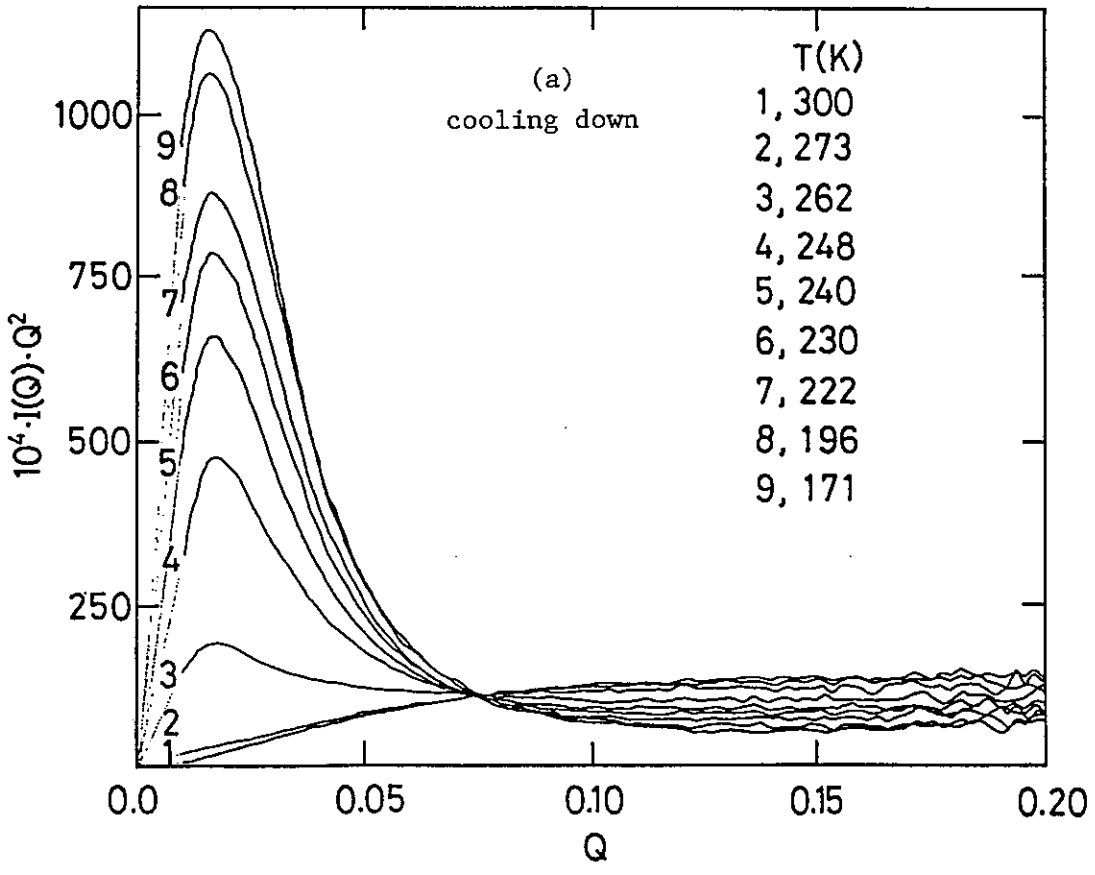

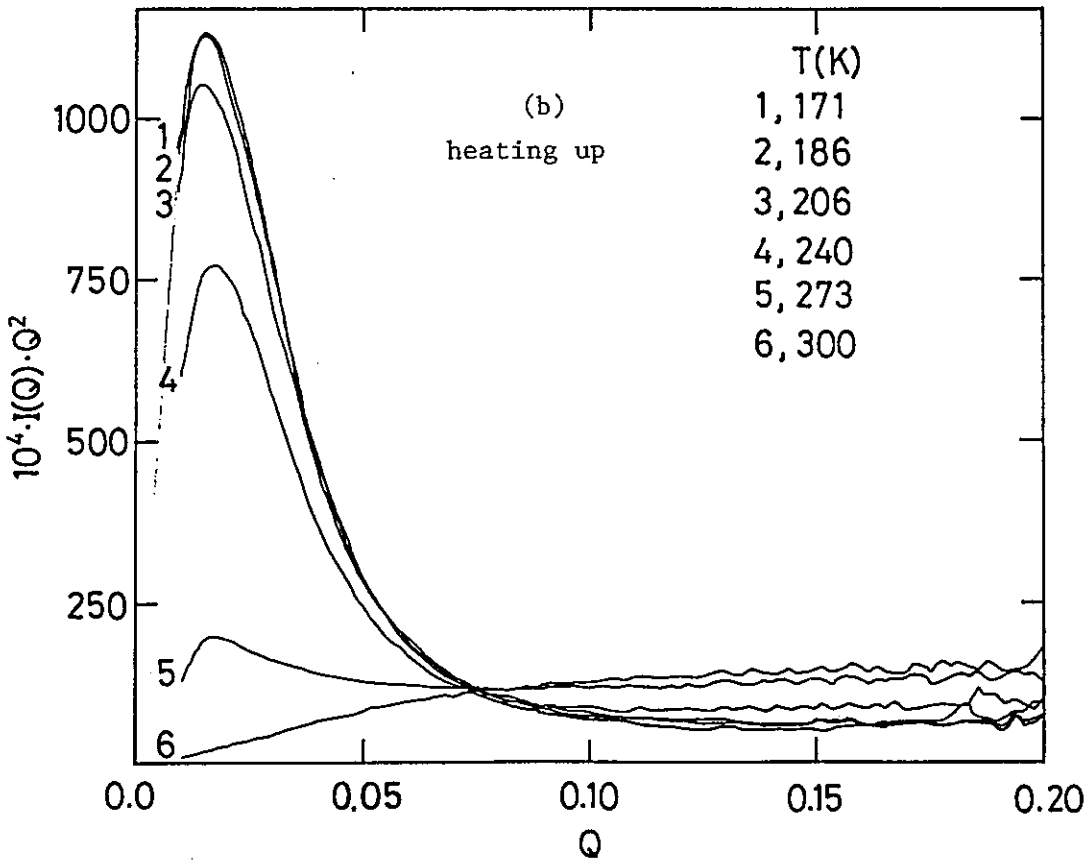

Fig. 2. Kratky plot for various temperatures.

Early Stages of Phase Separation in Critical Concentration alloy $Fe_{50}Cr_{50}$ Studied by Small Angle Neutron Scattering

Michihiro FURUSAKA and Sadae YAMAGUCHI[†]

Department of Physics, Tohoku University, Sendai 980
[†] Department of Nuclear Engineering, Tohoku University, Sendai 980

Phase separation processes in alloys has been studied extensively by X-rays and neutron scattering methods in past ten years. Recently, it has been discovered that the phase separation process in *off-critical* concentration sample is divided into two stages, namely, the early stages and the late stages by the small angel neutron scattering study.[1, 2] The very early stages are characterized by the q^{-2} dependence of scattering function I(q) at high q side, which reflects the abnormally enhanced thermal fluctuations. This q dependence is not explained by the linear theory of Cahn, but well explained by the nonlinear theory of Langer, Bar-on and Miller (LBM).[3] At the late stages, when the self similarity of the domain shapes are established,[4] the scattering function shows q^{-4} dependence at high q caused by the domain boundaries.

In the case of *critical* concentration samples, it is still unknown whether the same results hold or not. Some researchers expected to obtain the linear behavior predicted by Cahn at very early stages of phase separation, if it has critical concentration. From experimental view, there are only two alloys, AlZn and FeCr, which are suitable for the study of the mechanism of phase separation processes. The other alloys have relatively large elastic strain, therefore, not suitable for this purpose. In a case of critical concentration AlZn ($Al_{61}Zn_{39}$), it cannot be quenched rapidly enough to avoid phase separation while quenching sample. The only exception is $Fe_{50}Cr_{50}$ alloy. Although, this sample has σ phase around this concentration, there was no indication of σ precipitations in our results. Therefore, we performed an experiment with the *critical concentration* sample $Fe_{50}Cr_{50}$.

The sample was made from 99.995% iron and 99.999% chromium, melted several times in an arc furnace to avoid inhomogeneities. It was

homogeneized at 1000°C for about a day, and quenched into iced water. It was then annealed in the melted tin bath at 515°C and 540°C, followed also by quenching into iced water. The annealing time was ranging from 5 to 100 minutes.

Small angle neutron scattering experiment was performed at room temperature with SAN at KENS. Typical measuring time was about an hour. This is rather long because we were interested in high q regions where the scattering was very weak.

The time evolutions of scattering intensity thus obtained at very early stages were shown in Fig. 1. The scattering function of $Fe_{50}Cr_{50}$ seemed to be almost identical to the $Fe_{60}Cr_{40}$ and $Fe_{70}Cr_{30}$, if they were scaled by peak positions. However, some differences existed as follows, (i) time evolution of scattering intensity was rather slow, in conjunction with the slow diffusion rate of this sample compared with the other samples, (ii) peak positions were at lower q side than the other samples.

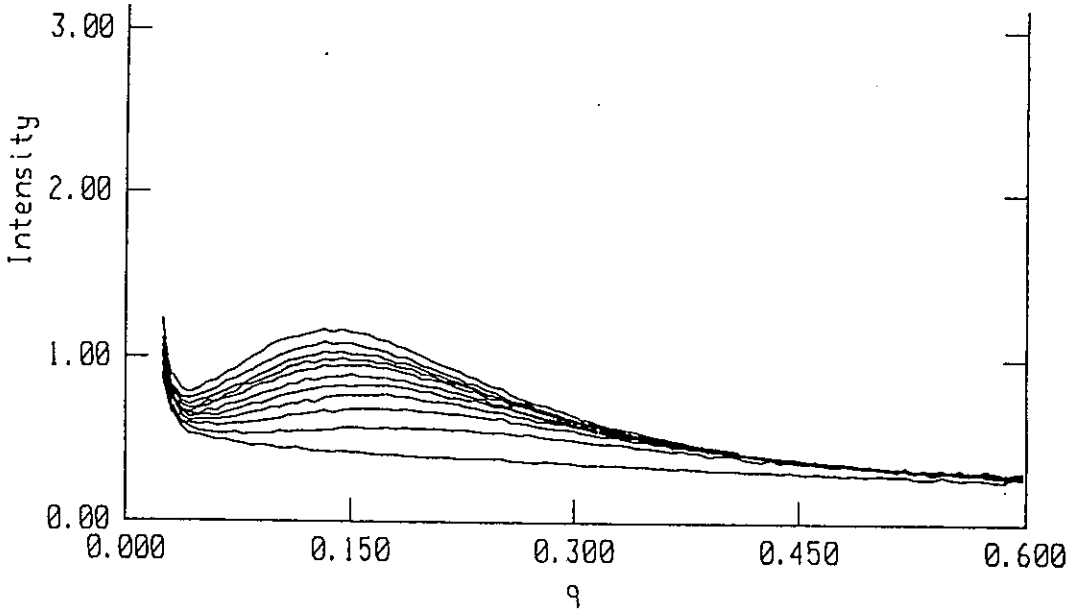

Fig. 1. Time evolution of scattering intensity from $Fe_{50}Cr_{50}$ critical concentration alloy annealed at 540°C. Annealing times were, as quenced, 5, 10, 15, 20, 30, 40, 50 , 60, 80 and 100 minutes.

The above results are explained qualitatively by the theory of LBM as follows. LBM scaled free energy f(X) as,[3]

$$f(X) = \frac{k_B T}{a^3} f_0 \phi\left(\frac{X}{X_S}\right), \qquad (1)$$

where a is the coarse grain length, ϕ is a dimensionless function, f_0 is a constant defined by the normalization of ϕ, and X, X_S are scaled concentration and critical concentration. If f_0 is small, i.e. the potential well is "shallow", thermal fluctuation term which leads to the q^{-2} behavior at high q plays an important role. The concentration dependence of the thermal fluctuation term is expected to be small if f_0 is small. Therefore, concentration dependence of the time evolutions of the scattering intensity must also be small.

In the case of FeCr sample, f_0 is expected to be small deduced from the flat shaped miscibility gap. Therefore, the above argument might hold for this sample. In opposite to the FeCr alloy, AlZn has larger f_0 value. In such a case, thermal fluctuation terms becomes less dominant. The system enters quickly into the late stages when the scaling law [$F(q) \propto q^3 \cdot I(q)$] holds.[4] This behavior was observed as $I(q) \propto q^{-4}$ behavior at high q in our experiments. The theory of LBM did not hold at these late stages.

To summarize, the time evolution of scattering intensity from critical concentration sample ($Fe_{50}Cr_{50}$) was measured. We observed the $I(q) \propto q^{-2}$ behavior at high q side of the scattering function. It was almost identical to the scattering function of off critical concentration sample $Fe_{60}Cr_{40}$ and $Fe_{70}Cr_{30}$, if we scale q with a peak position. The result was well explained by the theory of LBM, indicating that the parameter f_0 to be small.

References

1) M. Furusaka, Y. Ishikawa, S. Yamaguchi and Y. Fujino: J Phys. Soc. Jpn. **55** (1986) 2253.
2) M. Furusaka, Y. Ishikawa and M. Mera: Phys. Rev. Lett. **54** (1985) 2611.
3) J. S. Langer, M. Bar-on and H. D. Miller: Phys. Rev. **A11** (1975) 1417.
4) H. Furukawa: Phys. Rev. Lett. **43** (1979) 136.

Localized Motions of Polymers above Melting Temperatures

Kazuhiko INOUE, Keisuke KAJI*, Toshiji KANAYA*,
Koji NISHIDA and Ryozo KITAMARU*

Depertment of Nuclear Engineering, Hokkaido University,
Sapporo, 060 Hokkaido, Japan

* Institute for Chemical Research, Kyoto University,
Uji, 611 Kyoto-fu, Japan

The quasielastic neutron spectra of poly(butadiene), poly(chloroprene), poly(isobutylene) and poly(ethylene) were measured at temperatures above melting points (Tm) by using the LAM-80 spectrometer [1]. The dimensions of these samples (PB, PC, PIB and PE) were 13.5 mm diameter with 0.15 ∿ 0.2 mm thickness and 60 mm height. The samples were heated by electric heater and the temperature was controled with accuracy of ± 0.2°C. The spectra are shown in Fig. 1 ∿ 4. The sample temperatures are written in the figures. As seen from Fig. 4, an exceptional result is the Q-dependence of central peak intensity in the spectra of PE, which drops much steeper than the Q-dependences in the cases of remaining three polymers. For the sake of comparison, Fig.5 illustrates spectra of four polymers which are normalized for peak intensities at scattering angle 135° in PB, PC and PIB and at 35° in PE. In PB, PC and PIB, sharp central peaks are definitely revealed in the spectra at maximum Q-value (2.9 $\mathring{A}^{-1}$). Situation in PE is similar to these three polymers only for smaller Q-region.

The translational diffusion coefficient can be immediately estimated by relationship [2],

$$D \sim D_1 N^{-2}. \qquad (1)$$

The factor D_1 should be comparable with the diffusion coefficient in a liquid of monomers and N is the degree of polymerization which is large number in present case. Thus D is expected to be very small. At extremely small Q-values, the corresponding quasielastic peak width should be $\Delta E_{1/2} = 2\hbar Q^2 D$.

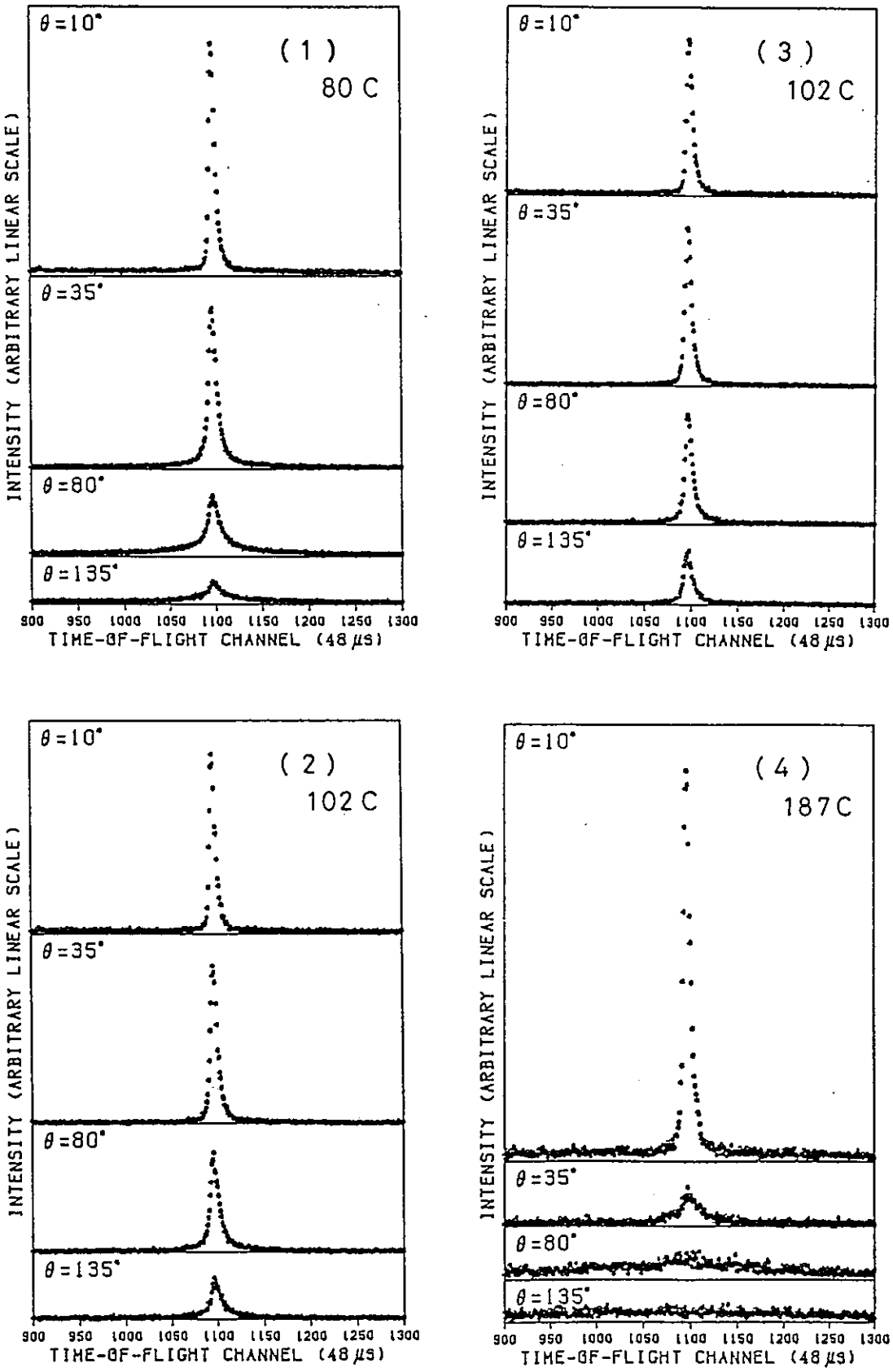

Figures 1 ∿ 4. Experimental neutron spectra from (1) poly(butadiene), (2) poly(chloroprene), (3) poly(isobutylene) and (4) poly(ethylene) measured by the LAM-80 spectrometer.

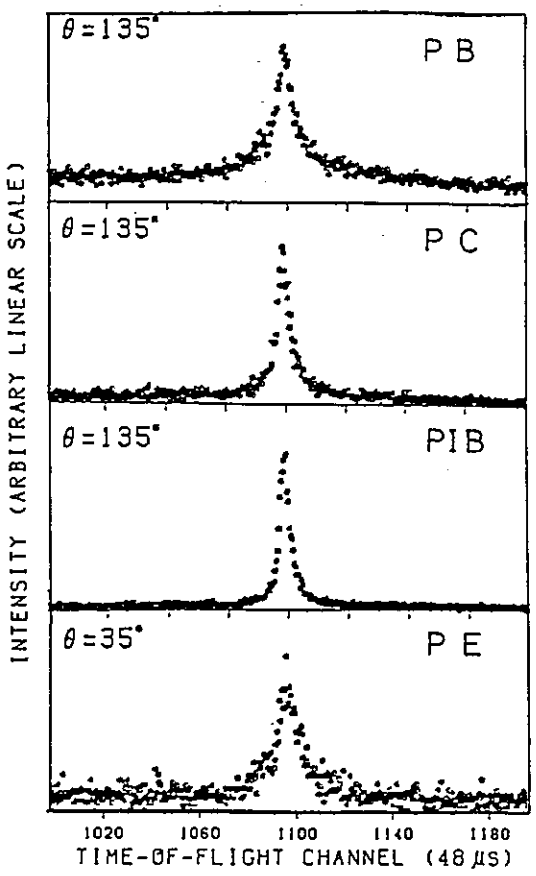

Fig. 5. Comparison of spectra from four polymers (PB, PC, PIB and PE).

Numerical estimates of the peak width lead to values much smaller than the resolution of spectrometer, even if we assume Q^4 dependence for the region where Q is 1 ∿ 2 $\mathring{A}^{-1}$. Then, for the present measurements, quasielastic peak concerning the translational diffusion might be revealed as a peak of which shape is the resolution function.

We assume the incoherent intermediate scattering function as a product of intermediate scattering functions,

$$I_{inc}(Q,t) \simeq I^{(tra)}(Q,t).I^{(loc)}(Q,t).I^{(vib)}(Q,t), \qquad (2)$$

where (tra), (loc) and (vib) mean the translational diffusion, the localized random motions and the vibrations, respectively. According to above discussion we expect $I^{(tra)}(Q,t) \sim 1$. For small energy quasielstic scattering $I^{(vib)}(Q,t) \simeq e^{-2W}$ might be reasonable. The incoherent scattering function of localized random motions is given by [3]

$$S^{(loc)}(Q,\omega) = A(Q)\delta(\omega) + S'(Q,\omega), \qquad (3)$$

where $S'(Q,\omega)$ represents quasielastic component having finite peak width.

Under this composit spectrum assumption, we conducted curve fitting for

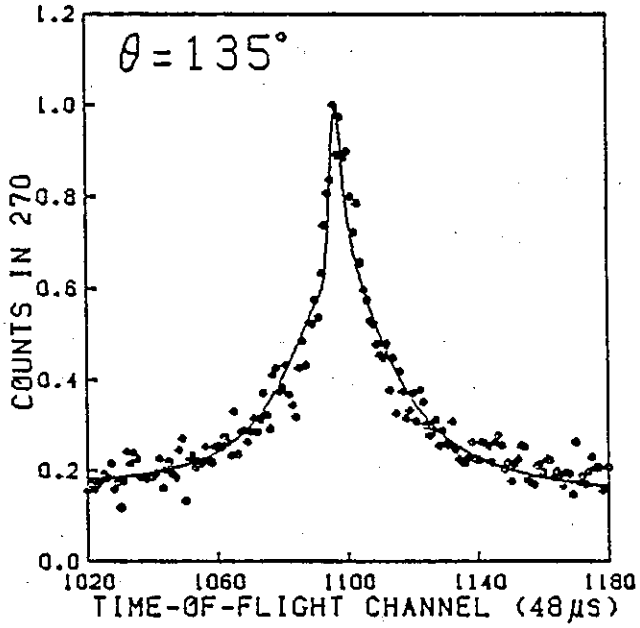

Fig. 6. Curve-fitting for the spectrum from PB at 135° scattering angle at 80°C.

the scattered spectrum from poly(butadiene) at 135° scattering angle at 80°C sample temperature. Assumed cross section was composed of the δ-function and two broad quasielstic components. A preliminary result is shown in Fig. 6 and fitting is satisfactorily well.

From above analysis, we can conclude that the measured spectra of PB, PC, PIB and PE contain very narrow peak components of translational diffusion, and the peak width of these components cannot be measured by the LAM-80. These data also confirm the existense of two localized random modes other than the translational diffusion. For this point a explanatory picture of two modes is as follows. A mode with short time constant exists below and above Tm, and the second mode with relatively long time constant appears above Tm. The former mode relates to the transverse freedom around polymer chain, and the latter to the logitudinal freedom along polymer chain. Concerning the steep intensity drop of central sharp peak component in PE, the coefficient A(Q) in Eq.(3) will suddenly decreases as Q increases because of the large flexibility of PE. We are now performing systematic measurements and detailed analysis, and the results will be reported elsewhere.

References

1) K. Inoue et al., Nucl. Instr. and Meth., A238(1985)401.
2) P. G. de Gennes, Scaling Concepts in Polymer Physics (Cornell University, London, 1979).
3) T. Springer, Springer Tracts in Modern Physics, Vol.64 (Springer-Verlag, Berlin, 1972).

Temperature Dependence of Neutron Quasielastic Scattering Spectra of Some Rubber Polymers

Toshiji. KANAYA.[a], Keisuke. KAJI.[a]
Kazuhiko. INOUE.[b] and Ryozo. KITAMARU [a]

a) Institute for Chemical Research, Kyoto University, Kyoto 611, Japan
b) Department of Nuclear Engineering, Hokkaido University, Sapporo 060, Japan

Neutron quasielastic scattering from some rubber polymers (cis-1,4-polybutadiene (PB), cis-1,4-polyisoprene (PI) cis-1,4-polychloroprene (PC), and polyisobutyrene (PIB)) were measured in the wide temperature range from 50 K to 450 K. All the measurements were carried out with the inverted geometry time-of-flight (TOF) spectrometer LAM-40 coupled with the pulsed spallation cold neutron source at KENS.

The observed TOF spectra at various temperatures are shown for PIB in Fig. 1. The spectra at high temperatures (for example, above 350 K for PIB) can be represented by the sum of the two Lorentzians. In this temperature range, we can get a lot of information about local fluctuation motions in rubber polymers by analysing the spectra.[1] As the temperature decreases, the shape of the spectra gradually deviates from the Lorentzian and finally an anomalous broad peak apperars at 2-3 meV below a certain temperature. This temperature is slightly different for each polymer, for example, ca. 220 K for PIB. The spectra for all the rubber polymers vary with temperature in the similar manner. We calculated TOF spectra on the basis of the generalized Mori-Langevin equation[2] and fitted to the observed TOF spectra using the computer code QUESA40.[3] The results are shown in Fig. 2 for PB at various temperatures. It was found that the change of the spectra can be phenomerogically described in terms of the generalized Mori-Langevin equation. It means that the stochastic process for the local motions in these polymers is not described as a Markov process but by a non-Markov one. As regards the anomalous peak at 2-3 meV in the low temperature range, we observed the similar phenomena in some disordered materials.[4]-[6] These low energy excitations are related with the anomalous thermal properties of disordered materials at low

temperatures.[7]

In conclusion, it is noted that polymer is one of the best materials to investigate characteristic properties of amorphous materials.

1) T. Kanaya, K. Kaji, R. Kitamaru and K. Inoue, KENS Report, 3, 125 (1985).

2) H. Mori, Progr. Theor. Phys., 33, 423 (1965); 34 399 (1965). K. Inoue, Bull. Facul. Eng., Hokkaido Univ., 127,1 (1985).

3) K. Inoue et al.,KENS Report, 5, 121 (1984).

4) T. Kanaya et al.,in this report.

5) M. Arai,in this report.

6) M. Misawa,in this report.

7) "Amorphous Solids - Low Temperature Properties" (Topics in Current Physics 24), ed. W. A. Phillips, Springer Verlag, Berlin, 1981;

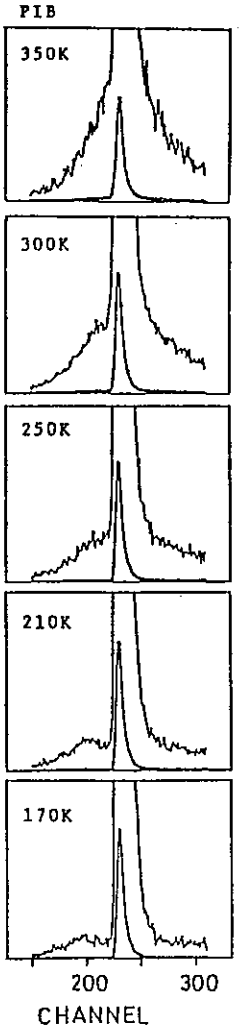

Fig. 1. TOF spectra of PIB at various temperatures. Q=1.4 A^{-1}.

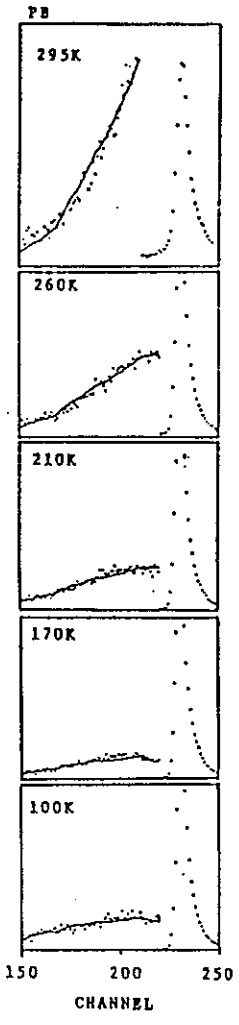

Fig. 2. Results of curve fitting for PB on the basis of the generalized Mori-Langevin equation by using QUESA40.

NEUTRON QUESIELASTIC SCATTERING FROM ATACTIC POLYSTYRENE

T.ISHIDA, T.KANAYA, K.KAJI, R.KITAMARU, K.INOUE*

Institute for Chemical Research, Kyoto University,
Uji, Kyoto-fu 611
*Department of Nuclear Engineering, Hokkaido University,
Sapporo 060

We have been investigating local motions in the amorphous regions of rubber polymers by neutron quasielastic scattering(NQS). [1] In this study, we intended to separate the motion in the main chain and that in the side chain and to explore the effects of the glass transition to the motions. We carried out NQS experiments on amorphous atactic polystyrene with the spectrometer LAM-40 [2] above and below the glass transition temperature (Tg)(ca.90 °C). The energy resolution of this spectrometer is ca. 100 μeV. In order to distinguish the motions in the main chain from those in the side chain (phenyl group), we prepared hydrogenated polystyrene (PS-h8) and partially deuterated polystyrene (PS-d5) where only the phenyl side groups were selectively deuterated. In the latter , we observe only the motions of main chain, because hydrogen atoms have large incoherent scattering cross-section compared with deuterium and carbon atoms. Figs.1 and 2 show the observed time-of-flight (TOF) spectra for PS-h8 and PS-d5 at 120°C, respectively. These spectra were analyzed by using the computer code QUESA40 [3]. It is found that the sum of the three Lorentzian functions give the best fit between the observed and the calculated spectra. In this calculation, however, the width of the narrowest component is fixed because the width is almost the same as that of the resolution function of LAM-40 spectrometer so that we can not evaluate it precisely. Fig.3 shows the evaluated full widths at half-maximum (FWHM) of the two broad components (G_1, G_2) as a function of temperature . There is no difference between the FWHM of PS-h8 and PS-d5. This means that in the time reasion investigated in the present work ($10^{-11}\sim10^{-13}$ sec) the main chain and the side chain have same relaxation time. The FWHM of PS-h8 and PS-d5 are independent of temperature. This temperature dependence suggests that these motions for G_1 and G_2 may be fluctuations within the potential wells.

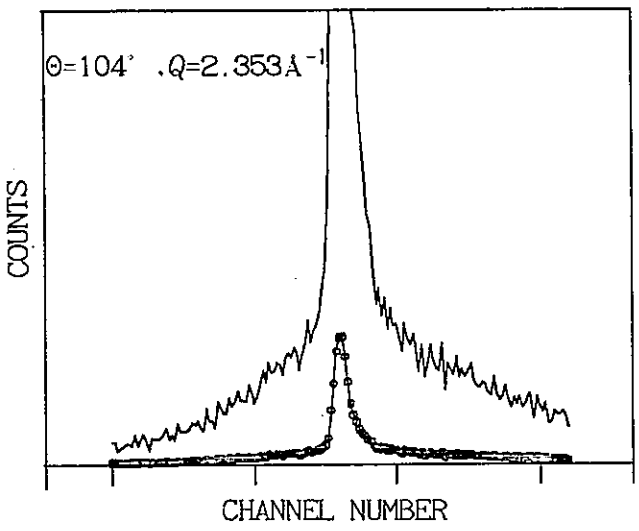

Figure 1. TOF spectrum of PS-h8

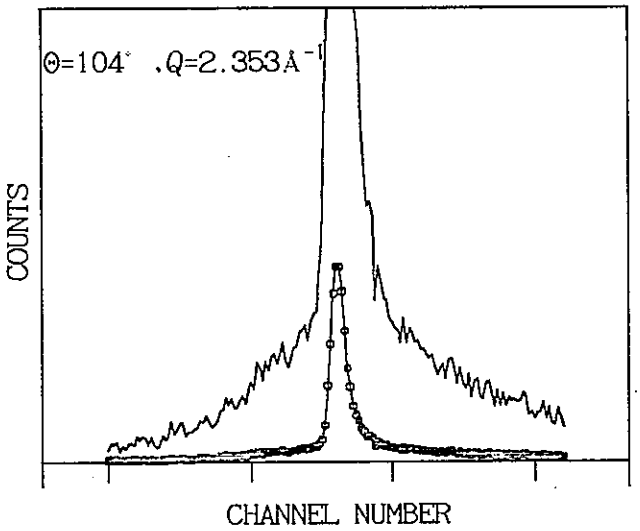

Figure 2. TOF spectrum of PS-d5

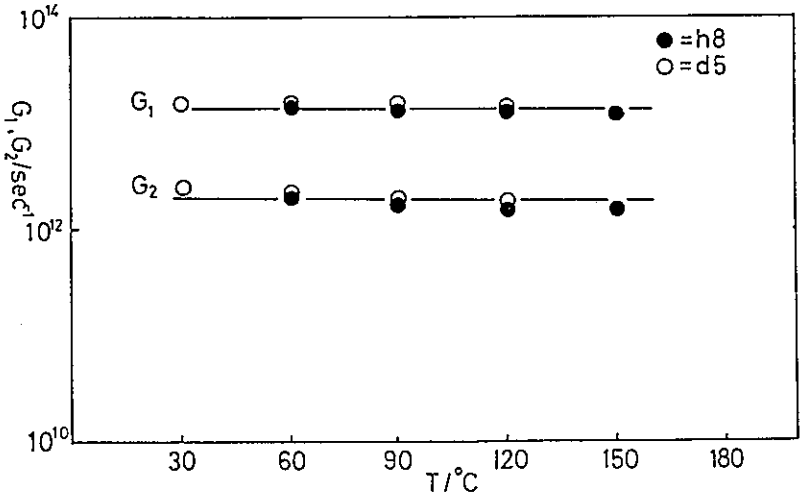

Figure 3. Log-log plot of FWHM G_1,G_2 as a function of temperature at Θ=104° ,Q=2.353Å^{-1}

REFERENCES

1) T. Kanaya, KENS REPORT,4, 125(1983).

2) K. Inoue et al., KENS REPORT,5, 121(1984).

3) K. Inoue, KENS REPORT,5, 125(1984).

Neutron Inelastic and Quasielastic Scattering from Cross-linked Polybutadiene

Toshiji KANAYA,[a], Keisuke KAJI,[a]
Kazuhiko INOUE,[b] and Ryozo KITAMARU [a]

a) Institute for Chemical Research, Kyoto University, Kyoto 611, Japan
b) Department of Nuclear Engineering, Hokkaido University, Sapporo 060, Japan

We reported[1] that a broad peak related to the cross-linking was observed at ca. 350 cm^{-1} in the density of phonon states for cross-linked polymers, such as vulcanized polyisoprene (PI) and γ-ray irradiated polybutadiene (PB). In the previous experiment, however, the degree of cross-linking for γ-ray irradiated PB was very low, so that the peak intensity was insufficient. In this work, we therefore prepared the PB with a high degree of cross-linking by irradiating Co^{60} γ-ray (272 Mrad) and confirm such a peak more clearly. The measurements of the density of phonon states were made by the spectrometer LAM-D. In addition, we carried out neutron quasielastic scattering experiments on the same cross-linked PB by using the LAM-40 and LAM-80 spectrometers. Both are the time-of-flight (TOF) spectrometers with crystal analyzer mirrors. The energy resolution of the former is ca. 100 μeV and that of the latter is ca. 10 μeV.

Fig. 1(a) shows the observed TOF spectum of the cross-linked PB. In the spectrum of the cross-linked PB, we can clearly see the broad peak at 350 cm^{-1}. On the other hand, such a peak is absent in the unirradiated PB[1] as shown in Fig. 1(b). Therefore, we conclude that this peak is attributable to the cross-linking.

Quasielestic scattering spectra of the cross-linked PB measured by LAM-40 at room temperature are shwon in Fig. 2(a). No quasielastic broadening is observed in the central component in the spectra of the cross-linked PB, while the unirradiated PB shows the quasieleastic broadening at the same temperature (Fig. 2(b)).[2] This was also confirmed from the measurement of quasielastic scattering with the high resolution spectrometer LAM-80 (see Fig. 3). The full-width at half-maximun (FWHM)

obtained from the spectra measured by LAM-80 are plotted for the cross-linked PB and the unirradiated PB in Fig. 4 as a function of Q. This result indicates that local motions in PB are strongly suppressed by the cross-linking. In the expanded spectra of the cross-linked PB measured by LAM-40 (upper curve in Fig. 2(a)), a broad inelastic peak can be found at ca. 1 meV. This peak is very similar to the anomalous broad peaks observed in some amorphous polymers in low tempertures. [3)-5)] Less mobility of the segments of the cross-linked PB may make it possible to observe the anomalous peak even in room temperature. This may be supported by the fact that the broad peak at ca. 2 meV is observed in epoxy resin at room temperature.[6)]

1) K. Inoue, T. Kanaya, K. Kaji, and R. Kitamaru, KENS Report, 5, 162 (1984).
2) T. Kanaya, K. Kaji, R. Kitamaru and K. Inoue, KENS Report, 4, 125 (1983).
3) K. Inoue et al.,in this report.
4) T. Kanaya et al.,in this report.
5) T. Kanaya et al.,in this report.
6) M. Arai, in this report.

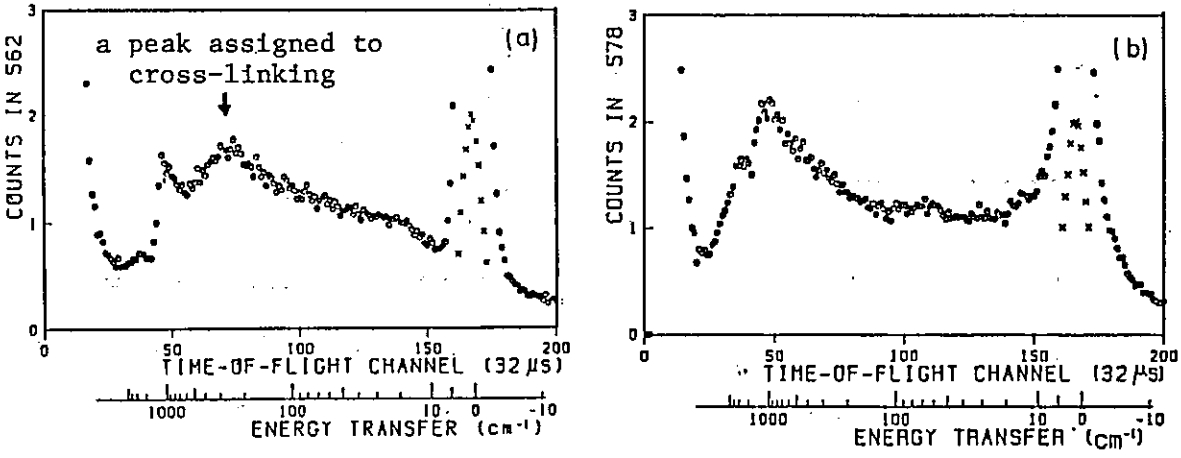

Fig. 1. TOF spectra of cross-linked (a) and unirradiated (b) polybutadienes measured by LAM-D at room temperature.

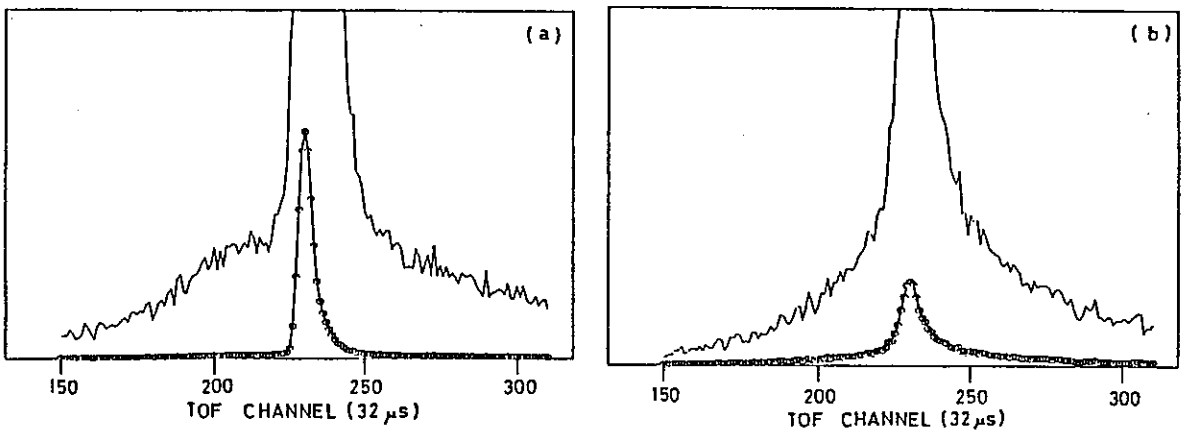

Fig. 2. TOF spectra of cross-linked (a) and unirradiated (b) polybutadienes measured by LAM-40 at room temperature (scattering angle = 88°). Upper curves are expanded ones by a factor 30 and 10 for (a) and (b), respectively.

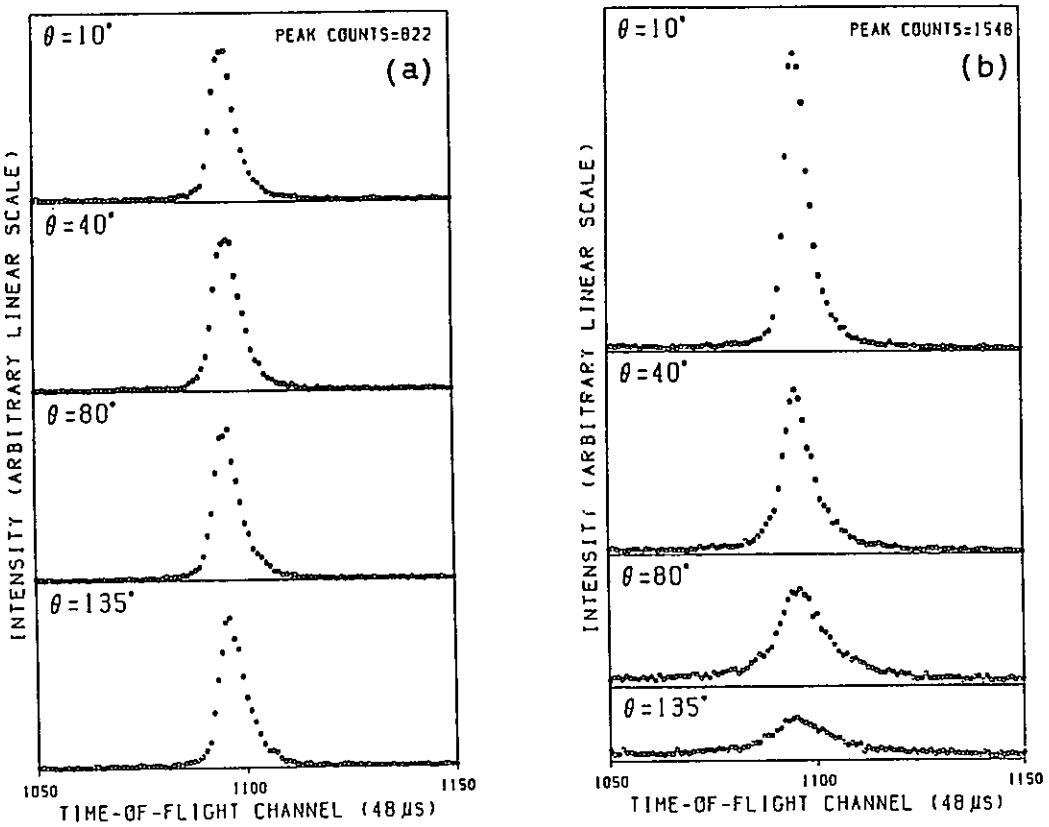

Fig. 3. TOF spectra of cross-linked (a) and unirradiated (b) polybutadienes measured by LAM-80 at room temperature.

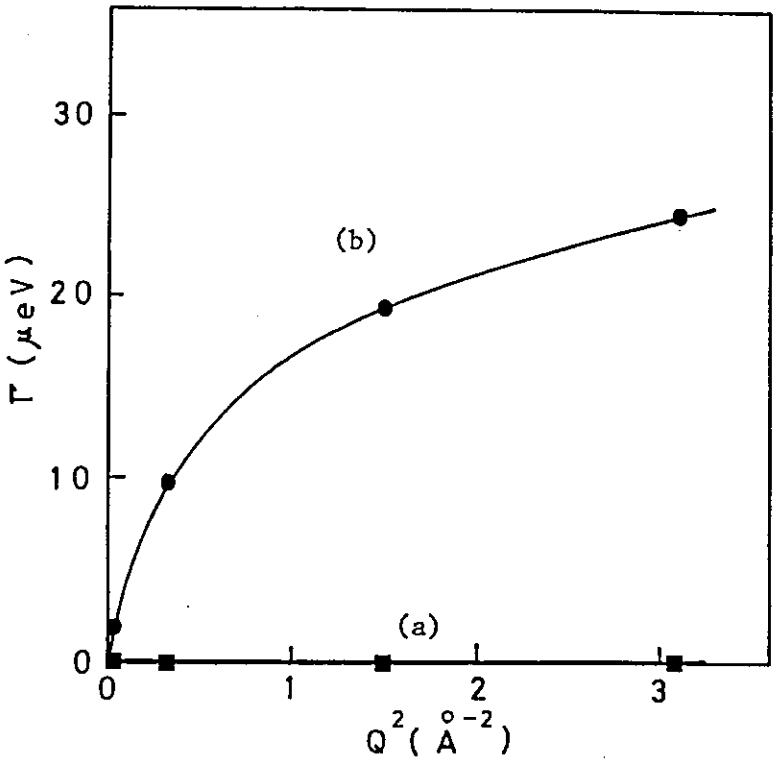

Fig. 4. Apparent FWHM for cross-linked (a) and unirradiated (b) polybutadienes evaluated from TOF spectra measured by LAM-80.

Molecular Motion of Water in Concentrated Zinc Chloride Aqueous Solutions

Yoshio NAKAMURA, Yoshinobu IZUMI and Kazuhiko INOUE*

Faculty of Science and *Faculty of Engineering,
Hokkaido University, 060 Sapporo, Japan.

Zinc chloride ($ZnCl_2$) is hygroscopic and very soluble in water. The mole ratio, R, of water to $ZnCl_2$ is 1.8 in the most concentrated solution at room temperature. In such concentrated solutions of strong electrolytes the hydration sheath is incomplete and the molecular motion of water is strongly impeded by the interaction with the dissolved ions. These solutions show very high viscosities and low diffusion coefficients of water[1]. In this report, we present some preliminary results of neutron quasielastic scattering experiments made on concentrated $ZnCl_2$ aqueous solutions with the LAM-40 and LAM-80 spectrometers.

Sample solutions were prepared from the reagent grade anhydrous $ZnCl_2$ and distilled water. Measurements were carried out at room temperature for three sample solutions with R=6, 4 and 2. The sample container used was a system of two precision quartz tubes with teflon plugs at each end. The thickness of the tube wall was 0.5 mm and the inner diameter of the outer tube and the outer diameter of the inner tube were respectively 14 and 13 mm. Sample solutions were introduced in the annular region between the two tubes. The quartz tube system was then placed in an aluminum container with the wall thickness of 0.2 mm.

Fig. 1 shows the time of flight spectra from the pure water and the solution with R=2 measured with the LAM-40 spectrometer. Fig. 2 shows the time of flight spectra for the solutions with R=6 and R=2 measured with LAM-80. These results indicate that the motion of water molecules in the solutions becomes much slower with increasing the concentration of $ZnCl_2$. After an appropriate correction for the scattering from the sample container, we can deduce the parameters of molecular motion of water in the present solutions, which are to be compared with those determined from the NMR method[1] and the previous neutron scattering experiment[2]. Such an analysis is now in progress.

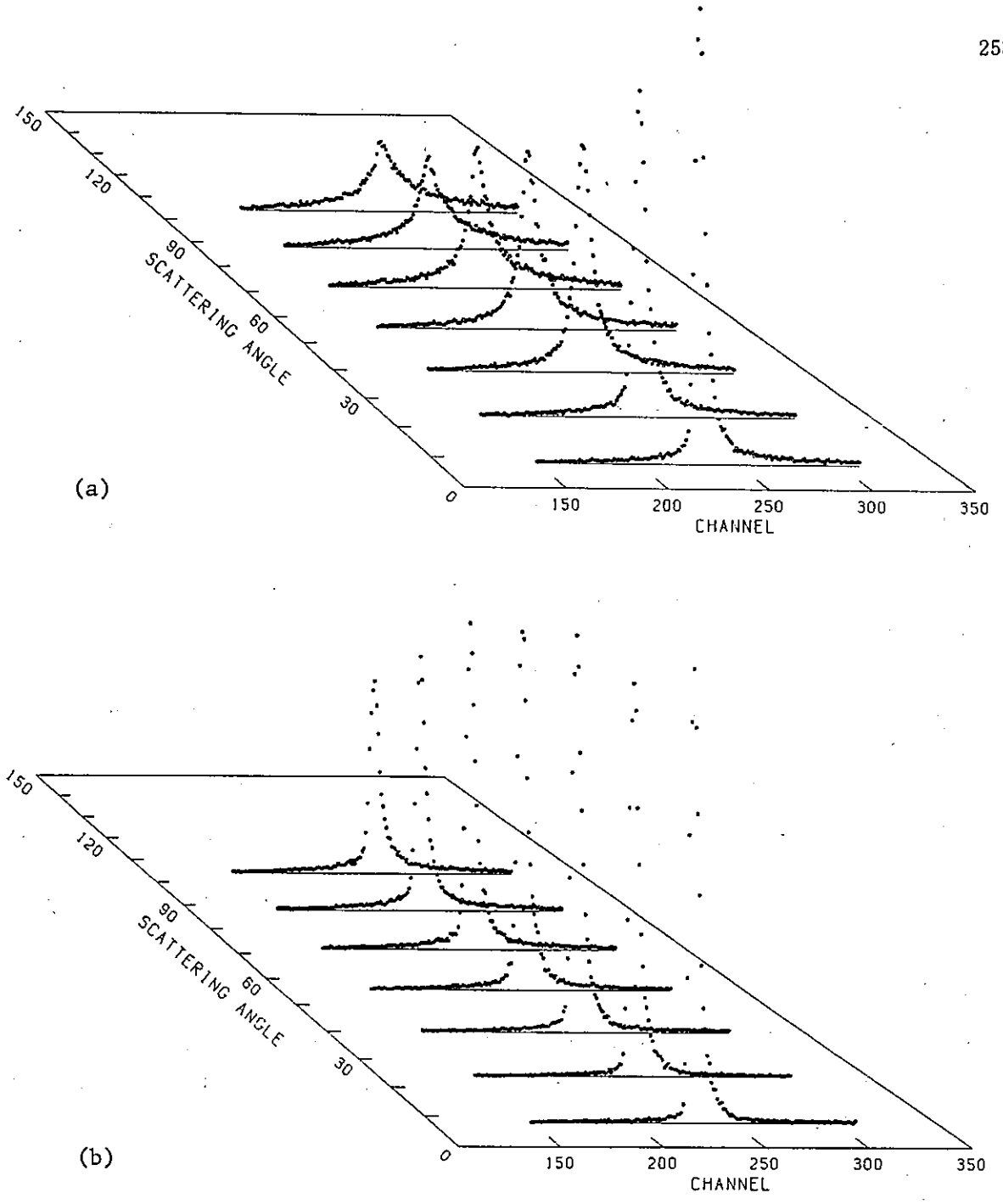

Fig. 1 Time of flight spectra measured with LAM-40 at room temperature. (a) Pure water, (b) $ZnCl_2$ aqueous solution with R=2.

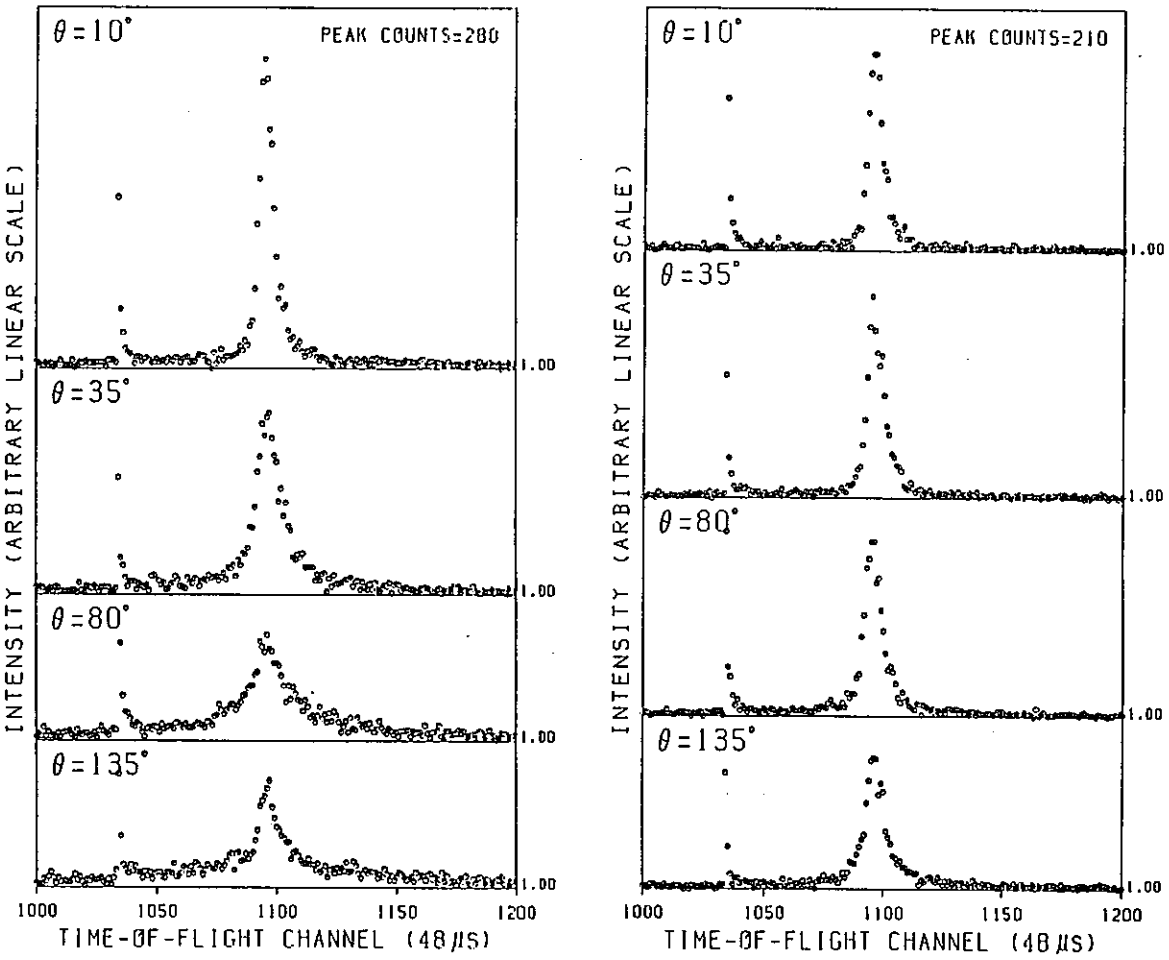

(a) (b)

Fig. 2 Time of flight spectra from $ZnCl_2$ aqueous solutions, measured with LAM-80 at room temperature. (a) Solution with R=6, (b) solution with R=2.

References

1) Y.Nakamura, S.Shimokawa, K.Futamata and M.Shimoji, J. Chem. Phys., 77, 3258 (1982).

2) M.C.Bellisent-Funel, R.Kahn, A.J.Dianoux, M.P.Fontana, G.Maisano, P.Migliardo and F.Wanderlingh, Mol. Phys., 52, 1479 (1984).

Small-angle Neutron Scattering from Polyelectrolyte Solutions with Added Salts

Kimio KURITA, Hidekazu KUMANO, Hiroshi ABE, Shigeru SHIMIZU, Eiichi WADA, Koji OKANO*, Shinya NAKAJIMA** and Michihiro FURUSAKA***

College of Science and Technology, Nihon University, Tokyo 101
*Department of Applied Physics, University of Tokyo, Tokyo 113
**Kanagawa Dental College, Yokosuka 238
***Department of Physics, Tohoku University, Sendai 980

Small angle neutron scattering from polyelectrolyte solutions in the presence of added salt were studied in dilute and semidilute range. In the presence of a large amount of added salt, we expect that due to the strong screening effect polyelectrolyte molecules in aqueous solution will behave as if they were nonelectrolyte macromolecules. We also expect that, if the amount of added salt is sufficiently large, polyelectrolyte solutions may be regarded as even poor solvent systems subject to the conditions[1]:

$$\beta_1 b^{-3} N^{1/2} < 1 \quad , \quad \beta_2 b^{-6} < 1 \tag{1}$$

for dilute solutions, and

$$\beta_1 b^{-6} \rho < 1 \quad , \quad \beta_2 b^{-6} < 1 \tag{2}$$

for semidilute solutions, where b^2 is the mean square length of a polymer segment, N is the number of segments contained in a polymer chain, β_1 and β_2 are respectively the binary and ternary cluster integrals of polymer segments, and ρ is the number density of polymer segments in solution.

In the latter case the angular dependence of the scattered intensity I(q) in the intermediate momentum range q, q being the scattering vector, is given by[1,2]

$$I(q)^{-1} = I(0)^{-1}(1 + \xi^2 q^2) \tag{3}$$

and

$$\xi^{-2} = \frac{6}{MA^2} + 12N_A\frac{B_1}{A^2}Cp + 36N_A{}^2\frac{B_2}{A^2}Cp^2 \qquad (4)$$

where N_A is Avogadoro's number, M and Cp are the molecular weight and the concentration of the polymer, A^2, B_1, B_2 and Cp are defined respectively as, $MA^2=Nb^2$, $M^2B_1=N^2\beta_1$, $M^3B_2=N^3\beta_2$ and $(Cp/M)N_A=\rho/N$.

In this report we will show that Eqs.(3) and (4) in fact work well for semidilute polyelectrolyte solutions in the presence of a large excess salt. Based on these equations we were able to determine the interaction parameters B_1 and B_2 as function of the amount if added salt.

Sodium polystyrene sulfonate (NaPSS) used was prepared by sulfonation[3] of the narrow molecular weight polystyrene ($Mw=1\times10^5$, $Mw/Mn\leqq1.06$, Pressure Chemical Co.). There was about 93% or more sulfonated styrene per chain. The solvents used were of the NaCl D_2O solutions. The salt (Cs) and polyelectrolyte (Cp) concentrations are shown in Table I.

Table I

Cs (M)	Cp (g/ml)
2.00	0.0584, 0.0699, 0.1002
3.00	0.0875, 0.0994, 0.1488
4.17	0.0243, 0.0730, 0.0973, 0.1154, 0.1216, 0.1457

The measurements were performed with the KENS-SAN instrument at KEK. The excess scattering intensity of NaPSS solution against the solvent was determined after the transmission correction made for both the solution and solvent. To compensate the uniform incoherent scattering due to the hydrogen atoms we added H_2O into the solvent so that solvent and sample solution have the same number of protons. The incoherent neutron spectrum as well as the detector efficiency of two-dimensional position sensitive detector was corrected by employing the incoherent scattering intensity from water. The measurements were made at 40°C, and the camera length was 3m.

A Kratky plot (Fig.1) in the dilute regime clearly shows a plateau in the range of $0.04\leqq q\leqq0.1$ ($\mathring{A}^{-1}$). This suggests that the θ temperature for Cs=4.17M might be in the vicinity of 40°C. From the q* value (Fig.1), which shows the transition from the scattering of a Gaussian chain to that of a rod particle, the persistence length l_p was estimated as 19$\mathring{A}$ using Koyama's theory[4].

In the semidilute regime, the measured angular dependence of the

scatterd intensity (Fig.2) showed a Lorentzian form in accordance with Eq.(3), then we could determine the screening length ξ for every Cp and Cs. Fig.3 shows the concentration Cp dependences of ξ at several Cs. They agree well with the prediction of Eq.(4), which enables us to determine B_1 and B_2 separately by use of A=0.42Å [5].

In order to study the contribution of the electrostatic interaction to B_1 and B_2 the Debye screening length κ^{-1} is calculated by Guéron's equation:

$$\kappa^2 = 4\pi Q(2Cs + 0.7\frac{l}{Q}Cp) ,$$

where l is the monomer length (l=2.5Å) and Q is the Bjerrum length. Figs.4 and 5 show the plots of B_1 and B_2 against κ^{-1}. As shown in the figures, with increasing κ^{-1}, B_1 increases monotonically from negative to positive values and vanishes at about 1.5Å showing the θ point for the solution at Cs=4.2M, and B_2 also increases with κ^{-1}.

These behaviors can be explained in terms of the increase, with the increase of κ^{-1}, of the diameter of the correlation tube of a polyelectrolyte segment having cylindrical symmetry.

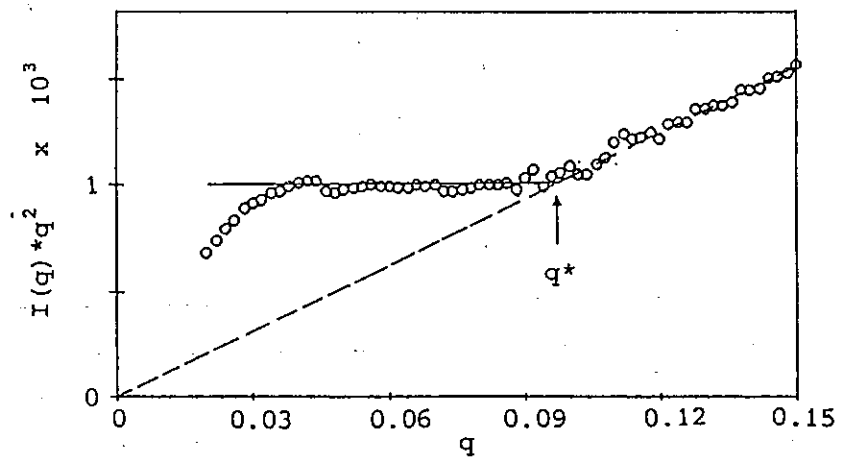

Fig.1 Kratky plot for Cp=0.0243(g/ml) and Cs=4.17M.

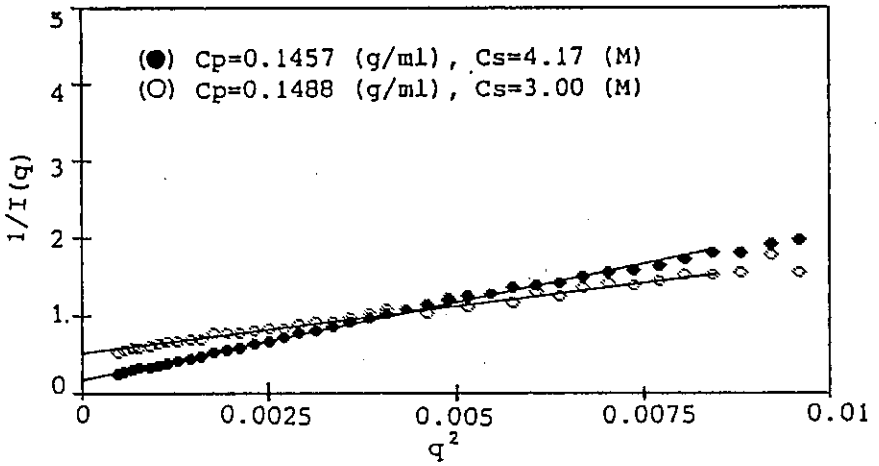

Fig.2 Examples of the measured angular dependence of SANS.

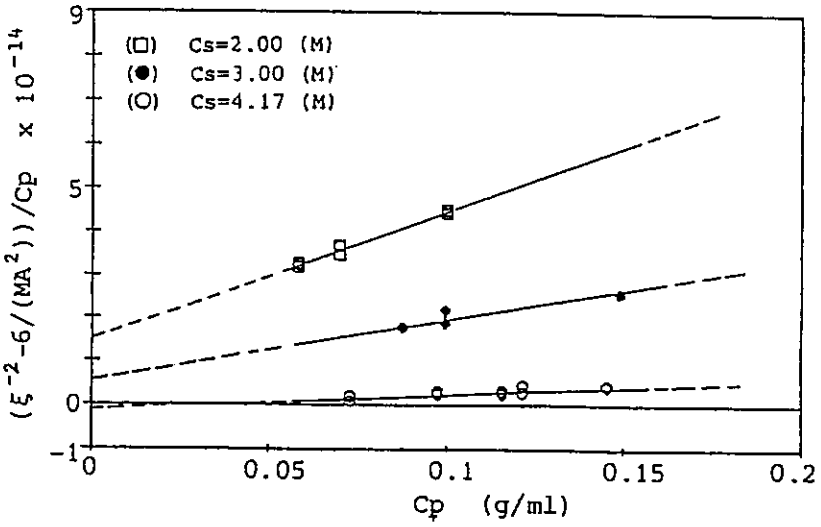

Fig. 3 Concentration dependence of ξ for several Cs at 40°C.

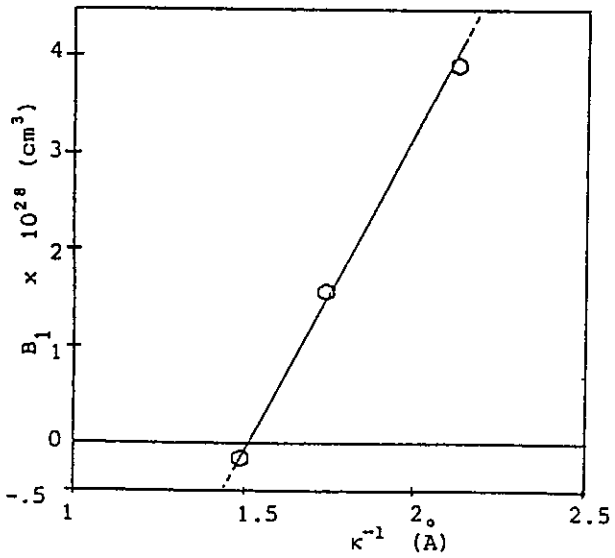

Fig.4 Binary cluster integral B_1 plotted against κ^{-1}.

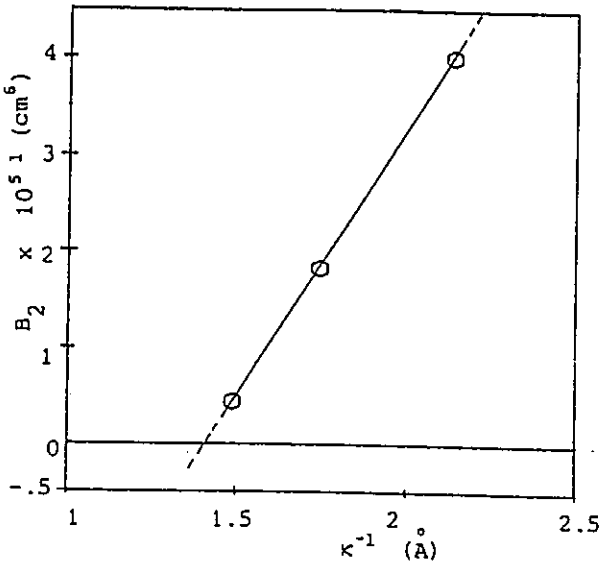

Fig.5 Ternary cluster integral B_2 plotted against κ^{-1}.

References

1) K.Okano, E.Wada, K.Kurita, H.Fukuro, J.Appl.Cryst.,11,507(1978).

2) M.A.Moore, J.Phys.(Paris),38,265(1977).

3) H.Vink, Makromol.Chem.,182,279(1981).

4) R.Koyama, J.Phys.Soc.Japan,34,1029(1973).

5) A.Takahashi, T.Kato, M.Nagasawa, J.Phys.Chem.,71,2001(1967).

Parity non-conserving effect in the neutron radiative capture reaction

Yasuhiro MASUDA, Toshikazu ADACHI, Shigeru ISHIMOTO,
Eiji KIKUTANI, Haruyo KOISO and Kimio MORIMOTO

National Laboratory for High Energy Physics
Oho-machi, Tsukuba-gun, Ibaraki-ken 305, Japan

and

Akira MASAIKE

Department of Physics, Kyoto University, Kyoto, 606 Japan

Helicity dependence was observed for the resonance of the neutron radiative capture reaction of ^{139}La using a polarized neutron beam. The polarized neutron beam was produced by a dynamically polarized proton filter.

The neutron capture γ-ray intensity was measured as a function of the neutron TOF. Observed TOF spectra around the p-wave resonance of ^{139}La at 0.734 eV are shown in Fig. 1. The thick and thin lines refer to the spectra for the parallel and antiparallel neutron polarization to the beam, respectively. A large difference was found between these spectra. Asymmetry in the γ-ray count, which was defined as

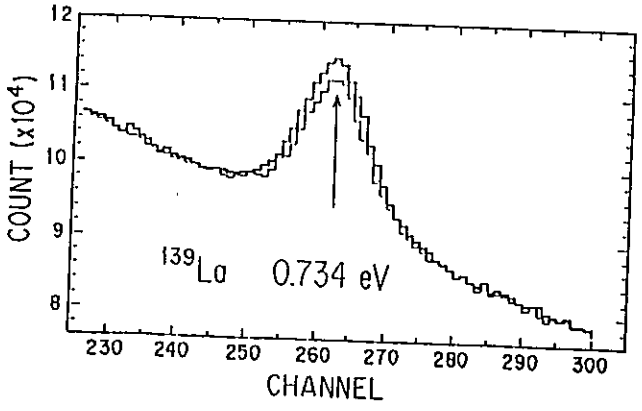

Fig. 1 TOF spectra around the 0.734eV resonance of ^{139}La.

$$A = \frac{1}{P_n} \cdot \frac{N(+) - N(-)}{N(+) + N(-)} ,$$

was calculated from the spectra. Here, N(+) and N(-) are the γ-ray counts in the peaks for the neutron polarization directions parallel and antiparallel to the neutron beam, respectively, and P_n is the neutron polarization. The neutron polarization was determined by the transmissions through the filter with and without proton polarization. The value was obtained to be (71 ± 4.3) %. The preliminary result of the asymmetry in the γ-ray count was (9.5 ± 1.2) % using the value of the neutron polarization. Experiments were also carried out for ^{98}Mo, ^{108}Pd and ^{129}Xe. Such a large asymmetry as that found in ^{139}La was not observed in these nuclei.

For the resonance at 0.734 eV of ^{139}La, an asymmetry in the neutron transmission was observed at Dubna.[2] The value of the asymmetry was (7.3 ± 0.5) %. A small difference was found between Dubna's result and our result. The difference is probably due to the following. The asymmetry in the total cross section was obtained from the transmission measurement, while the one in the radiative capture cross section was obtained from the γ-ray measurement.

References

1) Y. Masuda et al., to be published in Hyperfine interactions.
2) V. P. Alfimenkov et al., Nucl. Phys. A 398 (1983) 93.

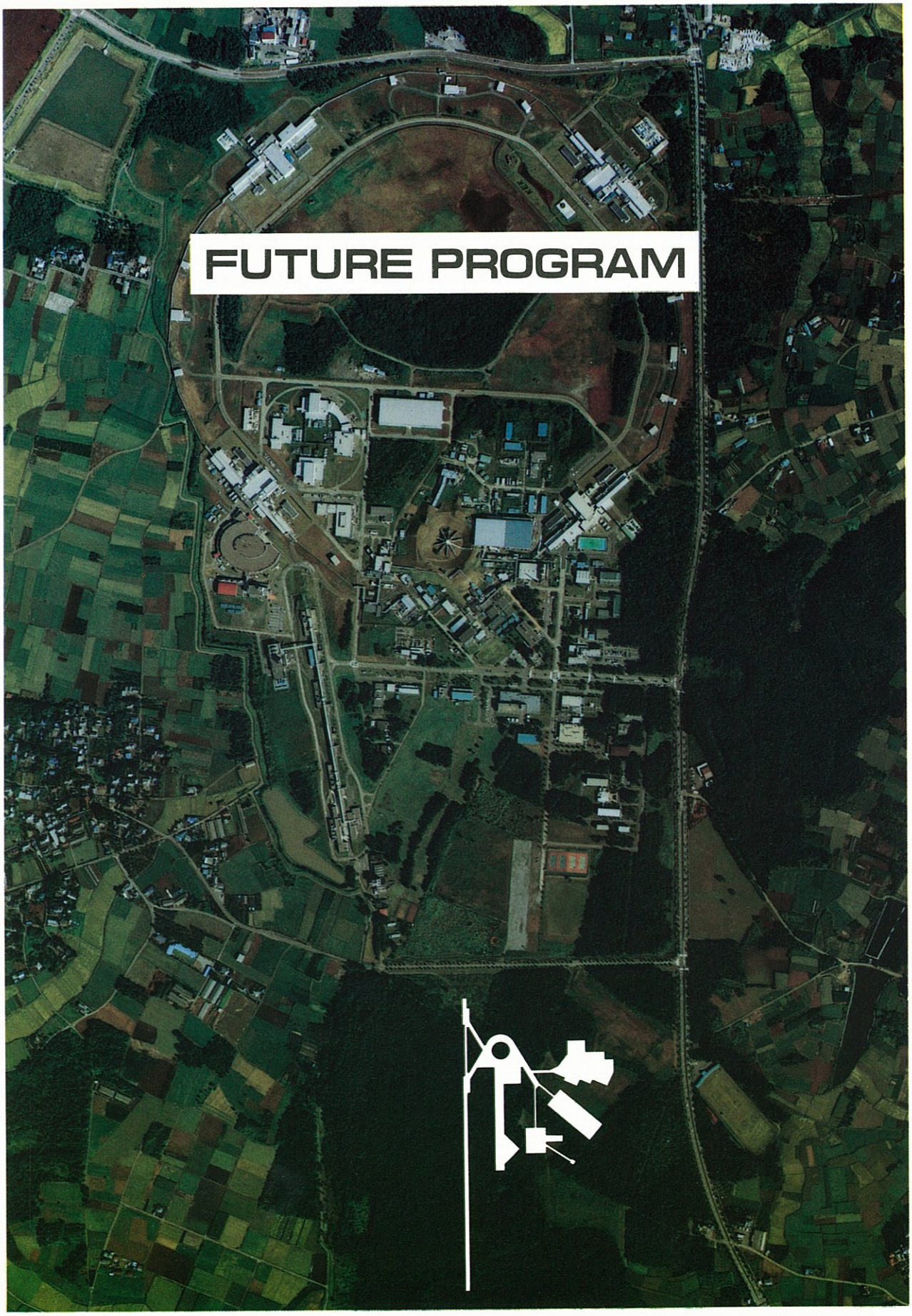
FUTURE PROGRAM

CONTENTS

Preliminary Calculation on Acceptable Maximum Proton Energy for Neutron Production in KENS-II

Masatoshi ARAI , Yoshiaki KIYANAGI*, Noboru WATANABE,
Yasuaki NAKAHARA** and Takahiko NISHIDA**

National Laboratory for High Energy Physics
Oho-machi, Tsukuba-gun, Ibaraki 305, Japan

*Faculty of Nuclear Engineering, Hokkaido University
Sapporo 060, Japan

** Japan Atomic Energy Research Institute
Tokai-mura, Ibaraki 319-11, Japan

As a next generation neutron source in Japan we proposed an intense pulsed spallation neutron source KENS-II with the construction of a high intensity proton synchrotron GEMINI (a Generator of Meson Intense and Neutron Intense beam), which was designed to provide 800 Mev with a time averaged beam current of 500 μA and with a repetition of 50 Hz. Recently a group of scientists in the field of nuclear physics have proposed a future program so called Super Hadron Project aiming to produce intense kaon and anti-proton beam. Since then the both projects are being unified to coexist. Now KENS-II project is getting a wide range support among the Japanese scientists and expected to be authorized as a part of the Super Hadoron Project.

The first ring accelerator in the new project may correspond to the GEMINI . Requirements for the first ring are of wide variety group by group. Neutron group requests pulsed proton beam with lower energies (<1.5 GeV) and a repetition rate not larger than 50 Hz but with possible highest beam current, while μSR group dose with higher energies (>1.5 GeV), better emittance and more flexibility in pulse width and repetition rate. It may be natural to understand such difference, because the cross section for the pion production (stopped π) increases significantly above 1.0 GeV and saturate at about 1.5 GeV. The nuclear physics group requests higher energies, 3 GeV or more, and sometimes stretched beam with better emittance.

In order to make our standpoint more clear, we performed a neutronic computer study for various proton energies in the range of 0.5 - 3 GeV, using a high energy transport code NMTC/JAERI[1], because there is no available data beyond 2 GeV.

The model target used in the calculation is a cylinder, 10 cm in diameter and 32 cm long (64 cm for 3 GeV proton), of a uniform mixture of uranium, coolant and cladding in their average proportions , which is the same as the model target for ISIS in Ref. 2. The parameters of the target are summarized in Table I.

The calculation was performed using a spatially meshed structure shown in Fig.1. The coordinate system for the calculation was chosen such that the z axis is parallel to the proton beam axis. Beam profile of incident protons upon the target was assumed to be cylindrical, 4.7 cm in diameter, which is designed size on GEMINI.

In the following four paragraphs we discuss the results without sub-15 MeV neutron transport calcuration, which will add about 10 % more neutrons. The conclusion is, however, not to be influenced awfully with this treatment.

Figure 2 shows the total neutron yield for various proton energies. Neutron yield is almost proportional to the incident proton energy below 1 GeV, but there is no advantage for energies much greater than about 1GeV. 3 GeV proton produces only two times as many neutrons as 800 MeV proton.

Figure 3 shows axial distributions of source neutrons integrated over the radial direction. The maximum luminosity is increased by only 15 % and the peak position shifts toward down stream by about 7.5 cm with increasing proton energy from 800 MeV to 3GeV. But higher energy protons give much longer bright zone.

Figure 4 shows the spatial distributions of energy deposition along the z-axis which have the similar trend as the source neutron distribution. The maximum heat load is also unchanged with proton energy .

Figure 5 shows the radial distributions of source neutrons integrated over the finite length along the z axis. The distribution almost preserves the profile of the incident proton beam in spite of the difference of the proton energy.

In order to obtain the escaped neutron energy spectra in the whole energy range, we have achieved a sub-15 MeV transport calcuration using TWOTRAN-II[3], a two dimensional neutron transport code, and the results were joined in a reasonable fashion at 15 MeV with those from NMTC.

Figure 6 shows the neutron spectra, escaped from the target, produced by 800 MeV and 3 GeV proton. The results indicate that the 3 GeV proton gives higher intensity over the whole energy range by a factor about two, but three around 20 MeV, than 800 MeV proton.

Slow neutron (thermalized neutron) beam intensity was calculated using the TWOTRAN-II. We usually use a moderator, 10 x 10 x 5 cm^3 for a neutron station. But in the two dimensional calculation, we assumed an annular water moderator , 10 cm wide and 5 cm thick, and a beryllium reflector, 25 cm thick, surrounding the target as shown in Fig.7. In the present TWOTRAN calculation, five energy-group structure was used for saving time, where source neutrons below 15 MeV produced in target were collapsed into the group one. The difference of source neutron spectrum is , therefore , not taken into account in the present calculation of slow neutrons. Table II summarizes a preliminary estimate on relative intensity of thermal neutrons emitted from the moderator for various proton energies. The rate of increment in thermal neutron yield is less than that in the source neutrons.

In conclusion, we would say that the maximum acceptable proton energy is around 1.5 GeV for the neutron beam facility, even as a consequence of compromise with other groups.

More exact calculation is under progress in order to discuss the merit and demerit of higher proton energy in more details.

References

1) Y. Nakahara and T.Tsutsui : JAERI-M 82-198 (1982)
2) F. Atchison : RL-81-006 (1981)
3) K. D. Lathrop and F. W. Armstrong : LA-4848 (1973)

Table I Nuclear Densities (unit of nuclei A^{-3})

Target mixture	^{238}U	0.0390
	^{2}H	0.0091
	^{16}O	0.0045
	^{91}Zr	0.0017

Table II Thermal Neutron Yeild

Ep (GeV)	Thermal Neut. Yield (arb. unit)	Total No. of Source Neut.
0.8	59.8	3962
1.5	82.85	6010
2.0	96.97	7119
3.0	106.03	8199

Fig. 1 Computational model for NMTC

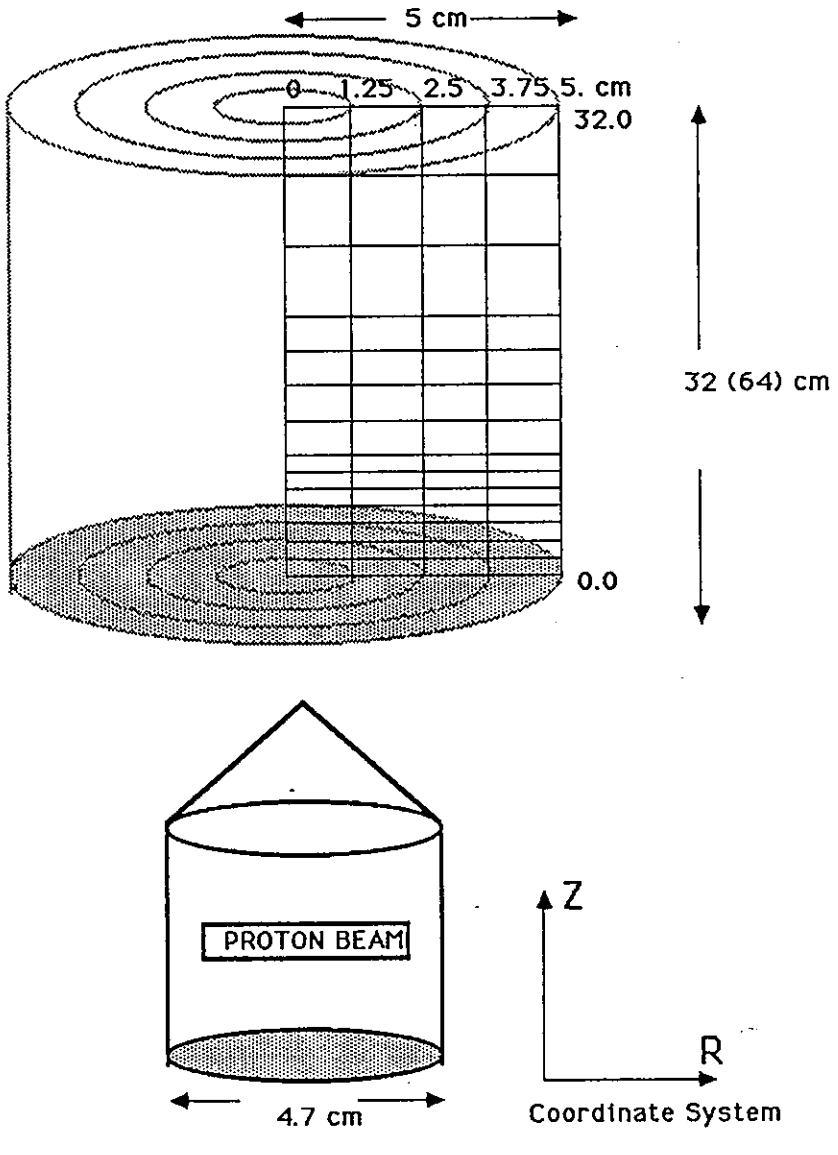

Fig.2 Proton Energy Dependence of Neutron Total Yield

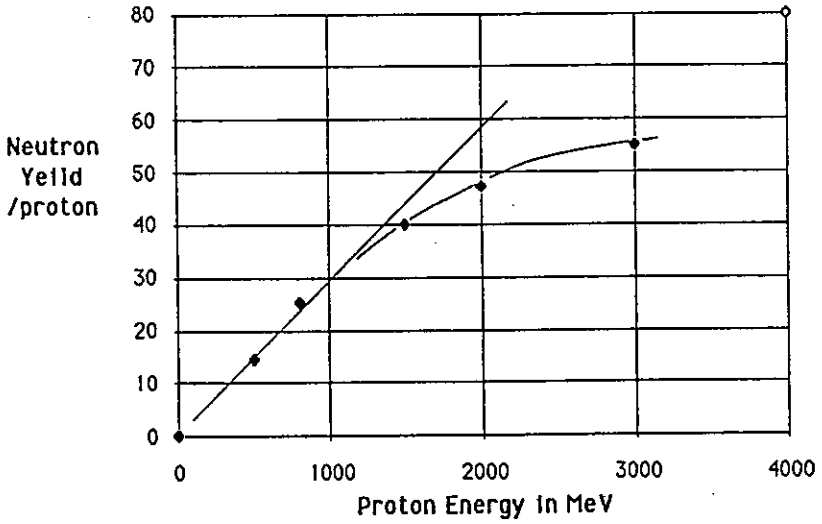

Fig. 3 Neutron Distribution along Z axis

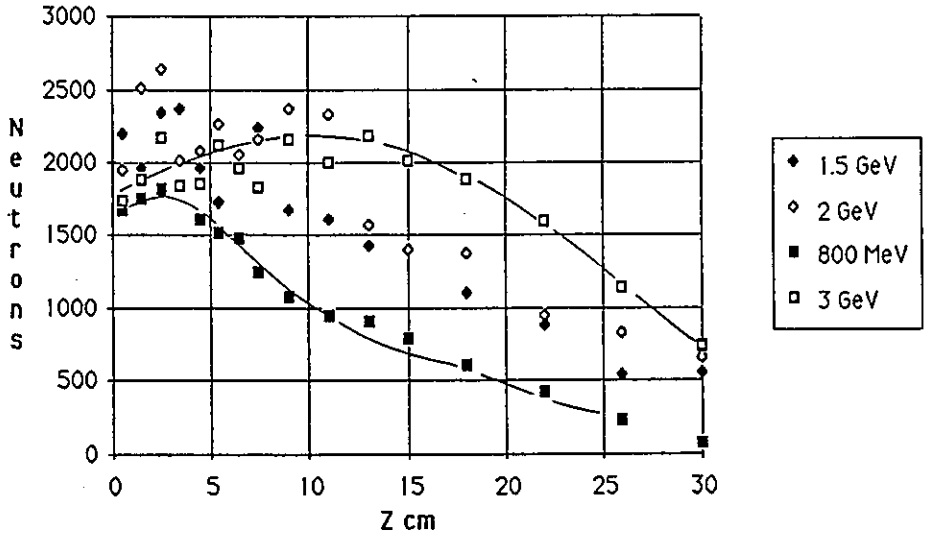

Fig.4 Heat Deposit Distribution

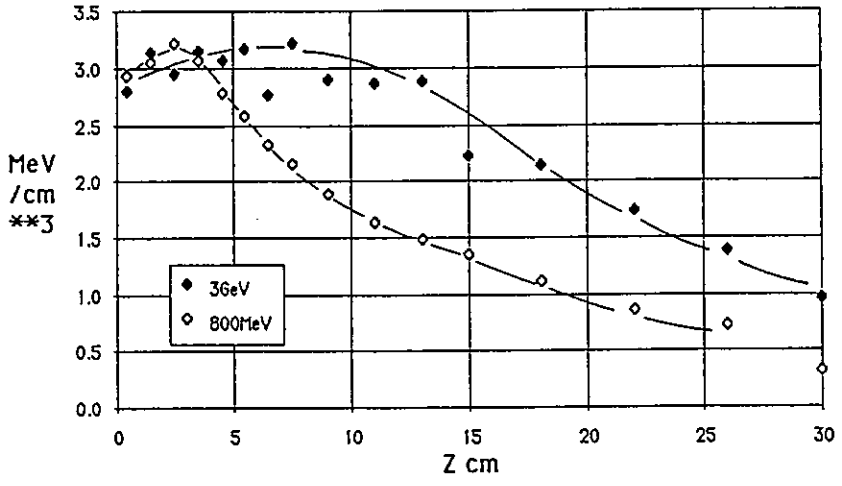

Fig. 5 (a) Radial Distribution for 3GeV

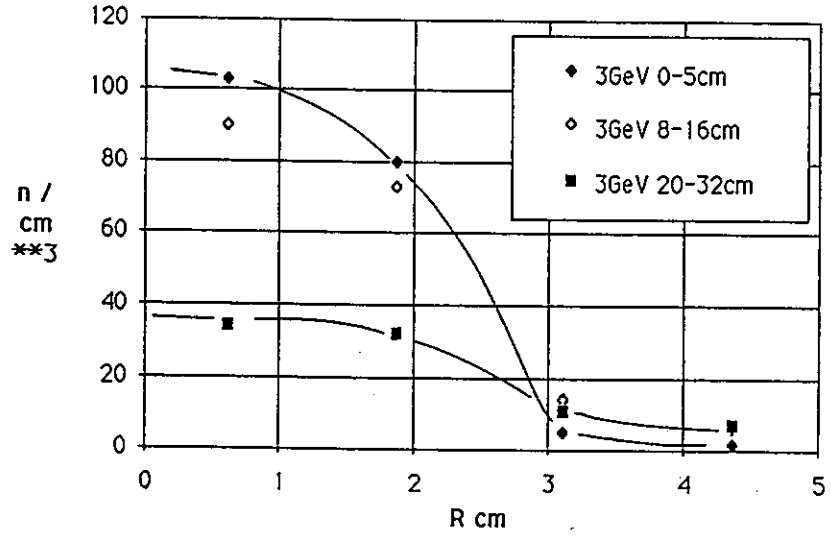

Fig. 5 (b) Radial Distribution for 800 MeV

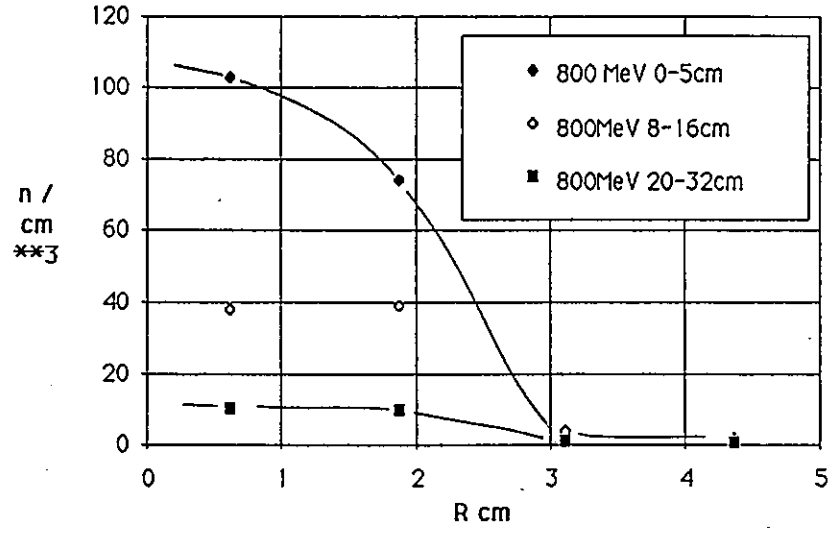

Fig. 6 ENERGY SPECTRUM

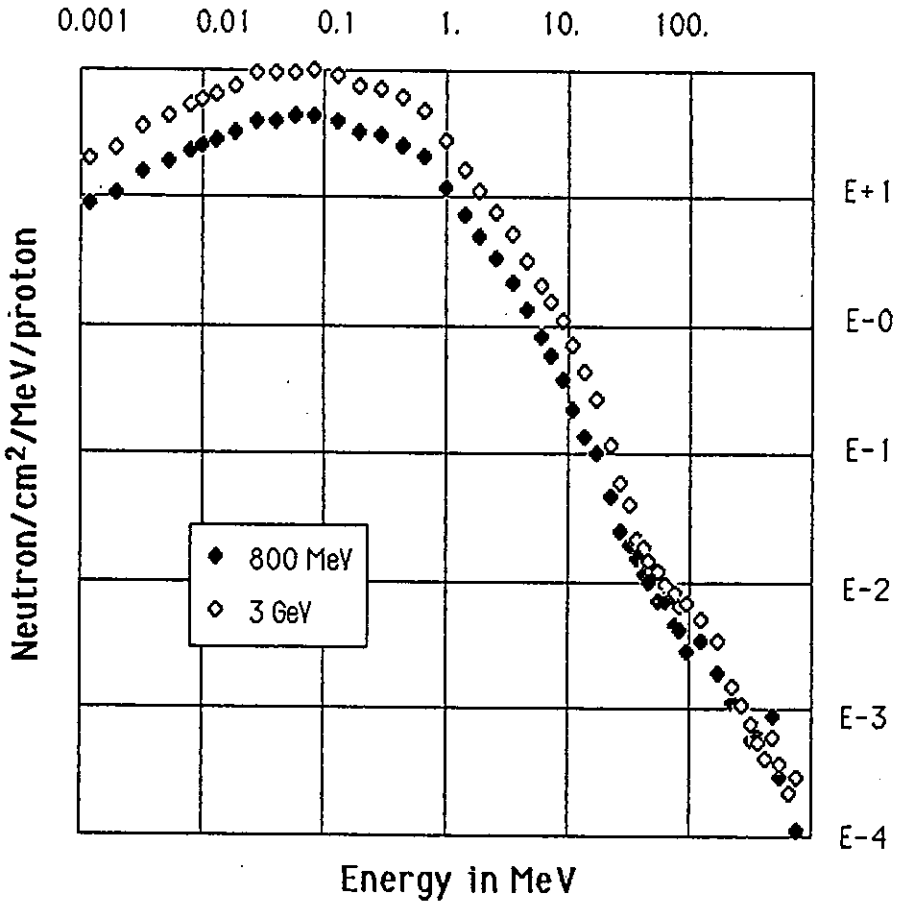

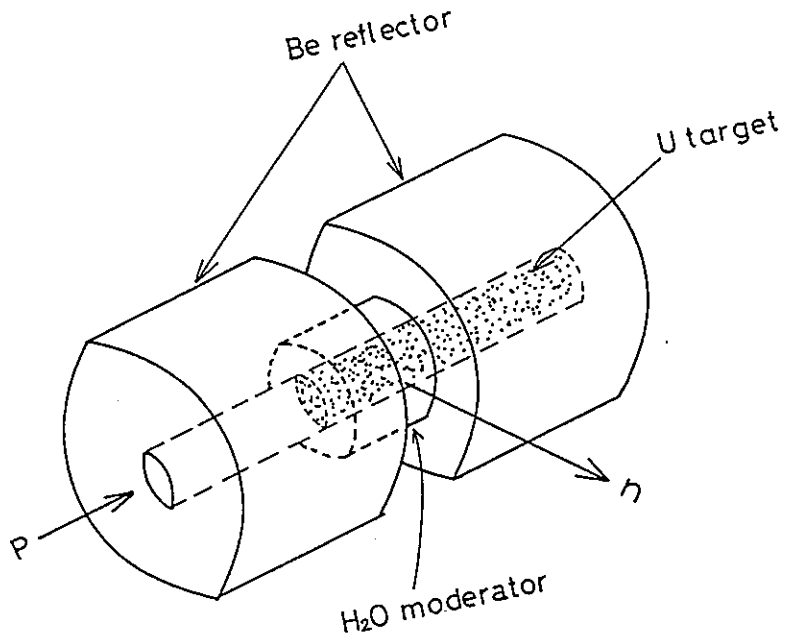

Fig. 7 Geometry in TWOTRAN calculation

Preliminary Experiment for Cold Moderator Assembly for KENS-II

(Cold neutron spectra emitted from the cold moderators)

Yoshiaki KIYANAGI, Kazuhiko INOUE, Noboru WATANABE*

and Hirokatsu IWASA

Department of Nuclear Engineering, Faculty of Engineering, Hokkaido University, Sapporo 060, Japan

* National Laboratory for High Energy Physics, Oho-machi, Tukuba-gun, Ibaraki-ken 305, Japan

High efficiency and reliable cold neutron source has been equipped in the KENS-I. It has been used effectively. Usefulness of solid methane for the cold moderator is established from the operations up to now. Solid methane has various merits for the pulsed cold neutron source. (a) Cold neutron intensity is higher than that of other materials. (b) Refrigeration and gas transfer systems are very simple because methane is used in solid phase in the operation and evaporates naturally in the off operation. This simplicity increases reliability, safety and stability. (c) Use at low temperature solid phase suppresses the polimalization rate extremely.

The KENS-II project aims to produce the neutron intensity one order higher than that in the KENS-I'. In the KENS-II the solid methane moderator will be expected to bring a large benefit for the neutronic aspects but the feasibility is not clear. The other candidate for the cold neutron moderator is liquid hydrogen if

methane can not be adopted. It is supposed, however, that the intensity will be reduced considerably compared with methane. Therefore, it is necessary to obtain the information about cold neutron gains for both moderator materials in the assemblies with reflectors simulating actual operation conditions. Then, we performed time-of-flight measurements to obtain such informations for methane and hydrogen.

Figure 1 shows an experimental set up at Hokkaido University linac. The neutrons emitted from a viewed surface of the moderator are measured by a ^{3}He counter placed at about 5.7 m from the moderator. The moderator assembly for reflected case is shown in Fig. 2. The reflector is graphite with a thickness of more than 20 cm. A Cd decoupler is inserted between reflector and moderator. The moderator chamber thicknesses were 5 cm and 15 cm for the hydrogen moderator and 5 cm for the methane moderator. The width and the height of the chamber were 15 cm and 14cm, respectively.

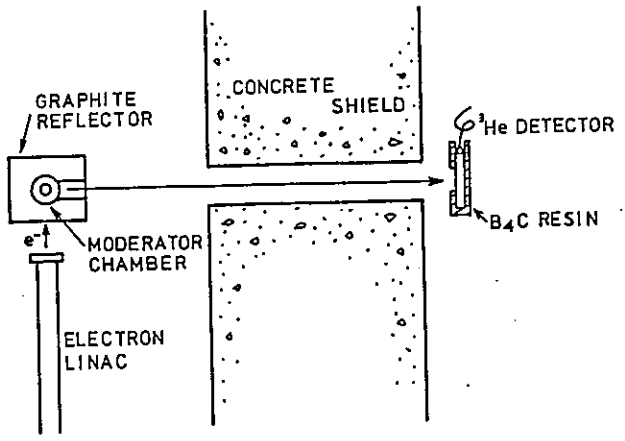

Fig. 1 Experimental arrangement.

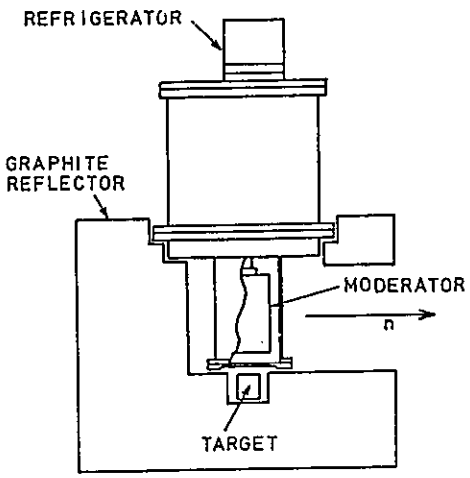

Fig. 2 Cold moderator assembly.

Figure 3 shows measured spectra in the case of the bare moderator. The intensity of the cold neutrons from the 15 cm thick hydrogen moderator is considerably larger than the one from the 5 cm thick hydrogen moderator. A characteristic peak around 15 meV is observed in both spectra from two hydrogen moderators. The intensity from methane moderator is much higher than that from hydrogen moderator at longer wave length. As a reference the neutron intensity from a polyethylene moderator is also depicted. In the case of bare system, the cold neutron intensity of 15 cm thick hydrogen moderator is about 2.7 times as large as the one of 5 cm thick hydrogen moderator. The results depicted in Fig. 4 demonstrate the effectiveness of reflector for the purpose of increasing neutron intensities. However, as seen from the figure, the ratio of intensities between 15 cm and 5 cm hydrogen moderators reduces to smaller value mentioned above. To clarify

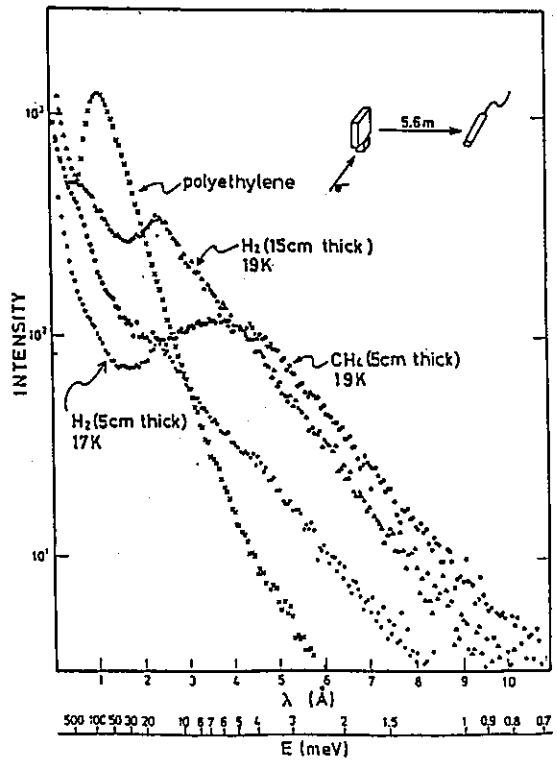

Fig. 3 Energy spectra for bare moderators.

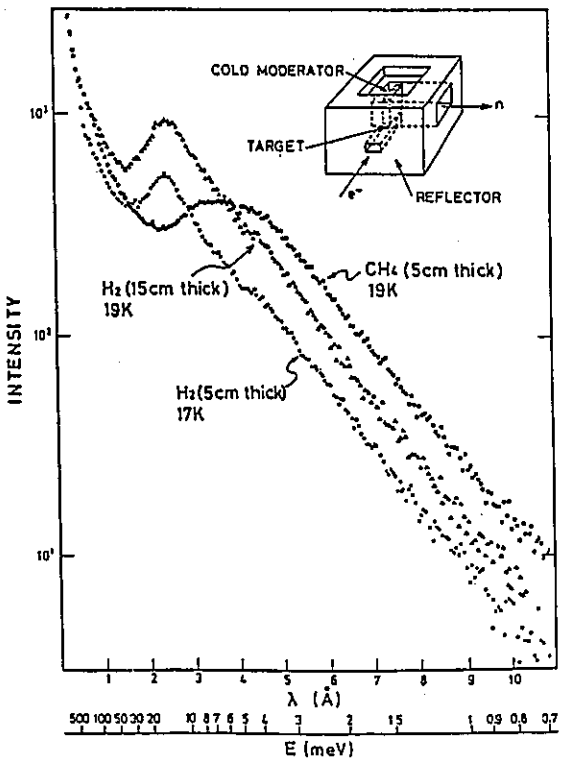

Fig. 4 Energy spectra for reflected moderators.

these circumstances, the ratio between the intensity from the methane moderator($I(CH_4)$) to that from hydrogen moderator($I(H_2)$) is shown in Fig. 5 in the case of reflected system. The cold neutron gain in 5 cm thick methane moderator is twice as large as the one in 15 cm hydrogen moderator and this value becomes three times in 5 cm hydrogen moderator. These results indicates that the thickness of 5 cm is not enough due to the small number density in liquid hydrogen. Figure 6 shows similar data for the case of bare moderator.

we are now preparing the emission time measurement.

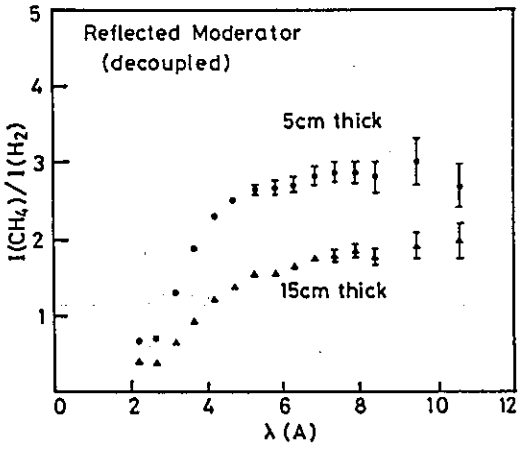

Fig. 5 Intensity ratios for reflected moderators.

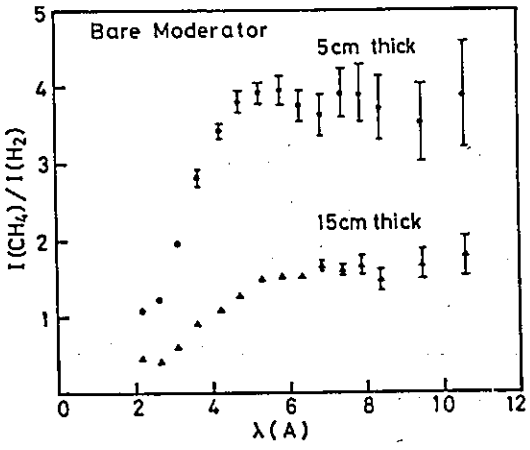

Fig. 6 Intensity ratios for bare moderators.

Recent progress of accelerator design study in the GEMINI project

Hiroshi SASAKI, Toshikazu ADACHI, Hitoshi BABA, Shigemi INAGAKI, Yoshiro IRIE, Naokatsu KANEKO, Tadamichi KAWAKUBO, Masayuki KUMADA, Satoru MATSUMOTO, Masayuki MIKI, Masaru NAKANISHI, Izumi SAKAI, Hirohiko SOMEYA, Yoshiharu YANO and Shigeki ARAI*

National Laboratory for High Energy Physics
Oho-machi, Tsukuba-gun, Ibaraki-ken, 305 Japan
* Institute for Nuclear Study University of Tokyo
Tanashi, Tokyo, 188 Japan

The design studies on the next generation pulsed spallation neutron and muon source at KEK started just after completion of BSF in 1980. In 1982, a rapid-cycling 800 MeV synchrotron was proposed as GEMINI project for the KENS-II program and the Super-BOOM project.[1)] This accelerator system of GEMINI aims at delivering a 500 μA proton beam in time average with repetition rate of 50 Hz. The beam should be extracted in the form of two shortly bunched beams, each of which is supplied to the neutron and muon facility, respectively. The accelerator will consist of an H^- ion source, a 1 MeV RFQ linac, a 100 MeV Alvarez-type linac driven by 400 MHz klystrons, and an 800 MeV rapid-cycling synchrotron. Parameters of the GEMINI synchrotron are listed in Table 1.

For past five years the design studies of the accelerator system for the GEMINI project were extensively performed. Recently scientists in the field of nuclear physics have proposed a future program so called Super Hadron project aiming to produce intense kaon and anti-proton beam. There is a movement toward the unification of GEMINI and Super Hadron Project. The accelerator system in this program is still open, but may include a high energy proton linac and a 1.5 to 2 GeV rapid cycling synchrotron for neutron and pion production, which corresponds to the GEMINI part, with or without a stretcher ring for nuclear physics. Anyway, the results obtained so far in the design studies for GEMINI will effectively contribute to the new program.

Table 1 A New Pulsed Neutron and Meson Source GEMINI

Maximum kinetic energy	800 MeV
Maximum intensity	6×10^{13} p/p
Repetition rate	50 Hz (100/3 Hz & 100 Hz)
Average beam current	500 μA
Injection energy	100 MeV
Injected H^- beam current	30 mA
Number of turns of injected beam	>240
Beam pulse width of injected beam	>330 μs
Magnet radius	7.00 m
Average radius	27.00 m
Number of period	24
Length of straight section	3.008 m
Structure	FBDO
Betatron frequency per revolution	
Horizontal	6.8
Vertical	7.3
Revolution frequency	0.757 - 1.489 MHz
Maximum beta-function	
Horizontal	12.4 m
Vertical	12.9 m
Momentum compaction factor	2.71×10^{-2}
Transition energy/rest energy	6.07
Beam emittance	
800 MeV	0.29 x 0.16 $(\pi \text{ mm rad})^2$
100 MeV	0.97 x 0.52 $(\pi \text{ mm rad})^2$
Number of bending magnets	24
Length of bending magnets	1.833 m
Length of quadrupole magnets	
Focussing magnet	0.525 m
Defocussing magnet	0.565 m
Bending magnet field	
800 MeV	0.697 T
100 MeV	0.212 T
Quadrupole magnet peak field gradient	4.18 T/m
Peak energy gain per turn	90.6 keV (60.4 keV)
Harmonic number	2
RF frequency	1.513 - 2.978 MHz
Maximum RF voltage	214 kV (166 kV)
RF bucket area	1.89 eV·sec
Number of RF stations	8
Incoherent space charge limit	7.2×10^{13} protons

Technical problems and R & D in the GEMINI project

There exist many technical problems to be solved in order to realize a high intensity proton synchrotron such as GEMINI, which accelerates protons with an intensity of the order of 100 times present operating accelerators :

1. Handling of beam with large emittance in extraction, transportation and targeting.
2. Flexibility of selection of focussing tune in the resonant magnet power supply.
3. Power dissipation due to eddy current in the magnet coil and core.
4. Dual-frequency mode operation of the guide magnet system for reduction of RF accelerating voltage.
5. Required high RF accelerating voltage and heavy beam-loading of RF accelerating system.
6. Realization of a very short bunched beam for μSR experiments.
7. Fabrication and impedance of a cross-sectionally large ceramic vacuum chamber.
8. Focussing quadrupole magnet built in the drift tube of the 400 MHz Alverez linac.
9. Beam loss, activation and radiation damage of accelerator components, and so on.

Some of those items mentioned above are in close relation to each other. R & D for some of technical problems has been done and is still in progress. Results and the present status of R & D will be described below.

Beam chopper for reduction of beam loss[2)]

Beam loss in a GEMINI-like synchrotron with a large trans-verse acceptance mainly comes from mismatching between the beam emittance and the acceptance in the longitudinall phase space at injection. In order to reduce such a beam loss in RF trapping process, a beam chopper has been developed, which sweeps out a part of the injection beam to the linac in synchronization with the RF accelerating voltage

Table 2 Parameters of beam chopper for 1 MeV H^- ion beam

type of deflector	travelling-wave type
length of deflector	1 m
aperture of deflector	25 mm
width of deflector	100 mm
kick angle	10 mrad
longitudinal velocity of deflecting pulse	14 mm/ns
voltage of deflecting pulse	1 kV
length of pulse train	> 420 μs
width of deflecting pulse	> 130 ns
frequency of deflecting pulse	1.513 MHz

Table 3 Parameters and performance of model deflector

Pitch of strip conductor	16.0 mm	
width of strip	15.5 mm	
thickness of dielectric plate	3.6 mm	
width of deflector	140 mm	
length of deflector	500 mm	
	calcu.	measured
characteristic impedance	50 ohm	49.1 ohm
longitudinal velocity of deflecting pulse	7.6 mm/ns	7.7 mm/ns
rise and fall time	< 25 ns	
output voltage of amplifier	± 500 V	

of the synchrotron. According to a computer simulation it was confirmed that the trapping efficiency more than 99 % is achievable with the 20 % chopped linac beam having a full momentum spread of 0.75 % injected into a RF bucket which is provided by 65.5 kV RF accelerating voltage. For 1 cm input aperture of the drift tube of the linac, a 1 m long beam chopper must fulfill the conditions listed up in in Table 2 to deflect a 1 MeV H^- ion beam. A coaxial-plate type deflector electrode, which is made of a 3.6 mm thick epoxy plate

printed by copper foil on the surface as shown in Fig. 1, was driven by a power mos FET. The parameters and performance are listed in Table 3. The chopper will be formed by two deflector electrodes and driven in push-pull mode.

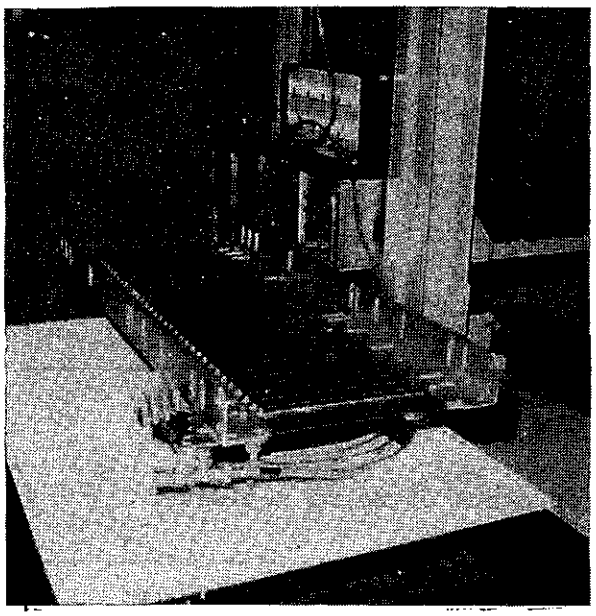

Fig.1
model of deflector electrode for beam chopper

Permanent quadrupole magnet built in the drift tube[3,4)]

For simplicity and convenience in maintenance, permanent quadrupole magnets are proposed to be built in the drift tubes of the 400 MHz Alverez linac. Transverse acceptance strongly depends upon the field gradient of the focussing quadrupole magnet and the maximum attainable acceptance is given by the field gradient of the magnet in the first drift tube as shown in Fig. 2. The field gradient more than 150T/m is required in order to achieve a normalized acceptance of several mm.mrad with a drift tube with 10 mm bore diameter.

On the other hand, there is every reason to expect that a very high field gradient will be realized, i.e., recent developments of sintered-metal permanent magnet containing rare earth element such as SmCo or NdFeB and its application to segmented magnet proposed by K. Halbach.[5)] The surprising fact with such anisotropically magnetized sectors, which are positioned along a circumference, is that the maximum field strength is able to reach a level higher than the remanent field of the magnet material itself at the central bore.

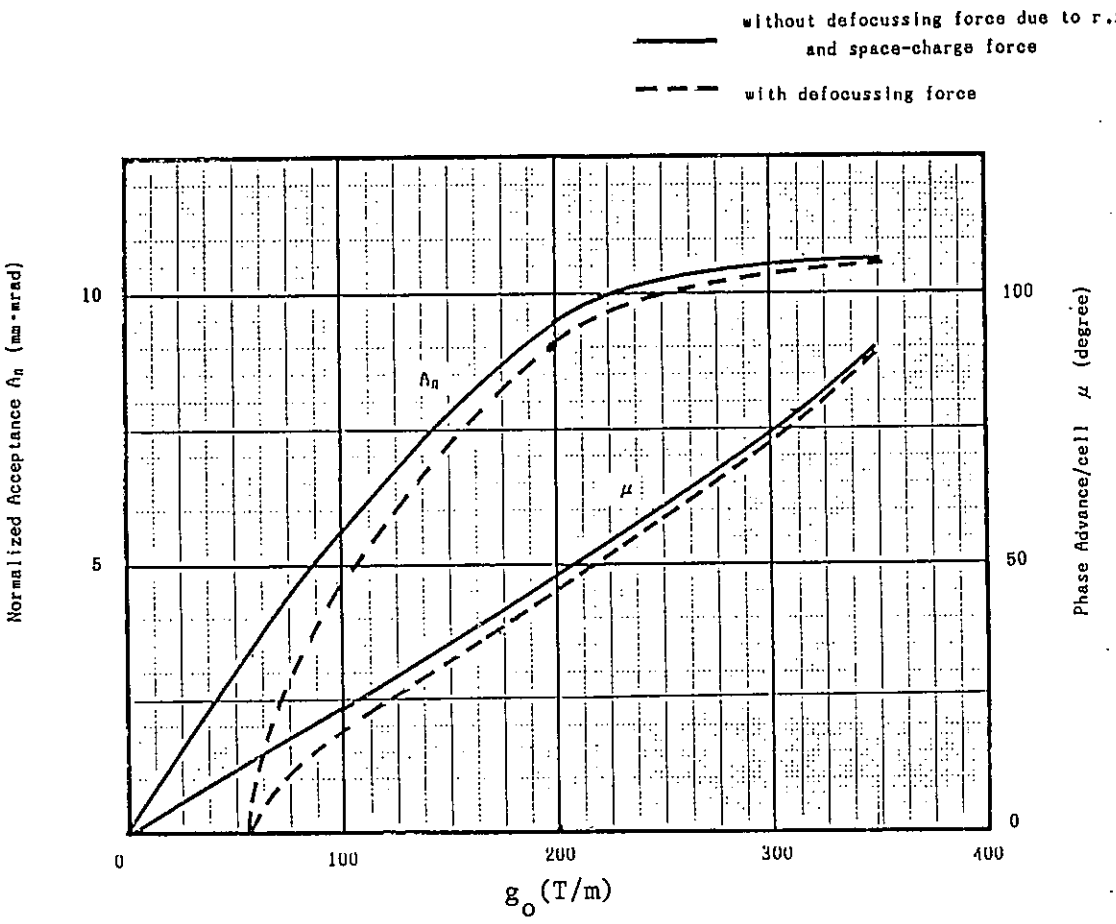

Fig. 2 hormalized acceptance and phase advance per-cell for the field gradient of the first quadrupole magnet in the 100 MeV Alverez linac

Four different types of high gradient permanent quadrupole magnets, of which two magnets are conventional iron-pole tip SmCo magnet Mark I and III and the others are segmented magnet Mark II and IV made of SmCo and NdFeB respectively, are fabricated and tested on the assumption of the quadrupole magnet to be built in the first drift tube. Fig. 3 shows the relationship between the field gradient in the central bore and the field strength on the pole face of those magnets together with fabricated ones at other laboratories. The attained pole tip field and field gradient for the four model magnets Mark I to IV are 0.77, 1.21, 0.455 and 1.65 T and 128, 161, 76 and 254T/m, respectively. Thus, we realized the world highest field and field gradient by using the rare-earth permanent magnet material SmCo of 22 MGOe in $(BH)_{max}$ and NdFeB of 30 MGOe. It was also confirmed that a drift tube housing the permanent magnet was possible to be welded by means of a laser beam.

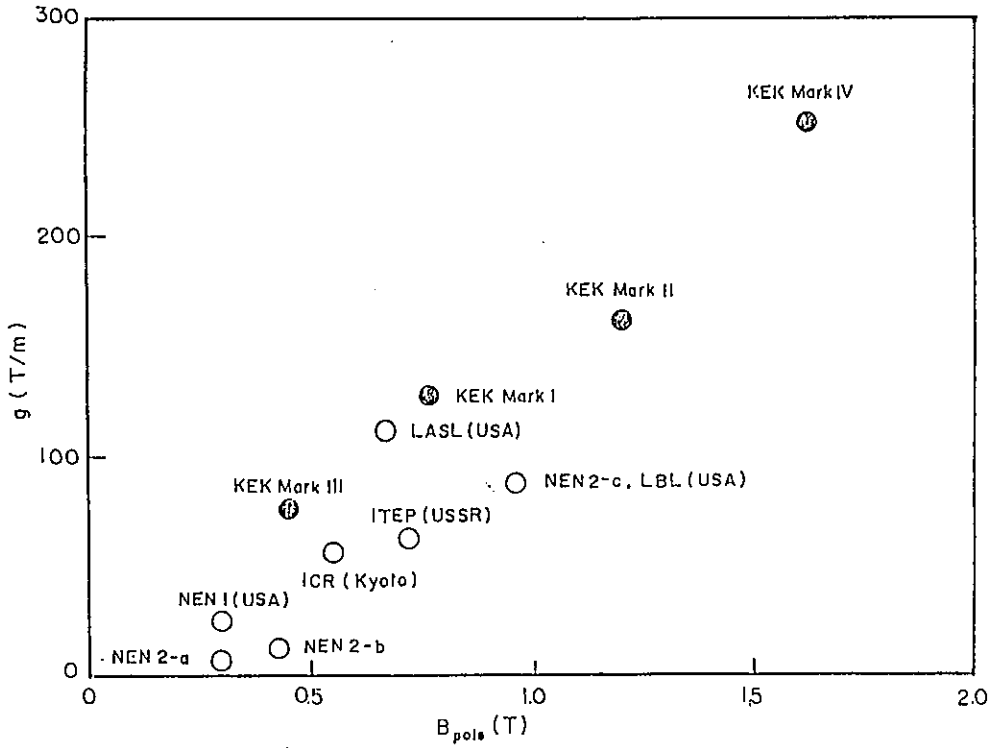

Fig. 3 Pole-tip field and field gradient of the permanent quadrupole magnets fabricated at various laboratories

Operation of rapid-cycling synchrotron magnet in dual frequency mode

The high repetition rate (50Hz) of the GEMINI synchrotron makes the use of a resonant type power supply system for the guide magnet advantageous. The system operates in a dual frequency mode, where the magnet current increases with a half-cycle cosine waveform of 100/3 Hz during acceleration period and resets back to the injection value with another faster waveform of 100 Hz. Thus, it is possible to reduce the required maximum RF accelerating voltage by lowering the rise rate of the magnetic field in keeping the repetition rate of 50 Hz constant as compared with a single resonant frequency mode. In GEMINI, the RF voltage of 214 kV required in the single frequency system can be reduced to 166 kV by replacing to the dual frequency system. In order to operate the magnet system in such a mode, a part of resonant capacitor should be removed from a resonant circuit by means of a suitable switching device. An inverter-type thyristor was proposed was the switching device originally by ANL people.[6] In our circuit, the inverter-type thyristor is replaced by a gate-turn-off (GTO) thyristor. By this improvement, the switching circuit is very simplified.[7] In a tentative design of the GEMINI magnet system, the

GTO thyristor should switch off a peak current of about 1.6 kA and with stand a forward voltage of 16.8 kV at off-state.

In order to demonstrate the principles of this system a model circuit as shown in Fig. 4 was designed and built. The model circuit operated in stable by using a GTO thyristor with a nominal controllable current of 90 A and a forward voltage of 600 V at off-state.[8] As a high power test, moreover, we have constructed a full AC power supply for exciting a proto-type bending magnet of GEMINI, in which the GTO thyristor should control a peak current of 1.6 kA under the condition of the forward and reverse voltage of 3.3 kV and 1.1 kV at off-state. Output waveforms are shown in Fig. 5. Even in this case, however, the forward voltage at off-state of GTO thyrister is too low as compared with those of the present design of GEMINI. It may be necessary to reduce those voltages in the design of GEMINI by any suitable means, e.g., increase of the number of mesh in the resonant circuit, parallel connection of exciting coils of resonant magnet, reduction of the number of turns of magnet coil, and so on.

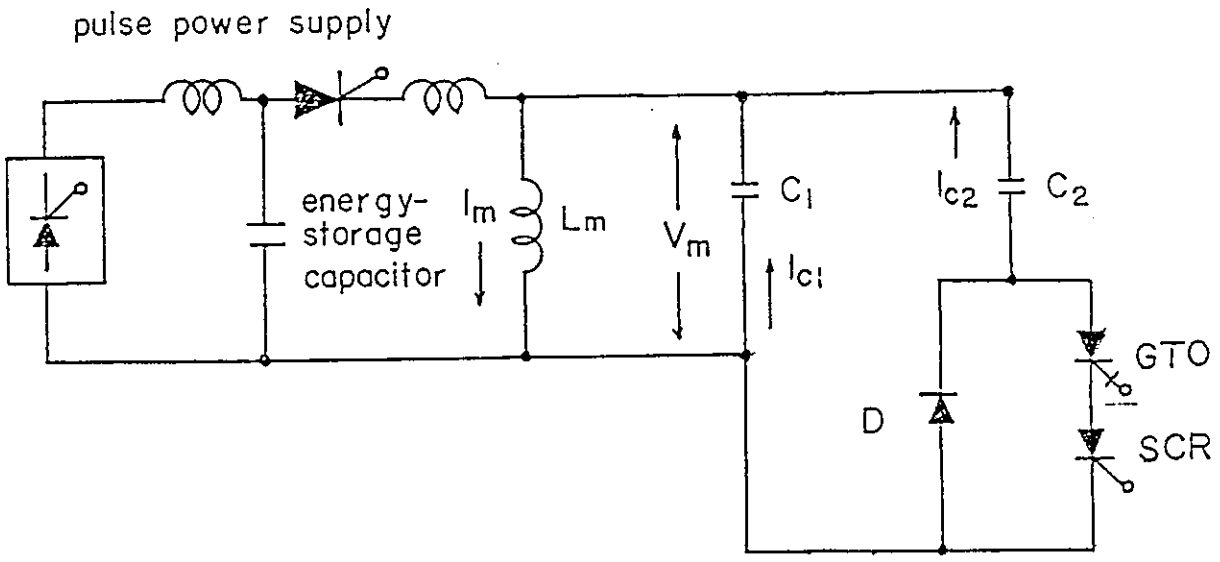

Fig. 4 Simplified circuit of a pulse power supply for dual-frequency-mode operation of rapid cycling magnet

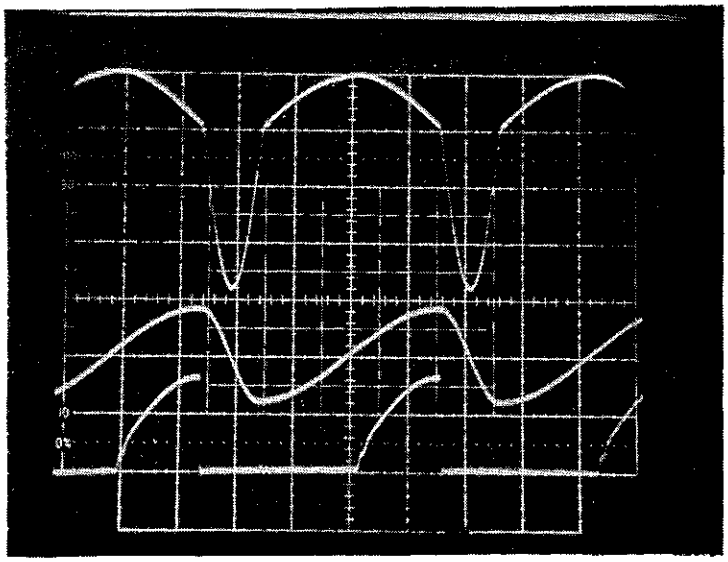

V_m : 1.0kV/div.

I_m : 1.67kA/div.

I_{GTO} : 0.83 kA/div.

Horizontal scale : 5ms/div.

Fig. 5 Output waveform of the pulse power supply

Stranded cable for the exciting coil of rapid-cycling magnet

On the assumption that an infinitely long conductor is imposed by an AC magnetic field and the width of the conductor is smaller than the skin depth of the conductor material, the power dissipation due to an induced eddy current is given by

$$P_{eddy} / volume = (\omega w B)^2 / 24\sigma ,$$

where ω is the angular frequency of the AC magnetic field (rad/sec), B the amplitude of the field (Tesla), w the width of conductor perpendicular to the magnetic field (m) and σ the specific resistance of the conductor material (ohm•m). To wind a magnet coil with a fine conductor in many turns for the reduction of the eddy-current power dissipation is limited by an induced high AC voltage across the coil. In the booster synchrotron for the 12 GeV proton synchrotron at KEK, which operates with a repetition rate of 20 Hz, the magnet coil was wounded by two insulated hollow conductors in parallel and the input and output terminals of pancakes were transposed in their connection points. If the same procedure is applied to the GEMINI magnet, the power dissipation due to eddy current will be saved by about 25 % by

using a parallel circuit of hollow copper conductors of 19 mm x 23 mm with a water cooling channel of 6 mm x 12 mm. In spite of this, a quarter of total power consumption of the magnet corresponds to the eddy-current power dissipation as shown in Table 5, which amounts to 600 kW in total.

As a conductor free from the eddy-current power dissipation a stranded cable has been developed. The cross section of the cable is 30 mm x 30 mm. The cable consists of 84 aluminum wires of 3 mm in diameter and a 14 mm outer diameter and 1.5 mm thick copper pipe, carrying 1.65 kA DC current and 0.88 kA peak AC current of 50 Hz. Fig. 6 shows an exterior and a cross sectional view of the cable. In taking the form of magnet coil, the minimum bending radius of the cable was limited to 10 cm while the goal was less than 8 cm. This will be attainable by choosing a more suitable aluminum alloy for the conductor material. Any process was not applied on the surface of the aluminum wires to insulate each other at manufacturing the cable. In the fabrication process of the magnet coil, however, it was impregnated by epoxy resin in vacuum for the surface insulation of wires and for the reduction of aging effects of electric properties due to mechanical vibration.

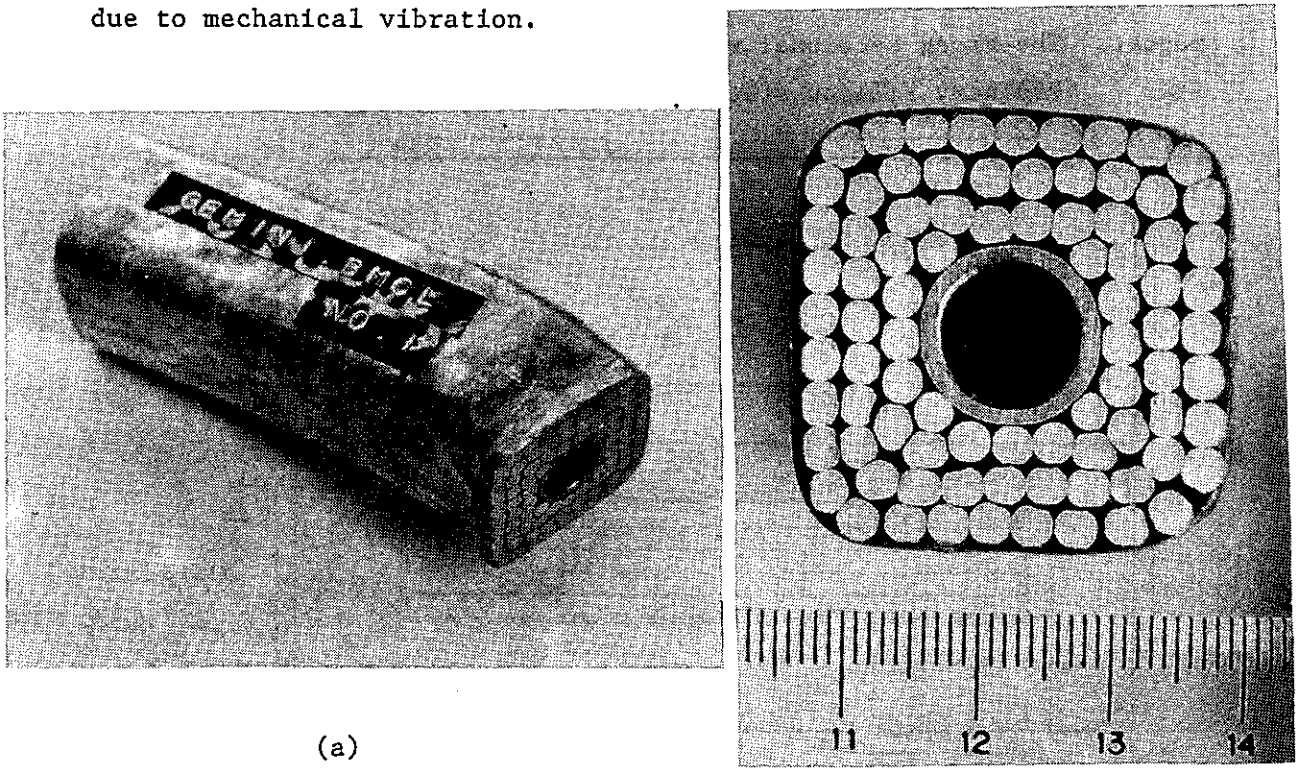

(a) (b)

Fig. 6 Stranded cable for magnet coil

Table 5 Power Consumption of GEMINI magnet with a parallel circuit of hollow copper conductor of 19 mm x 23 mm in outer dimensions and with a water channel of 6 mm x 12 mm

power loss	BM	QM
eddy current loss	13.6 kW/mag	5.2 kW/mag
ohmic loss	36.1	20.8
iron loss	3.8	1.1
total power loss	53.5 kW/mag	27.1 kW/mag

Proto-type bending magnet

A proto-type bending magnet for the GEMINI synchrotron has been constructed for the purpose to investigate electro-magnetic behaviours of the magnet in the dual frequency mode in addition to the check and survey of the mechanical and electro-magnetic properties of the magnet. The cross sectional view of the proto-type magnet is shown in Fig. 7. Ordinary silicon steel laminations of 0.5 mm in thickness are

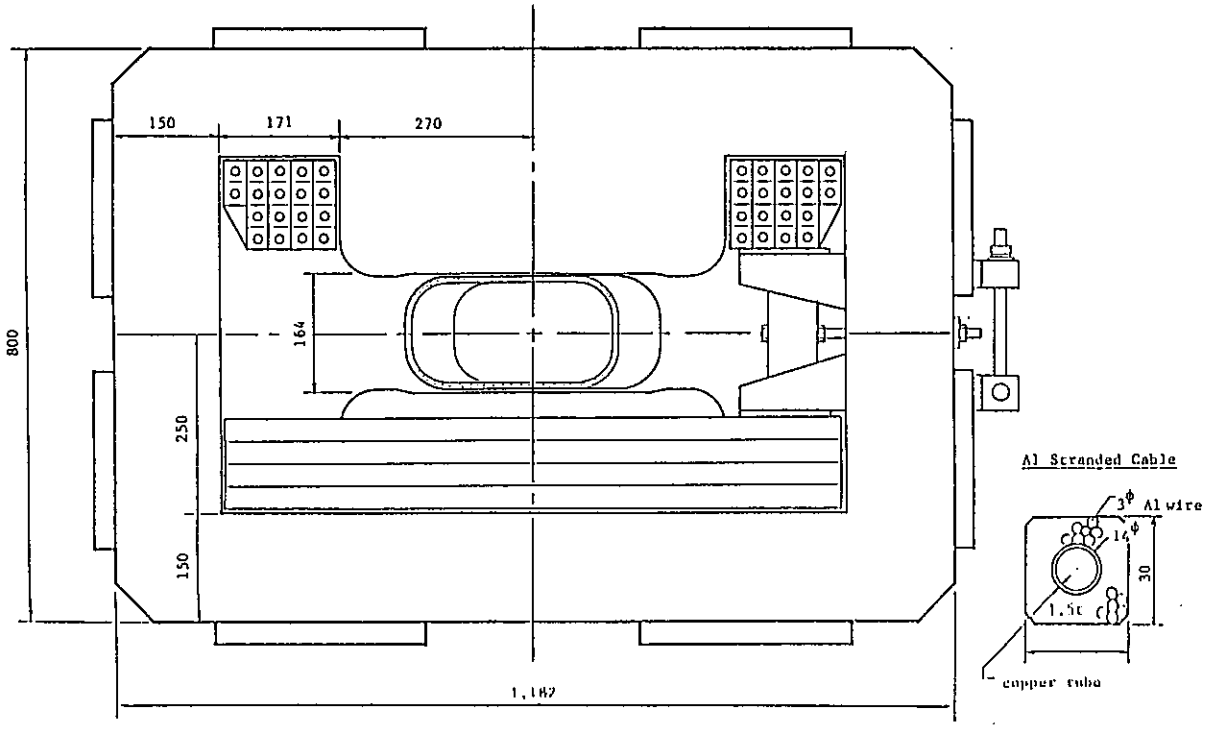

Fig. 7 Cross sectional view of Proto-type magnet for GEMINI

stacked in length of 1.8 m and welded with tie bars and end plates made of stainless steel. For simplicity, the magnet is not fanning but straight in shape because of a small segitta of one tenth of the pole width. Accelerator components in the GEMINI synchrotron, which aims at delivering a very intense proton beam, might be highly activated in spite of every effort to depress the beam loss in acceleration period. Therefore, working under high radiation level will be assigned, and the magnet should be capable of quick handling in the decomposition of magnet yoke and the disconnection of feeder line.

RF system

RF acceleration system is the most important accelerator component especially for hight intensity accelerator such as GEMINI. It is not too much to say that the RF acceleration system is every thing in the synchrotron from the view point of the performance of accelerator. The circulating beam current in the GEMINI synchrotron is about 10 A in the DC component or 20 A in the first harmonic component at the instant when the maximum accelerating RF voltage is required. In order to keep the phase shift of RF voltage due to the beam loading within 0.1 radian, the output impedance of the RF power supply system should be less than 50 ohms for the maximum cavity voltage of 10 kV.

A prototype RF amplifier with cathode follower is under development to investigate the feasibility for GEMINI RF system. Although cathode follower has a notorious difficulty that the gain is less than unity, it has a great advantage that it can provide a low output impedance. A single 40 kW plate-dissipation triode (Eimac 3CW 40,000H3) excites two ferrite-loaded cavities which are coupled by eight-turn bias winding. DC power supply in hand is used for biasing the cavity ferrite, and thus measurements on the characteristic of the present system were made under an unswept frequency mode.

An LRC resonating circuit was adopted in the drive stage to save the driving power. Shunt impedance of cavity itself and output

impedance seen by the beam were measured by low-level excitation. Shunt impedance obtained at 2 MHz agrees with the calculation within 10 % error. As for an output impedence, 40 to 80 ohms were obtained over a whole frequency range of the GEMINI synchrotron. Maximum output voltage across the gap is around 1.0 kV so far. Another power amplifier which is ready for use will be connected soon in paralled with the present one. The two amplifiers are expected to produce enough voltage to test the voltage limitation due to the non-linear response of ferrite ring.

References

1) H. Sasaki and GEMINI study group, Proc. of the 7th meeting of the international collaboration on advanced neutron sources, Chalk River Nuclear Lab. 50, Sept. 1983.
2) Y. Yano, T. Kawakubo, M. Kumada and H. Sasaki, Proc. of 5th Symp. on Accelerator Science and Technology, KEK, Sept. 1984, 166.
3) M. Kumada, N. Kaneko, H. Baba, S. Inagaki and H. Sasaki, Proc. of the 9th meeting on Magnet Technology, 1985, Zülich.
4) M. Kumada, S. Inagaki, N. Kaneko, H. Baba and H. Sasaki, Proc. of the 11th meeting Linac Accelerator, KEK, Sept. 1986, 120.
5) K. Halbach, Nucl. Instr. and Meth., 169 (1980) 1.
6) M. Foss and W. Praeg, IEEE trans. Nucl. Sci. NS-28, 2856 (1981).
7) H. Someya, T. Adachi, M. Kumada, H. Baba, S. Matsumoto, H. Sasaki and I. Sakai, the 4th Symp. on Accelerator Science and Technology, at IPCR (1982) 317.
8) H. Someya, T. Adachi, Y. Irie, Y. Yano and H. Sasaki, the 5th Symp. on Accelerator Science and Technology, KEK, (1984) 221.

APPENDICES

Members of Committee for Booster Synchrotron Utilization Facility

DOKE, Tadayoshi	(Waseda University)
ENDOH, Yasuo	(Tohoku University) (86.4--)
FUKUMOTO, Sadayoshi	(KEK, Accelerator Department)
HIRABAYASHI, Hiromi	(KEK, Director of Experimental Planning & Program Coordination)
ISHIKAWA, Yoshikazu	(Tohoku University) (--86.3)
KAMEI, Tohru	(KEK, Director of Accelerator Department)(--86.3)
KIHARA Motohiro	(KEK, Director of Accelerator Department)(86.4--)
KATOH, Kazuaki	(KEK, Engineering Research & Scientific Support Department)
KITAGAWA, Toshio	(University of Tsukuba)
SASAKI Hiroshi	(KEK, Booster Synchrotron Utilization Facility)
TANABE, Kohsai	(Saitama University) (Chairman)
WATABABE, Noboru	(KEK, Booster Synchrotron Utilization Facility)
YAMAZAKI, Toshimitsu	(University of Tokyo)

List of Staffs in Booster Synchrotron Utilization Facility

Director

SASAKI, Hiroshi	ADACHI, Toshikazu	ARAI, Masatoshi
	IKEDA, Susumu	IRIE, Yoshiro
KANEKO, Naokatsu	MASUDA, Yoshihiro	MIKI, Masayuki (--85.8)
MISAWA, Masakatsu	NAKANISHI, Masaru	SATOH, Setsuo
WATANABE, Noboru	YANO, Yoshiharu	

Visiting Scientist

ARAI, Shigeaki (University of Tokyo)
ISHIKAWA, Yoshikazu (Tohoku University) (--86.3)
ENDOH, Yasuo (Tohoku University) (86.4--)

List of Publications (1981 - Oct.1986)

Publications in Periodical journals and Conference Proceedings

General

The Booster Synchrotron Utilization Facility at KEK
H. Sasaki
Proc. ICANS-IV (1981) 77

Present Status of the KENS Facility
Y. Ishikawa
ibid. 89

Present Status and Future Program of KENS
N. Watanabe, H. Sasaki, Y. Ishikawa, Y. Endoh and K. Inoue
Proc. ICANS-V (1981) A2

Neutron Scattering Experiments at Pulsed Spallation Neutron Source
Ishikawa, Y. Endoh, N. Watanabe and K. Inoue
Proc. Symp. Neutron Scattering (Argonne, Aug. 12-13, 1981)

Status and Neutron Scattering Experiments at KENS
N. Watanabe, H. Sasaki, Y. Ishikawa, Y. Endoh and K. Inoue
Proc. ICANS-VI (1982) ANL-82-80, P. 15

Studies of Condensed Matter with Pulsed Neutron Source (KENS)
Y. Ishikawa
Physica 120B (1983) 3

Present Status of Booster Synchrotron Utilization Facility at KEK
H. Sasaki
Proc. 4th Symp. on Accelerator Science and Technology (RIKEN, 1982) 21

Present Status of Booster Synchrotron Utilization Facility at KEK
H. Sasaki
Proc. ICANS- VII (1983) 15

Neutron Scattering and μSR
Y. Ishikawa
Proc. Yamada Conf. VII, Muon Spin Rotation (Shimoda, 1984)
Hyperfine Interactions 17-19 (1984) 17

Neutron Scattering Spectrometers at KENS Cold Spallation Neutron Source
Y. Ishikawa, Y. Endoh and K. Inoue
Proc. International Conf. on Neutron Scattering in '90s (Julich, 14-18 Jan. 1985), IAEA, VIENNA, IAEA-CN-46/027 (1985) 285

Present Status and Future Project of KENS Facility
Y. Ishikawa and the KENS Group
Proc. ICANS-VIII (1985) 17

Pulsed Polarized Neutron Studies at KENS
Y. Endoh and Y. Ishikawa
Proc. Int. Conf. on Neutron Scattering (Santa Fe, Aug. 19-23, 1985)

Cold Neutron facility, KENS Neutron scattering in the Ninties
Y. Ishikaws, Y. Endoh and K. Inoue
(1985) p 285-290 (IAEA Vienna)

Present Status and Future Project of KENS Facility
Y. Ishikawa and the KENS group
Proc. ICANS-VIII (1985)17

Physics of Spallation Neutrons
Y. Endoh
Phys. Chem. Research 80 (1986) 38-43

Accelerator and Beam Line

500 MeV Proton Beam Line for KEK Booster Synchrotron Utilization Facility
I. Sakai, H. Someya, T. Adachi, Y. Irie and H. Sasaki
Proc. 3rd. Symp. on Accelerator Science and Technology (Research Center for Nuclear Physics, Osaka Univ. 1980) 33

Injection System of H^- Beam in KEK Booster Synchrotron
T. Kawakubo, H. Sasaki, I. Sakai and M. Suetake
Proc. 3rd. Symp. on Accelerator Science and Technology (Research Center for Nuclear Physics, Osaka Univ. 1980) 31

BSF Beam Control System
Y. Irie
Proc. ICANS-IV (1981) 406

Proton Synchrotron for Intense Neutron and Meson Beam
T. Adachi, S. Inagaki, Y. Irie, N. Kaneko, T. Kawakubo, N. Kumada, I. Sakai, H. Sasaki, Y. Someya, H. Baba, S. Matsumoto, M. Miki and Y. Yano
Proc. 4th Symp. on Accelerator Science and Technology, (RIKEN, 1982) 281

Bi-resonant Circuit for Excitation of Synchrotron Magnet
H. Someya, T. Adachi, M. Kumada, H. Baba, S. Matsumoto, H. Sasaki and I. Sakai
Proc. 4th Symp. on Accelerator Science and Technology, (RIKEN, 1982) 317

Optimization on the End-Shaping of a Quadrupole Magnet
M. Kumada, H. Sasaki, H. Someya and I. Sakai
Nucl. Instr. Meth. 211 (1983) 283

Accelerator Project GEMINI for Intense Pulsed Neutron and Meson Source at KEK
H. Sasaki and GEMINI Study Group
Proc. ICANS-VII (1983) 50 and Proc. 5th Symp. on Accelerator Science and Technology (KEK, 1984) 394

Magnetic field measurement of high gradient $SmCo_5$ permanent quadrupole magnets
M. Kumada, N. Kaneko, S. Inagaki, H. Baba and H. Sasaki
Proc. 5th Symp. on Accelerator Science and Technology (KEK, 1984) 203

Application of a GTO thyristor to a dual resonant frequency circuit for excitation of synchrotron magnet
H. Someya, T. Adachi, Y. Irie, Y. Yano and H. Sasaki
Proc. 5th Symp. on Accelerator Science and Technology (KEK, 1984) 221

The first acceleration test of H^- charge exchange injection in the KEK Booster
T. Kawakubo, I. Sakai, M. Suetake and H. Sasaki
KEK Report 84-6 and Proc. 5th Symp. on Accelerator Science and Technology (KEK, 1984) 274

Application of a GTO thrystor to a dual resonant frequency circuit for the magnet of a rapid-cycling synchrotron
H. Someya, T. Adachi, H. Baba, Y. Irie, S. Matsumoto,
The 1985 Particle Accelerator Conf., Vancouver, May 1985

250T/m rare earth permanent quadrupole magnet
M. Kumada, H. Baba, N. Kaneko, S. Inagaki and H. Sasaki
The 9th International Conf. on Magnet and technology, Zurich, Sept. 1985

Beam Loading Effect in the SNS Synchrotron
Y. Irie
SNS/RF/N2/85 (Rutherford Appleton Laboratory)

Application of a GTO thyristor to a dual resonant frequency circuit for the magnet of a rapid-cycling synchrotron
H. Someya, T. Adachi, H. Baba, Y. Irie, S. Matsumoto, H. Sasaki and Y. Yano
IEEE NS-32 (1985) 3775

Neutron Source

KENS Target Station
N. Watanabe, S. Ikeda and Y. Ishikawa
Proc. ICANS-IV (1981) 181

KENS Cold Neutron Source
S. Ikeda, Y. Ishikawa and K. Inoue
ibid. 200

Some Neutronic Aspects of Solid Methane Moderator System
Proc. ICANS-V (1981) 519
N.watanabe, S. Ikeda and Y. Ishikawa

Characteristics of KENS Cold Neutron Guide Tube
J. Mizuki, Y. Endoh, Y. Ishikawa and S. Ikeda
Proc. ICANS-IV (1981) 521

KENS Radiation Shield
S. Ban and H. Hirayama
Proc. ICANS-IV (1981) 355

KENS Radiation Activity: Structural materials
H. Hirayama and S. Ban
ibid. 376

Radioactivity and Radiolysis of the Solid Methane used as a Cold Neutron Moderator in the KENS Target Assembly
K. Kondo and K. Hozumi
ibid. 381

Experimental Studies of the Induced Radioactivities in a Uranium Target
K. Katoh, S. Ban, H. Hirayama, S. Ikeda, K. Irie, K. Kondo, M. Miyajima, S. Sato, N. Watanabe and S. Yamaguchi
ibid. 392

Grooved Cold Moderator Test
K. Inoue, Y, Kiyanagi, H. Iwasa, N. Watanabe, S. Ikeda, J.M. Carpenter and Y. Ishikawa
Proc. ICANS-VI (1982) ANL-82-80, P. 391

Grooved Cold Moderator at KENS
Y. Ishikawa, S. Ikeda, N. Watanabe, K. Kondoh, K. Inoue, Y. Kiyanagi, H. Iwasa and K. Tsuchihashi
Proc. ICANS-VII (1983) 230

On the 20K Methane Moderator and its Application to the Intense Pulsed Cold Neutron Source
K. Inoue
Nucl. Inst. Meth. 216 (1983) 537

Neutron Scattering

Instrumentation

The High Intensity Total Scattering Spectrometer (HIT)
N. Watanabe, T. Fukunaga, T. Shinohe, K. Yamada and T. Mizoguchi
Proc. ICANS-IV (1981) 539

Large Analyser Mirror Low Energy Spectrometer LAM(KEK) and LANDAM(HU), and Electron linac Cold Source
K. Inoue, Y. Kiyanagi, M. Kohgi, Y. Ishikawa, N. Watanabe, H. Iwasa, Y. Sakamoto and K. Jinguji
Proc. ICANS-IV(1981) 592

Multi Analyser Crystals Spectrometer at KENS
K. Tajima, K. Kanai, Y. Ishikawa, S. Tomiyoshi and C.G. Windsor
Proc. ICANS-IV (1981) 600

Small Angle Scattering Spectrometer (KENS-SAN)
Y. Ishikawa, M. Furusaka, M. Arai, N. Niimura, S. Ikeda and, K. Hasegawa
Proc. ICANS-IV (1981) 563

Time of Flight Spectrometer with Optical Polariser
Y. Endoh, J. Mizuki and H. Ono
Proc. ICANS-IV (1981) 609

Neutron Polarisation by Polarised Proton Filter
S. Ishimoto
Proc. ICANS-IV (1981) 630

The Ultra Cold Neutron Production at KENS
H. Yoshiki
Proc. ICANS-IV (1981) 715

KENS Data Acquisition System
N. Niimura, M. Kohgi, M. Arai, S. Tomiyoshi, K. Tajima, M. Isobe, M. Furusaka and Y. Fujino
Proc. ICANS-IV (1981) 663

Application of Position Sensitive Detectors to Structure Analysis Using Pulsed Neutron Source
N. Niimura, Y. Ishikawa, M. Arai and M. Furusaka
Proc. Symp. Neutron Scattering (Argonne, Aug. 12-13, 1981)

Polarized Epithermal Neutron Spectrometer at KENS
M. Kohgi
Proc. ICANS-VI (1982), ANL-82-80 P.171

Test of a Resonance Detector Spectrometer for Electron-Volt Spectroscopy
J.M. Carpenter, N. Watanabe, S. Ikeda, Y. Masuda and S. Sato
Proc. ICANS-IV (1982), ANL-82-80, 265

Analyzer TOF Spectrometer (CAT) for High Energy Incoherent Neutron Scattering
N. Watanabe, S. Ikeda and K. Kai
Proc. ICANS-VI, ANL-82-80 (1982) 279

A Multi Analyser Crystal Spectrometer (MAX) for Pulsed Neutron Source
K. Tajima, Y. Ishikawa, K. Kanai, C.G. Windsor and S. Tomiyoshi
Nucl. Instr. Meth. 201 (1982) 491

Multi-Analyzer Crystal Spectrometer (MAX) for Pulsed Neutron Source and Its Application to Various Problem
K. Tajima, Y. Ishikawa, K. Kanai, S. Tomiyoshi and Y. Todate
Physica 120B (1983) 136

Polarized Neutron Scattering using Pulsed Spallation Neutron Source at KEK
Y. Endoh, Y. Sasaki, H. Ono, S. Mitsuda and S. Ikeda
Physica 120B (1983) 45

Time Focussing and Resolution in Resonance Detector Neutron Spectrometer
J.M. Carpenter and N. Watanabe
Nucl. Instr. Meth. 213 (1983) 311

A Resonance Detector Spectrometer at KENS
J.M. Carpenter, N. Watanabe, S. Ikeda, Y. Masuda and S. Sato
Physica 120B (1983) 126

Crystal Analyzer TOF Spectrometer (CAT)
S. Ikeda, N. Watanabe and K. Kai
Physica 120B (1983) 131

Position Sensitive Neutron Detectors using Li-6 Glass Scintillator and Fibre Optic Encoding
N. Niimura, K. Yamada, T. Kubota, A. Matsumoto and S. Hoshino
Nucl. Instr. Meth. 211 (1983) 203

Position Sensitive Neutron Detectors using Li-6 Glass Scintillators
N. Niimura, K. Yamada, T. Kubota, A. Matsumoto and S. Hoshino
Physica 120B (1983) 104

Detector Resolution of a Resonance Detector Neutron Spectrometer
H. Rauh and N. Watanabe
Nucl. Instr. Meth. 222 (1984) 507

Experimental Study of the Time-Focussing Effect in Resonance Detector Neutron Spectrometer
H. Rauh, S. Ikeda and N. Watanabe
Nucl. Instr. Meth. 224 (1984) 469

Resonance Detector Instruments
N. Watanabe
Proc. 1984 Workshop on High-Energy Excitation in Condensed Matter (Los Alamos, Feb.13-15, 1984) P.56

Resonance Detection Methods in Spectrometers
N. Watanabe
Proc. International Conf. on Neutron Scattering in '90s (Jülich 14-18, Jan. 1984), IAEA, VIENNA, IAEA-CN-46/026 (1985) 279

High Resolution TOF Crystal Analyzer Spectrometer for Largy Energy Transfer Incoherent Neutron Scattering
S. Ikeda and N. Watanabe
Nucl. Instr. Meth. 221 (1984) 571

Simple thermo-level meter for He I and He II by a dynamic method
H. Yoshiki
Cryogenics (1984) 704

Crystal Analyser Type Quasielastic Spectrometers Using the Pulsed Cold Neutron Source
K. Inoue, Y. Ishikawa, N. Watanabe, K. Kaji, Y. Kiyanagi, H. Iwasa and M. Kohgi
Nucl. Instr. Meth. A238 (1985) 401

TOF Type Small Angle Scattering Spectrometer SAN at KENS Pulsed Cold Neutron Source
Y. Ishikawa, M. Furusaka, N. Niimura, M. Arai and K. Hasegawa
Proc. ICANS-VIII (1985) 454

TOF Spectrometer with Optical Polarizer for Cold Neutrons
Y. Endoh, S. Ikeda, S. Mitsuda and H. Fujimoto
Nucl. Instr. Method A240 (1985) 115-121

Dynamically Polarized Proton Filter for a Low Energy Neutron Polarizer
Y. Masuda, S. Hiramatsu, S. Isagawa, M. Ishida, Y. Ishikawa S. Ishimoto, M. Kohgi, A. Masaike, K. Morimoto and T. Nakajima
Proc. 6th Int. Symp. on Polarization Phenomena in Nucl. Phys. (Osaka, 26-30 Aug. 1985) Supplement to Phys. Soc. Jpn. 55 (1986)

Development of Polarized Epithermal Neutron Spectromete PEN at KENS
M. Ishida, Y. Ishikawa, S. Ishimoto, M. Kohgi, A. Masaike Y. Masuda, K. Morimoto and T. Nakajima
Proc. ICANS-VIII, RAL-85-110, 2 (1985) 612

Crystal Structures

Refinement of the Structure of Ta_2D by High-Resolution Powder Neutron Diffraction
H. Murata, H. Asano, F. Izumi, S. Tomiyoshi, H. Iwasa, S. Sato and N. Watanabe
Trans. Jpn. Inst. Met. 26 (1985) 795

Neutron diffraction study on the low-temperature monoclinic form of $CeCu_6$
H. Asano, M. Umino, Y. Onuki, T. Komatsubara, F. Izumi and N. Watanabe
J. Phys. Soc. Jpn. 55 (1986) 454

Time-of-flight neutron diffraction study of Li_3N at high temperature
I. Kawada, M. Isobe, F. Okamura H. Watanabe K. Ohsumi, H. Horiuchi T. Sata and T. Ishii
Mineral. J., 13 (1986) 28

Structurs of Liquids and Glasses

High Resolution Short-range Structure of Ni-Ti and Cu-Ti Alloy Glasses by Pulsed Neutron Total Scattering
T. Fukunaga, K. Kai, M. Naka, N. Watanabe and K. Suzuki
Proc. 4th Int. nat'l Conf. Rapidly Quenched Metals (Sendai, Aug. 24-28, 1981) 347

Structure and Properties of Amorphous Metal Hydrides
K. Suzuki
J. Less-Common Met. 89 (1981) 183

Structure and Physical Properties of Amorphous (Fe, Co, Ni, Pd)-Zr Alloys
T. Mizoguchi, S. Yamada, T. Suemasa, J. Nishioka, N. Akutsu, N. Watanabe and S. Takayama
ibid. 363

Structure Modification of Pd-Zr Alloy Glasses due to Hydrogen Absorption
K. Kai, T. Fukunaga, T. Nomoto, N. Watanabe and K. Suzuki
ibid. 1609

Structure Characterization of Amorphous Alloys by T-O-F Pulsed Neutron Scattering using Accelerator Neutron Source
K. Suzuki
ibid. 309

Neutron Diffraction Study of Amorphous Binary Alloys
T. Mizoguchi, J. Nishioka, S. Yamada, T. Suemasa, S. Yoda, A. Akutsu, H. Narumi, T. Kudoh, M. Aimitsu, N. Watanabe, M. Nishi, and K. Motoya
J. de Physique 43 (1982) C9-659

Local Structures of Amorphous As-Chalcogenide Systems by Means of High-Q Neutron Scattering and Infrared Reflection
T. Arai, S. Onari, M. Kato, T. Mori, H. Saegusa, H. Yasuoka, M. Hatori. K. Ohkawa, T. Fukunaga and N. Watanabe
Physica 117B & 118B (1983) 965

Chemical Short-Range Structure of $Ni_x Ti_{1-x}$ (x=0.26-0.40) Alloy Glasses
T. Fukunaga, N. Hayashi, K. Kai, N. Watanabe and K. Suzuki
Physica 120B (1983) 352

Layer Correlation in $a\text{-}As_2 (Se_x S_{1-x})_3$ System
T. Mori, H. Yasuoka, H. Saegusa, K. Okawa, M. Kato, T. Arai, T. Fukunaga and N. Watanabe
Jpn. J. Appl. Phys. 22 (1983) 1784

Exprimental Determination of Partial Structures in $Ni_{40}Ti_{60}$ Glass
T. Fukunaga, N. Watanabe and K. Suzuki
J. Non-Cryst. Solids 61 & 62 (1984) 343

Hydrogen Atom Enviroment in A Hydrogenated ZrNi Glass
K. Suzuki, N. Hayashi, Y. Tomizuka, T. Fukunaga, K. Kai and N. Watanabe
J. Non-cryst. Solids 61 & 62 (1984) 637

Indirect and Direct Correlations Between Unlike Inons in Incomplitely Hydrated Solution
K. Ichikawa, Y. Kameda, T. Matsumoto and M. Misawa
J. Phys. C. Solid State 17 (1984) L 725

Partial Structure Functions of NiZi Alloy Glass Determined by an Isotope-Substitution Neutron Diffraction Methods
T. Fukunaga, N. Hayashi, N. Watanabe and K. Suzuki
Proc. 5th International Conf. Rapidly Quenched Metals, Elsevier Science Publishers B.V. (1985) 475

Compositional Variations in the Short-range Structure of $Ni_{1-x}B_x$ (x=0.18-0.40) Alloy Glasses
K. Suzuki, T. Fukunaga, F. Itoh and N. Watanabe
Proc. 5th International Conf. Rapidly Quenched Metals, Elsevier Science Publishers B.V. (1985) 479

Structure and Local Anisotropy of Amouphous Tb-Fe Alloys
S. Hatta, T. Mizoguchi and N. Watanabe
Proc. 5th International Conf. Rapidly Quenched Metals, Elsevier Science Publishers B.V. (1985)

Local Atomic and Magnetic Structures of Amorphous $Fe_{1-x}B_x$ Alloys Studied by Neutron Scattering
Ze Xianyu, Y. Ishikawa, T. Fukunaga and N. Watanabe
J. Phys. F : Met Phys. 15 (1985) 1799

Structural Analysis of Sodium Silicate Glasses Containing TiO_2 by Pulsed Neutron Scattering Measurement
H. Hidaka, N. Iwamoto, N. Umesaki, T. Fukunaga and K. Suzuki
J. Mat. Sci. 20 (1985) 2497-2502

The structure of same univalent metal nitrate melts studied by means of pulsed neutron diffraction
T. Yamaguchi, Y. Tamura, I. Okada, H. Ohtaki, M. Misawa and N. Watanabe
Z. Naturforsch. 40a, (1985)

What difference exists in the structure of SiO_2 and GeO_2 between melt-quenched bulk glass and sputter-deposited Amorphous film
K. Suzuki, M. Misawa and Y. Kobayashi
J. de Physique 46 (1985) C8-617

Magnetic Structures and Excitations

Studies on the Magnetism at the Surface and Interface Using Polalized Neutrons
Y. Endoh
J. de Physique C7 (1982) 159

Magnetism of Fe Interface Studied by Neutron Diffraction
Y. Endoh, H. Ono, N. Hosoito and T. Shinjo
J. Mag. Mag. Mater. 31-34 (1982) 881

Application of Neutron Diffraction to the Study of Interface Magnetization on Thin Films with Artificial Superlattices
Y. Endoh, N. Hosoito, and T. Shinjo
J. Mag. Mag. Mater 35 (1982) 93

Spin Glass Properties and Magnetic Correlation in $FeTiO_3$-Fe_2O_3 System
Y. Ishikawa, M. Arai, N. Saitoh, M. Kohgi and H. Takei
J. Mag. Mag. Mater. 31-34 (1983) 1381

Interface Magnetism of Fe-Sb Multilayer Films with Artificial Superstructure from ^{57}Fe and ^{121}Sb Mössbauer Spectroscopy, Neutron Diffraction and NMR Experiments
T. Shinjo, N. Hosoito, K. Kawaguchi, T. Tabata, Y. Endoh, Y. Ajiro and J. M. Friedt
J. Phys. Soc. Jpn. 52 (1983) 3154

Magnetic Properties of $Cr_{1/3}NbS_2$
M. Miyadai, K. Kikuchi, H. Kondo, S. Sakka, M. Arai and Y. Ishikawa
J. Phys. Soc. Jpn. 52 (1983) 1394

Magnetic Phase Diagram of MnSi near Critical Temperature Studied by Neutron Small Angle Scattering
Y. Ishikawa and M. Arai
J. Phys. Soc. Jpn. 53 (1984) 2726

Re-Entrant Spin-Glass Behavior of the Randomly Mixed Insulating Ferromagnet and Antiferromagnet, $Rb_2Mn_{(1-x)}Cr_xCl_4$
K. Katsumata, M. Tanimoto, S. Mitsuda and Y. Endoh
J. Phys. Soc. Jpn. 53 (1984) 3315

Magnetism of Iron Interface in Contact with Vanadium
T. Shinjo, N. Hosoito, K. Kawaguchi, T. Takada and Y. Endoh
J. de Phys. 45 (1984) C5-361

A New Oxide Spin Glass System of (1-x) $FeTiO_3$-xFe_2O_3 I. Magnetic Properties
Y. Ishikawa, N. Saito, M. Arai, Y. Watanabe and H. Takei
J. Phys. Soc. Jpn. 54 (1985) 312

A New Oxide Spin Glass System of (1-x) $FeTiO_3$-xFe_2O_3 II. Neutron Scattering Studies of a Cluster type Spin Glass $90FeTiO_3$-$10Fe_2O_3$
M. Arai, Y. Ishikawa, N. Saito and H. Takei
J. Phys. Soc. Jpn. 54 (1985) 781

A New Oxide Spin Glass System of (1-x) $FeTiO_3$-$10Fe_2O_3$ III. Neutron Scattering Studies of Magnetization Processes in a Cluster Type Spin Glass of 90 $FeTiO_3$-$10Fe_2O_3$
M. Arai and Y. Ishikawa
J. Phys. Soc. Jpn. 54 (1985) 795

A New Oxide Spin Glass System of (1-x) $FeTiO_3$-xFe_2O_3 IV. Neutron Scattering Studies on a Re-entrant Spin Glass of $79FeTiO_3$-$21FeO_3$ Single Crystal
M. Arai, Y. Ishikawa and H. Takei
J. Phys. Soc. Jpn. 54 (1985) 2279

Helicity of the Helical Spin Density Wave in MnSi - II polarized Neutron Diffraction
M. Ishida, Y. Endoh, S. Mitsuda, Y. Ishikawa, M. Tanaka and H. Takayashi
J. Phys. Soc. Jpn. 54 (1985) 2975

Neutron Depolarization Studies on Magnetization Process Using Pulsed Polarizing Neutrons
S. Mitsuda and Y. Endoh
J. Phys. Soc. Jpn. 54 (1985) 1570

Magnetic Properties of Fe-V Multi Layered Films with Artificial Superstructures
N. Hosoito, K. Kawaguchi, T. Shinjo, T. Takada and Y. Endoh
J. Phys. Soc. Jpn. 53 (1984) 2659

Evidence for the correlation of the magnetic inhomogeneous structure with the fluctuation of chemical composition in Fe-Ni invar alloys
S. Komura, T. Takeda and Y. Endoh
J. Mag. Mag. Mater 50 (1985) 69

Crystal chirality and Helicity of the Helical Spin Density Wave in MnSi II Polarized Neutron Diffraction.
M. Ishida, Y. Endoh, S. Mitsuda, Y. Ishikawa and M. Tanaka
J. Phys. Soc. Jpn. 54 (1985) 2975-2982

Time of Flight Spectrometer with Optical Polarizer for Cold pulsed Neutrons
Y. Endoh, S. Mitsuda, S. Ikeda and H. Fujimoto
Nucl. Instr. & Meth. A 240 (1985) 115-121

Pulsed Polarized Neutron Studies
Y. Endoh and Y. Ishikawa
Physica 136 B (1985) 64-69

Magnetic Properties of Artificial Metallic Superlattices
T. Shinjo, N. Hosoito K. Kawaguchi, N. Nakayama, T. Takada and Y. Endoh
J. Magn. & Magn. Mater. 54-57 (1985) 737-742

Stability and Winding of the Long Period Helical Spin Structure in $Fe_{1-x}Co_xSi$.
K. Ishimoto, Y. Yamaguchi, S. Mitsuda, M. Ishida and Y. Endoh
J. Magn. & magn. Mater. 54-57 (1985) 1003-1004

Neutron Scattering Study on Artificial Metallic Superlattices
Y. Endoh
Applied Magnetism Seminar. (1986) 37-43

Spin Dynamics in a Quasi 2-Dimensional Antiferromagnet $MnTiO_3$
Y. Todate, Y. Ishikawa, K. Tajima, S. Tomiyoshi and F. Takei
J. Phys. Soc. Jpn 55 (1986) in press

Dynamics in Solids and Liquids

The Local Environment around Hydrogen Atoms in Hydrogenated $NiTi_2$ Alloy Glass
K. Kai, S. Ikeda, T. Fukunaga, N. Watanabe and K. Suzuki
Physica 120B (1983) 342

Neutron Compton Spectroscopy of Pyrolitic Graphite
H. Rauh and N. Watanabe
Phys. Lett. 100A (1984) 224

High-Q Neutron Scattering with the Resonance Detector Neutron Spectrometer RAT at the Pulsed Spallation Neutron Source KENS
H. Rauh and N. Watanabe
Presented at Symp. neutron Scattering (Berlin, Aug. 6-8, 1984)

Determination of the Momentum Distribution of Scattering Particles from High Q Scattering Spectra of a Resonance Detector Neutron Spectrometer
H. Rauh and N. Watanabe
Nucl. Instr. Meth. 228 (1984) 147

Low energy excitations in Ag_3SI
K. Shibata and S. Hoshino
J. Phys. Soc. Jpn. 54 (1985) 3671

Polymers and Biology

Compensation Point in Semi-Dilute Polymer Solutions as Observed by SANS
K. Okano, K. Kurita, S. Nakajima, E. Wada, M. Furusaka and Y. Ishikawa
Physica 120B (1983) 413

Small Angle Neutron Scattering Studies of the Structure of Nucleosome Cores at Low Ionic Strength
K. Mita, M. Zama, S. Ichimura, N. Niimura, K. Kaji, M. Hirai and Y. Ishikawa
Physica 120B (1983) 436

Neutron Quasi-elastic Scattering Studies of Molecular Liquids and Polymers by Pulsed Cold Neutron Source
K. Inoue, Y. Kiyanagi, M. Kohgi and K. Kaji
Physica 120B (1983) 422

Folding-Unfolding of α-Lactalbumin
Y. Izumi, Y. Miyake, K. Kuwajima, S. Sugai, K. Inoue, M. Iizumi and S. Katano
Physica 120B (1983) 444

Neutron Inelastic Scattering Spectra of Native and Regenerated Celluloses
K. Kaji, T. Kanaya, K. Inoue, R. Kitamaru and I. Sakurada
Cellulose Chem. Technol. in Press

Molecular Spectroscopy of Polymers
K. Kaji, T. Kanaya and K. Inoue
Proc. 1st SPSJ Int. Polymer Conf. (KYoto, Aug. 20-24, 1984)

Non-Equilibrium Systems

Spinodal Decomposition in Fe-Cr Alloys Studied by Small Angle Neutron Scattering
M. Furusaka, Y. Ishikawa, Y. Yamaguchi and Y. Fujino
Physica 120B (1983) 383

Early stage of phase separation proccesses in FeCr and AlZn alloys
M. Furusaka, Y. Ishikawa and M. Mera
Phys. Rev. Lett. 54 (1985) alloys 2611

Publications in Japanese

Pulsed Spallation Neutron Source and Neutron Scattering at KEK
N. Watanabe, H. Sasaki and Y. Ishikawa
J. At. Energy Soc. Jpn. 23 (1981) 389

Neutron Position Sensitive Detector using ^{6}Li-glass Scintillator
N. Niimura
J. Cryst. Soc. Jpn. (1982) 396

Neutron Scattering Studies on Biological Materials (I),(II),(III),(IV)
N. Niimura and H. Kaji
Chemistry and Biology 21 (1983) 250, 328, 405, 466

Neutron Scattering Facility at National Laboratory for High Energy Physics
N. Watanabe and Y. Ishikawa
Butsuri 39 (1984) 826

Neutron Scattering Instruments at National Laboratory for High Energy Physics
N. Watanabe
J. Cryst. Soc. Jpn. 26 (1984) 294

High Intensity Proton Synchrotron GEMINI and Intense Pulsed Neutron Source KENS-II
H. Sasaki and N. Watanabe
Spallation Neutron Engineering, Atomic Energy Society Japan (1984) 173

Generation and Utilization of Ultra-Cold Neutrons, Application in Condensed Matter Research and Elementary Particle Physics
M. Utsuro and H. Yoshiki
Gekkan Physics 5 (1984) 135

Structural Studies of Materials by Neutron Diffraction
H. Horiuchi and I. Kawada
Ceramics 19 (1984) 658

Pulsed Neutron Source and its Utilization in Condensed Matter Research
N. Watanabe
Gekkan Physics 5 (1984) 127

Neutrons in Biology
N. Niimura
Gekkan Physics 5 (1984) 96

Accelerator Based Cold Neutron Source and Cryogenic System
K. Inoue, M. Yanai and Y. Ishikawa
Cryogenic Eng. 20 (1985) 63

Spin Glasses in Dense Random System
Y. Ishikawa
Solid State Phys. 20 (1985) 229

Direct Observation of Bose Condensation in ^{4}He-II by Neutron Scattering with Very Large Momentum Transfer
N. Watanabe and S. Ikeda
Butsuri 40 (1985) 283

List of Proposals accepted through 1983-1985

FOX

58-B1-7
I. Kawada, National Institute for Research in Inorganic Materials; Studies of Phase Transitions using Single Crystal Diffractometer.
60-B1-7
I. Kawada, National Institute for Research in Inorganic Materials; Studies of Phase Transitions using Single Crystal Diffractometer.

HIT

58-B1-1
N. Watanabe, KEK ; Structure studies of disordered system by neutron total scattering.
58-B2-2
H. Ootaki, Tokyo Inst. of Technology ; Structure of liquids and electrolyte solutions.
58-B2-3
T. Kudoh , Gakushuin Univ. ; Structure of Ni-Zr and Ni-Hf alloy glasses .
58-B2-4
S. Tamaki, Niigata Univ. ; Neutron diffraction of liquid Bi-Ga alloy.
58-B2-5
K. Suzuki, Tohoku Univ. ; Structural study of Bi_2O_3 based oxide glasses.
58-B2-6
S. Hatta, Gakushuin Univ. ; Photostructural change in As_2S_3 glass by neutron diffraction.
58-B2-7
M. Sakata, Nagoya Univ. ; Chemical short range structure of $^{60}Ni_{60}Nb_{40}$ alloy glass.
58-B2-8
K. Ichikawa , Hokkaido Univ. ; Structural relaxation of network structure glass near glass transition temperature.
58-B2-9
Y. Miyake, Hokkaido Univ. ; Short range order in a binary critical mixture.
58-B2-10
T. Kuzumegi, KEK ; Structural study of dense liquids.
60-B1-1
M. Misawa , KEK; Structure Study of Liquids and Amorphous Solids by Neutron Total Scattering
60-B2-1
J. Mochinaga, Faculty of Engineering, Chiba Univ. ; Structure of Molten Potassium Hydrosulfide.
60-B2-2
H. Ootaki, Tokyo inst. of technology ; Structure of LiCl-NaCl-KCl molten salt.
60-B2-3
Y. Endoh, Kyoto Univ. ; structure of one dimensional atomic chain in Molderite.
60-B2-4
I. Yasui, Univ. of Tokyo ; Structure of Oxide Glasses including Heavy Metallic Ions.
60-B2-5
K. Suzuki, Tohoku Univ. ; Structure of mercury-alkali metalliquid alloy.
60-B2-6
K. Ichikawa, Hokkaido Univ. ; Structure Analysis of Dense LiCl Solution and a-$Ge_{20}Te_{80}$ near Glass Transition Temperature using Isotope Substitutes.

HRP/MRP

58-A1-6
H. Asano, Tsukuba Univ. ; Construction of Medium Resolution Powder Diffractometer (MRP).
58-A2-3

N. Watanabe, KEK ; Construction of High Resolution Powder Diffractometer (HRP).
60-B1-9
N. Watanabe, KEK ; High Resolution Powder Diffractometry
60-B1-10
H. Asano, Tsukuba Univ. ; Structure study by MRP
60-B2-25
T. Komatsubara, Tsukuba Univ. ; Structure analysis of $LaCu_6$ and $CeCu_6$
60-B2-26
M. Hirabayashi, Tohoku Univ. ; Powder Diffractometry of Ti_5Si_3 and Ti_5SiD
60-B2-27
K. Suzuki, Tohoku Univ. ; Engineering application of neutron diffraction
(1) Internal strain in Mn-Steel gas tank.
60-B2-28
K. Kosuge, Kyoto Univ. ; Cation distribution in $(M'_xM_{1-x})_3Se_4$.
60-B2-29
T. Shinohara, Tohoku Univ. ; Study on defect structure of cold - worked Pd_2MnSn by neutron diffraction
60-B2-30
M. Koiwa , Tohoku Univ. ; Structure analyses of γ - TiD.

INC

60-A1-8
M. Kohgi, Tohoku Univ. ; A Development of Chopper Spectrometer

LAM

58-B1-4
K. Inoue, Dep. Nuclear Eng., Facul. Eng., Hokkaido Univ. ; Neutron scattering Studies of Random and Low Energy Modes in Molecular System.
58-B2-26
Y. Ito, Institute for Solid State Physics, Univ. of Tokyo ; Studies of Constrained Dynamics of the Phase Transition if the Artificial Bilayer Membrance of Dialkyl Ammonium Ammpliphile.
58-B2-27
S. Hoshino, Institute for Solid State Physics , Univ. of Tokyo ; Study of Structure and Dynamics in Random System.
58-B2-28
Y. Miyake, Dep, Polymer Science, Facl. of Science , Hokkaido Univ. ; A study of molecular motions near coexistent faces of a binary solution.
58-B2-30
S. Yamaguchi, Dep. of Nuclear Eng., Facul. Eng., Tohoku Univ. ; A study of hydrogen atoms by lattice defects in BCC metals.
58-B2-32
R. Kitamaru, Institute for Chemical Research, Kyoto Univ. ; Local motions of polysthylene on Solution.
60-B1-4
K.Inoue, Faculty of Eng., Hokkaido Univ. ; Neutron scattering studies of fluctuational and low energy modes in condensed matters.
60-B2-16
Y.Ito, Inst. for Solid State Physics, Univ. of Tokyo ; Studies of constrained dynamics of the phase transition on the artificial bilayer menbrance of dialkyl ammonium anpliphile.
60-B2-17
S. Yamaguchi, Dep. of Nuclear Eng., Facul. Eng., Tohoku Univ. ; Interaction between hydrogen and impuridies in V group metals.
60-B2-19
M. Arai KEK ; Fracton measurement in Epoxy Resin.

60-B2-20
R. Kitamaru, Institute for Chemical Research, Kyoto Univ. ; Local Motions in Deuterated Polyethylene.
60-B2-21
M. Misawa , KEK ; A study on glass transition by means of neutron quasielastic scattering.
60-B2-22
S. Hoshino, Institute for Solid State Physics , Univ. of Tokyo ; Neutron scattering study of dynamics in random system.
60-B2-23
Y. Miyake, Dep. Polymer Science, Facul. of Science , Hokkaido Univ. ; A study of motional modes of polymer molecules in solution by neutron quasielastic scattering.
60-B2-24
Y. Nakamura, Dep. Chem., Facul. Sci., Hokkaido Univ. ; Molecular motion of solvent molecules in concentrated $ZnCl_2$ solutions.
60-urgent-2
Y. Abe , Dep. Nucl. Eng., Facul. Eng., Hokkaido Univ. ; Phonons in Layered Semiconductor InSe.

MAX

58-B1-6
Y. Ishikawa, Tohoku Univ. ; Study of elementary excitation in Non-equilibrium system with MAX.
60-B1-6
Y. Ishikawa, Tohoku Univ. ; Study of high energy excitations with Epi-thermal neutrons.

PEN

58-B1-5
Y. Ishikawa, Tohoku Univ. ; Neutron scattering using Epi-thermal Polarized Neutron.
60-B1-5
Y. Ishikawa, Tohoku Univ. ; Neutron scattering using Epi-thermal Polarized Neutron.

RAT

58-A2-1
N. Watanabe, KEK ; Development of a crystal analyzer type epithermal neutron spectrometer.
60-B1-8
N. Watanabe, KEK ; High Energy and High Momentum Transfer Neutron Scattering in Condensed Matter using an eV Neutron Spectrometer.

SAN

58-B1-2
Y. Ishikawa, Faculty of Science, Tohoku University ; Study of Macro Structure of Condensed Matters, especially the Time Evolutions of Them by Cold Neutron Small Angle Scattering
58-B2-11
S. Yabuki, Gunma Univ. ; Structure Analysis of Tri-Phosphoinocitid-water system
58-B2-13
H. Inoue, National Institute of Agrobiological Resources ; Small Angl Neutron Scattering Measurements of Rice Dwarf Virus
58-B2-16
K. Mita, National Institute of Radiological Sciences ; Structure analysis of Nucleosome Core Particles
58-B2-17
T. Hamanaka, Osaka Univ. ; Study on the Structure of Disk Membrane by Neutron Diffraction -- Determination of the position of the Retinal.
58-B2-19
H. Okano, Faculty of Engineering Tokyo University ; Structure of Polyelectrolyte in a Semi-dilute

Solution
58-B2-20
K. Katsumata, Faculty of Science, Hokkaido University ; Study of Insulator Spinglass by Neutron Scattering
60-B1-2
Y. Ishikawa, Faculty of Science, Tohoku University ; Study of Macro Structure of Condensed Matters, especially the Time Evolutions of Them by Cold Neutron Small Angle Scattering
60-B2-7
K. Mita National Institute of Radiological Sciences ; Structure analysis of Nucleosome Core Particles
60-B2-8
M. Arai National Laboratory for High Energy Physics ; Study of Fructal Structure in Epoxy Resin
60-B2-9
H. Okano , Faculty of Engineering, Tokyo University ; Structure of Polyelectrolyte in a Semi-dilute Solution
60-B2-10
H. Inoue, National Institute of Agrobiological Resources ; Small Angle Neutron Scattering Measurements of Rice Dwarf Virus
60-urgent-1
T. Satoh, Faculty of Science, Tohoku University ; Study of Spin Fluctuations in Dense Kondo Alloy CeSix

TOP

58-A2-4
Y.Endoh, Tohoku Univ. ; μeV Spectroscopy using Polarized neutrons.
58-B1-3
Y. Endoh, Tohoku Univ. ; Polarized neutron scattering with TOP.
58-B2-23
A. Itoh, Ochanomizu Univ. ; Determination of domain distribution and magnetization process in amorphous ferromagnets.
58-B2-24
Y. Yamaguchi, Tohoku Univ. ; Helicity determination of H.S.D.W. in $Fe_{1-x}Co_xSi$.
58-B2-25
S. Komura, Hiroshima Univ. ; Polarized neutron small angle scattering from FeNi invar alloy.
60-A2-1
Y.Endoh, Tohoku Univ. ; μeV Spectroscopy using Polarized neutrons.
60-B1-3
Y. Endoh, Tohoku Univ. ; Polarized neutron scattering studies with TOP
60-B2-14
H. Katsumata, Tohoku Univ. ; Polarized neutron studies form random magnet.
60-B2-15
Y. Yamaguchi, Tohoku Univ. ; Helicity determination of H.S.D.W. in $Fe_{1-x}Co_xSi$.
60-B2-31
S. Komura, Hiroshima Univ. ; Small angle scattering with polarized beams from FeNi invar alloy.

UCN

58-A2-2
H. Yoshiki, KEK; Generation and Storage of Ultra Cold Neutrons by means of HeII.
60-A2-2
H. Yoshiki, KEK; Generation and Storage of Ultra Cold Neutrons by mean of HeII.

WIT

60-A1-7
N. Niimura, Laboratory of Nuclear Science Tohoku Univ. ; Development and Construction of Thermal Neutron Small Angle Scattering Instrument WIT.